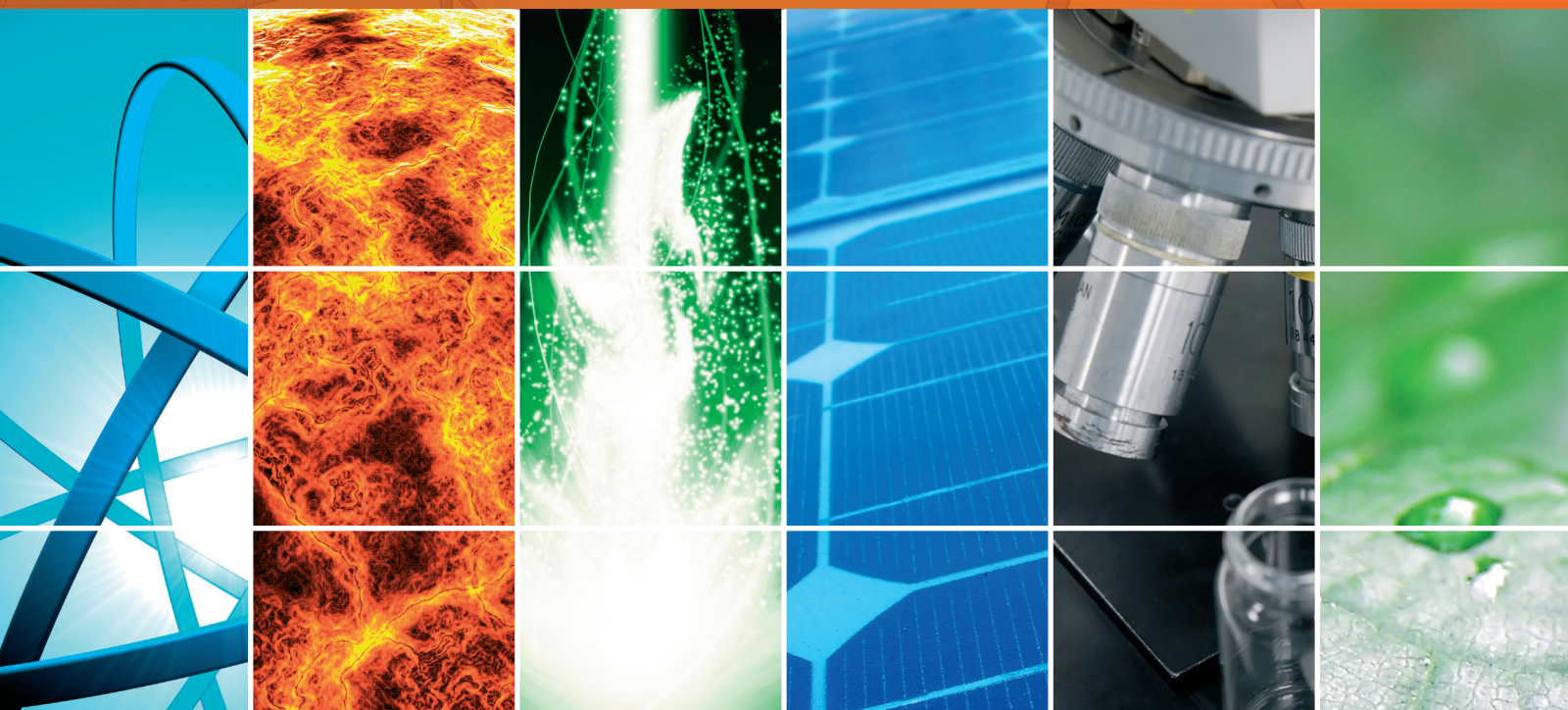


Towards Sustainability: Photochemical and Electrochemical Processes Applied for Environmental Protection

Lead Guest Editor: Reyna Natividad

Guest Editors: Carlos B. Díaz, Carlos A. Martínez-Huitle,
and Juan M. R. Rodriguez





Towards Sustainability: Photochemical and Electrochemical Processes Applied for Environmental Protection

Towards Sustainability: Photochemical and Electrochemical Processes Applied for Environmental Protection

Lead Guest Editor: Reyna Natividad

Guest Editors: Carlos B. Díaz, Carlos A. Martínez-Huitle,
and Juan M. R. Rodriguez



Copyright © 2018 Hindawi. All rights reserved.

This is a special issue published in “International Journal of Photoenergy.” All articles are open access articles distributed under the Creative Commons Attribution License, which permits unrestricted use, distribution, and reproduction in any medium, provided the original work is properly cited.

Editorial Board



M. S.A. Abdel-Mottaleb, Egypt
Angelo Albini, Italy
Alberto Álvarez-Gallegos, Mexico
Vincenzo Augugliaro, Italy
Detlef W. Bahnemann, Germany
Simona Binetti, Italy
Fabio Bisegna, Italy
Thomas M. Brown, Italy
Joaquim Carneiro, Portugal
Yatendra S. Chaudhary, India
Věra Cimrová, Czech Republic
Juan M. Coronado, Spain
P. Davide Cozzoli, Italy
Dionysios D. Dionysiou, USA
Abderrazek Douhal, Spain
Mahmoud M. El-Nahass, Egypt
Polycarpos Falaras, Greece
Chris Ferekides, USA
Paolo Fornasiero, Italy
Manuel Fuentes Conde, Spain

Germà Garcia-Belmonte, Spain
Elisa Isabel Garcia-Lopez, Italy
M. Ashraf Gondal, Saudi Arabia
Giulia Grancini, Switzerland
Pierluigi Guerriero, Italy
Michael D. Heagy, USA
Wing-Kei Ho, Hong Kong
Jürgen Hüpkens, Germany
Mohammad Tariq Iqbal, Canada
Adel A. Ismail, Kuwait
Chun-Sheng Jiang, USA
Cooper H. Langford, Canada
Manuel Ignacio Maldonado, Spain
Santolo Meo, Italy
Claudio Minero, Italy
Antoni Morawski, Poland
Fabrice Morlet-Savary, France
Mohammad Muneer, India
Maria da Graça P. Neves, Portugal
Tsuyoshi Ochiai, Japan

Kei Ohkubo, Japan
Leonardo Palmisano, Italy
Thierry Pauporté, France
Philippe Poggi, France
Francesco Riganti-Fulginei, Italy
Leonardo Sandrolini, Italy
Jinn Kong Sheu, Taiwan
Zofia Stasicka, Poland
Elias Stathatos, Greece
Jegadesan Subbiah, Australia
K. R. Justin Thomas, India
Nikolai V. Tkachenko, Finland
Ahmad Umar, Saudi Arabia
Thomas Unold, Germany
Mark van Der Auweraer, Belgium
Wilfried G.J.H.M. Van Sark, Netherlands
Xuxu Wang, China
Huiqing Wen, China
Yanfa Yan, USA
Jiangbo Yu, USA

Contents


Towards Sustainability: Photochemical and Electrochemical Processes Applied for Environmental Protection

Reyna Natividad , Carlos Barrera-Díaz , Carlos A. Martínez-Huitile ,
and Juan M. Rodríguez-Rodríguez 
Editorial (3 pages), Article ID 4834652, Volume 2018 (2018)


Synthesis and Characterization of TiO₂/SiO₂ Monoliths as Photocatalysts on Methanol Oxidation

Rigoberto Regalado-Raya, Rubí Romero-Romero , Osmín Avilés-García , and Jaime Espino-Valencia 
Research Article (8 pages), Article ID 8478240, Volume 2018 (2018)


Treatment of a Textile Effluent by Electrochemical Oxidation and Coupled System Electrooxidation–*Salix babylonica*

Alejandra Sánchez-Sánchez, Moisés Tejocote-Pérez, Rosa María Fuentes-Rivas, Ivonne Linares-Hernández, Verónica Martínez-Miranda, and Reyna María Guadalupe Fonseca-Montes de Oca 
Research Article (12 pages), Article ID 3147923, Volume 2018 (2018)


Pretreatment of Real Wastewater from the Chocolate Manufacturing Industry through an Integrated Process of Electrocoagulation and Sand Filtration

Marco A. García-Morales , Julio César González Juárez, Sonia Martínez-Gallegos, Gabriela Roa-Morales, Ever Peralta, Eduardo Martín del Campo López, Carlos Barrera-Díaz, Verónica Martínez Miranda, and Teresa Torres Blancas
Research Article (7 pages), Article ID 2146751, Volume 2018 (2018)


ID TiO₂ Nanostructures Prepared from Seeds Presenting Tailored TiO₂ Crystalline Phases and Their Photocatalytic Activity for *Escherichia coli* in Water

Julieta Cabrera, Dwight Acosta, Alcides López, Roberto J. Candal, Claudia Marchi, Pilar García, Dante Ríos, and Juan M. Rodríguez 
Research Article (6 pages), Article ID 1862597, Volume 2018 (2018)



Photocatalytic Activity under Simulated Sunlight of Bi-Modified TiO₂ Thin Films Obtained by Sol Gel

D. A. Solís-Casados , L. Escobar-Alarcón, V. Alvarado-Pérez, and E. Haro-Poniatowski
Research Article (9 pages), Article ID 8715987, Volume 2018 (2018)


Photovoltaic Energy-Assisted Electrocoagulation of a Synthetic Textile Effluent

Thelma Beatriz Pavón-Silva , Hipólito Romero-Tehuiztil, Gonzálo Munguia del Río, and Jorge Huacuz-Villamar
Research Article (9 pages), Article ID 7978901, Volume 2018 (2018)

A Comparative Analysis of 2-(Thiocyanomethylthio)-Benzothiazole Degradation Using Electro-Fenton and Anodic Oxidation on a Boron-Doped Diamond Electrode

Armando Vázquez, Lucía Alvarado, Isabel Lázaro , Roel Cruz, José Luis Nava, and Israel Rodríguez-Torres 
Research Article (9 pages), Article ID 5290975, Volume 2018 (2018)

The Effect of Microcrack Length in Silicon Cells on the Potential Induced Degradation Behavior

Xianfang Gou, Xiaoyan Li, Shaoliang Wang, Hao Zhuang , Xixi Huang, and Likai Jiang
Research Article (6 pages), Article ID 4381579, Volume 2018 (2018)

Modelling and Simulation of the Radiant Field in an Annular Heterogeneous Photoreactor Using a Four-Flux Model

O. Alvarado-Rolon, R. Natividad , R. Romero , L. Hurtado , and A. Ramírez-Serrano 

Research Article (16 pages), Article ID 1678385, Volume 2018 (2018)

Determination of Ketorolac in the Effluent from a Hospital Treating Plant and Kinetics Study of Its Photolytic Degradation

Hector Hugo Ortega Soto, Jorge Javier Ramírez García, Paula Gamboa Suárez,
and Angie Michelle Dávila Estrada

Research Article (9 pages), Article ID 6781310, Volume 2017 (2018)

Editorial

Towards Sustainability: Photochemical and Electrochemical Processes Applied for Environmental Protection

Reyna Natividad ¹, Carlos Barrera-Díaz ¹, Carlos A. Martínez-Huitle ^{2,3},
and Juan M. Rodríguez-Rodríguez ⁴

¹Centro Conjunto de Investigación en Química Sustentable UAEM-UNAM, km 14.5 Carr. Toluca-Atlaconulco, Universidad Autónoma del Estado de México, Toluca, MEX 50200, Mexico

²Universidade Federal do Rio Grande do Norte, Campus Universitário s/n, Lagoa Nova, 59078-970 Natal, Brazil

³Unesp, National Institute for Alternative Technologies of Detection, Toxicological Evaluation and Removal of Micropollutants and Radioactives (INCT-DATREM), Institute of Chemistry, P.O. Box 355, 14800-900 Araraquara, SP, Brazil

⁴Universidad Nacional de Ingeniería, Av. Tupac Amaru 210, Lima, Peru

Correspondence should be addressed to Reyna Natividad; reynanr@gmail.com, Carlos Barrera-Díaz; cebarrerad@uaemex.mx, Carlos A. Martínez-Huitle; mhuitle@hotmail.com, and Juan M. Rodríguez-Rodríguez; jrodriguez@uni.edu.pe

Received 13 May 2018; Accepted 13 May 2018; Published 23 September 2018

Copyright © 2018 Reyna Natividad et al. This is an open access article distributed under the Creative Commons Attribution License, which permits unrestricted use, distribution, and reproduction in any medium, provided the original work is properly cited.

In the last century, public policy around the globe was mainly focused on economic growth leaving out of this perspective, social concerns and the environment detriment that this merely economic approach was causing. It was until the last quarter of the 20th century that people started to be aware of the growing poverty and of the jeopardy of the planet as a result of human being activities. In consequence, the concept of sustainable development emerged in the United Nations as a call to all countries to integrate economic growth with social needs and environmental protection, in such a way that our activities as earth inhabitants stopped compromising the quality of life and needs satisfaction of future generations.

More recently, in 2016, effective 17 sustainable development goals established within the United Nations came officially. The embracement of these goals implies the design and execution of strategies that pursue poverty elimination by also addressing social needs and environmental protection. In this sense, the development of cleaner technologies and more effective sanitation systems is imperative and this has motivated the assessment of new technologies, many of them based on photochemical and electrochemical phenomena. Thus, this special issue aims to present original results

regarding relevant aspects of such processes. For this purpose, ten manuscripts have been included.

Within the framework of photochemical processes, different issues were addressed ranging from novel photocatalysis approaches, photocatalyst synthesis improvements, emerging contaminant degradation, and photoreactor modeling and simulation.

Although TiO_2 has been the preferred and therefore most assessed photocatalyst by the scientific community, the manuscripts included in this special issue show that there is still enough room for improvement taking as base such a material. Currently, one of the most important challenges regarding this material, that is, shifting its activation wavelength towards the visible region, is successfully addressed by synthesizing Bi-modified TiO_2 films where the bismuth titanates were found to be responsible of the improvement exhibited by photoactivity under simulated solar radiation.

By the first time, the synthesis and characterization of SiO_2 monoliths coated with TiO_2 was presented. This type of materials opens a window of photocatalytic process improvement not only from the point of view of photocatalysis but also from the corner of photoreactor design. Because of the exhibited characteristics, this type of material allows

to conduct multiphase photoreactions in packed bed reactors under different flow regimes with the consequent effect on yield and selectivity. In this matter, the use of photocatalysis beyond organic compound removal has been also demonstrated but the oxidations were selectively conducted, achieving the selective production of formaldehyde from the photooxidation of methanol.

Regardless of the resulting material, it is observed that the sol-gel method remains as the preferred one for the photocatalyst synthesis and it can be also used as complementary step of the hydrothermal method to obtain 1D TiO_2 . It was shown that crystalline phase ratio, that is, anatase-rutile, not only dictates the well-known photoactivity of TiO_2 to conduct oxidation reactions but also the resulting 1D TiO_2 shape (tubes or rods) and the bactericidal effect by using 1D photocatalyst. Interestingly, the effect of the morphology, tubes or rods, of the synthesized 1D TiO_2 is strongly correlated to the anatase-rutile ratio generated in the seeds by adjusting the pH and type of acid during the first step of the sol-gel method, hydrolysis.

An important issue within effluent sanitation is emerging contaminants. The challenge in this regard is not only their removal but also their detection. At this point, it is worth noticing that the adjective “emerging” does not mean that these compounds did not exist but that they were not actually detected by the available analytical techniques some decades ago. Thus, little or no attention was given to their detrimental effects on the environment. As fatal consequence, many compounds were not included in the current environmental legislations around the world so industries and many other service providers do not yet pay attention on their adequate disposal. Within this group of emerging contaminants, the widely used nonsteroidal anti-inflammatory drugs (NSAID) can be found. This is one of the topics that one of the included manuscripts focuses on. The results therein not only demonstrate that ketorolac (an NSAID) can be photochemically degraded but also, by analyzing a hospital effluent in a developing country and establishing a correlation with elsewhere published studies regarding toxicity, urge the update of environmental legislation in developing countries not only to regulate the pollutant discharge but also mainly to motivate the update of current treatment plants with the implementation of cutting-edge technologies, either photochemical or electrochemical. Interestingly enough, it also shows the feasibility of quantifying ketorolac by working out an adequate analytical method using standard techniques rather than sophisticated and expensive ones.

When dealing with chemical reactions activated by any source of energy, one should not forget the process core, the reactor. A nonadequate reactor design can lead to the subutilization of even the most efficient catalyst. An important tool on designing a reactor and elucidating the effect of reaction variables is modeling and simulation. This has been applied in one of the included manuscripts, not only to establish a relative simple mathematical model of an annular photoreactor but also to show the important variables whose effect should be observed at the time of assessing a photocatalyst. The established model managed to represent the radiant field within an annular photoreactor with high accuracy.

It also shows how the radiant field determines the permissible photocatalyst loading. Therefore, the presented results highlight the importance of optimizing both, radiant field and catalyst concentration, when assessing photoactivity or a photoprocess efficiency.

This special issue also deals with the assessment of electrochemical processes for environmental protection. In this context, the potential and importance of electrochemical processes are evidenced by the treatment of effluents of three different industries, paper, textile, and food. These works pursue the removal of organic compounds either by electrooxidation, electro-generated oxidant species, or by electrocoagulation. Within these works, a constant search for the improvement of existent electrochemical processes by applying innovative strategies such as coupling them with phytoremediation, for instance, can be appreciated. Although the latter did not lead to an improvement on chemical oxygen demand decrease, it was shown that it makes a significant difference on the total color and turbidity removal of a textile industry effluent. In another study, the efficiency of anodic oxidation conducted with boron diamond-doped electrodes was contrasted with electro-Fenton and the superiority of the former was established. Regarding the food industry effluent (chocolate manufacturing plant), the coupling of an electrocoagulation process with a filtration unit was concluded to be an alternative of pretreatment for such wastewater in order to significantly improve water quality.

For long time, both photochemical and electrochemical processes were highly criticized and their application was limited due to the required input of energy, to energize either an array of lamps or electrodes. It is undeniable that this aspect decreases, in many cases, the sustainability of a process. However, a twist of facts has been originated by the commercialization of solar photovoltaic modules. This topic is being addressed in one of the manuscripts by showing the feasibility of conducting an electrocoagulation process by using solar photovoltaic modules. Such research highlights the importance of correlating effluent residence time with current intensity and organic compound removal rate. As expected, current intensity was dependent on solar radiation and this fact motivates the further search of materials and devices capable of harvesting solar energy in a more efficient way than the existent ones. In this matter, a work that presents the effect of microcracks in silicon cells on the output power of the module is also included. Such work is a call to carefully look for microcracks in photovoltaic modules since they lead to current leakage.

Finally, it can be concluded that the recent results are sound and promising, even when important advances have been achieved by photochemical and electrochemical processes in the last decades; nevertheless, there are still challenges that deserve special attention in order to further strengthen one of the three pillars of sustainability and environmental protection.

Acknowledgments

We would like to express gratitude to all reviewers that, through their valuable comments, improved the overall

quality of the manuscripts submitted to this special issue. We also acknowledge all authors for their contributions. Reyna Natividad and Carlos Barrera-Díaz are grateful to CONACYT (SNI and Project 168305), Mexico. Carlos A. Martínez-Huitle is grateful to National Council for Scientific and Technological Development (CNPq 465571/2014-0, 446846/2014-7, and 401519/2014-7) and FAPESP (2014/50945-4), Brazil. Juan M. Rodríguez-Rodríguez is grateful to MINEDU-CONCYTEC, Peru.

Reyna Natividad
Carlos Barrera-Díaz
Carlos A. Martínez-Huitle
Juan M. Rodríguez-Rodríguez

Research Article

Synthesis and Characterization of $\text{TiO}_2/\text{SiO}_2$ Monoliths as Photocatalysts on Methanol Oxidation

Rigoberto Regalado-Raya,¹ Rubí Romero-Romero ,² Osmín Avilés-García ,¹ and Jaime Espino-Valencia ¹

¹Facultad de Ingeniería Química, Universidad Michoacana de San Nicolás de Hidalgo, Edif. V1, Ciudad Universitaria, 58060 Morelia, Michoacán, Mexico

²km 14.5 Carretera Toluca-Atacomulco, San Cayetano, Piedras Blancas, Centro Conjunto de Investigación en Química Sustentable UAEMéx-UNAM, Toluca, Estado de México, Mexico

Correspondence should be addressed to Jaime Espino-Valencia; jespinova@yahoo.com.mx

Received 21 July 2017; Revised 6 November 2017; Accepted 13 March 2018; Published 23 September 2018

Academic Editor: Juan M. Rodriguez

Copyright © 2018 Rigoberto Regalado-Raya et al. This is an open access article distributed under the Creative Commons Attribution License, which permits unrestricted use, distribution, and reproduction in any medium, provided the original work is properly cited.

Photocatalytic materials based on silica-titania ($\text{SiO}_2\text{-TiO}_2$) were synthesized by sol-gel and dip-coating method. TEOS and titanium butoxide were used as precursors of the silica-titania, respectively. A thin film with anatase phase was obtained on the surface of the support. The effect of variables as dispersion mechanism, immersion time, and number of treatment cycles were studied. The materials were characterized using X-ray diffraction, scanning electron microscopy, energy dispersion scanning, and N_2 adsorption-desorption. The highest crystallinity of TiO_2 on silica, high specific surface area in $\text{TiO}_2\text{-SiO}_2$ materials, and thin film formation were obtained by using a stirring plate and minimum immersion time. The so synthesized catalyst allowed the production of formaldehyde from the photocatalyzed methanol oxidation in a packed-bed reactor.

1. Introduction

Among the advanced oxidation processes (AOPs), heterogeneous photocatalysis has been widely applied in the degradation of organic compounds, hydrogen production from water, reduction of heavy metals, and selective oxidation reactions [1–4]. Selective oxidation of alcohols to aldehydes by photocatalysis is an attractive route because it can be carried out under mild conditions (room temperature, atmospheric pressure, and neutral pH) [5, 6]; particularly, formaldehyde is a highly important intermediate compound in the chemical industry because of its use in the synthesis of adhesives, fertilizers, pyridines, drugs, polyols, and dyes among others [7, 8]. The industrial production of formaldehyde is performed from the oxidation and dehydrogenation of methanol with iron molybdate and silver catalysts, respectively [9, 10].

The most studied semiconductor in the field of heterogeneous photocatalysis is titanium dioxide (TiO_2) due to its high oxidative capacity, nontoxicity, low cost, high chemical and physical stability, corrosion resistance, and chemical inertness [11, 12]. TiO_2 has been widely used in both powders and thin films [13, 14]. When it is used as suspended particles, a separation step such as filtration or centrifugation is required at the end of the process. For this reason, the immobilization of the particles in an appropriate substrate has attracted great interest [15].

There are several methods for the preparation of TiO_2 thin films, and the physicochemical properties strongly depend on the selected method [16–19]. Among all the techniques, the dip-coating sol-gel method is the most widely used because of its good homogeneity, simplicity, low cost, and low temperature during the process [20]. On the other hand, the nature and type of substrate should not be left

aside. Amorphous SiO_2 has shown to be an excellent support due to its mechanical properties, good adsorption capacity, and high surface area [21, 22].

This work aims to elucidate the effect on morphological, textural, and structural properties of three important variables involved in the synthesis of TiO_2 coated SiO_2 monoliths. These variables are the mechanism to disperse Ti alkoxide species in an appropriate medium allowing the hydrolysis-condensation processes, dipping time, and number of coating cycles (dip + drying + calcination). In order to evaluate the photocatalytic activity of the synthesized catalysts, the photooxidation of methanol was carried out in a bench-scale continuous-flow packed-bed reactor. This reaction was elected because of its industrial importance and because it is a consecutive reaction, whose selectivity towards intermediate compounds may help to prove the application of TiO_2 in selective oxidation processes instead of the organic compounds mineralization. This process could offer the advantage being performed at mild temperature and pressure conditions unlike other existing processes that occur at relatively high temperatures.

2. Experimental

2.1. Preparation of SiO_2 Monoliths. Silica dioxide monoliths were synthesized by sol-gel method. The synthesis of the silica support was performed using tetraethyl orthosilicate (TEOS) $[\text{Si}(\text{OC}_2\text{H}_5)_4]$ as alkoxide precursor of the Si sol.

First, the ethanol was added into a beaker and it was maintained under continuous stirring until the temperature reached 60°C . At this point, alkoxide was added and mixed into the beaker for 15 min. After this time, a water and nitric acid solution (1:0.0012 molar ratio) was added and the mixture was kept under stirring and keeping the temperature constant for one hour. The molar ratio of water:ethanol:TEOS was of 16:4:1, respectively.

After that, 2.5 ml of the resulting sol were poured into one container to begin the aging process. This was repeated several times to obtain various monoliths. The container lids were previously drilled to allow solvent diffusion. During this step, alkoxide groups are removed by acid- or base-catalyzed hydrolysis reactions, and link networks O-Si-O are formed in subsequent condensation reactions involving hydroxyl groups [23, 24]. Depending upon the water:alkoxide molar ratio R , pH, temperature, and solvent, condensation leads to different polymeric structures such as linear, entangled chains, clusters, and colloidal particles [25].

The obtained monoliths were then dried from room temperature to 100°C during 14 hours with a slow heating profile to eliminate the solvent. The drying was performed in an Iso-temp Vacuum Oven programmable stove model 282 A. The drying treatment was slow to lead the formation of open pores. The drying profile was as follows: 1 h at 40°C , 2.5 h at 50°C , 13 h at 60°C , 2.5 h at 70°C , 3.5 h at 80°C , 2.5 h at 90°C , and 27 h at 100°C . This procedure was performed in order to keep the structure, since a fast drying profile could cause a structure collapse causing cracking of the monolith.

Finally, to provide the monoliths with the appropriate structural and mechanical properties, they were calcined

from room temperature (25°C) to 550°C for 6 h at a heating rate of $2.5^\circ\text{C}/\text{min}$ using a Jeltus muffle with 2 steps. Amorphous silica compounds without a defined crystalline phase are found at this temperature.

2.2. TiO_2 Synthesis. Ethanol, water, titanium butoxide, and diethanolamine (basic catalyst) were used to obtain Ti sols via sol-gel method. Titanium butoxide $[\text{Ti}[\text{O}(\text{CH}_2)_3\text{CH}_3]_4]$ was dispersed in the ethanol. Immediately, a diethanolamine and water solution was dropped into the volume. It is necessary to maintain a 1:1 alkoxide:water molar ratio. Once the solution addition was completed, the agitation was maintained for two hours. After this time, the solution was aged for further two hours without any stirring. Diethanolamine was elected because of its low reactivity during sol-gel process, this makes the hydrolysis reactions slow by favoring the thin film formation [26].

Finally, SiO_2 monoliths were immersed into the Ti sol obtained. In this process, the studied variables were the dispersion mechanism (mechanic or ultrasound) and the residence time into the Ti sol. For the former, a stirring plate and an ultrasonic cleaner were utilized as agitation media. Regarding residence time in the Ti sol, this variable was studied at three levels (half, one, and three hours) for each stirring medium. The number of cycles (immersion-drying-calcination) was also studied in order to establish its relationship with the amount of titania on SiO_2 .

The monoliths coated with titanium species were dried at room temperature for 24 h and calcined under an air flow at 550°C for 5 hours.

2.3. Catalysts Characterization. A Bruker Advance 8 diffractometer was employed to carry out the X-ray diffraction analysis and determine the presence of anatase in the synthesized catalysts. The patterns were obtained using $\text{CuK}\alpha$ radiation at 20 kV and 20 mA. Data were collected over 2θ range of $5-50^\circ$ with a step of $0.5^\circ/\text{min}$.

A JEOL JSM-6510LV electron microscope coupled with an energy dispersive X-ray spectrometer was employed to observe the surface morphology of the prepared catalysts and to perform elemental analysis of the catalysts.

Autosorb-1 Quantachrome sorption equipment was employed to determine the specific surface area and average pore diameter of the synthesized samples by using liquid nitrogen (77 K). The pore size distributions and the specific surface areas of the materials were estimated by Dubinin-Astakhov (DA) and Brunauer Emmett-Teller (BET) methodologies, respectively.

2.4. Bench-Scale Photocatalytic Reactor. The photooxidation of methanol was performed using a bench-scale continuous packed-bed reactor. An eight-watt UV lamp emitting 254 nm waves was placed right in the center of the reactor. 30 monoliths constituted the catalytic bed. Compressed air was used as carrier gas to help methanol to flow through the packed-bed reactor. The air flow was constant at 50 ml/min. The methanol liquid was heated at 65°C in order to vaporize it. The reactor set-up is depicted in Figure 1.

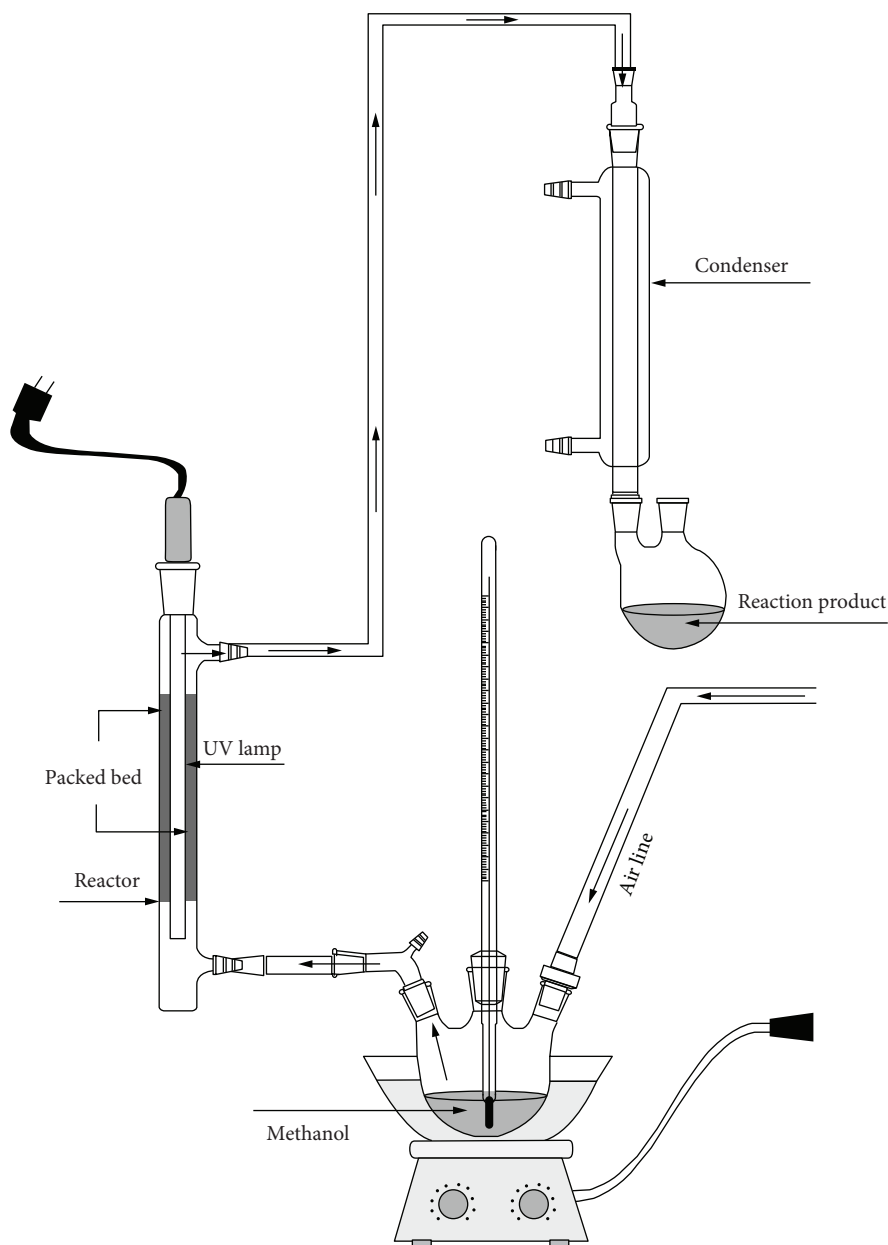


FIGURE 1: Bench-scale photocatalytic reactor set-up.

Identification of formaldehyde by photooxidation of methanol was carried out according to the following methodology: a proper container with a 2,4-dinitrophenylhydrazine (2,4-dnph) solution was placed instead of the condenser (see Figure 1), in such a way that the exit stream was directly bubbled into the solution. This was conducted with all synthesized materials. If there was formaldehyde in such a stream, then a precipitate was observed. This precipitate was the 2,4-dinitrophenylhydrazone, which is the product of the reaction between the 2,4-dnph and the aldehyde as depicted in Figure 2 [27].

The 2,4-dnph solution was prepared as follows: 2 ml of concentrated sulfuric acid was mixed under stirring with 0.4 gr of 2,4-dnph and 3 ml of water until total dissolution

appears. At this point, 10 ml of ethanol at 95% are added to the solution.

The quantitative analysis of formaldehyde after photooxidation of methanol was verified by collecting the condensed reaction product in a container at 4°C and analyzed in a Varian GC 3800 using a 52 CP WAX column (30 m × 0.320 mm).

3. Results and Discussion

SiO₂ monoliths with a diameter of 15 mm and thickness of 1 mm approximately were obtained following the methodology described in the previous section. Figure 3 shows such monoliths. It can be observed that they are totally transparent. This is expected to allow an excellent light transmittance

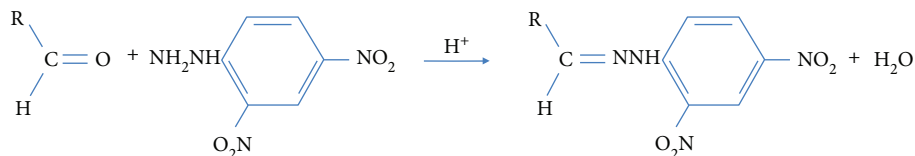
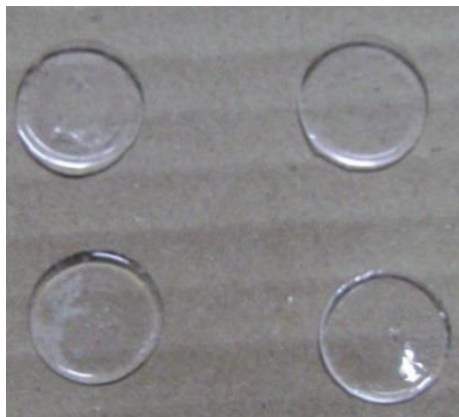


FIGURE 2: 2,4-Dinitrophenylhydrazine general reaction with aldehyde functional groups.

FIGURE 3: SiO₂ monoliths obtained by sol-gel technique.

and an appropriated use in photocatalytic reactions using UV light.

In total, 8 samples were characterized in order to decide at what conditions the monoliths for the methanol photooxidation should be synthesized. From the 8 monoliths, 7 were coated with TiO₂ while the left one was only SiO₂. The nomenclature used to name the samples is explained in Table 1.

Figure 4 shows the diffraction patterns with respect to the agitation mechanism and number of immersion-drying-calcination cycles. The obtained crystalline phase is mainly anatase, and this is expected because of the calcination temperature (550°C) [28]. Usually, when the calcination temperature is increased to more than 550°C, the anatase phase is observed to gradually change into a rutile phase with a larger particle size that results unfavorable for photocatalytic degradation reactions [29].

The average crystallite size of samples was estimated using the Scherrer's equation through the full width at half maximum of the anatase (101) peak (see Table 2). Based on these results, it can be observed that the agitation mechanism has a significant effect on crystallinity since the monoliths coated in the ultrasound bath exhibit the smallest crystalline size (Figure 4(d)) than that of prepared with mechanical stirring (Figure 4(c)) to the same number of cycles (3 cycles) and residence time in the sol (3 hours). The diffraction pattern for commercial Degussa P-25 is included on the top right corner of Figure 4 for reference purposes. It can also be observed that the obtained SiO₂ is amorphous (Figure 4(e)). As can be seen in Table 2, the number of treatment cycles decreases crystal growth. In addition, the increase in immersion time for samples with 3 treatment cycles decreased the crystallinity. The sample with the largest crystalline size corresponds

TABLE 1: Nomenclature of synthesized materials (B by ultrasound bath and P by stirring plate).

Sample name	Number of immersion-drying-calcination cycles	Immersion time (hours)
3ST12B	3	1/2
3ST12P	3	1/2
3ST1B	3	1
3ST1P	3	1
3ST3B	3	3
3ST3P	3	3
4ST1P	4	1

to 3 treatment cycles and half an hour of immersion (sample 3ST12P). It is worth mentioning that more than 3 cycles were unsuccessfully attempted since monoliths got broken, with the exception of those with 1 hour immersion time. In this case, monoliths did not stand the fifth cycle.

Regarding samples 3ST1B and 3ST12B, these were discarded because the ultrasound influenced the structure to an extent that the SiO₂ monolith was broken. This may be ascribed to the vibrational movements caused by ultrasonic, causing the structure to become weaker. This is a consequence of the immersion under ultrasound presence during TiO₂/SiO₂ monoliths preparation as well as the decrease in crystallinity.

Figure 5 (3ST12P sample) shows the surface morphology of TiO₂ film obtained after 3 cycles of immersion-drying-calcination treatments. The residence time was half an hour for each of the immersion processes. The film exhibits a homogeneous morphology with a lineal growing up with almost totally flat surface. The EDS analysis shows the Ti presence. Figure 6 (3ST1P sample) presents the surface of the TiO₂ film obtained after 3 cycles of immersion-heating-calcination treatments and one hour of residence time for each immersion process.

Figure 7 (3ST3P sample) illustrates the characteristic morphology of a TiO₂ film after 3 treatment cycles and 3 hours of immersion under mechanical stirring. The comparison of Figures 7 and 5 make it clear that the amount of material deposited on the surface increases with immersion time. This increase is not related to the crystalline growth of anatase on the surface as has been evidenced by XRD analysis. The clusters presented in Figure 7 can be ascribed to the time given to the monolith in the sol where hydrolysis and condensation reactions are occurring, so the longer the immersion time, the larger the agglomerate.

By comparing Figures 5–7, it can be observed that the residence time has a significant effect on the morphology of

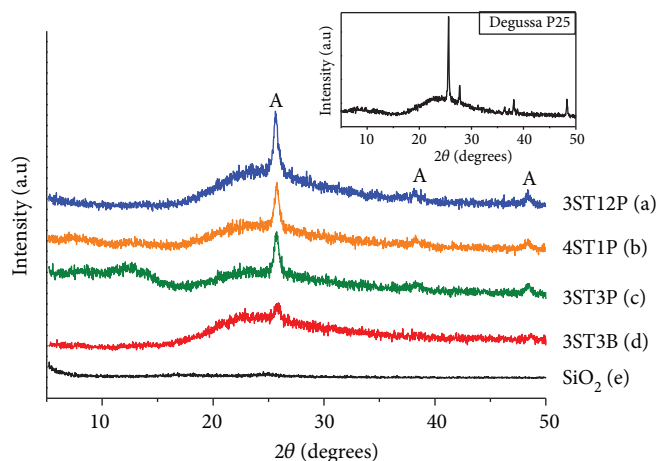


FIGURE 4: XRD patterns of $\text{TiO}_2/\text{SiO}_2$ and pure SiO_2 samples.

TABLE 2: Average crystallite size of the synthesized materials in Figure 4.

Sample	Average crystallite size (nm)
3ST12P	19.4
4ST1P	17.0
3ST3P	16.3
3ST3B	13.5

the coating. A time higher than half an hour (Figures 6 and 7) promotes the appearance of microcracks, and therefore the film loses homogeneity. These microcracks may be ascribed to a stress effect during the drying-calcination treatment due to thermal shrinkage and expansion phenomena. The stress is caused by chemical reactions during the drying and thermal expansion coefficients difference between the support ($5 \times 10^{-7}^\circ\text{C}$) and TiO_2 film ($2.1\text{--}2.8 \times 10^{-6}^\circ\text{C}$) [30]. It seems that the effect of this phenomenon becomes stronger when the amount of TiO_2 increases due to the drying and calcination process. The crystallinity of the sample shown in Figure 5 may be related to the absence of cracking since with the growth of the crystal and densification of the film, the compressive stresses are reduced.

Figure 8 (4ST1P sample) shows an image of a TiO_2 film after 4 treatment cycles and 1 hour of immersion under mechanical stirring. The comparison of the EDS analysis of this with that in Figure 6 confirms that the amount of TiO_2 is a direct function of the number of dip coating/heat treatment cycles and that the extent and frequency of the microcracks increase with the number of cycles [31, 32].

The final percentage in weight gained of TiO_2 by the SiO_2 monoliths is shown in Table 3. It can be observed that the increase in immersion time (samples 3ST12P and 3ST1P) favors the amount of TiO_2 deposited on the monoliths. On the other hand, the increase in the number of treatment cycles (samples 3ST1P and 4ST1P) decreases the final percentage of weight gained of TiO_2 .

Table 4 shows the specific surface area and average pore diameter of synthesized materials. All samples presented type

I isotherms and average pore sizes of 18 \AA , which according to the IUPAC classification corresponds to materials with microporous texture. It can be seen that the pure SiO_2 monolith presented the highest surface area ($339 \text{ m}^2/\text{g}$). As the immersion time of the monoliths increases, the surface area decreases by about 50% (3ST3P sample). This decrease can be attributed to the amount of TiO_2 on the SiO_2 surface. Although the surface area decreases, the pore size distribution and the mean diameter are maintained.

It can be said that the synthesis conditions in which better crystallinity of the anatase phase is obtained; the highest specific surface area as well as a better uniformity of the formed film are with half an hour immersion, 3 cycles and stirring plate as dispersion mechanism. Therefore, these conditions were used to synthesize 30 monoliths to pack the bed reactor in order to perform the photocatalytic oxidation of methanol.

The minimum air flow rate to carry the methanol gas through the reactor was established as 50 ml/min . Two sets of experiments by triplicate were performed; one set without catalyst and the other one with the catalyst. In the former case, no formaldehyde was detected by the employed analysis method (2,4-dnph), and therefore the production of formaldehyde by photolysis was discarded. In the latter set of experiments, formaldehyde was identified. The analytical technique for the qualitative analysis of formaldehyde with a 2,4-dnph solution was carried out. The formation of micelles as precipitates is due to the formation of 2,4-dinitrophenylhydrazone indicating the presence of formaldehyde during the photocatalytic reaction. A precipitate indicating the presence of the aldehyde was only observed with the material 3ST12P. This does not mean that the other materials did not have photoactivity but that this could be so high that total methanol oxidation rather than selective oxidation was attained. To determine the amount of formaldehyde formed during photooxidation of methanol, the first condensed reaction product was evaluated by gas chromatography (GC). The final concentration of produced formaldehyde corresponds to a value of 457 micromol/L (13.7 mg/L). This result is superior to those obtained with other titania-silica systems [33].

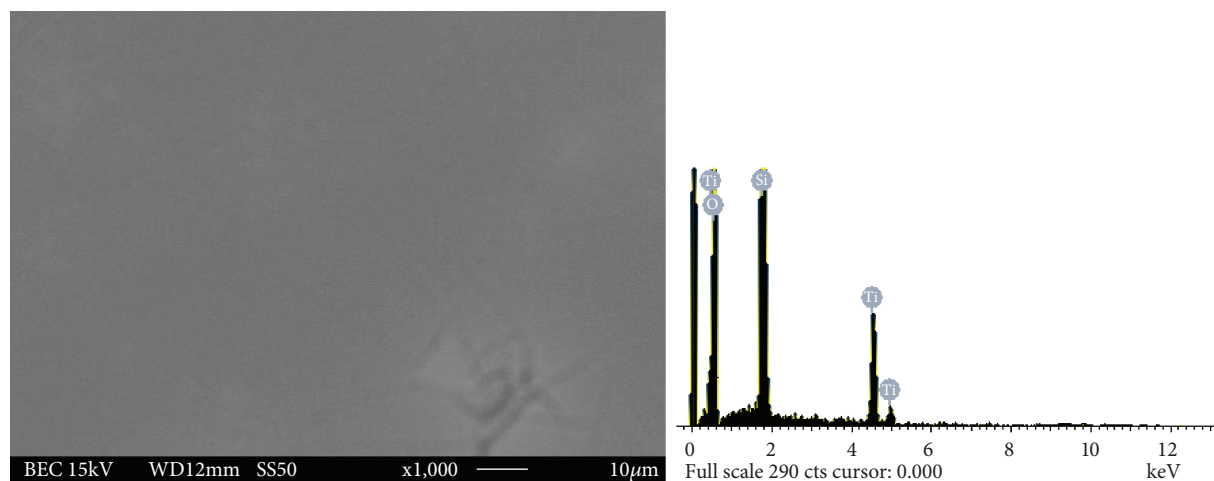


FIGURE 5: SEM image of TiO_2 film morphology obtained after 3 treatment cycles using a stirring plate and half an hour of immersion.

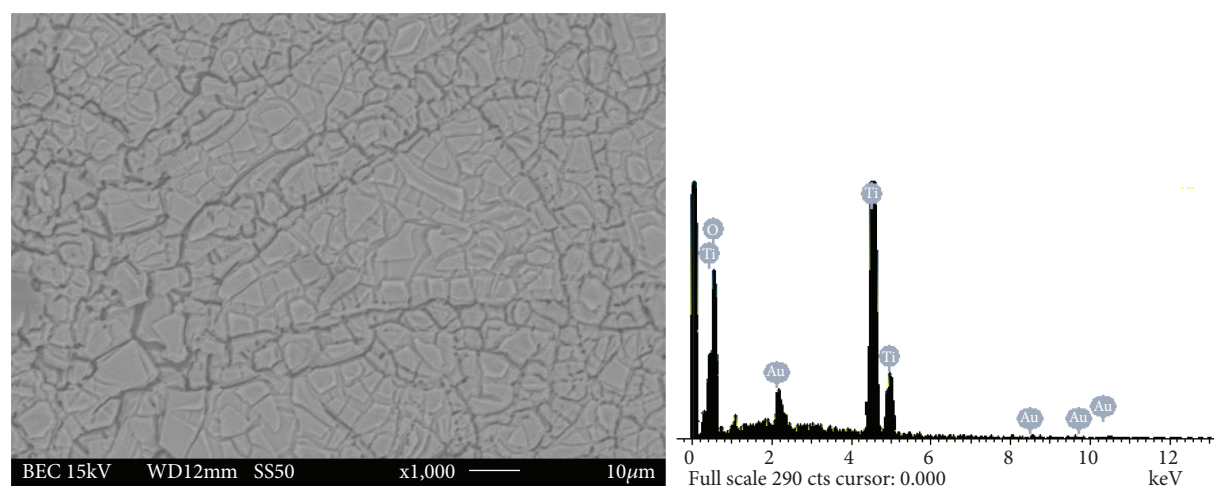


FIGURE 6: SEM image after 3 treatment cycles using stirring plate and 1 hour of immersion.

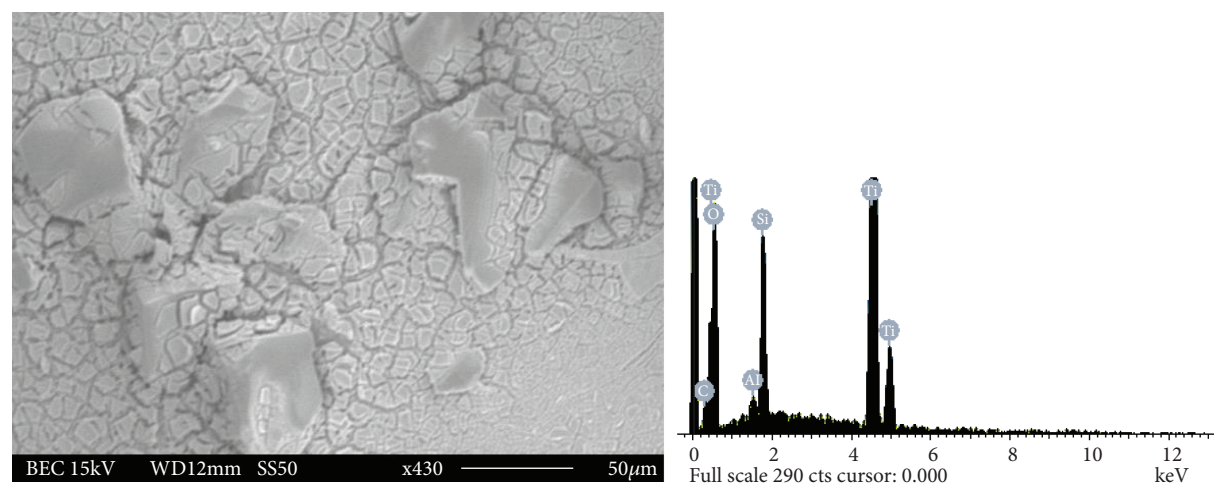


FIGURE 7: SEM image after 3 treatment cycles using stirring plate and 3 hours of immersion.

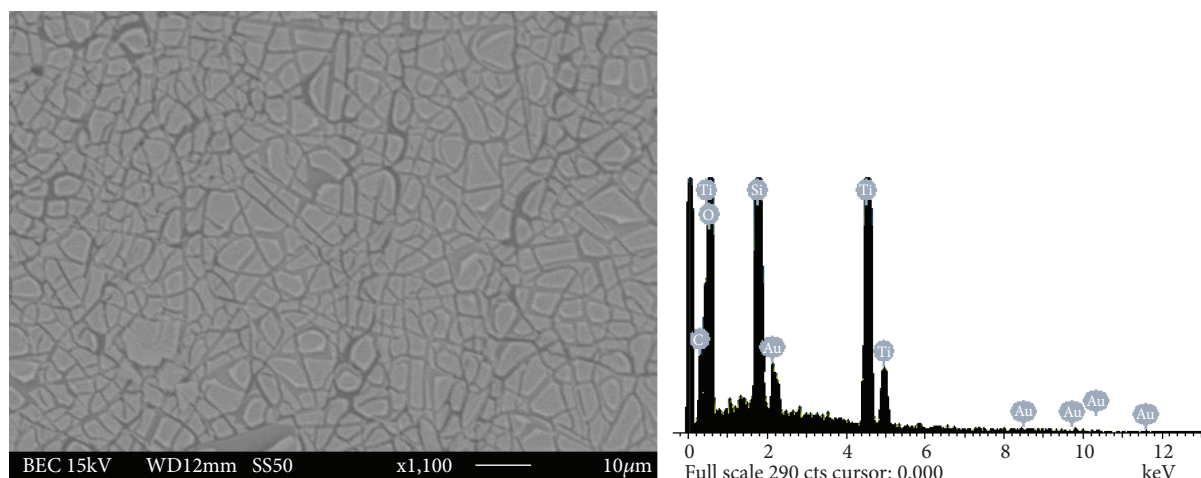


FIGURE 8: SEM image of TiO_2 film after 4 treatment cycles and 1 hour of immersion under mechanical stirring.

TABLE 3: Final percentage in weight gained of TiO_2 on the SiO_2 monoliths.

Sample	Percentage in weight gained of TiO_2 (%)
3ST12P	14.3
3ST1P	18.5
4ST1P	17.4

TABLE 4: Specific surface area and average pore size of the synthesized materials.

Sample	Specific surface area ($\text{m}^2 \text{g}^{-1}$)	Average pore size (\AA)
SiO_2	339	18
3ST12P	241	18
3ST1P	210	18
3ST3P	170	18
4ST1P	240	18

4. Conclusions

SiO_2 monoliths coated with thin films of TiO_2 anatase phase were successfully prepared by using a dip-coating sol-gel method. The dispersion mechanism, the immersion time, and the number of dip-coating cycles of the SiO_2 monoliths into the Ti sol were found to affect both the morphology and crystallinity of the TiO_2 deposit. SiO_2 monoliths coated with crackle-free TiO_2 films were obtained after three dip-coating cycles, with a dip time of 30 minutes. It can also be concluded that mechanical stirring should be preferred over ultrasound dispersion since the former favors the structural stability of the monolith and increases the film crystallinity, while the ultrasound dispersion method leads to monolithic structure breakage and also increases film cracks. Immersion time diminished both TiO_2 film and homogeneity. Immersion time and number of cycles also affect the surface area and deposit crystallinity. The surface area of the SiO_2 - TiO_2 materials was decreased when the immersion time

increased, which is related to the amount of TiO_2 on the SiO_2 surface. The highest anatase phase crystallinity and specific surface area were obtained after 3 dip-coating cycles and half an hour of immersion under mechanical stirring. Under these preparation conditions, the attained surface area was $241 \text{ m}^2/\text{g}$ and the crystallite size was 19.4 nm. The weight percentage gained by SiO_2 monoliths was 14.3% (TiO_2 film).

A formaldehyde concentration of 13.7 mg/L was attained at mild conditions of pressure and temperature in a continuous flow reactor packed with SiO_2 monoliths coated with TiO_2 anatase films prepared with 3 dip-coating cycles and 0.5 hours of immersion time.

Conflicts of Interest

The authors declare that there is no conflict of interests.

Acknowledgments

The authors are grateful to UAEMex for the financial support through project 4373/2017/CI and to CONACYT (project 269093). R. Regalado would like to thank CONACYT for the financial support and to CCIQS from UAEM for the granted support.

References

- [1] Z. Li, S. Cong, and Y. Xu, "Brookite vs anatase TiO_2 in the photocatalytic activity for organic degradation in water," *ACS Catalysis*, vol. 4, no. 9, pp. 3273–3280, 2014.
- [2] H. Park, C. D. Vecitis, W. Choi, O. Weres, and M. R. Hoffmann, "Solar-powered production of molecular hydrogen from water," *The Journal of Physical Chemistry C*, vol. 112, no. 4, pp. 885–889, 2008.
- [3] J. Wang, Z. Bian, J. Zhu, and H. Li, "Ordered mesoporous TiO_2 with exposed (001) facets and enhanced activity in photocatalytic selective oxidation of alcohols," *Journal of Materials Chemistry A*, vol. 1, no. 4, pp. 1296–1302, 2013.
- [4] M. Pera-Titus, V. García-Molina, M. A. Baños, J. Giménez, and S. Espluga, "Degradation of chlorophenols by means of

- advanced oxidation processes: a general review," *Applied Catalysis B: Environmental*, vol. 47, no. 4, pp. 219–256, 2004.
- [5] A. Tanaka, K. Hashimoto, and H. Kominami, "Selective photocatalytic oxidation of aromatic alcohols to aldehydes in an aqueous suspension of gold nanoparticles supported on cerium(IV) oxide under irradiation of green light," *Chemical Communications*, vol. 47, no. 37, pp. 10446–10448, 2011.
 - [6] Y. Zhang, Z. R. Tang, X. Fu, and Y. J. Xu, "Engineering the unique 2D mat of graphene to achieve graphene-TiO₂ nanocomposite for photocatalytic selective transformation: what advantage does graphene have over its forebear carbon Nanotube?," *ACS Nano*, vol. 5, no. 9, pp. 7426–7435, 2011.
 - [7] G. Reuss, W. Disteldorf, O. Grundler, and A. Hilt, "Formaldehyde," in *Ullmann's Encyclopedia of Industrial Chemistry*, I. F. Ullmann, W. Gerhartz, Y. S. Yamamoto, F. T. Campbell, R. Pfefferkorn, and J. F. Rounsaville, Eds., VCH, Deerfield Beach, FL, USA, 1985.
 - [8] H. R. Gerberich, A. L. Stautzenberger, and W. C. Hopkins, "Formaldehyde," in *Kirk-Othmer Encyclopaedia of Chemical Technology*, pp. 231–250, John Wiley and Sons, New York, 1980.
 - [9] E. Cao and A. Gavrilidis, "Oxidative dehydrogenation of methanol in a microstructured reactor," *Catalysis Today*, vol. 110, no. 1–2, pp. 154–163, 2005.
 - [10] K. I. Ivanov and D. Y. Dimitrov, "Deactivation of an industrial iron-molybdate catalyst for methanol oxidation," *Catalysis Today*, vol. 154, no. 3–4, pp. 250–255, 2010.
 - [11] K. Nakata, T. Ochiai, T. Murakami, and A. Fujishima, "Photoenergy conversion with TiO₂ photocatalysis: new materials and recent applications," *Electrochimica Acta*, vol. 84, pp. 103–111, 2012.
 - [12] K. Nakata and A. Fujishima, "TiO₂ photocatalysis: design and applications," *Journal of Photochemistry and Photobiology C: Photochemistry Reviews*, vol. 13, no. 3, pp. 169–189, 2012.
 - [13] S. Shamaila, A. K. L. Sajjad, F. Chen, and J. Zhang, "Synthesis and characterization of mesoporous-TiO₂ with enhanced photocatalytic activity for the degradation of chloro-phenol," *Materials Research Bulletin*, vol. 45, no. 10, pp. 1375–1382, 2010.
 - [14] C. P. Lin, H. Chen, A. Nakaruk, P. Koshy, and C. C. Sorrell, "Effect of annealing temperature on the photocatalytic activity of TiO₂ thin films," *Energy Procedia*, vol. 34, pp. 627–636, 2013.
 - [15] W. Dai, X. Wang, P. Liu, Y. Xu, G. Li, and X. Fu, "Effects of electron transfer between TiO₂ films and conducting substrates on the photocatalytic oxidation of organic pollutants," *The Journal of Physical Chemistry B*, vol. 110, no. 27, pp. 13470–13476, 2006.
 - [16] Y. Cui, J. Sun, Z. Hu et al., "Synthesis, phase transition and optical properties of nanocrystalline titanium dioxide films deposited by plasma assisted reactive pulsed laser deposition," *Surface and Coatings Technology*, vol. 231, pp. 180–184, 2013.
 - [17] X. Zhao, M. Liu, and Y. Zhu, "Fabrication of porous TiO₂ film via hydrothermal method and its photocatalytic performances," *Thin Solid Films*, vol. 515, no. 18, pp. 7127–7134, 2007.
 - [18] D. Li, M. Carette, A. Granier, J. P. Landesman, and A. Goullet, "In situ spectroscopic ellipsometry study of TiO₂ films deposited by plasma enhanced chemical vapour deposition," *Applied Surface Science*, vol. 283, pp. 234–239, 2013.
 - [19] A. Arunachalam, S. Dhanapandian, C. Manoharan, and R. Sridhar, "Characterization of sprayed TiO₂ on ITO substrates for solar cell applications," *Spectrochimica Acta Part A: Molecular and Biomolecular Spectroscopy*, vol. 149, pp. 904–912, 2015.
 - [20] A. Y. Shan, T. I. M. Ghazi, and S. A. Rashid, "Immobilisation of titanium dioxide onto supporting materials in heterogeneous photocatalysis: a review," *Applied Catalysis A: General*, vol. 389, no. 1–2, pp. 1–8, 2010.
 - [21] M. A. L. Vargas, M. Casanova, A. Trovarelli, and G. Busca, "An IR study of thermally stable V₂O₅-WO₃-TiO₂ SCR catalysts modified with silica and rare-earths (Ce, Tb, Er)," *Applied Catalysis B: Environmental*, vol. 75, no. 3–4, pp. 303–311, 2007.
 - [22] W. Chang, L. Yan, Bin Liu, and R. Sun, "Photocatalytic activity of double pore structure TiO₂/SiO₂ monoliths," *Ceramics International*, vol. 43, no. 8, pp. 5881–5886, 2017.
 - [23] C. J. Brinker, "Hydrolysis and condensation of silicates: effects on structure," *Journal of Non-Crystalline Solids*, vol. 100, no. 1–3, pp. 31–50, 1988.
 - [24] G. Andrade-Espinosa, V. Escobar-Barrios, and R. Rangel-Mendez, "Synthesis and characterization of silica xerogels obtained via fast sol-gel process," *Colloid and Polymer Science*, vol. 288, no. 18, pp. 1697–1704, 2010.
 - [25] M. Ahmad, J. R. Jones, and L. L. Hench, "Fabricating sol-gel glass monoliths with controlled nanoporosity," *Biomedical Materials*, vol. 2, no. 1, pp. 6–10, 2007.
 - [26] Y. Farhang Ghoje Biglu and E. Taheri-Nassaj, "Investigation of phase separation of nano-crystalline anatase from TiO₂-SiO₂ thin film," *Ceramics International*, vol. 39, no. 3, pp. 2511–2518, 2013.
 - [27] S. Uchiyama, Y. Inaba, and N. Kunugita, "Derivatization of carbonyl compounds with 2,4-dinitrophenylhydrazine and their subsequent determination by high-performance liquid chromatography," *Journal of Chromatography B*, vol. 879, no. 17–18, pp. 1282–1289, 2011.
 - [28] M. S. Lee, S. S. Park, G. D. Lee, C. S. Ju, and S. S. Hong, "Synthesis of TiO₂ particles by reverse microemulsion method using nonionic surfactants with different hydrophilic and hydrophobic group and their photocatalytic activity," *Catalysis Today*, vol. 101, no. 3–4, pp. 283–290, 2005.
 - [29] R. Kaplan, B. Erjavec, G. Dražić, J. Grdadolnik, and A. Pintar, "Simple synthesis of anatase/rutile/brookite TiO₂ nanocomposite with superior mineralization potential for photocatalytic degradation of water pollutants," *Applied Catalysis B: Environmental*, vol. 181, pp. 465–474, 2016.
 - [30] Z. Fu, U. Eckstein, A. Dellert, and A. Roosen, "In situ study of mass loss, shrinkage and stress development during drying of cast colloidal films," *Journal of the European Ceramic Society*, vol. 35, no. 10, pp. 2883–2893, 2015.
 - [31] N. Arconada, A. Durán, S. Suárez et al., "Synthesis and photocatalytic properties of dense and porous TiO₂-anatase thin films prepared by sol-gel," *Applied Catalysis B: Environmental*, vol. 86, no. 1–2, pp. 1–7, 2009.
 - [32] C. M. Malengreaux, G. M. L. Léonard, S. L. Pirard et al., "How to modify the photocatalytic activity of TiO₂ thin films through their roughness by using additives. A relation between kinetics, morphology and synthesis," *Chemical Engineering Journal*, vol. 243, pp. 537–548, 2014.
 - [33] J. M. Stokke, D. W. Mazyck, C. Y. Wu, and R. Sheahan, "Photocatalytic oxidation of methanol using silica-titania composites in a packed-bed reactor," *Environmental Progress*, vol. 25, no. 4, pp. 312–318, 2006.

Research Article

Treatment of a Textile Effluent by Electrochemical Oxidation and Coupled System Electrooxidation–*Salix babylonica*

Alejandra Sánchez-Sánchez,¹ Moisés Tejocote-Pérez,² Rosa María Fuentes-Rivas,³
Ivonne Linares-Hernández,¹ Verónica Martínez-Miranda,¹
and Reyna María Guadalupe Fonseca-Montes de Oca ¹

¹Centro Interamericano de Recursos del Agua, Universidad Autónoma del Estado de México, Carretera Toluca-Atlaconulco, Km 14.5 Unidad San Cayetano, 50200 Toluca, MEX, Mexico

²Centro de Investigación en Ciencias Biológicas Aplicadas, Universidad Autónoma del Estado de México, Carretera Toluca-Atlaconulco, Km 14.5 Unidad San Cayetano, 50200 Toluca, MEX, Mexico

³Facultad de Geografía, Universidad Autónoma del Estado de México, Cerro de Coatepec s/n, Ciudad Universitaria, 50110 Toluca, MEX, Mexico

Correspondence should be addressed to Reyna María Guadalupe Fonseca-Montes de Oca; mgfonsecam@uaemex.mx

Received 2 October 2017; Revised 20 March 2018; Accepted 1 April 2018; Published 3 May 2018

Academic Editor: Carlos A Martínez-Huitle

Copyright © 2018 Alejandra Sánchez-Sánchez et al. This is an open access article distributed under the Creative Commons Attribution License, which permits unrestricted use, distribution, and reproduction in any medium, provided the original work is properly cited.

The removal of pollutants from textile wastewater via electrochemical oxidation and a coupled system electrooxidation–*Salix babylonica*, using boron-doped diamond electrodes was evaluated. Under optimal conditions of pH 5.23 and $3.5 \text{ mA}\cdot\text{cm}^{-2}$ of current density, the electrochemical method yields an effective reduction of chemical oxygen demand by 41.95%, biochemical oxygen demand by 83.33%, color by 60.83%, and turbidity by 26.53% at 300 minutes of treatment. The raw and treated wastewater was characterized by infrared spectroscopy to confirm the degradation of pollutants. The wastewater was oxidized at 15-minute intervals for one hour and was placed in contact with willow plants for 15 days. The coupled system yielded a reduction of the chemical oxygen demand by 14%, color by 85%, and turbidity by 93%. The best efficiency for the coupled system was achieved at 60 minutes, at which time the plants achieved more biomass and photosynthetic pigments.

1. Introduction

The textile industry is one of the greatest generators of liquid effluent pollutants due to the high quantities of water used in the dyeing processes. The chemical composition involves a wide range of pollutants: inorganic compounds, polymers, and organic products [1–3]. Treatment of textile dye effluent is difficult and ineffective with conventional processes because many synthetic dyes are very stable in light and high temperature, and they are also nonbiodegradable. Moreover, partial oxidation or reduction can generate very toxic by-products [4–6].

Advanced oxidation processes (AOPs) have emerged as potentially powerful methods that can transform recalcitrant pollutants into harmless substances. AOPs rely on the

generation of very reactive free radicals and very powerful oxidants, such as the hydroxyl radical, $\text{HO}\cdot$ (redox potential $E = 2.8 \text{ V}$) [7, 8]. These radicals react rapidly with most organic compounds, either by addition to a double bond or by the abstraction of a hydrogen atom from organic molecules [9, 10].

The resulting organic radicals, then, react with oxygen to initiate a series of degradative oxidation reactions that lead to products, such as CO_2 and H_2O [1, 11]. Electrochemical oxidation is carried out by indirect and/or direct anodic reactions in which oxygen is transferred from the solvent (water) to the product to be oxidized [12]. The main characteristic of this treatment is that it uses electrical energy as a vector for environmental decontamination [13]. During direct anodic oxidation, pollutants are initially adsorbed on the

TABLE 1: Percentage of removal performance of color, turbidity, nitrogen, and COD by electrochemical or electrochemical with other electrochemical or biological procedures.

Treatment	Sample	Optimal operating conditions	Removal performance	References
Vertical-flow constructed wetlands with planted <i>Phragmites australis</i>	Acid Blue 113 (AB113), Basic Red 46 (BR46)	7 mg·L ⁻¹ (AB113); 208 mg·L ⁻¹ (BR46) 48 h (AB113); 96 h (BR46) contact times	Nitrate nitrogen (NO ₃ -N) 85–100%	Hussein and Scholz (2018)
Electrochemical oxidation	Malachite green oxalate (MG)	pH = 3; stainless steel cathode Boron-doped diamond (BDD) anode 32 mA·cm ⁻² current density Na ₂ SO ₄ supporting electrolyte	COD 98% (60 min) COD 91% (180 min)	Guenfoud et al. [1]
Electrocoagulation-phytoremediation (<i>Myriophyllum aquaticum</i>)	Industrial wastewater	pH = 8; Fe electrode; 45.45 A·m ⁻² current density	COD 94%, color 97% Turbidity 98%	Cano-Rodriguez et al. [35]
Electrochemical Fenton (EF) Chemical Fenton (CF)	Textile wastewater	H ₂ O ₂ 1978 mg·L ⁻¹ 350 mA electrical current	COD 70.6% (EF) COD 72.9% (CF) (60 min)	Eslami et al. [36]
Electrochemical oxidation	Textile dyehouse	pH = 1; 8 mA·cm ⁻² current density Boron-doped diamond (BDD) anode 0.25 M HClO ₄ supporting electrolyte	Color 100% Mineralization 85% (180 min)	Tsantaki et al. [37]
Electrochemical	Dyestuff effluent	Boron-doped diamond (BDD) anode; pH = 10; 60°C, 40 mA·cm ⁻² current density	COD 100%, color 100% (15 h)	Martínez-Huitile et al. [15]
Combined electrochemical, microbial, and photocatalytic	Procion blue dye	RuO _x -TiO _x catalytic anode 2 A and 30 V power source	COD 80% to 95%	Basha et al. [16]
Electrochemical	Novacron Deep Red C-D (NDRCD) Novacron Orange C-RN (NOCRN)	pH = 3; 170 A·m ⁻² current density Graphite carbon as anode and cathode Potential: +1.0 to -0.4 V (NDRCD) and +0.5 to -0.2 V (NOCRN); 300.15 K NaCl (7 g·L ⁻¹) supporting electrolyte	Color 99% (NDRCD); 97% (NOCRN) COD 88% (NDRCD); 82% (NOCRN)	Kariyajiannavar et al. [6]

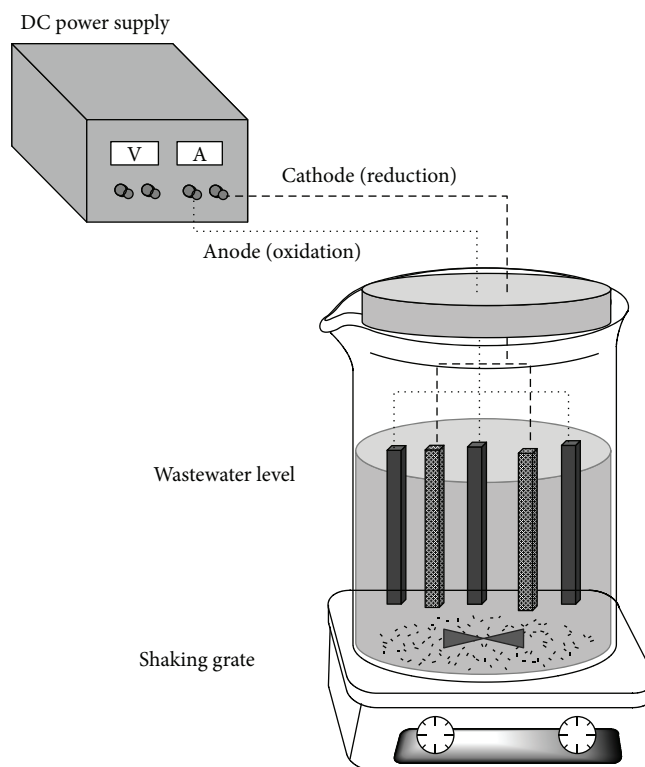


FIGURE 1: A schematic diagram of the electrochemical reactor.

surface of the anode, where the anodic electron transfer reaction degrades them [6]. In indirect anodic oxidation, strong oxidants, such as hypochlorite, chlorine, ozone, or hydrogen peroxide, are electrochemically generated.

The pollutants are degraded via the oxidation reactions with these strong oxidants [11]. Boron-doped diamond (BDD) thin films are electrode materials that possess several technologically important characteristics, including an inert surface with low adsorption properties, an acceptable conductivity, and remarkable corrosion stability even in strongly acidic media and extremely high O_2 evolution overvoltage [14, 15].

On the other hand, biotechnology continues to be used to solve environmental problems [16–18]. Phytoremediation (PR) is a green technology that uses plant systems for the remediation and restoration of contaminated sites [19]. PR's advantages are solar energy dependence and an esthetically pleasant method of treatment [20]. Plants have inbuilt enzymatic characteristics that are capable of degrading complex structures, and they can be used for cleaning contaminated sites [17].

Plants, however, remove pollutants predominantly via adsorption, accumulation, and subsequent enzyme-mediated degradation [20]. Therefore, plants are considered organisms with complex metabolic activity when referring to the assimilation of toxic substances. Plant species that have different growth forms have been proposed for the treatment of textile effluents, for instance, *Glandularia pulchella*, *Phragmites australis*, *Tagetes patula*, *Alternanthera philoxeroides*, *Eichhornia crassipes*, *Nasturtium officinale*,

TABLE 2: Experimental design of the electrooxidation process.

Experiment	pH	Current density
1	5.23	3.5
2	5.23	7
3	5.23	10
4	7	3.5
5	7	7
6	7	10
7	10	3.5
8	10	7
9	10	10

Hydrocotyle vulgaris, *Petunia grandiflora*, and *Gaillardia grandiflora* [17, 18, 21–24].

Another alternative is to use species of fast-growing woody plants with high biomass production and high genetic variability [25–27]. Trees from the Salicaceae family with the genera *Salix* and *Populus* are suitable candidates for this purpose [28–30]. Willows (*Salix* spp.) have several characteristics that make them ideal plant species for PR application, including easy propagation and cultivation, a large amount of biomass, a deep root system, a high transpiration rate, tolerance to hypoxic conditions, and high metal accumulation capability [30, 31].

Salix babylonica has been used to solve the problems associated with aquifers contaminated with ethanol-blended gasoline [32] and studies of the biotransformation and

metabolic response of cyanide and dieldrin [33, 34]. In recent years, several authors have described dye removal by electrochemical (EC) or coupled electrochemical with other chemical, electrochemical, or biological procedures (Table 1). However, no studies have been conducted on the implementation of coupled electrochemical oxidation-phytoremediation with weeping willow in the remediation of textile effluents, and because it is an introduced species, is noninvasive, and is widely distributed in Mexico, the aim of this study was to evaluate the removal of the pollutants of a textile effluent using an electrochemical oxidation process and to compare their performance with *Salix babylonica*.

2. Materials and Methods

2.1. Wastewater Sampling. A textile wastewater sample was collected from a textile industry whose business is the dyeing and washing of denim garments in Almoloya del Río, State of Mexico, Mexico. The wastewater that this industry discharges does not receive any treatment and is discharged into the sewage system, so it is necessary to give it some kind of treatment to improve its quality. The textile wastewater sample was placed in plastic containers and transported to the laboratory, where it was refrigerated at 4°C for analysis and for conducting the electrochemical oxidation and coupled system electrooxidation-*Salix babylonica*.

2.2. Electrochemical Reactor. In this study, a batch electrochemical reactor was used. The reactor contained five vertical parallel electrodes of BDD (titanium/BDD) that CONDIAS DIACHEM manufactured, two as cathodes and three as anodes. Each electrode was 20.5 cm long and 2.5 cm wide, resulting in an area of 102.5 cm² for each electrode and a total anodic area of 307.5 cm². A schematic diagram of the electrochemical reactor is shown in Figure 1. The tests were carried out in a 1 L cylindrical reactor. The reactor was operated at different pH values (5.23, 7, and 10). A current density power supply provided 1, 2, and 3 A and 5–6.75 V, corresponding to a current density of 3.5, 7, and 10 mA·cm⁻².

The experiment design used included the two factors of pH and current density. The levels of each of the factors are listed in Table 2. Different aliquots were taken, and the chemical oxygen demand (COD), biochemical oxygen demand (BOD₅), color, turbidity, and conductivity were analyzed. The boron-doped diamond electrodes (BDD) were cleaned for one hour in Na₂SO₄ (0.03 M) after each experiment to remove adsorbed molecules at the electrode surface, and then they were rinsed with distilled water.

2.3. Coupled System with *Salix babylonica* Treatment. For *Salix babylonica* treatment, secondary branches of weeping willows located in five regions near the discharge site were collected based on some defined phenotypic characteristics: intense green color, wide coverage, height greater than 8 meters, absence of pests, and straight shaft. Branch cuttings of 20 cm in length were placed in hydroponics [28] in 1 L containers with 300 mL of distilled water. They

TABLE 3: Physicochemical characterization of textile wastewater.

Parameter	Raw wastewater
pH	5.23
Acidity (mg/L CaCO ₃)	962.8
Alkalinity (mg/L CaCO ₃)	1000
BOD (mg/L)	1400
BOD/COD	0.7
COD (mg/L)	2022
Color (Pt-Co U)	3000
Chlorides (mg/L Cl ⁻)	843.71
EC (mS/cm)	2.811
Hardness (mg/L CaCO ₃)	546.2
N-NO ₂ (mg/L)	0.848
N-NO ₃ (mg/L)	17.28
N-NH ₃ (mg/L)	4.72
Phosphorus (mg/L P)	715.1
Sulfates (mg/L SO ₄ ²⁻)	429.5
Turbidity (NTU)	735
TOC (mg/L)	1396.6
TDS (mg/L)	1367
Ca ²⁺ (mg/L)	36.537
K ⁺ (mg/L)	64.43
Mg ²⁺ (mg/L)	17.346
Na ⁺ (mg/L)	392.79

were kept at room temperature (19–22°C) for a normal photoperiod (12 h light, 12 h dark). Ten willows per region were placed in jars of 1 L and were then placed in 500 mL of textile wastewater. They remained in contact with wastewater for 15 days, and water aliquots were taken at baseline and at intervals of eight days. Likewise, the development of plants during those time periods was assessed.

3. Methods of Analysis

3.1. Physicochemical Characterization. The characterization of textile wastewater was performed. During both electrochemical and phytoremediation treatment, COD, BOD₅, color, turbidity, pH, and electrolytic conductivity analyses were performed as indicated in the standard methods procedures by the American Public Health Association [38]. In addition, infrared spectroscopy of the raw and treated water was performed.

3.2. Biological Parameters. Once roots and leaves were developed in hydroponics, they were weighed on an analytical balance (BEL Engineering), and the lengths of the plants and roots were measured using a vernier. The numbers of roots and leaves were counted, and the leaf areas and photosynthetic pigments were measured by using the method that Val et al. [39] and Moisés et al. [40] established. These measurements were performed at the beginning of biological treatment and every eight days.

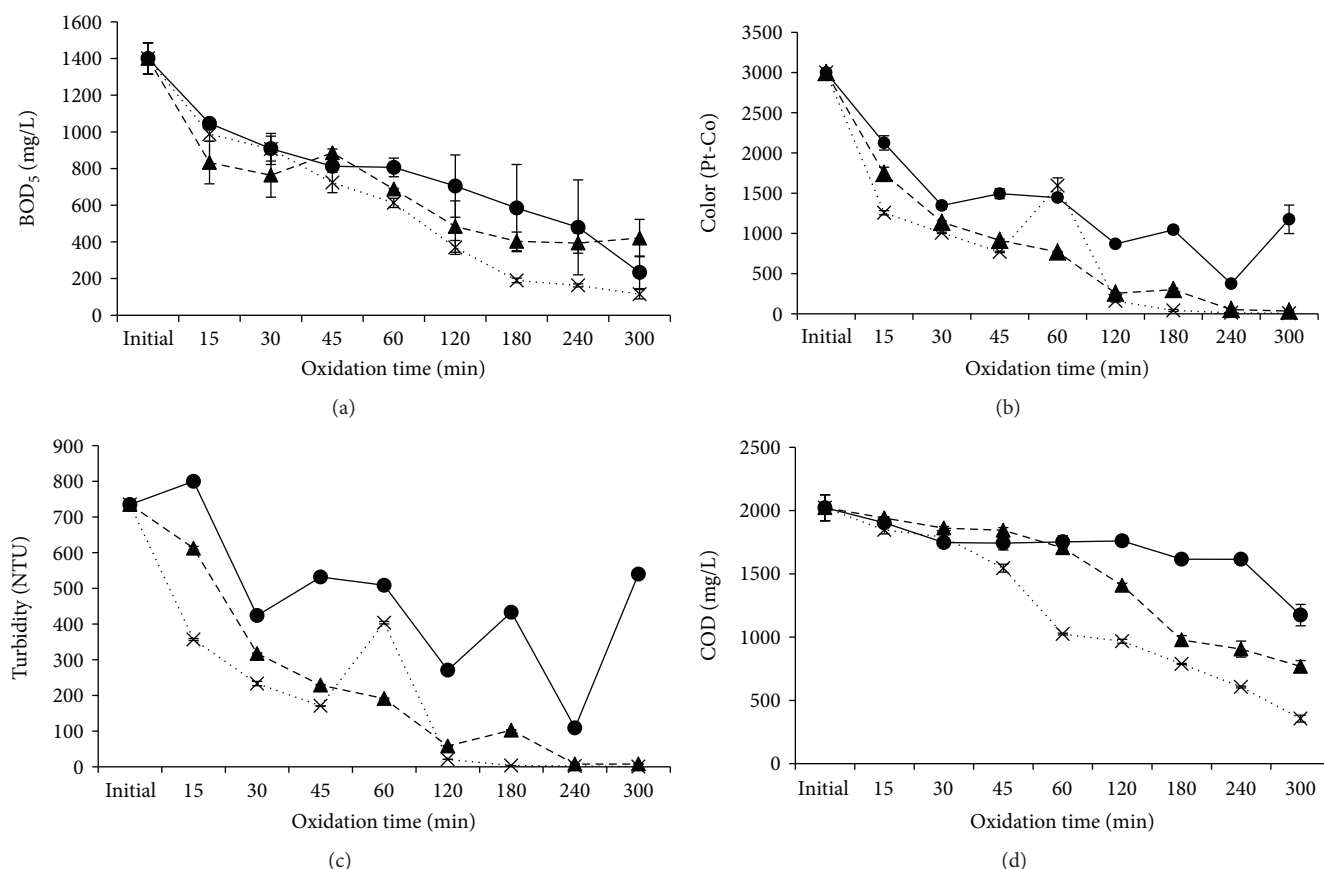


FIGURE 2: Behavior of (a) BOD₅, (b) color, (c) turbidity, and (d) COD. Applying three current densities: 3.5 mA·cm⁻² (●), 7 mA·cm⁻² (▲), and 10 mA·cm⁻² (X), at pH 5.23.

4. Results and Discussion

4.1. Wastewater Characterization. Physicochemical characterization of textile wastewater is shown in Table 3. The organic parameters indicate for the BOD₅ a value of 1400 mg/L. According to Mexican regulation, the allowed limit for discharging wastewater into rivers is 150 mg/L. The COD was 2022 mg/L; in this situation, the BOD/COD ratio (0.7) indicates good biodegradability [9]. The TOC was 1396.6 mg/L, and the color was 3000 Pt-Co U; this high level of color stemmed from the indigo blue dye in the textile effluent. Regarding inorganic matter, different ions contribute to high conductivity (2.811 mS/cm). This parameter could be beneficial to the electrooxidation process because it was not necessary to add any support electrolyte. However, the presence of ions as nitrates, phosphates, and alkalinity could reduce the oxidation speed of organic compounds; on the other hand, chlorides (843.71 mg/L) could improve the indirect organic oxidation.

4.2. Electrooxidation Treatment

4.2.1. Current Density Effect. An important operating variable of the electrochemical process is the current density, which is the input current divided by the surface area of

TABLE 4: Removal efficiencies of different parameters in the electrooxidation process.

Experiment	pH	Current densities	BOD (%)	Color (%)	Turbidity (%)	COD (%)
1	5.23	3.5	83.33	60.83	26.53	41.95
2	5.23	7	69.95	98.88	98.95	62.01
3	5.23	10	91.81	99.81	99.91	82.39
4	7	3.5	58.34	96.95	98.77	47.73
5	7	7	91.15	99.66	99.77	63.14
6	7	10	91.58	99.82	99.90	94.66
7	10	3.5	58.56	92.45	98.09	82.10
8	10	7	94.73	99.01	99.04	98.11
9	10	10	94.38	97.04	93.87	95.03

the electrode [11]. From other variables effective in the electrochemical process is current density as the rate of electrochemical reactions is controlled by this parameter. Further, the performance of electrodes is highly dependent on this parameter. Three different current densities were applied (3.5, 7, and 10 mA·cm⁻²) to investigate the effect in the oxidation process. All experiments were carried out at pH 5.23 (sample pH), and in all cases, a direct effect of the current densities was observed: If the current increases,

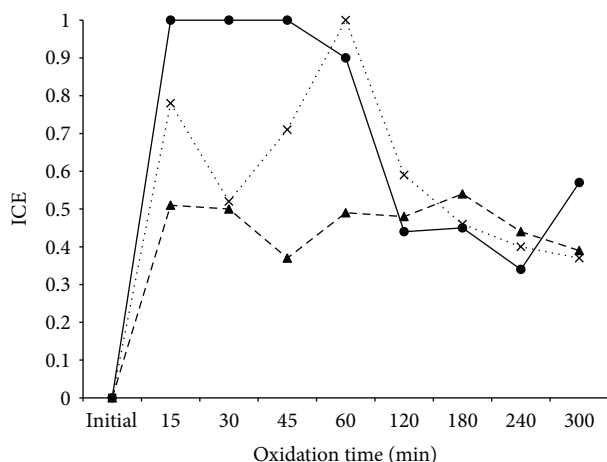


FIGURE 3: Instantaneous current efficiency (ICE) for the anodic oxidation process: 3.5 mA/cm² (●), 7.0 mA/cm² (▲), and 10 mA/cm² (X).

the removal efficiency increases. This could be due to the increased rate of the generation of oxidants, such as hydroxyl radicals and chlorine/hypochlorite at higher current densities [6]. The results at different densities are shown in Figure 2. The best removal efficiency was when 10 mA·cm⁻² was applied. BOD₅ was reduced considerably from 1400 mg/L to 114 mg/L with 92% of efficiency; COD was 2022 mg/L and was reduced to 356.05 mg/L with 82% of removal efficiency; color was reduced from 3000 Pt-Co U to 5.5 Pt-Co U (99.8% removal efficiency); and initial turbidity was 735 NTU and at the end of the process was 0.65 NTU, achieving 99.99% of removal efficiency. Efficiency was measured during 300 min of treatment time (Table 4).

The instantaneous current efficiency (ICE) for the anodic oxidation was calculated from the values of COD using

$$ICE = FV \frac{COD_i - COD_t}{8I\Delta t}, \quad (1)$$

where F is the Faraday constant (96487 C/mol), V is the volume (L), COD_i and COD_t are the chemical oxygen demand (g/L) at initial time and time t , I is the applied current (A), Δt is the treatment time (s), and 8 is the equivalent mass of oxygen (g·eq⁻¹). The instantaneous current efficiency (ICE) decreased during the electrolysis as wastewater was oxidized. This behavior is shown in Figure 3.

The best ICE percentage was when the lowest current was applied 1 A (3.5 mA·cm⁻²) in the middle stage of electrooxidation (15–45 min). This may be attributed to the presence of a higher concentration of organics near the electrodes. This indicates that the electrooxidation was under the current control regime at least in the middle stage of electrooxidation. The ICE decreased after 60 min of the electrooxidation process. This may be due to the depletion of the concentration of organics on the electrode surface.

The energy consumption per volume of treated effluent was estimated and expressed in kWh·m⁻³. The average cell voltage during the electrolysis (cell voltage is reasonably

constant with just some minor oscillations, and for this reason, the average cell voltage was calculated) was measured to calculate the energy consumption by using [15]

$$\text{Energy consumption} = \frac{\Delta E_c \times I \times t}{1000 \times V}, \quad (2)$$

where t is the time of electrolysis (h); ΔE_c (V) and I (A) are the average cell voltage and the electrolysis current, respectively; and V is the sample volume (m³). According to the results, 5.87 kWh·m⁻³ is required to oxidize the pollutants in the textile wastewater. In another study, a real textile effluent was treated using a BDD anode, applying a current density of 20 mA·cm⁻². The energy consumption was 20 kWh·m⁻³ [15].

The specific energy consumption (E_c) in kWh·(kg COD)⁻¹ removed was determined according to [37]

$$E_c = \frac{UIt/60}{(COD_0 - COD)V}, \quad (3)$$

where U is the mean applied voltage (V), I is the current (A), t is the treatment time (min), V is the liquid volume (L), and COD_0 and COD are the COD values (g O₂ L⁻¹) at times 0 and t . The results showed that 21.87 kWh·(kg COD)⁻¹ was required in the electrooxidation process. In a previous work, 95 kWh·(kg COD)⁻¹ was applied for the same COD removal [37].

4.2.2. pH Effect. The studies were performed at three different initial pH values (5.23, 7, and 10) to investigate their effects as depicted in Figure 4. The current density applied in these experiments was 3.5 mA·cm⁻². At alkaline pH (10), the best efficiencies were achieved: COD (85.9%), color (99.6%), BOD₅ (70.3%), and turbidity (99.7%). However, an addition of NaOH was required to adjust the pH, and this could be a disadvantage in the oxidation process.

The pH solution was an important factor for wastewater treatment. In anodic oxidation, many reports exist on the influence of pH solution, but the results are diverse and even contradictory due to different organic structures and electrode materials [1]. In an acidic solution, the degradation process of azo dyes is higher than in a basic solution, as in acidic solutions, chlorides are reduced to free chlorine, which is a dominant oxidizing agent [6]. During all experiments, the initial pH decreased during the treatment time (2.3–2.75). This could be attributed to the fragmentation of organic matter into carboxylic acids, carbonic acid, and ions as by-products of mineralization. Figure 5 shows the behavior of the conductivity during the treatment time; it increased at the end of the process probably as a result of the mineralization in the electrochemical oxidation process.

4.2.3. Degradation Mechanism. Previous research studies [41, 42] indicated that the oxidation of organics with concomitant oxygen evolution assumes that both organic oxidation and oxygen evolution take place on a BDD anode surface via the intermediation of hydroxyl radicals generated from the reaction with water shown in



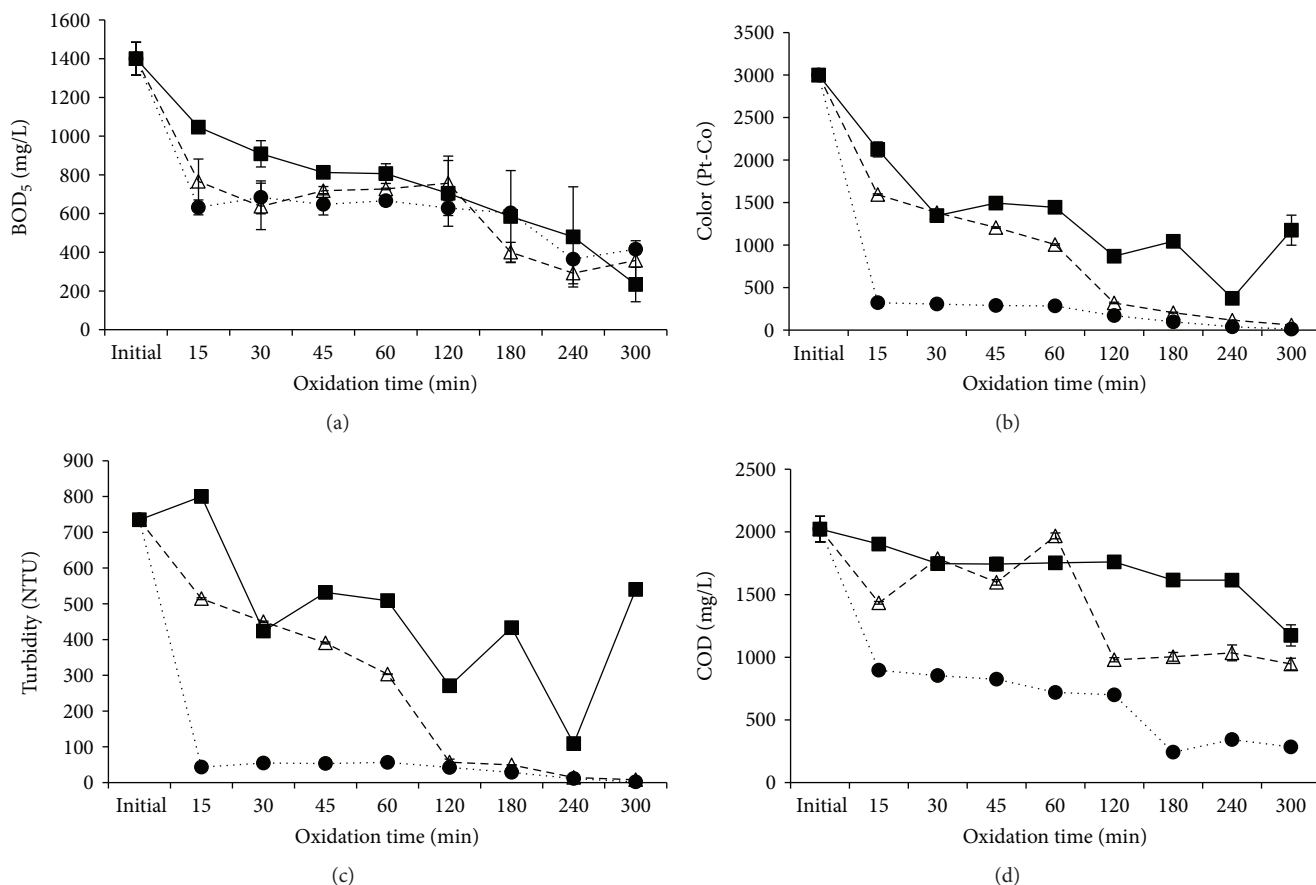


FIGURE 4: Behavior of (a) BOD₅, (b) color, (c) turbidity, and (d) COD. Applying 3.5 mA·cm⁻², at pH 5.23 (■), 7 (Δ), and 10 (●).

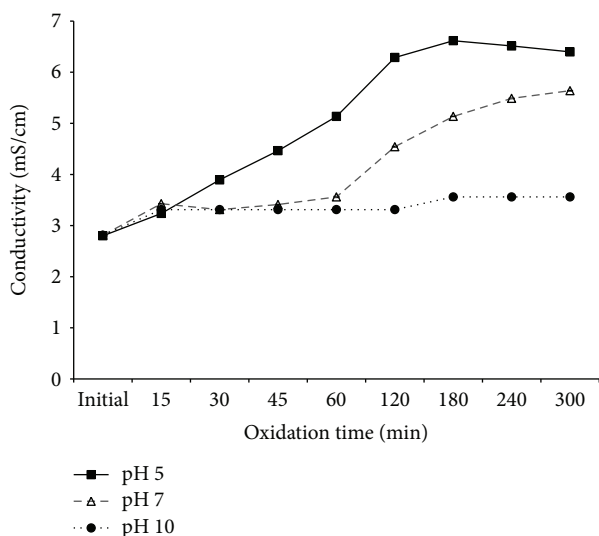
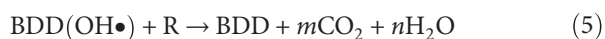
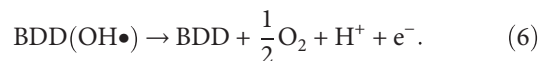


FIGURE 5: Conductivity behavior during the treatment time at three different pH values.



Reaction (4) is in competition with the side reaction of hydroxyl radical conversion to O₂ without any participation of the anode surface as indicated in



Textile wastewater was analyzed via infrared spectroscopy before and after the electrochemical oxidation process, and the spectra are shown in Figure 6. The principal functional groups found in the aqueous solution of dye were -NH- (3305 cm⁻¹), the C-H aromatic bond (2910 and 2845 cm⁻¹), -NH₃⁺ (2340 cm⁻¹), aromatic -C=C- (1614 cm⁻¹), sulfoxides (1101 and 1022 cm⁻¹), and C-CO-C in ketones (611 cm⁻¹). The spectra of oxidized water showed that the intensity of corresponding bands to sulfoxides and secondary amines diminished after treatment, whereas the bands of R-COOH and O-C=O increased. In accordance with the above, the proposed dye degradation mechanism is shown in Figure 6.

4.3. Phytoremediation with *Salix babylonica*

4.3.1. Textile Wastewater. After oxidation treatment, the oxidized water was placed in contact with plants for 8 and 15 days, as shown in Figure 7. Parameters of the COD, color, and turbidity were minimally reduced. However, at 15 days of contact time, a visible reduction in color and turbidity was noted. According to the results, the plants assimilated better with the pollutants in the raw water than in the oxidized water due to the structural changes that the compounds suffered with the electrooxidation treatment. The coupled system (electrooxidation + phytoremediation)

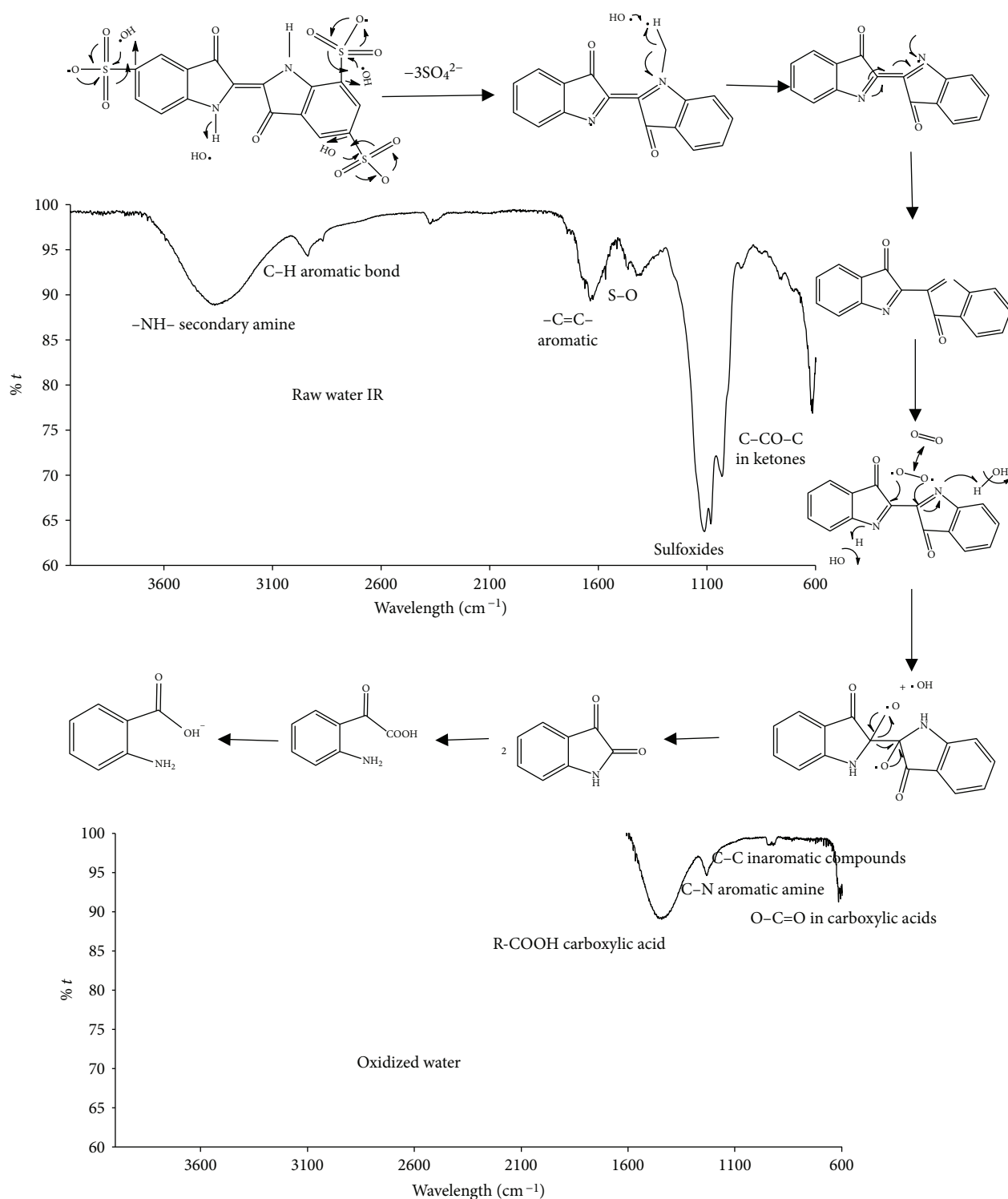


FIGURE 6: Diagram of the degradation mechanism proposed. Within the figure are shown the infrared spectra of raw water and oxidized water.

yielded a reduction of the COD by 14%, color by 85%, and turbidity by 93%.

4.3.2. *Salix babylonica* Biomass. The willow biomass tolerance was analyzed by using Minitab 15.1.20 statistic program

analysis of variance (ANOVA) to find significant differences between treatments. As shown in Figure 8(a), significant differences were found in the leaf numbers, leaf areas, and root numbers among the plants that were in contact with oxidized water for different amounts of time ($P < 0.05$; $F = 8.20$).

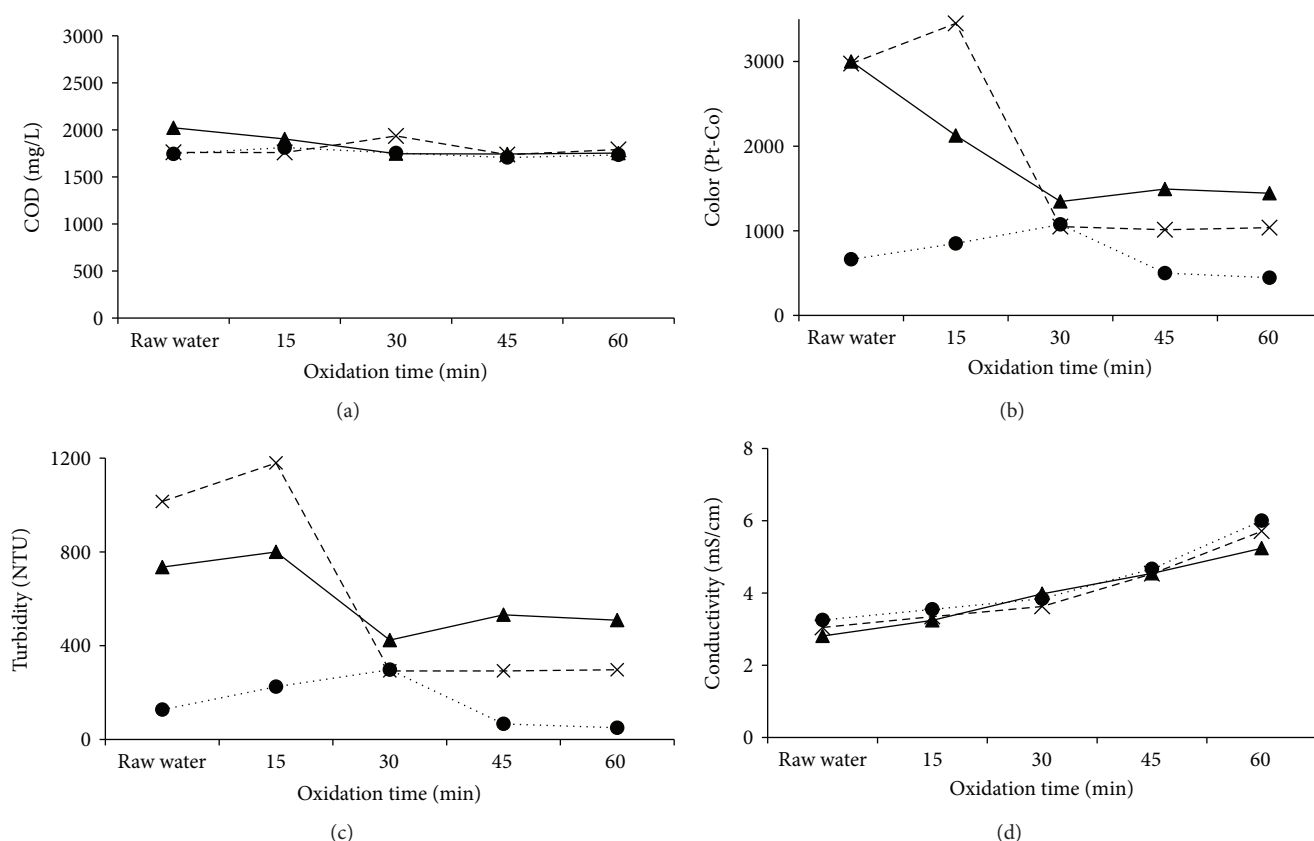


FIGURE 7: Behavior of (a) COD, (b) color, (c) turbidity, and (d) conductivity, with *Salix babylonica* contact at initial time (▲), 8 days (×), and 15 days (●).

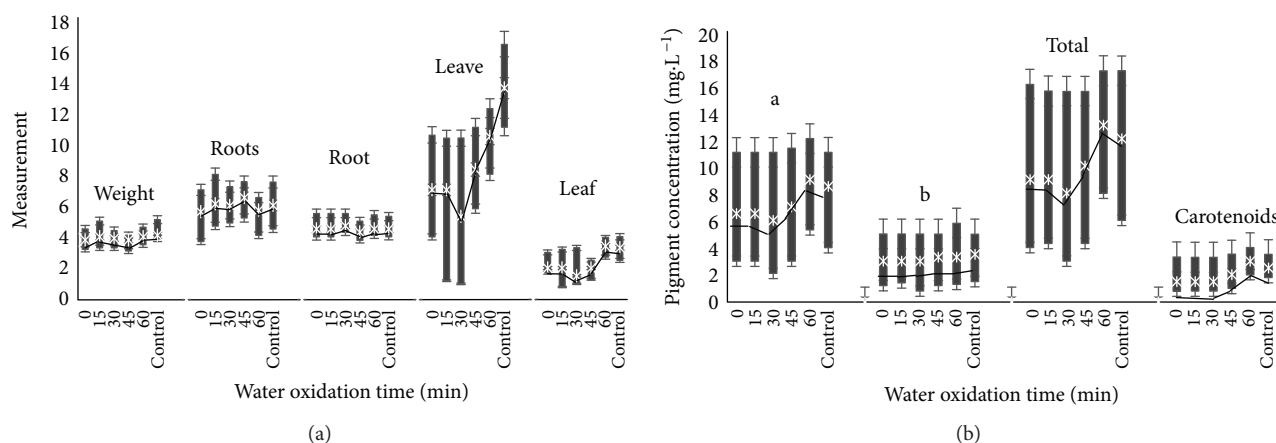


FIGURE 8: Willow tolerance (a) biomass parameters: weight (g), root number, root length (cm), leaf number, and leaf area (cm²); (b) pigment concentration (mg·L⁻¹) at different oxidized water contact times.

Willow plants in contact with oxidized water for 60 minutes reached a biomass close to that of the control plants. The same behavior was observed in the pigment concentration as shown in Figure 8(b). Willow plants tend to lose leaves in a stressful environment, but the root system and photosynthetic metabolism remain.

With respect to the contact time, willow plants reduced their photosynthetic metabolism and lost leaves at eight days

of contact time, but after this time, such plants recovered their photosynthetic metabolism to some extent as shown in Figure 9. This could be because willow plants became adapted to the new environmental conditions. The mechanism by which *Salix babylonica* decreases color and pollutant concentration is unknown, but an increase in the concentration of chlorophylls indicates that the plant is photosynthesizing and thus absorbing nutrients from wastewater.

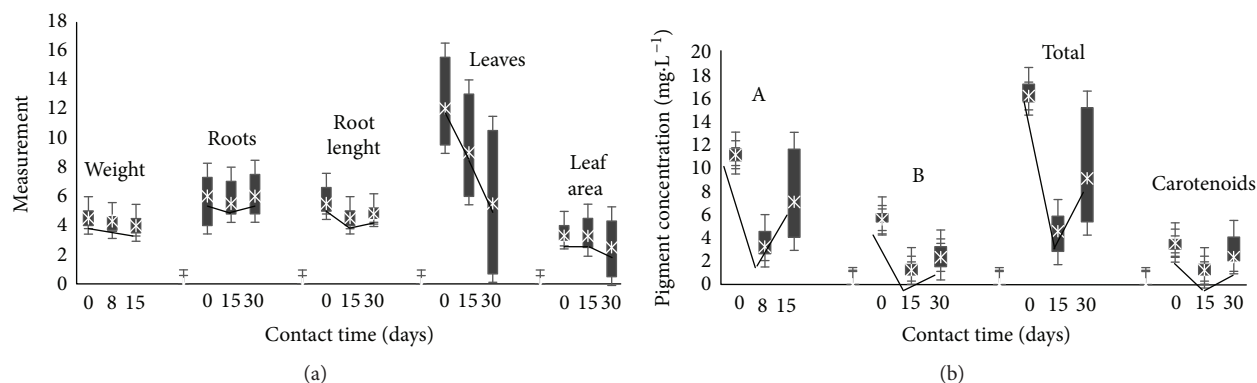


FIGURE 9: Willow tolerance (a) biomass parameters: weight (g), root number, root length (cm), leaf number, and leaf area (cm²); (b) pigment concentration (mg·L⁻¹) at different contact times.

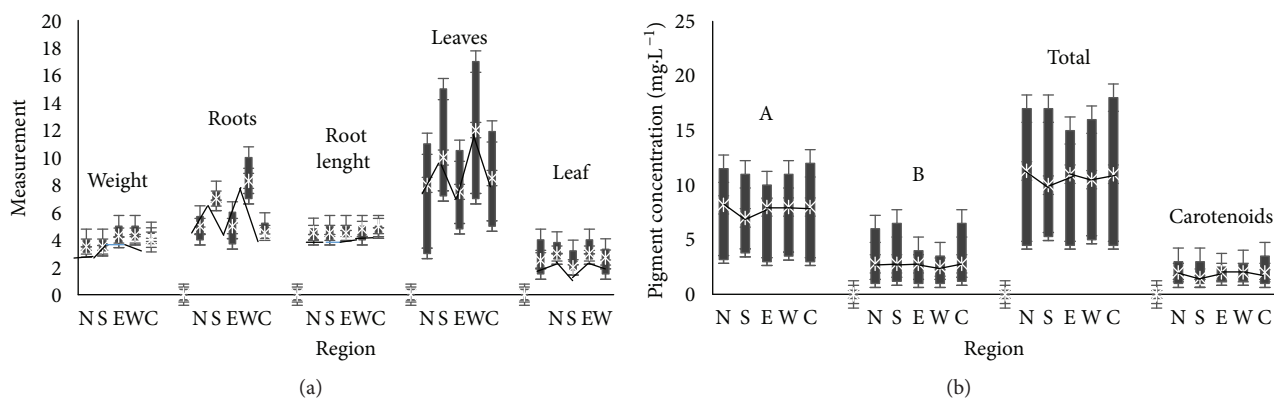


FIGURE 10: Willow tolerance (a) biomass parameters: weight (g), root number, root length (cm), leaf number, and leaf area (cm²); (b) pigment concentration (mg·L⁻¹) from different regions: north (N), south (S), east (E), west (W), and center (C).

Furthermore, the adsorption of contaminants in plant roots has been documented [20]. The results may indicate that the willow phenotype of the western region is characterized by very dense foliage and root system, by genetics, or by environmental influence, but in terms of photosynthetic metabolism, they are the same as the willows of the other regions (Figure 10).

5. Conclusions

Textile wastewater composition was favorable for carrying out electrochemical oxidation due to the high salt content. All experiments were carried out at the original pH (5.23), and it was determined that if the current density was increased, the removal efficiency increased. However, the current efficiency decreased during this process. For this reason, the lower current density was chosen (3.5 mA/cm²) as optimal. The infrared spectroscopy of the wastewater before and after electrooxidation showed a degradation of dye. The proposed degradation mechanism showed carboxylic acids and sulfates as degradation products. In the coupled system, a reduction of the COD was decreased by 14%, color by 85%, and turbidity by 93%. The biomass and pigment of

willow *Salix babylonica* demonstrated that this species has the ability to adapt to adverse conditions very quickly.

Conflicts of Interest

The authors declare that they have no conflicts of interest.

Acknowledgments

The authors thank Consejo Nacional de Ciencia y Tecnología Project 219743 and the scholarship 622274 for support during the development of this work.

References

- [1] F. Guenoud, M. Mokhtari, and H. Akrou, "Electrochemical degradation of malachite green with BDD electrodes: effect of electrochemical parameters," *Diamond and Related Materials*, vol. 46, pp. 8–14, 2014.
- [2] T. Robinson, G. McMullan, R. Marchant, and P. Nigam, "Remediation of dyes in textile effluent: a critical review on current treatment technologies with a proposed alternative," *Bioresource Technology*, vol. 77, no. 3, pp. 247–255, 2001.

- [3] R. G. Saratale, G. D. Saratale, J. S. Chang, and S. P. Govindwar, "Bacterial decolorization and degradation of azo dyes: a review," *Journal of the Taiwan Institute of Chemical Engineers*, vol. 42, no. 1, pp. 138–157, 2011.
- [4] I. Bazin, A. Ibn Hadj Hassine, Y. Haj Hamouda et al., "Estrogenic and anti-estrogenic activity of 23 commercial textile dyes," *Ecotoxicology and Environmental Safety*, vol. 85, pp. 131–136, 2012.
- [5] V. Buscio, M. Crespi, and C. Gutiérrez-Bouzán, "Sustainable dyeing of denim using indigo dye recovered with polyvinylidene difluoride ultrafiltration membranes," *Journal of Cleaner Production*, vol. 91, pp. 201–207, 2015.
- [6] P. Kariyajanavar, N. Jogtappa, and Y. A. Nayaka, "Studies on degradation of reactive textile dyes solution by electrochemical method," *Journal of Hazardous Materials*, vol. 190, no. 1–3, pp. 952–961, 2011.
- [7] A. Asghar, A. A. Abdul Raman, and W. M. A. Wan Daud, "Advanced oxidation processes for *in-situ* production of hydrogen peroxide/hydroxyl radical for textile wastewater treatment: a review," *Journal of Cleaner Production*, vol. 87, pp. 826–838, 2015.
- [8] S. Hussain, S. Shaikh, and M. Farooqui, "COD reduction of waste water streams of active pharmaceutical ingredient – atenolol manufacturing unit by advanced oxidation-Fenton process," *Journal of Saudi Chemical Society*, vol. 17, no. 2, pp. 199–202, 2013.
- [9] J. L. De Moraes and P. P. Zamora, "Use of advanced oxidation processes to improve the biodegradability of mature landfill leachates," *Journal of Hazardous Materials*, vol. 123, no. 1–3, pp. 181–186, 2005.
- [10] A. R. Ribeiro, O. C. Nunes, M. F. R. Pereira, and A. M. T. Silva, "An overview on the advanced oxidation processes applied for the treatment of water pollutants defined in the recently launched Directive 2013/39/EU," *Environment International*, vol. 75, pp. 33–51, 2015.
- [11] P. Asaithambi and M. Matheswaran, "Electrochemical treatment of simulated sugar industrial effluent: optimization and modeling using a response surface methodology," *Arabian Journal of Chemistry*, vol. 9, Supplement 2, pp. S981–S987, 2016.
- [12] C. A. Martínez-Huitle and E. Brillas, "Decontamination of wastewaters containing synthetic organic dyes by electrochemical methods: a general review," *Applied Catalysis B: Environmental*, vol. 87, no. 3–4, pp. 105–145, 2009.
- [13] S. A. Alves, T. C. R. Ferreira, N. S. Sabatini et al., "A comparative study of the electrochemical oxidation of the herbicide tebuthiuron using boron-doped diamond electrodes," *Chemosphere*, vol. 88, no. 2, pp. 155–160, 2012.
- [14] E. Butrón, M. E. Juárez, M. Solis, M. Teutli, I. González, and J. L. Nava, "Electrochemical incineration of indigo textile dye in filter-press-type FM01-LC electrochemical cell using BDD electrodes," *Electrochimica Acta*, vol. 52, no. 24, pp. 6888–6894, 2007.
- [15] C. A. Martínez-Huitle, E. V. Dos Santos, D. M. De Araújo, and M. Panizza, "Applicability of diamond electrode/anode to the electrochemical treatment of a real textile effluent," *Journal of Electroanalytical Chemistry*, vol. 674, pp. 103–107, 2012.
- [16] C. A. Basha, K. V. Selvakumar, H. J. Prabhu, P. Sivashanmugam, and C. W. Lee, "Degradation studies for textile reactive dye by combined electrochemical, microbial and photocatalytic methods," *Separation and Purification Technology*, vol. 79, no. 3, pp. 303–309, 2011.
- [17] A. V. Patil and J. P. Jadhav, "Evaluation of phytoremediation potential of *Tagetes patula* L. for the degradation of textile dye Reactive Blue 160 and assessment of the toxicity of degraded metabolites by cytogenotoxicity," *Chemosphere*, vol. 92, no. 2, pp. 225–232, 2013.
- [18] N. R. Rane, V. V. Chandanshive, A. D. Watharkar et al., "Phytoremediation of sulfonated Remazol Red dye and textile effluents by *Alternanthera philoxeroides*: an anatomical, enzymatic and pilot scale study," *Water Research*, vol. 83, pp. 271–281, 2015.
- [19] A. N. Kabra, R. V. Khandare, T. R. Waghmode, and S. P. Govindwar, "Phytoremediation of textile effluent and mixture of structurally different dyes by *Glandularia pulchella* (Sweet) Tronc," *Chemosphere*, vol. 87, no. 3, pp. 265–272, 2012.
- [20] R. V. Khandare and S. P. Govindwar, "Phytoremediation of textile dyes and effluents: current scenario and future prospects," *Biotechnology Advances*, vol. 33, no. 8, pp. 1697–1714, 2015.
- [21] L. C. Davies, C. C. Carias, J. M. Novais, and S. Martins-Dias, "Phytoremediation of textile effluents containing azo dye by using *Phragmites australis* in a vertical flow intermittent feeding constructed wetland," *Ecological Engineering*, vol. 25, no. 5, pp. 594–605, 2005.
- [22] S. Torbati, A. R. Khataee, and A. Movafeghi, "Application of watercress (*Nasturtium officinale* R. Br.) for biotreatment of a textile dye: investigation of some physiological responses and effects of operational parameters," *Chemical Engineering Research and Design*, vol. 92, no. 10, pp. 1934–1941, 2014.
- [23] F. Vafaei, A. Movafeghi, A. R. Khataee, M. Zarei, and S. Y. Salehi Lisar, "Potential of *Hydrocotyle vulgaris* for phytoremediation of a textile dye: inducing antioxidant response in roots and leaves," *Ecotoxicology and Environmental Safety*, vol. 93, pp. 128–134, 2013.
- [24] A. D. Watharkar and J. P. Jadhav, "Detoxification and decolorization of a simulated textile dye mixture by phytoremediation using *Petunia grandiflora* and *Gailardia grandiflora*: a plant-plant consortial strategy," *Ecotoxicology and Environmental Safety*, vol. 103, pp. 1–8, 2014.
- [25] M. N. Dos Santos Utmazian, G. Wieshammer, R. Vega, and W. W. Wenzel, "Hydroponic screening for metal resistance and accumulation of cadmium and zinc in twenty clones of willows and poplars," *Environmental Pollution*, vol. 148, no. 1, pp. 155–165, 2007.
- [26] K. Drzewiecka, M. Mleczek, M. Gąsecka, Z. Magdziak, and P. Goliński, "Changes in *Salix viminalis* L. cv. 'Cannabina' morphology and physiology in response to nickel ions – hydroponic investigations," *Journal of Hazardous Materials*, vol. 217–218, pp. 429–438, 2012.
- [27] W. Yang, Z. Ding, F. Zhao et al., "Comparison of manganese tolerance and accumulation among 24 *Salix* clones in a hydroponic experiment: application for phytoremediation," *Journal of Geochemical Exploration*, vol. 149, pp. 1–7, 2015.
- [28] C. Cosio, P. Vollenweider, and C. Keller, "Localization and effects of cadmium in leaves of a cadmium-tolerant willow (*Salix viminalis* L.): I. macrolocalization and phytotoxic effects of cadmium," *Environmental and Experimental Botany*, vol. 58, no. 1–3, pp. 64–74, 2006.
- [29] A. Evlard, K. Sergeant, B. Printz et al., "A multiple-level study of metal tolerance in *Salix fragilis* and *Salix aurita* clones," *Journal of Proteomics*, vol. 101, pp. 113–129, 2014.
- [30] M. Vaculík, C. Konlechner, I. Langer et al., "Root anatomy and element distribution vary between two *Salix caprea* isolates

- with different Cd accumulation capacities," *Environmental Pollution*, vol. 163, pp. 117–126, 2012.
- [31] M. Mleczek, M. Łukaszewski, Z. Kaczmarek, I. Rissmann, and P. Golinski, "Efficiency of selected heavy metals accumulation by *Salix viminalis* roots," *Environmental and Experimental Botany*, vol. 65, no. 1, pp. 48–53, 2009.
 - [32] H. X. Corseuil and F. N. Moreno, "Phytoremediation potential of willow trees for aquifers contaminated with ethanol-blended gasoline," *Water Research*, vol. 35, no. 12, pp. 3013–3017, 2001.
 - [33] S. V. Skaates, A. Ramaswami, and L. G. Anderson, "Transport and fate of dieldrin in poplar and willow trees analyzed by SPME," *Chemosphere*, vol. 61, no. 1, pp. 85–91, 2005.
 - [34] X.-Z. Yu, J. D. Gu, and S. Liu, "Biotransformation and metabolic response of cyanide in weeping willows," *Journal of Hazardous Materials*, vol. 147, no. 3, pp. 838–844, 2007.
 - [35] C. T. Cano-Rodríguez, G. Roa-Morales, A. Amaya-Chávez, R. A. Valdés-Arias, C. E. Barrera-Díaz, and P. Balderas-Hernández, "Tolerance of *Myriophyllum aquaticum* to exposure of industrial wastewater pretreatment with electrocoagulation and their efficiency in the removal of pollutants," *Journal of Environmental Biology*, vol. 35, no. 1, pp. 127–136, 2014.
 - [36] A. Eslami, M. Moradi, F. Ghanbari, and F. Mehdipour, "Decolorization and COD removal from real textile wastewater by chemical and electrochemical Fenton processes: a comparative study," *Journal of Environmental Health Science and Engineering*, vol. 11, no. 1, p. 31, 2013.
 - [37] E. Tsantaki, T. Velegraki, A. Katsaounis, and D. Mantzavinos, "Anodic oxidation of textile dyehouse effluents on boron-doped diamond electrode," *Journal of Hazardous Materials*, vol. 207–208, pp. 91–96, 2012.
 - [38] APHA and AWWA, *Standard Methods for Examination of Water and Wastewater*, American Public Health Association y Water Pollution Control Federation, Washington, DC, USA, 21st edition, 2005.
 - [39] J. Val, L. Heras, and E. Monge, "New equations for the determination of photosynthetic pigments in acetone," *Annals Aula Dei*, vol. 17, no. 3, pp. 231–238, 1985.
 - [40] T.-P. Moisés, B.-H. Patricia, C. E. Barrera-Díaz, R.-M. Gabriela, and R. Natividad-Rangel, "Treatment of industrial effluents by a continuous system: electrocoagulation – activated sludge," *Bioresource Technology*, vol. 101, no. 20, pp. 7761–7766, 2010.
 - [41] A. Kapalka, G. Fóti, and C. Comninellis, "Investigations of electrochemical oxygen transfer reaction on boron-doped diamond electrodes," *Electrochimica Acta*, vol. 53, no. 4, pp. 1954–1961, 2007.
 - [42] I. Linares-Hernández, C. Barrera-Díaz, B. Bilyeu, P. Juárez-GarcíaRojas, and E. Campos-Medina, "A combined electrocoagulation–electrooxidation treatment for industrial wastewater," *Journal of Hazardous Materials*, vol. 175, no. 1–3, pp. 688–694, 2010.

Research Article

Pretreatment of Real Wastewater from the Chocolate Manufacturing Industry through an Integrated Process of Electrocoagulation and Sand Filtration

Marco A. García-Morales ¹, Julio César González Juárez,¹ Sonia Martínez-Gallegos,¹ Gabriela Roa-Morales,² Ever Peralta,³ Eduardo Martín del Campo López,² Carlos Barrera-Díaz,² Verónica Martínez Miranda,² and Teresa Torres Blancas⁴

¹Instituto Nacional de México, Instituto Tecnológico de Toluca, Av. Tecnológico s/n, Col. Agrícola Buenavista, 52149 Toluca, MEX, Mexico

²Facultad de Química, Paseo Colón s/n, Residencial Colón, Universidad Autónoma del Estado de México (UAEMéx), 50120 Toluca de Lerdo, MEX, Mexico

³Universidad del Mar, Campus Puerto Angel, Ciudad Universitaria s/n, 70902 Puerto Angel, OAX, Mexico

⁴Instituto de Química, Carretera Toluca-Atlaquemulco Km 14.5, Universidad Nacional Autónoma de México and Centro Conjunto de Investigación en Química Sustentable UAEM-UNAM, 50200 Toluca, MEX, Mexico

Correspondence should be addressed to Marco A. García-Morales; magm0904@hotmail.com

Received 20 June 2017; Revised 20 December 2017; Accepted 7 March 2018; Published 3 April 2018

Academic Editor: Mark van Der Auweraer

Copyright © 2018 Marco A. García-Morales et al. This is an open access article distributed under the Creative Commons Attribution License, which permits unrestricted use, distribution, and reproduction in any medium, provided the original work is properly cited.

The purpose of this study was to evaluate the efficiency of removal of suspended solids in terms of turbidity, color, and chemical oxygen demand (COD) when integrating the electrocoagulation process using aluminum sacrificial anodes and the sand filtration process as a pretreatment of wastewater from the chocolate manufacturing plant in Toluca, México. Wastewater from the chocolate manufacturing industry used in this study is classified as nontoxic, but is characterized as having a high content of color (5952 ± 76 Pt-Co), turbidity (1648 ± 49 FAU), and COD (3608 ± 250 mg/L). Therefore, enhanced performance could be achieved by combining pretreatment techniques to increase the efficiencies of the physical, chemical, and biological treatments. In the integrated process, there was a turbidity reduction of $96.1 \pm 0.2\%$ and an increase in dissolved oxygen from 3.8 ± 0.05 mg/L (inlet sand filtration) to 6.05 ± 0.03 mg/L (outlet sand filtration) after 120 min of treatment. These results indicate good water quality necessary for all forms of elemental life. Color and COD removals were $98.2 \pm 0.2\%$ and $39.02 \pm 2.2\%$, respectively, during the electrocoagulation process (0.2915 mA/cm^2 current density and 120 min of treatment). The proposed integrated process could be an attractive alternative of pretreatment of real wastewater to increase water quality of conventional treatments.

1. Introduction

Chocolate has a uniquely attractive taste and might even be beneficial for health. The popularity of this food appears to be mainly due to its potential to arouse sensory pleasure and positive emotions. Chocolates are complex multiphase systems of particulate (sugar, cocoa, and certain milk components) and continuous phases (cocoa butter, milk fat, and emulsifiers) [1]. The industrial chocolate manufacturing process consists of the following steps: cocoa collection, cleaning,

fermentation, drying, roasting, grinding, pressing, spraying, and mixing, during which a large amount of water is used [2]. The wastewater in the chocolate manufacturing industry contains no hazardous ingredients, but it has a high content of color, total solids (TS), biochemical oxygen demand (BOD), and chemical oxygen demand (COD) [3].

The selection of treatment method is mainly based on the composition of the wastewater. Various treatment methods like (a) biological process, namely, anaerobic and aerobic; (b) physicochemical treatment, namely, adsorption,

membrane process, reverse osmosis, and coagulation/flocculation; and (c) oxidation processes, namely, ozone and Fenton, have been used for the treatment of industrial wastewater [4]. The aerobic process involves the use of free or dissolved oxygen by microorganisms (aerobes) in the conversion of organic wastes to biomass and CO_2 . In the anaerobic process, complex organic wastes are degraded into methane, CO_2 , and H_2O through three basic steps (hydrolysis and acidogenesis including acetogenesis and methanogenesis) in the absence of oxygen [5]. Although the biological method is widely applied for the treatment of wastewater, too many disadvantages tend to focus on other technologies: the need for longer aeration times, requirement of large land areas, high energy demand, excess sludge production, and microbial inhibition due to biomass poisoning [6]. The physicochemical treatment processes are effective for the treatment of industrial wastewater and are quick and compact but are not generally employed due to the associated high chemical and operational costs as well as complex sludge generation [7, 8]. Oxidation processes generate and use mainly hydroxyl radicals to oxidize the organic compounds. $\text{HO}\bullet$ has a high oxidation or standard reduction potential (2.8 V) [9]. The main characteristics of $\text{HO}\bullet$ are as follows: it is short-lived, it is simply produced, it is a powerful oxidant, it has an electrophilic behavior, it is ubiquitous in nature, it is highly reactive, and it is practically nonselective. It reacts with a wide variety of organic compound classes, producing shorter and simpler organic compounds, or in case of full mineralization [10]. Nevertheless, some researchers have reported that these processes were highly not effective for industrial application [11]. Decolorization through chemical treatment with ozone, Fenton's reagent, and $\text{H}_2\text{O}_2/\text{UV}$ leads to color reduction due to breaking of the conjugation and or bonds in chromophoric groups. In addition, the formation of potentially toxic oxidation intermediates may occur; therefore, these are not preferred solutions [4].

Due to the complexity of chocolate manufacturing plant wastewater, in which pollutants may be suspended, emulsified, or dissolved, electrocoagulation (EC) represents an interesting alternative for water remediation, providing comparable results with even some advanced oxidation processes in the removal of persistent compounds from pharmaceutical and food industrial effluents [12, 13]. Among the advantages of an EC process, the following can be highlighted: nonspecificity, similar treatment for drinking water and wastewater, low dosage of chemical reagents, low operating costs, low sludge production (compared to traditional chemical coagulation), absence of moving parts in the reaction setup, and low power consumption if solar energy is used [14]. From a practical point of view, EC must be considered a parallel mechanism that includes charge neutralization and adsorption. At the beginning of the process, realized ions destabilize the system forming metal hydroxide complexes that aggregate suspended particles (flocs) and adsorb dissolved particles [15, 16]. In addition to the above, at the cathode, gas formation takes place allowing floc floatation. The electrical corrosion of metal in the sacrificial electrode and the formation of hydroxyl anion are the essential reactions in

any EC process [17]. The floc formation is a complex process; according to the Derjaguin-Landau-Verwey-Overbeek (DLVO) theory, aggregates depend on interaction forces (van der Waals) and double-layer forces [18].

It is well known that iron and aluminum are the preferred materials to be used as sacrificial anodes. For iron, anode oxidation could lead to either ferrous or ferric ion formation; however, low solubility of Fe^{3+} ions suggests the release of Fe^{2+} ions, which are oxidized to ferric ions due to pH and dissolved oxygen concentration. For aluminum, anode oxidation leads to Al^{3+} ion formation. In both cases, the subsequent formation of hydroxide compounds induces the presence of monomeric and polymeric amorphous species that trap colloidal particles and promote the soluble pollutant adsorption [14]. Both metals are fine as construction materials for sacrificial electrodes, but for economics, iron has a slight advantage: it is nontoxic, meaning it can be used for drinking water, and it has a lower price. Otherwise, there are many studies that report the effectiveness of aluminum anodes in the EC process for emerging contaminants [17, 19, 20].

Sand filters are a natural medium that can be used as a filter for wastewater treatment. It displays two roles: the retention of solids and biomass fixation that could be developed on the granular material and the biodegradation of organic, phosphorus, and nitrogenous pollutants [21–23]. For disinfection of wastewater reuse, the turbidity and suspended solids must be reduced to prevent the hiding of pathogens and organisms that hide behind these solids. Currently, the most widely used process to remove residual TSS (total suspended solids) is treated effluent filtration [24, 25]. The main mechanisms contributing to the removal of suspended solids in sand filters are cast [22, 26]. This has been identified as the major operating mechanism for the removal of suspended solids during filtration of secondary effluent from processes and biological treatments. Perhaps, other mechanisms, such as interception, impact, and adhesion, are operational, although its effects are minor and mostly marked by the action of casting [27–30].

The purpose of this study is to evaluate the efficiency of integrated electrocoagulation and sand filtration processes as a pretreatment of wastewater from the chocolate manufacturing plants in terms of turbidity, color, and chemical oxygen demand (COD).

2. Materials and Methods

2.1. Sampling. The wastewater samples used in this study were collected at the effluent of an industrial chocolate manufacturing plant, preserved, and analyzed according to the standard methods for conventional characterization APHA/AWWA/WEF [31]. The electrocoagulation and filtration were monitored for turbidity, color, and COD, as well as pH variation. A UV-VIS spectrum of the effluent was done on a PerkinElmer Lambda 25 UV/VIS Spectrophotometer (USA). Color and turbidity were monitored at 465 and 860 nm wavelengths, respectively, using a Hach DR/4000U 110 spectrometer. COD was analyzed by the

closed reflux colorimetric method (Method 5220 D; according to APHA) [31].

2.2. Electrocoagulation Process. Electrocoagulation was carried out in a laboratory-scale batch reactor; two rectangular commercial aluminum plates (99.3 wt% Al) served as anode and cathode. The anodic and cathodic active surface area was 343 cm^2 immersed in wastewater with 0.1372 l/cm of the SA/V ratio. A DC power source supplied the system with 0.1 A , corresponding to 0.2915 mA/cm^2 current density which was kept for 120 min . Electrocoagulation was performed without additional electrolyte ($750 \text{ }\mu\text{S/cm}$ conductivity in wastewater). The electrodes were connected to a digital DC power supply (GW Instek GPR-1820HD, $0\text{--}18 \text{ V}$; $0\text{--}20 \text{ A}$, China). Twenty-five mL of sample was taken every 30 min during the 2 h electrocoagulation process. The efficiency of EC was evaluated by measuring the turbidity, color, and chemical oxygen demand (COD) [32].

2.3. Filtration Process. Two horizontal conventional down-flow filters (sand filter A and sand filter B) installed in parallel were used for the filtration process; the filter media of each filter included two beds composed of gravel $1/4 \times 1/8$ (24 cm) and gravel $1/8 \times 1/16$ (51 cm), each filter measuring 168 cm in length and 15 cm in diameter. The effective size for each filter was 0.71 mm . In the bottom of each filter, gravel particles ($3/4 \times 1/2$) were placed to support upper layers. The filtration process was carried out after completing the electrocoagulation process, as shown in Figure 1. At the filter outlet, turbidity and dissolved oxygen (DO) were monitored. Filtration experiments were performed without recirculation.

The removal efficiency was calculated using

$$Y(\%) = \frac{(y_0 - y)}{y_0}, \quad (1)$$

where Y is the removal efficiency of turbidity/color/COD and y_0 and y correspond to the initial and final values of a determined parameter, respectively.

3. Results and Discussion

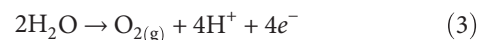
Table 1 presents the initial physicochemical parameters of wastewater from the chocolate manufacturing process. The wastewater contained pollutants, which were reflected in high levels of COD, due to ingredients used in chocolate manufacturing such as cocoa bean, chocolate liquor obtained from the broken beans that are ground, cocoa butter obtained from the broken-down cell walls, sugar, and emulsifiers in conjunction with the waste from the processes of cleaning, fermentation, drying, roasting, grinding, pressing, spraying, and mixing [1, 33]. The color and turbidity values obtained are harmful to aquatic life, obstructing light penetration in the water, inhibiting thus the photosynthesis-based biological processes [31]. The pH was about 7.5 , which was basically a neutral pH environment. Contaminants all achieved maximum removal in this pH condition [30]. Therefore, the following tests were performed using the raw water without pH adjustment, in agreement with previous studies, where

the wastewater was used directly for electrocoagulation experiments [34].

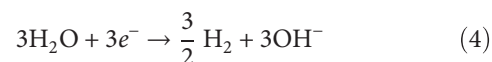
3.1. Electrocoagulation Process Efficiency. After 120 min of treatment, the reductions in turbidity, color, and COD for the electrocoagulation process were $87.8 \pm 0.6\%$, $98.2 \pm 0.2\%$, and $39.02 \pm 2.2\%$, respectively (Figure 2). The experiments were repeated three times to verify the reproducibility of the results; in any experiment, the values of the coefficient of variation were no higher than 5% , indicating that recollected data have an statistical acceptance criteria. Zhao et al. carried out EC experiments as a pretreatment applied to wastewater containing oil, grease, and other inorganic contaminants; their results showed a removal of 93.8% in turbidity under the following conditions: 5.56 mA/cm^2 of current density and 30 min of reaction time [34]. Regarding color removal, Ricordel and Djelal obtained a removal of 80% after EC treatment of landfill leachate, although not the same substrate; this had high levels of organic matter, refractory compounds, inorganic contaminants, and color [32]. In addition, an efficiency greater than 32% was obtained for Farhadi et al. by comparing electrocoagulation (1.83 mA/cm^2 of current density and 30 min of time reaction) and an advanced oxidation process during pharmaceutical wastewater treatment [35]. The removal of turbidity, color, and COD is attributed to sweep flocculation [34]. In the EC process, coagulating ions are produced in situ, involving three successive stages: (i) formation of coagulants by electrolytic oxidation of the sacrificial electrode of Al; (ii) destabilization of the contaminants, particulate suspension, and breaking of emulsions; and (iii) aggregation of the destabilized phases to form flocs. Al gets dissolved from the anode, generating corresponding metal ions that almost immediately hydrolyze to polymeric aluminum oxyhydroxides [4, 36]. These polymeric oxyhydroxides are excellent coagulating agents. When aluminum electrodes in the EC process are used as anode and cathode, the main reactions at the anode are as follows:



Also, oxygen evolution can compete with aluminum dissolution at the anode via



At the cathode, hydrogen evolution takes place via the following reaction, assisting in the floatation of the flocculated particles out of the water:



At high pH values, OH^- generated at the cathode during hydrogen evolution may attack the cathode by the following reaction [18, 37]:



Al^{3+} and hydroxyl ions are generated by electrode reactions as shown in (2), (4), and (5) to form various monomeric-polymeric species transformed initially into

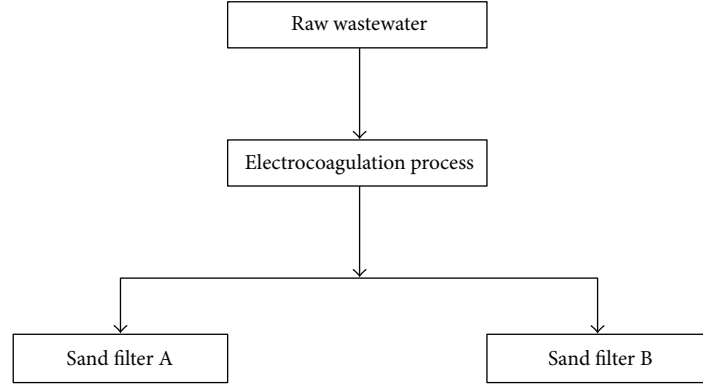
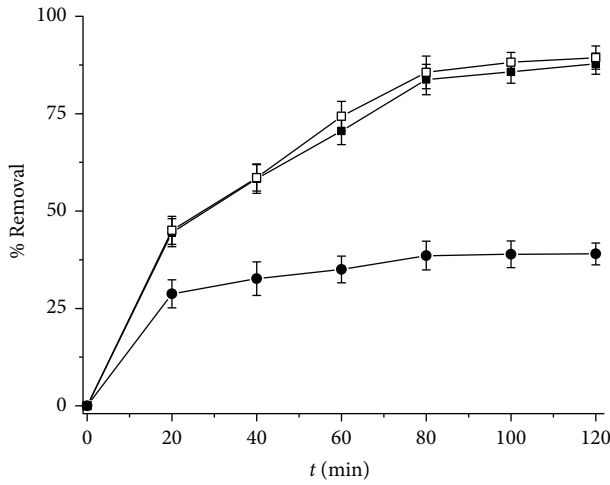


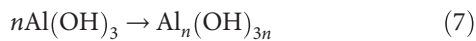
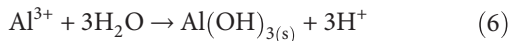
FIGURE 1: Flow chart used in this study.

TABLE 1: Initial and final physicochemical parameters from treated wastewater.

Parameter	Raw wastewater Value	Units	Parameter	Treated wastewater Value	Units	% Removal in the integrated process
COD	3608 ± 250	mg/L	COD	2200 ± 11	mg/L	39.02 ± 2.2
Color	5952 ± 76	Pt-Co	Color	101 ± 17	Pt-Co	98.2 ± 0.26
Turbidity	1648 ± 49	mg/L	Turbidity	64 ± 5	mg/L	96.1 ± 0.2
pH	7.4 ± 0.06		pH	9.11 ± 0.03		
Conductivity	750 ± 28	μS/cm	Conductivity	520 ± 9	μS/cm	
			Energy consumption	0.32	kWh/m ³	

FIGURE 2: Contaminant removal efficiency in wastewater treated after the electrocoagulation process at a current density of 0.2915 mA/cm²: turbidity (■), color (◊), and COD (●).

$\text{Al}(\text{OH})_{3(s)}$ and finally polymerized to $\text{Al}_n(\text{OH})_{3n}$ ((6) and (7)) in the solution [32, 37–39]:



Since the electrocoagulation process is based on removal of the colloidal/particulate COD fraction of wastewater, the

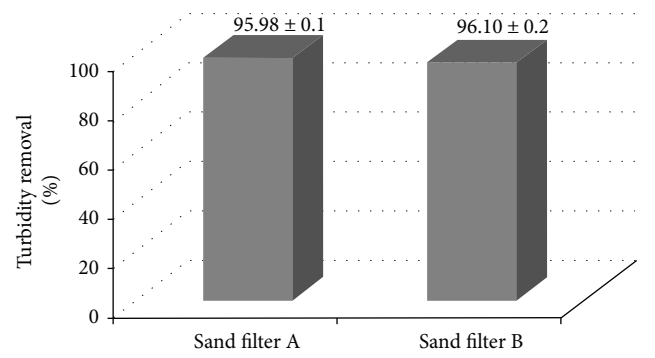


FIGURE 3: Turbidity removal efficiency in treated wastewater.

low efficiency of COD obtained in this process is attributed to the soluble COD fraction in raw wastewater [40].

3.2. Filtration Process Efficiency. As shown in Figure 3, the turbidity after the filtration processes was lower than the initial turbidity, which was 1648 ± 49 FAU in raw wastewater; turbidity removals (%) reached were 95.98 ± 0.1 and 96.10 ± 0.2 for filters A and B, respectively. The turbidity removal was due to the working-in stage (characterized by a rapid decrease in effluent turbidity) and working stage (the effective stage of filtration giving satisfactory effluent quality) [30]. Similar results were obtained by Ramadan, whose results reached 98.05% removal of total suspended solids (TSS) using nonconventional sand filters (TiO_2 was added

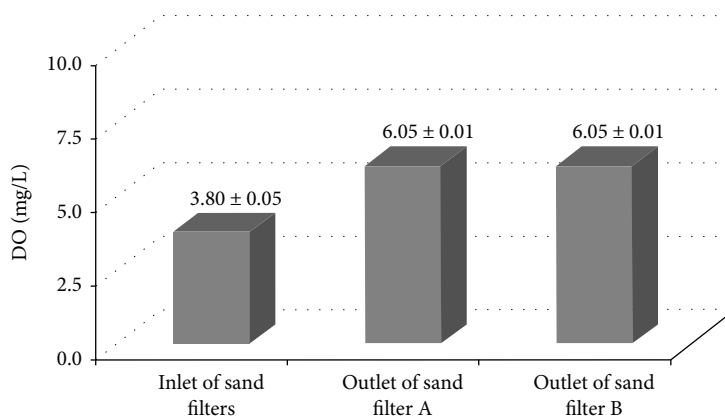
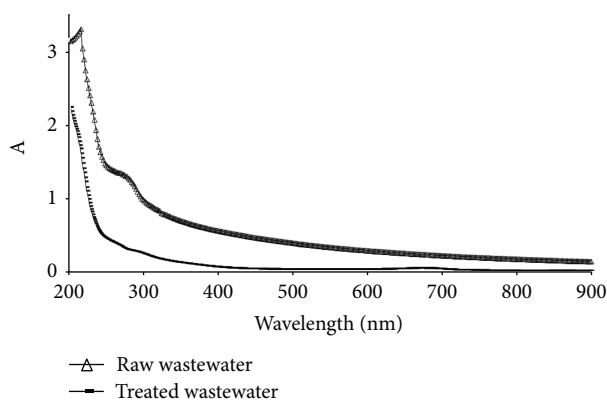


FIGURE 4: Dissolved oxygen in filtration process.

FIGURE 5: UV/VIS spectrum of the raw wastewater and treated wastewater in the electrocoagulation-filtration process at a current density of 0.2915 mA/cm^2 .

to the sand filter) in reducing pollutants from wastewater [41]. Finally, Achak et al. obtained results of 90% turbidity removal from olive mill wastewater generated by the olive oil extraction process [42]. After electrocoagulation, sand filtration could remove flocs by attaching them to the sand grain to improve the removal of turbidity from 87.80% in the EC process to 99.10% after filtration obtained an increase by 11.40%; a statistical test was performed, determining that a statistically significant difference exists between both processes (p value = 0.018).

The concentration of dissolved oxygen in the inlet of each sand filter increased from $3.8 \pm 0.05 \text{ mg/L}$ to $6.05 \pm 0.01 \text{ mg/L}$ after the filtration process during the 120 min experiment (Figure 4). The oxygenation of sand filters is due to the gaseous exchange between the atmosphere and the interstices of sand in the surface of the filter. These results are good because adequate dissolved oxygen is needed for good water quality and is necessary for all forms of elemental life.

3.3. UV/VIS Spectra of the Treated Wastewater. The spectrum for the raw wastewater (Δ) presented a baseline with one absorbance peak at 290 nm, which was associated with the contaminants in this matrix ($3608 \pm 250 \text{ mg/L}$

COD). For 120 min of reaction, treated wastewater by an electrocoagulation-filtration-coupled process (\blacksquare) showed the highest efficiency in removing turbidity, color, and COD together with a decrease in the baseline and in the absorbance peaks, as shown in Figure 5. The removal of contaminants (initial DQO = $3608 \pm 250 \text{ mg/L}$ and final DQO = $2200 \pm 11 \text{ mg/L}$) was indicated by the decrease in the absorption band at 290 nm and baseline [43].

4. Conclusions

Removal of contaminants was efficient by integrating electrocoagulation and filtration processes as a pretreatment of wastewater from chocolate manufacturing plants, which was reflected in increased removal percentages of turbidity and color and an increase in dissolved oxygen after the integrated filtration processes.

UV/VIS spectra intensity decreased between raw and treated wastewater, indicating the removal of pollutants in the integrated process.

The EC process removed the colloidal/particulate COD fraction in raw wastewater; however, the remaining COD due to the soluble COD fraction was not removed in the integrated process.

Disclosure

This work was presented as a poster with the title “Wastewater Treatment of Chocolate Manufacture Industry through an Integrated Process of Electrocoagulation and Filtration” at Electrochemical Treatments for Organic Pollutant Degradation in Water and Soils, 2014, ECS and SMEQ Joint International Meeting.

Conflicts of Interest

The authors declare that there is no conflict of interest regarding the publication of this paper.

Acknowledgments

The authors wish to acknowledge the support given by CONACYT and the Tecnológico Nacional de México for the development of this research through Project TecNM 5652.15-P.

References

- [1] M. El-kalyoubi, M. F. Khallaf, A. Abdelrashid, and E. M. Mostafa, "Quality characteristics of chocolate – containing some fat replacer," *Annals of Agricultural Science*, vol. 56, no. 2, pp. 89–96, 2011.
- [2] P. B. Botelho, M. Galasso, V. Dias et al., "Oxidative stability of functional phytosterol-enriched dark chocolate," *LWT - Food Science and Technology*, vol. 55, no. 2, pp. 444–451, 2014.
- [3] M. V. Copetti, B. T. Iamanaka, M. A. Nester, P. Efraim, and M. H. Taniwaki, "Occurrence of ochratoxin A in cocoa by-products and determination of its reduction during chocolate manufacture," *Food Chemistry*, vol. 136, no. 1, pp. 100–104, 2013.
- [4] E. Gengec, M. Kobya, E. Demirbas, A. Akyol, and K. Oktor, "Optimization of baker's yeast wastewater using response surface methodology by electrocoagulation," *Desalination*, vol. 286, pp. 200–209, 2012.
- [5] Y. J. Chan, M. F. Chong, C. L. Law, and D. G. Hassell, "A review on anaerobic-aerobic treatment of industrial and municipal wastewater," *Chemical Engineering Journal*, vol. 155, no. 1-2, pp. 1–18, 2009.
- [6] M. Luan, G. Jing, Y. Piao, D. Liu, and L. Jin, "Treatment of refractory organic pollutants in industrial wastewater by wet air oxidation," *Arabian Journal of Chemistry*, vol. 10, no. 1, pp. S769–S776, 2017.
- [7] M. S. Nawaz and M. Ahsan, "Comparison of physico-chemical, advanced oxidation and biological techniques for the textile wastewater treatment," *Alexandria Engineering Journal*, vol. 53, no. 3, pp. 717–722, 2014.
- [8] S. Renou, J. G. Givaudan, S. Poulain, F. Dirassouyan, and P. Moulin, "Landfill leachate treatment: review and opportunity," *Journal of Hazardous Materials*, vol. 150, no. 3, pp. 468–493, 2008.
- [9] D. Shahidi, R. Roy, and A. Azzouz, "Advances in catalytic oxidation of organic pollutants – prospects for thorough mineralization by natural clay catalysts," *Applied Catalysis B: Environmental*, vol. 174–175, pp. 277–292, 2015.
- [10] G. Boczkaj and A. Fernandes, "Wastewater treatment by means of advanced oxidation processes at basic pH conditions: a review," *Chemical Engineering Journal*, vol. 320, pp. 608–633, 2017.
- [11] L. Bilińska, M. Gmurek, and S. Ledakowicz, "Comparison between industrial and simulated textile wastewater treatment by AOPs – biodegradability, toxicity and cost assessment," *Chemical Engineering Journal*, vol. 306, pp. 550–559, 2016.
- [12] W. Baran, E. Adamek, M. Jajko, and A. Sobczak, "Removal of veterinary antibiotics from wastewater by electrocoagulation," *Chemosphere*, vol. 194, pp. 381–389, 2018.
- [13] D. T. Moussa, M. H. El-Naas, M. Nasser, and M. J. Al-Marri, "A comprehensive review of electrocoagulation for water treatment: potentials and challenges," *Journal of Environmental Management*, vol. 186, no. 1, pp. 24–41, 2017.
- [14] J. N. Hakizimana, B. Gourich, M. Chafi et al., "Electrocoagulation process in water treatment: a review of electrocoagulation modeling approaches," *Desalination*, vol. 404, pp. 1–21, 2017.
- [15] Y. A. Ouaisa, M. Chabani, A. Amrane, and A. Bensmaili, "Removal of tetracycline by electrocoagulation: kinetic and isotherm modeling through adsorption," *Journal of Environmental Chemical Engineering*, vol. 2, no. 1, pp. 177–184, 2014.
- [16] D. Valero, J. M. Ortiz, V. García, E. Expósito, V. Montiel, and A. Aldaz, "Electrocoagulation of wastewater from almond industry," *Chemosphere*, vol. 84, no. 9, pp. 1290–1295, 2011.
- [17] E. Nariyan, A. Aghababaei, and M. Sillanpää, "Removal of pharmaceutical from water with an electrocoagulation process; effect of various parameters and studies of isotherm and kinetic," *Separation and Purification Technology*, vol. 188, pp. 266–281, 2017.
- [18] S. Garcia-Segura, M. M. S. G. Eiband, J. V. de Melo, and C. A. Martínez-Huitle, "Electrocoagulation and advanced electrocoagulation processes: a general review about the fundamentals, emerging applications and its association with other technologies," *Journal of Electroanalytical Chemistry*, vol. 801, pp. 267–299, 2017.
- [19] S. Ahmadzadeh, A. Asadipour, M. Pournamdari, B. Behnam, H. Reza Rahimi, and M. Dolatabadi, "Removal of ciprofloxacin from hospital wastewater using electrocoagulation technique by aluminum electrode: optimization and modelling through response surface methodology," *Process Safety and Environmental Protection*, vol. 109, pp. 538–547, 2017.
- [20] M. Çırak, "High-temperature electrocoagulation of colloidal calcareo-argillaceous suspension," *Powder Technology*, vol. 328, no. 1, pp. 13–25, 2018.
- [21] S. E. Keithley and M. J. Kirisits, "An improved protocol for extracting extracellular polymeric substances from granular filter media," *Water Research*, vol. 129, pp. 419–427, 2018.
- [22] Y. Gherairi, A. Amrane, Y. Touil, M. Hadj Mahammed, F. Gherairi, and I. Baameur, "A comparative study of the addition effect of activated carbon obtained from date stones on the biological filtration efficiency using sand dune bed," *Energy Procedia*, vol. 36, pp. 1175–1183, 2013.
- [23] P. Laaksonen, A. Sinkkonen, G. Zaitsev, E. Mäkinen, T. Grönroos, and M. Romantschuk, "Treatment of municipal wastewater in full-scale on-site sand filter reduces BOD efficiently but does not reach requirements for nitrogen and phosphorus removal," *Environmental Science and Pollution Research*, vol. 24, no. 12, pp. 11446–11458, 2017.
- [24] S. Mtavangu, A. M. Rugaika, A. Hilonga, and K. N. Njau, "Performance of constructed wetland integrated with sand filters for treating high turbid water for drinking," *Water Practice and Technology*, vol. 12, no. 1, pp. 25–42, 2017.
- [25] R. Bauer, H. Dizer, I. Graeber, K.-H. Rosenwinkel, and J. M. López-Pila, "Removal of bacterial fecal indicators, coliphages and enteric adenoviruses from waters with high fecal pollution by slow sand filtration," *Water Research*, vol. 45, no. 2, pp. 439–452, 2011.
- [26] M. De Sanctis, G. Del Moro, S. Chimienti, P. Ritelli, C. Levantesi, and C. Di Iaconi, "Removal of pollutants and pathogens by a simplified treatment scheme for municipal wastewater reuse in agriculture," *Science of the Total Environment*, vol. 580, pp. 17–25, 2017.
- [27] C. N. Mushila, G. M. Ochieng, F. A. O. Otieno, S. M. Shitote, and C. W. Sitters, "Hydraulic design to optimize the treatment capacity of multi-stage filtration units," *Physics and Chemistry of the Earth, Parts A/B/C*, vol. 92, pp. 85–91, 2016.

- [28] E. Bar-Zeev, N. Belkin, B. Liberman, T. Berman, and I. Berman-Frank, "Rapid sand filtration pretreatment for SWRO: microbial maturation dynamics and filtration efficiency of organic matter," *Desalination*, vol. 286, pp. 120–130, 2012.
- [29] M. Elbana, F. Ramírez de Cartagena, and J. Puig-Bargués, "Effectiveness of sand media filters for removing turbidity and recovering dissolved oxygen from a reclaimed effluent used for micro-irrigation," *Agricultural Water Management*, vol. 111, pp. 27–33, 2012.
- [30] A. Y. Zahrim and N. Hilal, "Treatment of highly concentrated dye solution by coagulation/flocculation–sand filtration and nanofiltration," *Water Resources and Industry*, vol. 3, pp. 23–34, 2013.
- [31] APHA, AWWA, WEF, *Standard Methods for Examination of Water and Wastewater*, American Public Health Association, Washington, DC, USA, 22nd edition, 2012.
- [32] C. Ricordel and H. Djelal, "Treatment of landfill leachate with high proportion of refractory materials by electrocoagulation: system performances and sludge settling characteristics," *Journal of Environmental Chemical Engineering*, vol. 2, no. 3, pp. 1551–1557, 2014.
- [33] M. Gültekin-Özgüven, İ. Berktaş, and B. Özçelik, "Influence of processing conditions on procyanidin profiles and antioxidant capacity of chocolates: optimization of dark chocolate manufacturing by response surface methodology," *LWT - Food Science and Technology*, vol. 66, pp. 252–259, 2016.
- [34] S. Zhao, G. Huang, G. Cheng, Y. Wang, and H. Fu, "Hardness, COD and turbidity removals from produced water by electrocoagulation pretreatment prior to reverse osmosis membranes," *Desalination*, vol. 344, pp. 454–462, 2014.
- [35] S. Farhadi, B. Aminzadeh, A. Torabian, V. Khatibikamal, and M. Alizadeh Fard, "Comparison of COD removal from pharmaceutical wastewater by electrocoagulation, photo-electrocoagulation, peroxi-electrocoagulation and peroxi-photoelectrocoagulation processes," *Journal of Hazardous Materials*, vol. 219–220, pp. 35–42, 2012.
- [36] M. Kobya, M. S. Oncel, E. Demirbas, E. Şık, A. Akyol, and M. Ince, "The application of electrocoagulation process for treatment of the red mud dam wastewater from Bayer's process," *Journal of Environmental Chemical Engineering*, vol. 2, no. 4, pp. 2211–2220, 2014.
- [37] S. Tchamango, C. P. Nanseu-Njiki, E. Ngameni, D. Hadjiev, and A. Darchen, "Treatment of dairy effluents by electrocoagulation using aluminium electrodes," *Science of The Total Environment*, vol. 408, no. 4, pp. 947–952, 2010.
- [38] M. Mechelhoff, G. H. Kelsall, and N. J. D. Graham, "Electrochemical behaviour of aluminium in electrocoagulation processes," *Chemical Engineering Science*, vol. 95, pp. 301–312, 2013.
- [39] M. A. Sandoval, R. Fuentes, J. L. Nava, and I. Rodríguez, "Fluoride removal from drinking water by electrocoagulation in a continuous filter press reactor coupled to a flocculator and clarifier," *Separation and Purification Technology*, vol. 134, pp. 163–170, 2014.
- [40] Z. Hu, K. Chandran, B. F. Smets, and D. Grasso, "Evaluation of a rapid physical–chemical method for the determination of extant soluble COD," *Water Research*, vol. 36, no. 3, pp. 617–624, 2002.
- [41] M. Ramadan, "Efficiency of new Miswak, titanium dioxide and sand filters in reducing pollutants from wastewater," *Beni-Suef University Journal of Basic and Applied Sciences*, vol. 4, no. 1, pp. 47–51, 2015.
- [42] M. Achak, L. Mandi, and N. Ouazzani, "Removal of organic pollutants and nutrients from olive mill wastewater by a sand filter," *Journal of Environmental Management*, vol. 90, no. 8, pp. 2771–2779, 2009.
- [43] M. A. García-Morales, G. Roa-Morales, C. Barrera-Díaz, V. Martínez Miranda, P. Balderas Hernández, and T. B. Pavón Silva, "Integrated advanced oxidation process (ozonation) and electrocoagulation treatments for dye removal in denim effluents," *International Journal of Electrochemical Science*, vol. 8, pp. 8752–8763, 2013.

Research Article

1D TiO₂ Nanostructures Prepared from Seeds Presenting Tailored TiO₂ Crystalline Phases and Their Photocatalytic Activity for *Escherichia coli* in Water

Julieta Cabrera,¹ Dwight Acosta,² Alcides López,¹ Roberto J. Candal,³ Claudia Marchi,⁴ Pilar García,¹ Dante Ríos,¹ and Juan M. Rodríguez¹ 

¹Universidad Nacional de Ingeniería, Av. TúpacAmaru s/n, Rimac, Lima, Peru

²Instituto de Física, Universidad Nacional Autónoma de México, 20364 Ciudad de México, Mexico

³Instituto de Investigación e Ingeniería Ambiental, CONICET, Universidad Nacional de San Martín, Campus Miguelete, 25 de Mayo y Francia, 1650 San Martín, Provincia de Buenos Aires, Argentina

⁴Centro de Microscopías Avanzadas, FCEyN, Universidad de Buenos Aires, Ciudad Universitaria, 1428 Buenos Aires, Argentina

Correspondence should be addressed to Juan M. Rodríguez; jrodriguez@uni.edu.pe

Received 23 July 2017; Revised 4 December 2017; Accepted 28 December 2017; Published 2 April 2018

Academic Editor: Joaquim Carneiro

Copyright © 2018 Julieta Cabrera et al. This is an open access article distributed under the Creative Commons Attribution License, which permits unrestricted use, distribution, and reproduction in any medium, provided the original work is properly cited.

TiO₂ nanotubes were synthesized by alkaline hydrothermal treatment of TiO₂ nanoparticles with a controlled proportion of anatase and rutile. Tailoring of TiO₂ phases was achieved by adjusting the pH and type of acid used in the hydrolysis of titanium isopropoxide (first step in the sol-gel synthesis). The anatase proportion in the precursor nanoparticles was in the 3–100% range. Tube-like nanostructures were obtained with an anatase percentage of 18 or higher while flake-like shapes were obtained when rutile was dominant in the seed. After annealing at 400°C for 2 h, a fraction of nanotubes was conserved in all the samples but, depending on the anatase/rutile ratio in the starting material, spherical and rod-shaped structures were also observed. The photocatalytic activity of 1D nanostructures was evaluated by measuring the deactivation of *E. coli* in stirred water in the dark and under UV-A/B irradiation. Results show that in addition to the bactericidal activity of TiO₂ under UV-A illumination, under dark conditions, the decrease in bacteria viability is ascribed to mechanical stress due to stirring.

1. Introduction

TiO₂ nanomaterials are well-studied and commonly used photocatalysts for the degradation of organics, water splitting, and solar cells, among others [1–4]. In the last years, several approaches were explored to increase the photoefficiency of TiO₂, with the modification of the particle morphology and dimensionality being one of the newest [5]. One-dimensional (1D) nanostructures such as nanotubes, nanorods, nanowires, and nanobelts have attracted great attention because of their unique properties that may be beneficial for photocatalysis: (i) enhanced light absorption due to the high length/diameter ratio, (ii) rapid and long-distance electron transport capability, (iii) large specific surface area, and (iv) ion exchange ability [6]. Hydrothermal treatment of TiO₂ particles in alkaline solutions is

one of the simplest and cheapest techniques to produce 1D-layered titanate structures. The hydrothermal synthesis of TiO₂ nanotubes involves several steps where the structure of the TiO₂ precursor changes completely.

Results obtained in our laboratories show that 1D TiO₂ nanostructures display photocatalytic activity for dye degradation [7]. Although its performance as a photocatalyst is not as good as other industrially produced TiO₂, this form of TiO₂ can be easily recuperated from the solution.

Furthermore, since 1985 when Matsunaga et al. [8] published the first report of the photocatalytic biocide effects of TiO₂ under metal halide lamp irradiation, there has been increasing interest in photocatalytic disinfection. Use of TiO₂ nanoparticles in suspension is an efficient method for decontamination due to the large surface area of catalysts available to perform the reaction. It has, however, some

drawbacks before its scaling at the industrial level; for example, the necessity of removing the catalyst from the solution after decontamination using filtration increases the cost and time of the cleaning process [9].

In this sense, considering the advantages that our 1D TiO₂ nanostructures are more easily filterable than nanoparticles and can be easily removed from solutions—in addition to the fact that the efficiency of 1D TiO₂ as bactericide under UV-A irradiation was only briefly explored—in this work, we assess the photocatalytic activity of 1D TiO₂, obtained from nanoparticles with a controlled proportion of anatase and rutile made by the sol-gel method, for *E. coli* ATCC 25922 in water.

2. Materials and Methods

2.1. Materials. Titanium isopropoxide purity 98%, hydrochloric acid fuming 37%, nitric acid 65%, and pure sodium hydroxide pellets were purchased from Merck. All reagents were used as received.

2.2. Synthesis of TiO₂ Nanostructures. TiO₂ nanoparticles (TiO₂ NPs) were synthesized by the sol-gel method (SG). Titanium isopropoxide was added drop by drop to vigorously stirred HNO₃ or HCl solutions at pH 0.5, 0.8, and 1.0. Suspensions were heated at 70°C for 2 h, autoclaved in a stainless-steel chamber at 220°C for 12 h, washed by centrifugation, and dried at 60°C.

1D TiO₂ nanostructures were synthesized by hydrothermal treatment of 1 g TiO₂ NPs obtained by the sol-gel method in 40 mL of 10 M NaOH at 130°C for 24 h. After hydrothermal treatment, the obtained white powder was vacuum filtered, washed with HCl solution for ionic exchange, and then washed with distilled water until a neutral pH was reached. Finally, the samples were annealed at 400°C for 2 h to crystallize the material.

The obtained nanostructures were characterized by X-ray diffraction (XRD) in a Rigaku diffractometer using Cu K α radiation ($\lambda = 1.54056 \text{ \AA}$). The morphology was studied by field emission scanning electron microscopy (FE-SEM SUPRA 40, Carl Zeiss) and high-resolution transmission electron microscopy (HRTEM) using a JEOL JEM-2010F transmission electron microscope operating at 200 kV. TEM samples were prepared by dispersing a small amount of the sample in ethanol with the help of an ultrasonic bath. Small droplets of the freshly prepared dispersion were placed onto a copper grid covered with carbon to improve the conduction of the electrons.

2.3. Assessment of Photocatalytic Activity of TiO₂ Nanoparticles and 1D TiO₂ Nanostructures against *Escherichia coli* in Water. The photocatalytic activity for water disinfection was tested using *E. coli* ATCC 25922. Experiments were performed in a batch reactor, with illumination from above using an Ultra-Vitalux 300 W lamp (30 W/m²) and, under dark conditions, containing 100 mL aqueous solution with 10⁷ CFU/mL bacteria. 1.0 mL aliquots were collected after 0, 20, 40, and 60 min irradiation. Aliquots were diluted 1:10 with sterile water to fit in the range 10–500 CFU/mL.

1.0 mL samples of the final dilutions were vacuum filtered through a sterile filter; this results in all bacteria present in the water being retained on the filter. Finally, the filters were placed onto a paper pad soaked in “membrane lauryl sulphate broth” (Oxoid MM0615), which feeds *E. coli* bacteria but inhibits the growth of any other bacteria. The bacterial concentration was determined by counting after 18 h incubation at 37°C.

TiO₂ nanoparticle samples were codified with C or N (for samples made with HCl and HNO₃, resp.) accompanied by 0.5, 0.8, and 1.0, depending on the pH used in the sol-gel synthesis. In a similar way, 1D TiO₂ nanostructures were codified adding 1D to the nanoparticle code (e.g., N0.5 refers to TiO₂ nanoparticles obtained with HNO₃ in pH 0.5, and N0.5-1D refers to a one-dimensional TiO₂ nanostructure obtained for N0.5) resulting in twelve samples.

2.4. Assessment of Stirring in Bacteria Viability. In order to evaluate the mechanical stirring effect in bacteria viability, *E. coli* ATCC 25922 were tested in the dark under stirring (100 rpm) and without stirring at room temperature (20°C). 1.0 mL aliquots were collected after 0, 20, 40, and 60 min stirring.

3. Results and Discussion

3.1. 1D TiO₂ Nanostructures Prepared from Seeds Presenting Tailored TiO₂ Crystalline Phases. Figure 1 shows FE-SEM images of TiO₂ nanoparticles obtained by the sol-gel method (SG-TiO₂ NPs) using HNO₃ and HCl as catalysts in the acid hydrolysis reaction of titanium isopropoxide (pH = 0.5, 0.8, and 1). At pH 1, regardless of the acid, the images show spherical nanoparticles with average diameters of about 15 nm and 13 nm, with HNO₃ and HCl, respectively. Polyhedral structures (60–100 nm) were observed when the pH decreased to 0.8, and octahedral structures with edges of about 140 nm were obtained with HCl at pH 0.5.

XRD patterns (Figures 2(a) and 2(b)) show that the crystalline structures correspond mainly to anatase when acidic solutions with pH 1 were used with both catalysts. Both anatase and rutile were observed with acidic solutions at pH 0.8 and 0.5; a small amount of brookite was detected in most cases. The amount of rutile increased as the pH decreased, and it was the dominant phase when HCl at pH 0.5 was used. The small peak for brookite disappears in this case.

The average crystallite size for anatase and rutile (D_{anatase} and D_{rutile} , resp.), the anatase content, A_p , estimated with the Spurr-Myers equation [10] from the main diffraction peaks, and the pH of the acidic solution (HNO₃ and HCl) are shown in Table 1.

Figure 3 shows the morphology, by FE-SEM, of the 1D nanostructures obtained after alkaline hydrothermal treatment of the sol-gel TiO₂ nanoparticles presented in Figure 1 and Table 1. In the case of SG-TiO₂ synthesized with HNO₃, the particles displayed a tube-like shape, with an average diameter of $11 \pm 1 \text{ nm}$ in different anatase contents within 18% to 100%, respectively. On the other hand, using as precursor SG-TiO₂ synthesized with HCl acid, flake-like

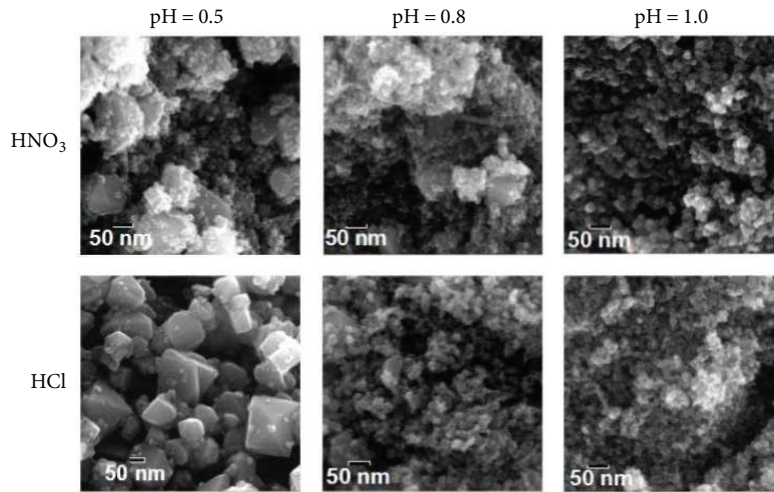


FIGURE 1: FE-SEM images of TiO_2 nanoparticles obtained from the sol-gel method using HNO_3 and HCl as catalysts of the titanium isopropoxide hydrolysis reaction (pH = 0.5, 0.8, and 1.0, from left to right, resp.).

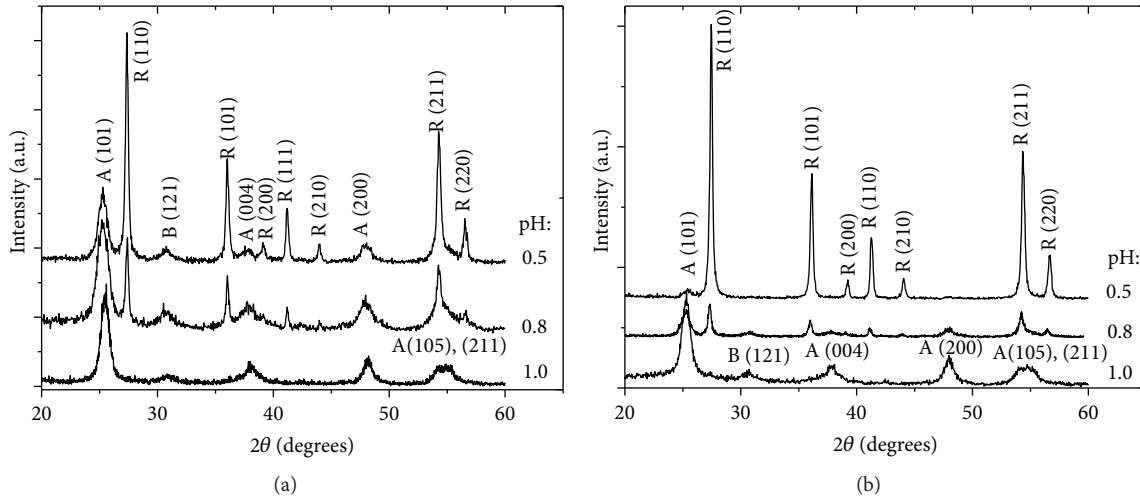


FIGURE 2: XRD patterns from sol-gel TiO_2 nanoparticles with a range of crystalline phases obtained with (a) HNO_3 and (b) HCl at pH = 0.5, 0.8, and 1.0. (A = anatase; R = rutile; B = brookite).

TABLE 1: Crystallite size, D_{anatase} or D_{rutile} , and anatase proportion, A_p , of the SG- TiO_2 powders prepared at the indicated pH using HCl or HNO_3 acid solutions.

Catalyst	pH	D_{anatase} (nm)	D_{rutile} (nm)	A_p
HNO_3	0.5	9.4 ± 0.2	26.8 ± 0.2	0.18
	0.8	7.4 ± 0.2	29.0 ± 0.2	0.56
	1	9.0 ± 0.2	—	1
HCl	0.5	—	29.7 ± 0.2	~ 0.03
	0.8	9.5 ± 0.2	25.9 ± 0.2	0.39
	1	9.8 ± 0.2	—	1

particles were identified together with tube-like structures. The proportion of flake-shaped particles increased as the pH decreased.

After the annealing process at 400°C for 2 h, TEM images (Figure 4) show nanotube structures in all the samples; depending on the seed material, some spherical and rod-shaped structures were also present. It can be seen that a sintering-like process took place during the annealing and that, as a consequence, bundles of tube-like structures and cracked structures were produced.

Tube-like structures seemed to be best conserved when obtained from TiO_2 nanoparticles with 56% of anatase, synthesized with HNO_3 . When seed material with lower anatase content ($\sim 18\%$) was employed, large and irregular particles measuring about 80 nm were accompanying the nanotube structures. These might be rutile seed aggregates that could not react in the hydrothermal treatment because of their large particle size. In contrast, needle-like shapes and nanotubes turning to nanorods were observed when anatase-rutile TiO_2 nanoparticles synthesized with HCl were used

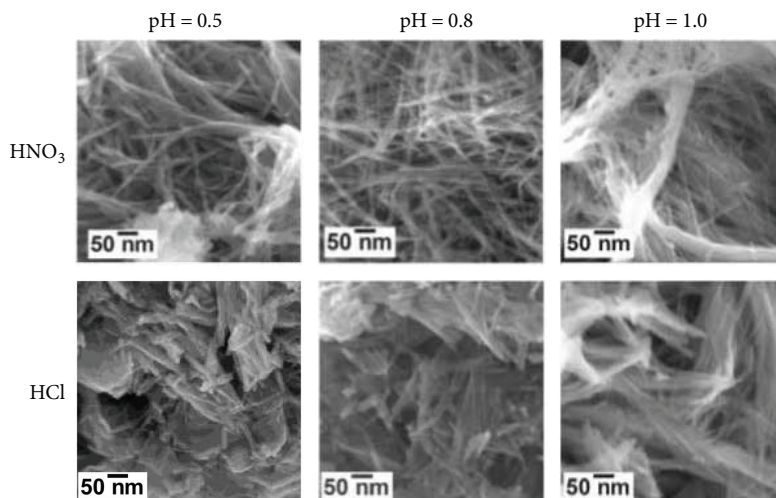


FIGURE 3: FE-SEM images of 1D TiO_2 nanostructures obtained from SG- TiO_2 , prepared with HNO_3 or HCl at $\text{pH} = 0.5, 0.8$, and 1 , after 24 h of hydrothermal treatment.

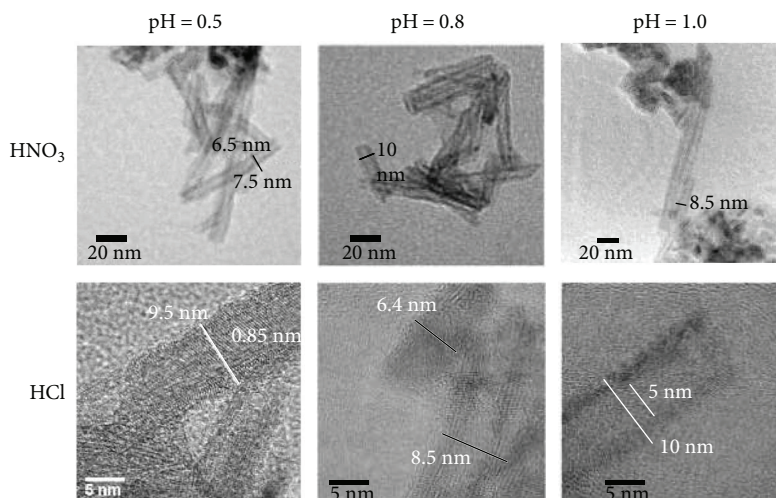


FIGURE 4: TEM images of 1D TiO_2 nanostructures obtained from SG- TiO_2 , prepared with HNO_3 or HCl at $\text{pH} = 0.5, 0.8$, and 1.0 , after annealing process ($400^\circ\text{C}/2$ h).

as seed materials. It must be mentioned that, because of the lack of homogeneity in the samples, it is difficult to represent the final TiO_2 structure in a single TEM image; the pictures shown represent the most typical structure in each sample.

The XRD analysis of the samples after hydrothermal treatment (Figure 5(a)) shows that the crystalline structure of the seed material changed and displayed peaks around $2\theta = 10, 24.5, 28.4$, and 48.3° . These peaks represent the diffraction of sodium titanate with the chemical formula $\text{Na}_2\text{Ti}_n\text{O}_{2n+1}$ ($n = 3, 6$, and 9). This is observed for samples where the anatase content in the seed material was higher than 55% . In other cases, rutile was also present as shown by the reflection peaks around $2\theta = 27.5, 36.1, 41.5, 54$, and 56° , corresponding to the (110), (101), (111), (211), and (220) planes in agreement with JCPDS No. 21-1276. This confirms that part of the rutile seeds could remain unreacted after the hydrothermal treatment. After the acid

treatment, the features corresponding to titanates almost disappeared, leaving those of the rutile TiO_2 polymorph (not shown).

After the annealing process (Figure 5(b)), a mix of anatase and rutile was observed for samples whose seed had a rutile content larger than 60% . Only peaks corresponding to anatase TiO_2 were observed for samples with anatase higher than 56% in seed. This suggests that when rutile was the dominant phase in the seed material, a portion of it remained unreacted, probably because of the large crystallite size of rutile (~ 28 nm), compared with the anatase crystallite size (~ 9 nm). The conditions of the hydrothermal treatment seem insufficient to carry out the dissolution-precipitation process that would be involved in the transformation of TiO_2 to sodium titanate, followed by proton exchange to produce hydrogen titanate and, finally, crystallization to anatase after thermal treatment. On the other hand, it can

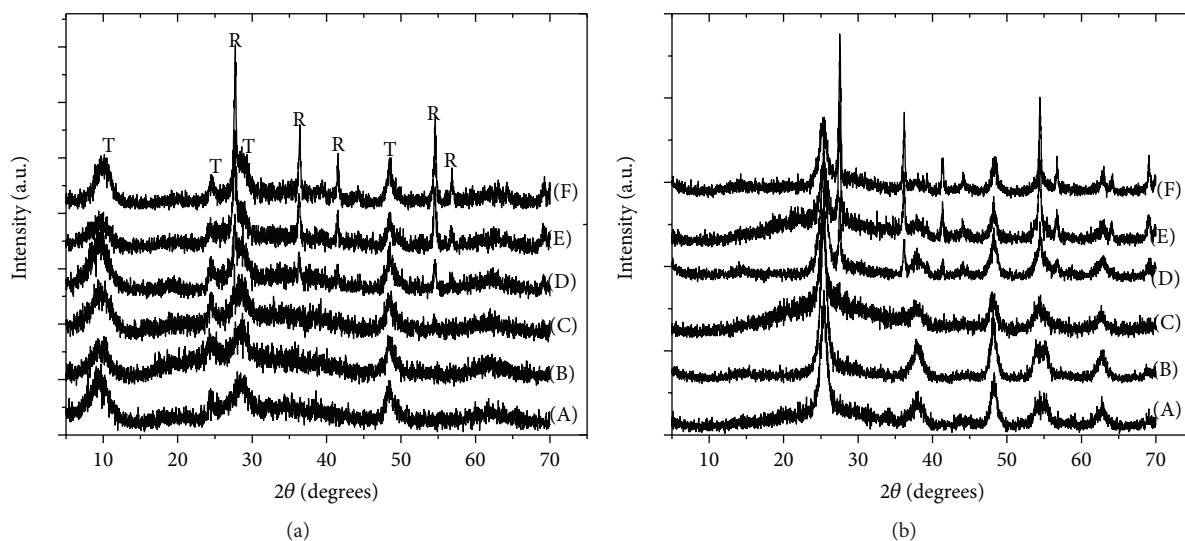


FIGURE 5: XRD patterns of 1D nanostructures obtained after 24 h of hydrothermal treatment of SG-TiO₂ NPs (a) and the products obtained after the final annealing process at 400°C for 2 h (b). The anatase contents in seeds were (A) ~100% (HNO₃, pH = 1), (B) ~100% (HCl, pH = 1), (C) ~56% (HNO₃, pH = 0.8), (D) ~39% (HCl, pH = 0.8), (E) ~18% (HNO₃, pH = 0.5), and (F) ~3% (HCl, pH = 0.5) (A = anatase; R = rutile).

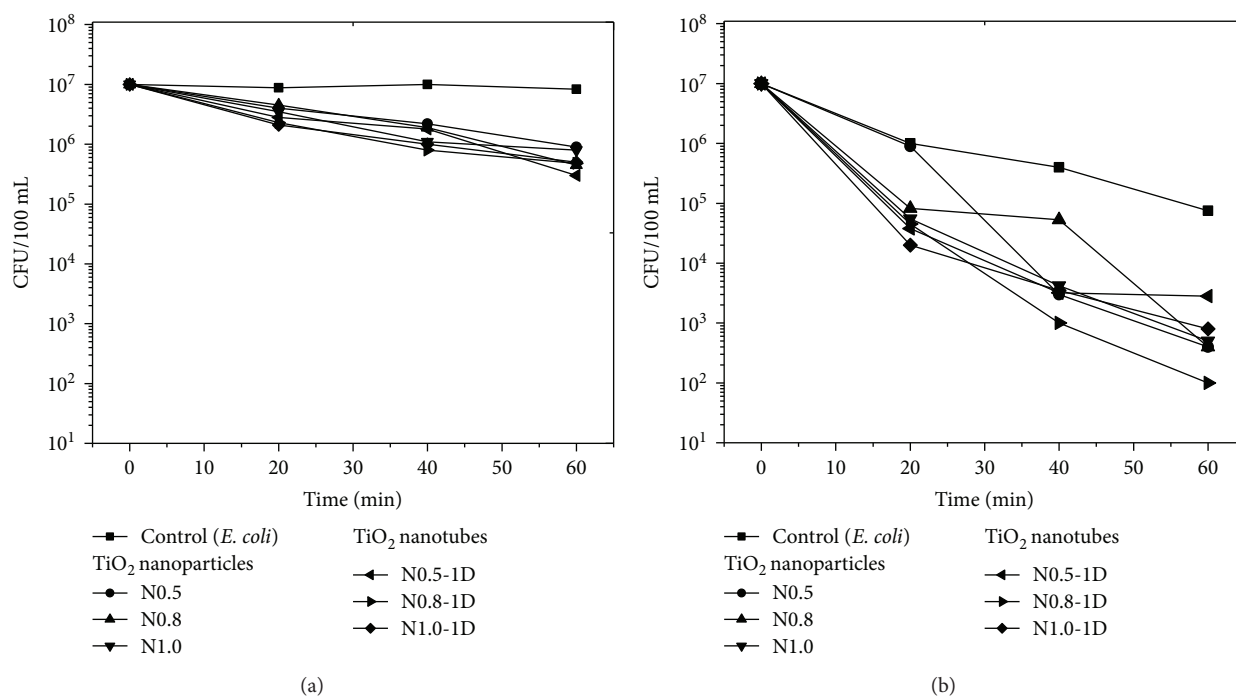


FIGURE 6: *E. coli* bacteria viability under stirring condition in (a) the dark and (b) under UV-A/B irradiation in the presence of TiO₂ nanoparticles and nanotubes.

be noted that the seed material obtained with HCl produced samples with the best crystallinity, as the X-ray reflections were well defined, compared to those obtained with HNO₃.

3.2. Assessment of the Photocatalytic Activity of TiO₂ Nanostructures for *Escherichia coli* in Water. Bacteria viability under the stirring process was determined by colony counting after 24 h of incubation. The results showed that the stirring process affects in 1, 3, and 5% (gradually for

20, 40, and 60 minutes, resp.). The assays without stirring were not performed because it was not possible to obtain a homogeneous bacteria distribution.

The effect of stirring in the presence of SG-TiO₂ nanoparticles and their corresponding 1D TiO₂ nanostructures against *E. coli* was evaluated in the dark and under UV-A/B irradiation. As shown in Figure 6, considering that the initial *E. coli* concentration was 1×10^7 CFU/mL, the presence of TiO₂ nanoparticles and nanotubes under stirring

conditions in the dark produced a diminution of bacteria viability of around two orders of magnitude (10^5 CFU/mL). It is ascribed to mechanical stress produced by the stirring process.

Also, as is reported in other studies [11], the photolysis is present in our experiments. It contributes to a decrease in bacteria viability at three orders of magnitude. The bactericidal activity of TiO_2 nanostructures is similar to the photolysis in consequence; the catalyst plus irradiation can decrease bacteria viability until five orders of magnitude. However, no major difference was observed for the bactericidal effect of nanoparticles and one-dimensional TiO_2 nanostructures. The latter have an important advantage since 1D TiO_2 nanostructures can be easily removed from solutions.

4. Conclusions

In summary, TiO_2 anatase 1D nanostructures, with different shapes such as tube- and rod-like shapes, were synthesized by hydrothermal treatment of seeds controlling the anatase-rutile proportion. The synthesized 1D TiO_2 nanostructure was effectively used for photocatalytic abatement of *E. coli* in water. Although the 1D TiO_2 nanostructures have a similar photocatalytic activity than the nanoparticles have, the use of one-dimensional TiO_2 nanostructures has an important advantage since the 1D TiO_2 nanostructure can be easily removed from solutions and could be reusable avoiding the necessity of use filtration that increases the cost and time of the cleaning process.

Conflicts of Interest

The authors declare that they have no conflicts of interest.

Acknowledgments

This work was partially supported by the Innovate Peru Project C.133-PNICE-PIAP-2015 and the Concytec Project 223-2015-FONDECYT-DE. The authors are also grateful to the Microscopy Centre of FCEyN, Universidad de Buenos Aires, and Central Microscopy Laboratory of the Institute of Physics (UNAM). Roberto J. Candal is a member of CONICET.

References

- [1] A. J. Cowan, J. Tang, W. Leng, J. R. Durrant, and D. R. Klug, "Water splitting by nanocrystalline TiO_2 in a complete photoelectrochemical cell exhibits efficiencies limited by charge recombination," *The Journal of Physical Chemistry C*, vol. 114, no. 9, pp. 4208–4214, 2010.
- [2] D. F. Ollis, E. Pelizzetti, and N. Serpone, "Photocatalyzed destruction of water contaminants," *Environmental Science & Technology*, vol. 25, no. 9, pp. 1522–1529, 1991.
- [3] Y. Ren, Z. Liu, F. Pourpoint, A. R. Armstrong, C. P. Grey, and P. G. Bruce, "Nanoparticulate $\text{TiO}_2(\text{B})$: an anode for lithium-ion batteries," *Angewandte Chemie International Edition*, vol. 51, no. 9, pp. 2164–2167, 2012.
- [4] J. Yan and F. Zhou, " TiO_2 nanotubes: structure optimization for solar cells," *Journal of Materials Chemistry*, vol. 21, no. 26, p. 9406, 2011.
- [5] C. W. Lai, J. C. Juan, W. B. Ko, and S. B. A. Hamid, "An overview: recent development of titanium oxide nanotubes as photocatalyst for dye degradation," *International Journal of Photoenergy*, vol. 2014, Article ID 524135, 14 pages, 2014.
- [6] N. Liu, X. Chen, J. Zhang, and J. W. Schwank, "A review on TiO_2 -based nanotubes synthesized via hydrothermal method: formation mechanism, structure modification, and photocatalytic applications," *Catalysis Today*, vol. 225, pp. 34–51, 2014.
- [7] J. Cabrera, H. Alarcón, A. López, R. Candal, D. Acosta, and J. Rodriguez, "Synthesis, characterization and photocatalytic activity of 1D TiO_2 nanostructures," *Water Science & Technology*, vol. 70, no. 6, pp. 972–979, 2014.
- [8] T. Matsunaga, R. Tomoda, T. Nakajima, and H. Wake, "Photoelectrochemical sterilization of microbial cells by semiconductor powders," *FEMS Microbiology Letters*, vol. 29, no. 1-2, pp. 211–214, 1985.
- [9] S. Ponce, E. Carpio, J. Venero et al., "Titanium dioxide onto polyethylene for water decontamination," *Journal of Advanced Oxidation Technologies*, vol. 12, no. 1, pp. 81–86, 2009.
- [10] R. A. Spurr and H. Myers, "Quantitative analysis of anatase-rutile mixtures with an X-ray diffractometer," *Analytical Chemistry*, vol. 29, no. 5, pp. 760–762, 1957.
- [11] N. Vermeulen, W. J. Keeler, K. Nandakumar, and K. T. Leung, "The bactericidal effect of ultraviolet and visible light on *Escherichia coli*," *Biotechnology and Bioengineering*, vol. 99, no. 3, pp. 550–556, 2008.

Research Article

Photocatalytic Activity under Simulated Sunlight of Bi-Modified TiO₂ Thin Films Obtained by Sol Gel

D. A. Solís-Casados ¹, L. Escobar-Alarcón,² V. Alvarado-Pérez,¹ and E. Haro-Poniatowski³

¹Universidad Autónoma del Estado de México, Centro Conjunto de Investigación en Química Sustentable UAEMéx-UNAM, Toluca, MEX, Mexico

²Departamento de Física, Instituto Nacional de Investigaciones Nucleares, Apartado Postal 18-1027, 11801 Mexico City, Mexico

³Departamento de Física, Universidad Autónoma Metropolitana, Apartado Postal 55-532, 09340 Mexico City, Mexico

Correspondence should be addressed to D. A. Solís-Casados; solis_casados@yahoo.com.mx

Received 20 July 2017; Revised 27 October 2017; Accepted 13 December 2017; Published 19 March 2018

Academic Editor: Juan Rodriguez

Copyright © 2018 D. A. Solís-Casados et al. This is an open access article distributed under the Creative Commons Attribution License, which permits unrestricted use, distribution, and reproduction in any medium, provided the original work is properly cited.

The synthesis of Bi-modified TiO₂ thin films, with different Bi contents, is reported. The obtained materials were characterized by energy-dispersive X-ray spectroscopy (EDS), X-ray photoelectron spectroscopy (XPS), Raman spectroscopy (RS), X-ray diffraction (XRD), photoluminescence (PL), and diffuse reflectance spectroscopy (DRS), in order to obtain information on their chemical composition, vibrational features, and optical properties, respectively. Compositional characterization reveals that the bismuth content can be varied in an easy way from 0.5 to 25.4 at. %. Raman results show that the starting material corresponds to the anatase phase of crystalline TiO₂, and Bi addition promotes the formation of bismuth titanates, Bi₂Ti₂O₇ at Bi contents of 10.4 at. % and the Bi₄Ti₃O₁₂ at Bi contents of 21.5 and 25.4 at. %. Optical measurements reveal that the band gap narrows from 3.3 eV to values as low as 2.7 eV. The photocatalytic activity was tested in the degradation reaction of the Malachite Green carbinol base dye (MG) as a model molecule under simulated sunlight, where the most relevant result is that photocatalytic formulations containing bismuth showed higher catalytic activity than pure TiO₂. The higher photocatalytic activity of MG degradation of 67% reached by the photocatalytic formulation of 21.5 at. % of bismuth is attributed to the presence of the crystalline phase perovskite-type bismuth titanate, Bi₄Ti₃O₁₂.

1. Introduction

Pollution in wastewaters is one of the most important environmental topics nowadays due to the increasing necessity of human beings of clean water. Some dyes in wastewaters are considered pollutants and, in most cases, are considered toxic to humans and other living organisms, even when they are present in low quantities. Several processes have been proposed to remove or degrade these pollutants from wastewaters; particularly, the photocatalysis is currently considered a promising alternative to remove dyes from water in an efficient way. Photocatalysis is an advanced oxidation technology (AOT), based on physicochemical processes that

produce changes in the chemical structure of the organic compounds including their mineralization. AOT processes are based on the generation and the use of highly reactive oxidizing species, such as the hydroxyl (OH[•]), hydroperoxyl (•OOH), and superoxide radicals (O₂[•]), which are reactive sites towards degradation of organic compounds until their complete mineralization [1]. Among the photocatalytic materials, titanium dioxide (TiO₂) has been the most used because of its specific properties, such as resistance to chemical corrosion, nontoxic, and inexpensive, and its high photoactivity with UV radiation. However, TiO₂ has two important drawbacks; the first one is that it is activated only by ultraviolet light, due to its relatively high band gap energy

of 3.2 eV for the anatase crystalline phase. The second one is the high recombination rate of the photogenerated electron-hole pairs that reduce its efficiency [2]. Several strategies have been proposed to improve the photocatalytic activity of TiO_2 such as doping it with metals and nonmetals, as well as the use of mixtures of the two main TiO_2 crystalline phases, anatase and rutile [3, 4]. Coupling of semiconductors has been also considered as an alternative route to develop high efficient photocatalytic materials that can compensate the disadvantages of the individual components inducing synergistic effects such as efficient charge separation, band gap narrowing, and consequently improvement of their photocatalytic performance. Therefore, the development of visible light-driven coupled photocatalysts is currently of great interest. Particularly, bismuth oxide ($\alpha\text{-Bi}_2\text{O}_3$) has been reported as an efficient photocatalyst due to its unique structure and band gap energy close to 2.8 eV which makes it active in the visible region of the electromagnetic spectrum [5, 6]. Several studies have reported that the system formed by mixtures of TiO_2 and Bi_2O_3 can result in the formation of different crystalline phases of bismuth titanates ($\text{Bi}_4\text{Ti}_3\text{O}_{12}$ and $\text{Bi}_{12}\text{TiO}_{20}$) depending on the proportion of TiO_2 and Bi_2O_3 [7, 8]. It is worth mentioning that the photocatalysts based on $\text{Bi}_{12}\text{TiO}_{20}$ [9] and $\text{Bi}_4\text{Ti}_3\text{O}_{12}$ [10] crystals have been tested in the photodecolorization of methyl orange under UV irradiation showing high photocatalytic activity, similar in both cases. The aim of this work is to investigate the degradation of the Malachite Green dye (MG), carbinol base, under visible light irradiation, using a simulated sunlight source, in an attempt to correlate the photocatalytic activity of titanium oxide modified with different amounts of Bi_2O_3 with their physicochemical properties in particular; the band gap energy, the microstructure, and the electron-hole recombination rate.

2. Experimental

2.1. Bi-Modified TiO_2 Thin Films. The precursor solutions were prepared by the sol-gel technique. Titanium isopropoxide ($[\text{Ti}(\text{OCH}(\text{CH}_3)_2)_4]$, Aldrich 97%), nitric acid (HNO_3 , Fermont 70%), 2-propanol ($\text{CH}_3\text{CHOHCH}_3$, Fermont 99.8%), bismuth nitrate pentahydrate ($\text{Bi}(\text{NO}_3)_3 \cdot 5\text{H}_2\text{O}$, J.T. Baker) were used as precursors. A sol was prepared under environmental conditions mixing 10 mL of 2-propanol with 1 mL of titanium isopropoxide, stirred for 1 h. Bismuth nitrate pentahydrate was added slowly under stirring to obtain theoretical amounts of 0, 5, 30, 50, 70, and 80 wt. % of Bi_2O_3 . 1 mL of nitric acid was added drop to drop to induce gelling as a variant of the sol-gel technique reported before [11]. The sol was sonicated in an ultrasonic bath during 5 min and aged for 12 h to obtain an incipient gelled solution. Afterwards, the precursor solution was deposited layer to layer by the spin coating technique onto borosilicate glass substrates (25 mm \times 25 mm \times 1 mm) functionalized with hydrofluoric acid (HF, 10% vol) to obtain homogeneous thin films. The spin coater was a KW-4A from Chemat Technology working at 1500 rpm under environmental conditions. Deposited thin films were thermally treated at 300°C during 1 h to eliminate organic residues, and

subsequently, the temperature was raised to 450°C at a heating rate of 3°C/min and maintained isothermally for 4 h to form a crystalline thin film.

2.2. Thin Film Characterization. Determination of the atomic bismuth content in the films was done by energy-dispersive X-ray spectroscopy (EDS) using a microprobe attached to a JEOL JSM 6510LV scanning electron microscope, and EDS analysis was carried out with an acceleration voltage of 15 kV; surface morphology was observed from micrographs obtained with the same microscope. The chemical bonding of the present elements was investigated by X-ray photoelectron spectroscopy (XPS). The wide and narrow XPS spectra were acquired using a JEOL JPS-9200 spectrometer. The adventitious carbon peak at 284.8 eV (1s) was used as the internal standard to compensate for sample charging. Raman spectroscopy (RS) was used to study the structural features of the films; spectra were acquired using an HR LabRam 800 spectrometer with an Olympus BX40 confocal microscope. A Nd:YAG laser beam (532 nm) was focused with a 50x objective onto the sample surface. A cooled CCD camera was used to record the spectra, and typically, an average of 50 accumulations of 10 seconds was done to improve the signal-to-noise ratio. The crystalline phases of the thin films were identified by the X-ray diffraction technique (XRD) with a Bruker D8 Advance Diffractometer using the $\text{Cu-K}\alpha$ radiation line ($\lambda = 1.54 \text{ \AA}$); the diffraction patterns were recorded in steps of 0.05°. Diffuse reflectance spectroscopy (DRS) spectra were acquired on a PerkinElmer Lambda 35 spectrophotometer with an integration sphere with a resolution of $\pm 1 \text{ nm}$; from the reflectance spectra, the Kubelka-Munk function was determined and the band gap energy was estimated [12, 13]. Photoluminescence spectra were acquired in a FluoroMax4, HORIBA Jobin Yvon spectrofluorometer, exciting the samples at 492 nm.

2.3. Photocatalytic Activity. The photocatalytic activity of the thin films was tested through the degradation of Malachite Green carbinol base dye ($\text{C}_{23}\text{H}_{26}\text{N}_2\text{O}$, Aldrich) contained in an aqueous solution (10 $\mu\text{mol/L}$). The reaction was carried out in a batch system in a borosilicate glass reactor, in which the thin film was introduced into a 25 mL of the MG solution; afterwards, the reaction system was stirred in dark condition in order to establish adsorption equilibrium between dye solution and photocatalyst. Thin films were activated by illumination with light emitted from a solar simulator SF150 of Sciencetech equipped with an AM1.0D filter which simulates the solar spectrum of direct light from the sun on the ground when the sun is at a zenith angle of 0°; the samples were irradiated with an average intensity of 60 mW/cm^2 keeping the distance between the liquid surface and the light source at 15 cm. The MG photodegradation was followed through the decrease of its characteristic absorption band peaking at 619 nm in the UV-Vis absorbance spectra. The spectra were obtained each 15 min in the first hour of reaction time, and afterwards, each 30 min during the second and third hours of reaction from the aliquots of 4 mL taken from reaction system and were returned to the reactor after each spectrum was taken. Absorbances obtained at each reaction time were

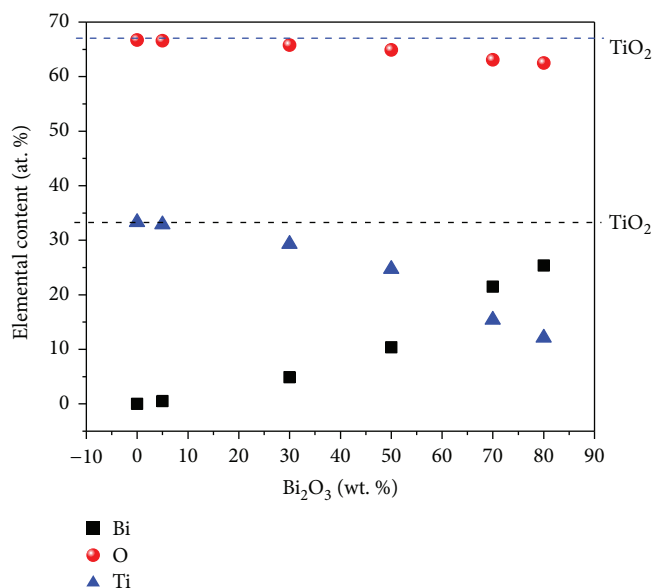


FIGURE 1: Atomic proportion of the thin films as a function of the Bi_2O_3 wt. %.

correlated to dye concentrations through a calibration curve. A nonlinear least square data treatment was used to determine the values of the kinetic constant considering a pseudo-first order kinetic model. Total organic carbon (TOC) was determined in each solution after reaction as ppm of carbon, TOC was obtained by the combustion method, and the mineralization degree was calculated taking the TOC content in the MG solution, at the initial concentration of $10 \mu\text{mol/L}$, 9.2 ppm of TOC as a reference.

3. Results and Discussion

3.1. Elemental Composition. The elemental chemical composition of the deposited thin films, as a function of the Bi_2O_3 wt. % used for their preparation, is shown in Figure 1 and Table 1 (EDS measurements). The results obtained from the EDS and XPS techniques showed good agreement following the same tendency. It is clearly observed that the film without Bi is almost stoichiometric TiO_2 . When Bi is incorporated increasing the Bi_2O_3 load, the Bi content in the film increases monotonically from 0.5 to 25.4 at. % whereas the O content remains around 65 at. %. Simultaneously, the Ti content decreases from 33 to 12 at. %. It is worth noting that the elemental composition of the sample prepared using 70 wt. % of Bi_2O_3 (Bi = 21.5 at. %, Ti = 15.4 at. %, and O = 63.1 at. %) agrees very well with the composition of the $\text{Bi}_4\text{Ti}_3\text{O}_{12}$ titanate (Bi = 21.0 at. %, Ti = 15.8 at. %, and O = 63.2 at. %).

3.2. Raman Spectroscopy. Figure 2 shows the Raman spectra corresponding to the thin films containing different bismuth contents, from 0.0 to 25.4 at. %. For Bi contents lower than 4.9 at. %, the spectra consist of four characteristic bands located at 144, 396, 516, and 637 cm^{-1} attributed to the anatase crystalline phase of TiO_2 [14]. The inset in Figure 2

TABLE 1: Elemental chemical composition, determined by EDS, of the thin films as a function of the theoretical Bi_2O_3 (wt. %).

Chemical composition (at. %)			
Bi_2O_3 (wt. %)	Ti	EDS O	Bi
0	33.3	66.7	0
5	32.9	66.6	0.5
30	29.3	65.8	4.9
50	24.7	64.9	10.4
70	15.4	63.1	21.5
80	12.1	62.5	25.4

reveals that as the Bi content increases, the band at 144 cm^{-1} shifts to higher frequencies and its intensity diminishes, and at the same time, its FWHM becomes wider. These changes are attributed to structural disorder induced by the incorporation of bismuth into the TiO_2 lattice. When the Bi content reaches 10.4 at. %, low intensity peaks associated to the anatase crystalline phase remain and new features appear at 83, 105, 256, 401, and 530 cm^{-1} , these signals that appear shifted and broader can be assigned to the bismuth titanate $\text{Bi}_4\text{Ti}_3\text{O}_{12}$ [9]. These spectra resemble an amorphous material indicating a high degree of structural disorder. At the highest Bi content, the Raman spectrum is characterized by signals at 235, 276, 350, 540, 615, and 856 cm^{-1} ; the presence of the Raman modes at 276, 540, and 856 cm^{-1} suggests the presence of the perovskite structure [9].

3.3. X-Ray Diffraction. Figure 3 shows the X-ray diffraction patterns from 20 to 40° of the samples with different Bi content. From Figure 3(a), the diffraction lines at $2\theta = 25.3$ and 37.8° characteristic of the TiO_2 in its anatase crystalline phase can be observed (JCPDS 89-4921). Small features of the anatase crystalline phase are observed as well (Figure 3(b)), in thin film containing 0.5 at. % of Bi. The film with bismuth content of 4.9 at. % shows diffraction lines at $2\theta = 14.9, 28.7, 29.96, 32.3, 34.74$, and 38.01° which are attributed to the bismuth titanate $\text{Bi}_2\text{Ti}_2\text{O}_7$ (JCPDS 32-0118) (Figure 3(c)). The film containing 10.4 at. % of Bi exhibits the same diffraction lines as is seen in Figure 3(d). Further increase in bismuth content up to 21.5 at. % shows new diffraction lines peaking at $2\theta = 22.1, 23.3, 27.2, 29.46, 30.1$, and 33.1° (Figure 3(e)), characteristics of the crystalline phase of bismuth titanate with molecular structure $\text{Bi}_4\text{Ti}_3\text{O}_{12}$ (JCPDS 35-0795) as is expected because of its elemental composition. From Figure 3(f), it can be observed that crystalline phase $\text{Bi}_4\text{Ti}_3\text{O}_{12}$ remains in the thin film with 25.4 at. % of bismuth content in good agreement with the Raman results.

3.4. X-Ray Photoelectron Spectroscopy. Shifts in the peak positions in photoelectron spectra are frequently used to determine the chemical state of elements if the shifts are large enough. Sometimes, peaks representing different chemical states are overlapped and a deconvolution procedure is required. Figure 4 shows the chemical shifts of the Ti 2p region in the XPS spectra of the Bi-modified TiO_2 thin films. Spectra were deconvoluted using Gaussian functions in order

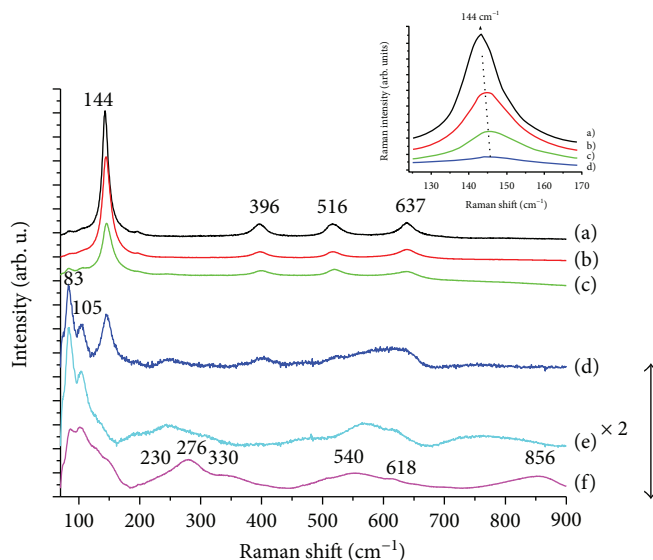


FIGURE 2: Raman spectra of the TiO_2 thin films modified with several bismuth contents of (a) 0, (b) 0.5, (c) 4.9, (d) 10.4, (e) 21.5, and (f) 25.4 at. %.

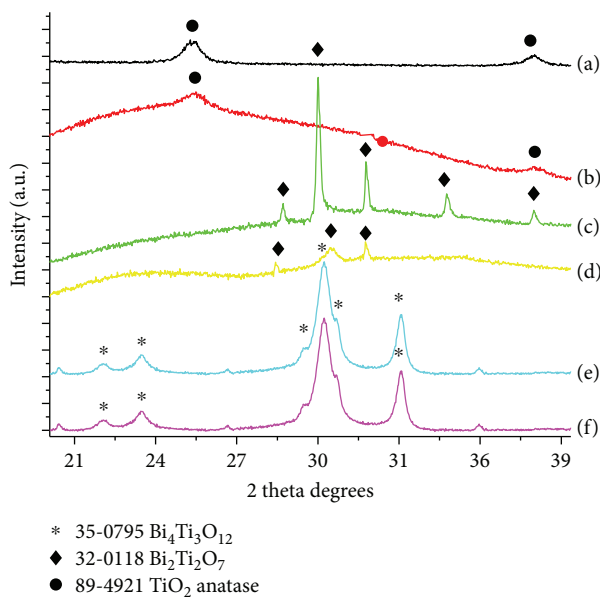


FIGURE 3: X-ray patterns of the TiO_2 thin films modified with several bismuth contents (a) 0, (b) 0.5, (c) 4.9, (d) 10.4, (e) 21.5, and (f) 25.4 at. %.

to obtain information about the interaction of the Ti atoms with the Bi and O atoms in the last atomic layer in the thin films as well as its chemical state (Figure 5). In Figure 5(a), two doublets can be observed; the first one with peaks located at 458.2 and 464.0 eV is attributed to the doublet of Ti-O bonds of the TiO_2 in its anatase phase, whereas the peaks at 456.7 and 462.9 eV could be attributed to a second doublet of Ti-O bonds in Ti_2O_3 (Figure 5(a)) [15]. The presence of Ti^{3+} due to oxygen vacancies has been reported before, resulting from the transfer of two electrons towards two adjacent Ti^{4+} to form Ti^{3+} on the surface. The spectrum of the Ti region in the sample with 10.4 at. % of bismuth (Figure 5(b)

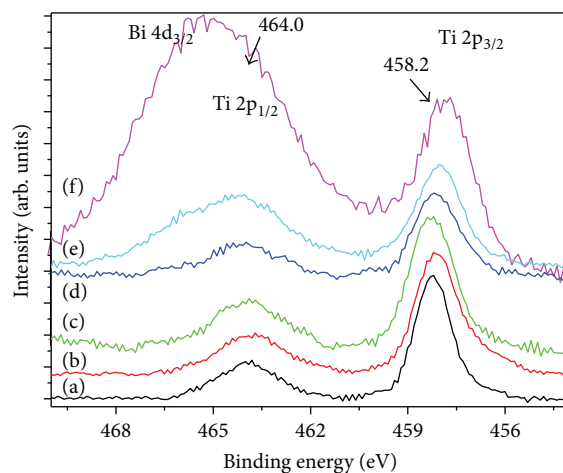


FIGURE 4: Ti 2p region spectra evolution as a function of bismuth content (a) 0, (b) 0.5, (c) 4.9, (d) 10.4, (e) 21.5, and (f) 25.4 at. %.

shows peaks attributed to three main doublets: the first one, located at 456.7 and 462.3 eV, is attributed to the Ti-O bonds as in Ti_2O_3 ; the second one, at 457.9 and 463.9 eV, has a closed binding energy than the one reported by Wang and Ma for the compounds similar to bismuth titanates, so this peaks are attributed to the Ti-Bi-O bonds in the bismuth titanate [16]; finally, the third one, with peaks located at 458.3 and 464.1 eV, could be attributed to the Ti-O bonds in the anatase phase of TiO_2 . Spectrum of the thin film with bismuth content of 25.4 at. % (Figure 5(c)) shows two doublets: the first doublet at 456.7 and 462.5 eV attributed to the Ti-O bonds in the Ti_2O_3 and the second doublet at 457.9 and 464.7 eV revealing the presence of Ti-Bi-O bonds as in the bismuth titanates $\text{Bi}_4\text{Ti}_3\text{O}_{12}$. $\text{Ti } 2p_{1/2}$ photoemission is overlapped in a partial way by the $\text{Bi } 4d_{3/2}$ core level peak [15, 16].

Figure 6 shows the Bi 4f photoelectron spectra of the thin films displaying a characteristic doublet located at

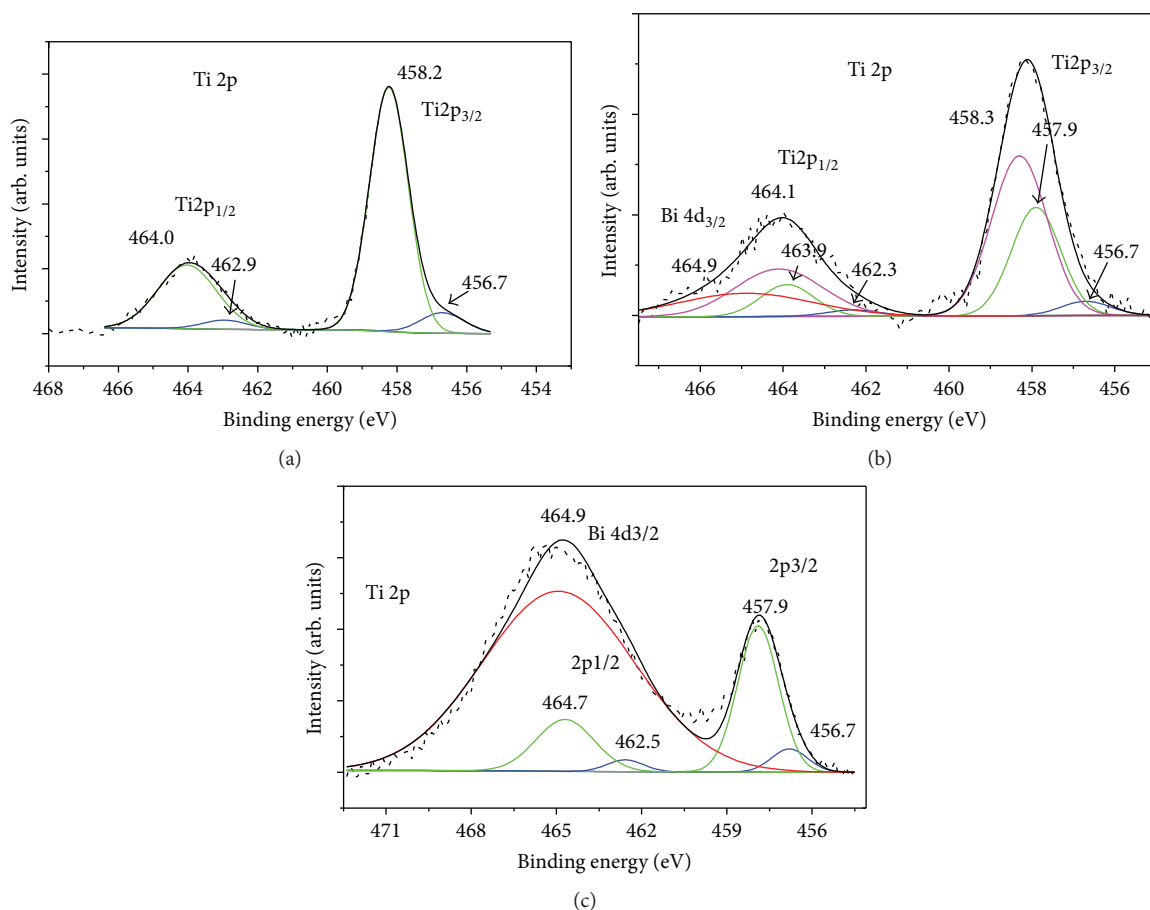


FIGURE 5: Gaussian deconvolution of the XPS spectra, Ti 2p region (a) 0 at. %, (b) 10.4 at. %, and (c) 25.4 at. % of bismuth.

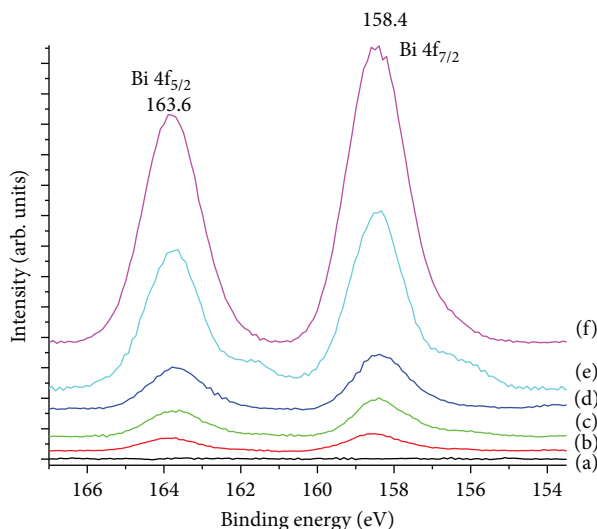


FIGURE 6: XPS spectra evolution of Bi 4f region as a function of bismuth content, (a) 0, (b) 0.5, (c) 4.9, (d) 10.4, (e) 21.5, and (f) 25.4 at. %.

158.4 and 163.6 eV. These signals were deconvoluted fitting two doublets: one of them located at 158.5 and 163.9 eV could be correlated to the Bi-Ti-O bonds in the layer $\text{Bi}_2\text{Ti}_3\text{O}_{10}^{2-}$ of the perovskite-type structure $\text{Bi}_4\text{Ti}_3\text{O}_{12}$

(Figure 7(a)), and the other doublet with peaks located at 156.8 and 161.9 eV could be assigned to the Bi-O bonds most probably as in the $(\text{Bi}_2\text{O}_2)^{2+}$ layer of the perovskite-type structure. These results suggest that the incorporation and further increase of Bismuth into the film changes the proportion of Bi-O bonds most probably in the $(\text{Bi}_2\text{O}_2)^{2+}$ layer, forming the perovskite structure at 21.5 at. % of Bi (Figure 7(b)). XPS spectrum of the sample with the highest bismuth content (25.4 at. %) increases the proportion of the doublet located at 158.4 and 163.8 eV correlated with the Bi-Ti-O bonds in the $\text{Bi}_4\text{Ti}_3\text{O}_{12}$, and the other doublet with peaks located at 156.6 and 162.4 eV assigned to the Bi-O bonds in the $(\text{Bi}_2\text{O}_2)^{2+}$ layer decreases probably due to starting of the Bi_2O_3 formation (Figure 7(c)). The line shape of the O 1s core level photoemission spectra of the thin films is shown in Figures 8(a)–8(f), and it is important to remark that two peaks are clearly observed. The first peak located at the low binding energy 529.8 eV can be assigned to the Ti-O bond while the second peak located at 532.5 eV can be attributed to the oxygen bonded to bismuth [17, 18]. Jovalekić et al. have reported that oxygen atom in a stronger Ti-O bond carries a higher effective negative charge than in a weaker Bi-O bond [17]. This correlation between the effective charge of oxygen atom and the binding energy of oxygen core electrons agrees with previous reports [17, 18].

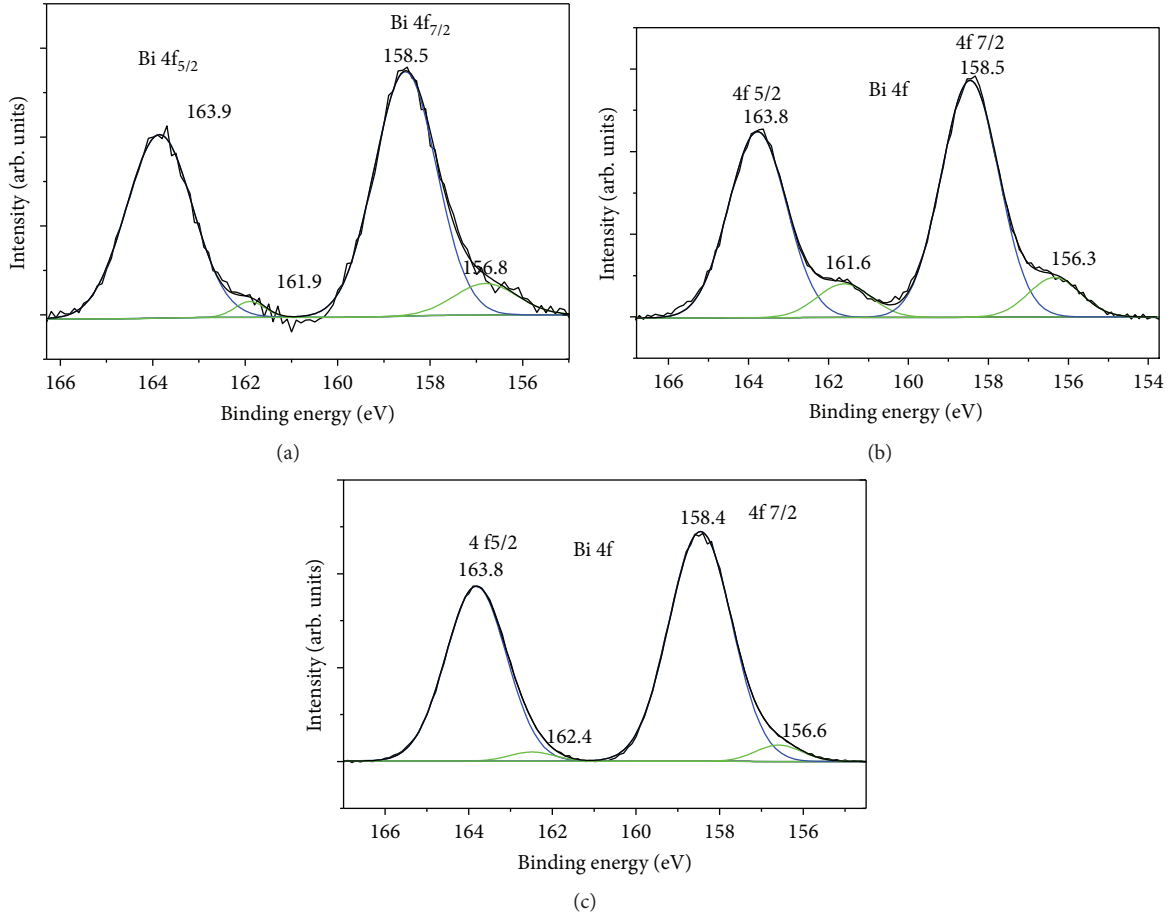


FIGURE 7: Gaussian deconvolution of the XPS spectra, Bi 4f_{7/2} region (a) 0.5, (b) 21.5, and (c) 25.4 at. % of bismuth.

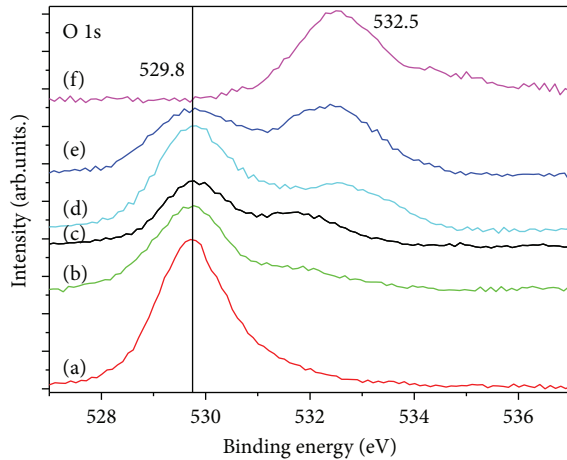


FIGURE 8: XPS spectra evolution of O 1s region as a function of bismuth content, (a) 0, (b) 0.5, (c) 4.9, (d) 10.4, (e) 21.5, and (f) 25.4 at. %.

3.5. Diffuse Reflectance Spectroscopy. Table 2 shows the optical band gap (E_g) values determined using the Kubelka-Munk method; this was done by transforming the reflectance spectra of the samples with different Bi contents to the Kubelka-Munk function, $F(R)$, and then plotting $(F(R)E)^{1/2}$ versus E , considering a direct allowed transition band gap.

TABLE 2: Effect of bismuth content on the band gap energy.

Bismuth content (at. %)	Band gap energy (eV)
0	3.3
0.5	3.3
4.9	3.2
10.4	3.1
21.5	2.9
25.4	2.7

The E_g values were obtained by a linear fit of the linear portions of the curve, determining its intersection with the photon energy axis [12]. The reflectance spectra of the samples and the $(F(R)E)^{1/2}$ versus E graphs as well as the linear fits for estimating the band gap energy are shown in Figure 9. In these cases, the employed method allows the determination of the band gap values with good accuracy [13]. As it is observed in Table 2, the obtained results reveal that when Bi content increases in the thin films, the band gap narrows from 3.3 eV to values as low as 2.7 eV ($\lambda = 459$ nm); these low band gap values make this material potentially active under light illumination in the visible region of the electromagnetic spectrum.

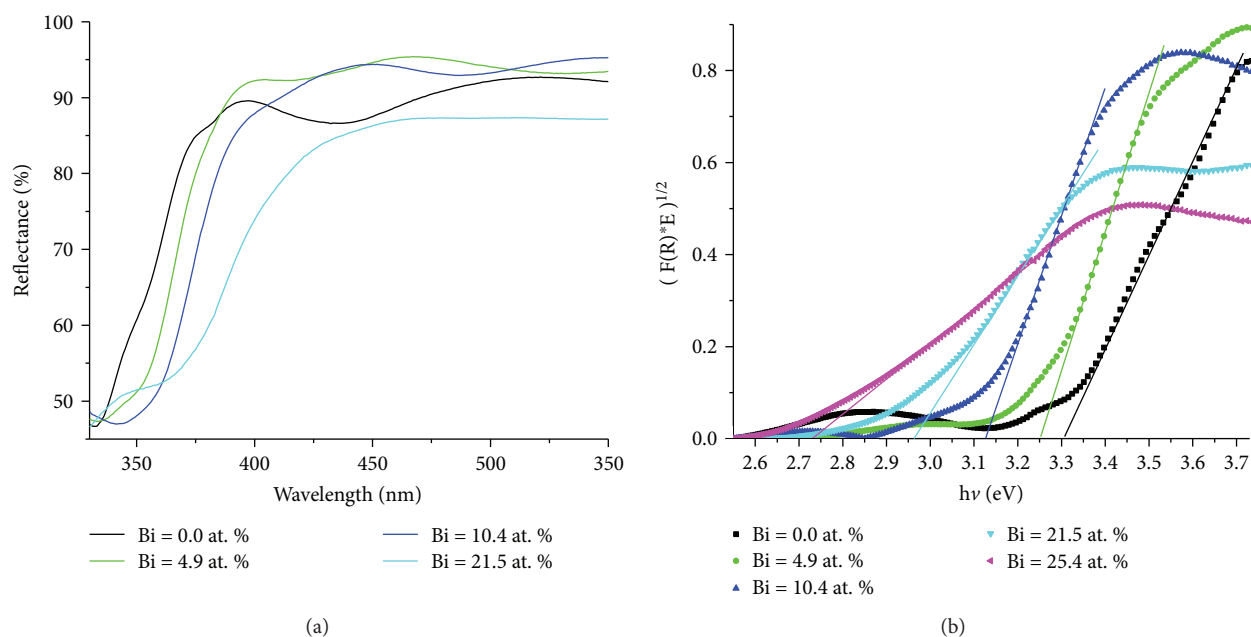


FIGURE 9: (a) Reflectance spectra and (b) $(F(R)E)^{1/2}$ versus E graphs of the prepared films.

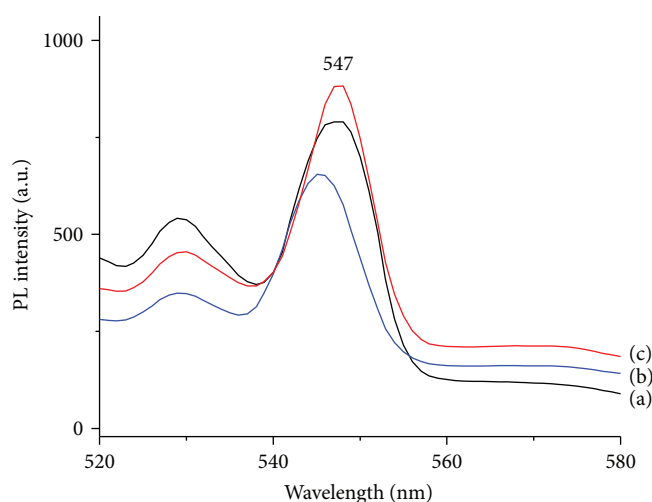


FIGURE 10: Photoluminescence spectra of (a) 0, (b) 21.5, and (c) 25.4 at. % of bismuth.

3.6. Photoluminescence Spectra. Figure 10 shows the photoluminescence spectra of the TiO_2 and the Bi-modified TiO_2 thin films. The PL spectrum of the TiO_2 is characterized by an intense band peaking at 547 nm. This can be interpreted as a higher electron hole recombination rate in the TiO_2 thin film as the PL intensity is related directly to the electron-hole recombination rate [19]. The same band with similar intensity is seen for the photocatalyst with 25.4 at. % of Bi. The PL intensity of the spectrum corresponding to the photocatalyst with 21.5 at. % of Bi is approximately 20% lower than the PL intensity determined as the area under the curve of the TiO_2 film, indicating that this sample exhibits the lowest recombination rate.

3.7. Photocatalytic Activity. To determine the photocatalytic activity, a photodegradation experiment of MG under

simulated solar light was performed. Figure 11 shows the MG degradation degree as a function of the reaction time using thin films with different bismuth content. The MG degradation due to the photolysis process was close to 27% after 180 minutes of irradiation, and it was the lowest degradation degree as is seen in Figure 11. The TiO_2 film without bismuth behaves similarly to the photolysis process reaching a slightly higher conversion close to 34.7%. The film containing 0.5 at. % of bismuth shows a higher photocatalytic activity, of approximately 10% greater than the TiO_2 catalyst. Further increase in the Bi content, 4.9 at. %, improves in 34% the degradation degree. For a Bi content of 10.4 at. %, a decrease in the photoactivity is observed. The film with a bismuth content of 21.5 at. % improves significantly the photocatalytic activity reaching 64.6% of MG degradation after 180 min of irradiation time, 84% higher than the activity of the TiO_2

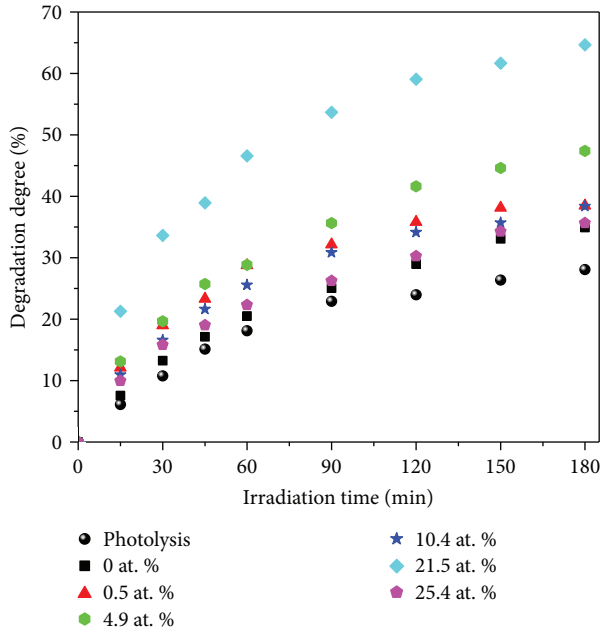


FIGURE 11: Photodegradation percent of MG dye using the Bi-modified TiO_2 thin films under solar simulated irradiation.

film. This enhanced photocatalytic activity could be attributed to the presence of $\text{Bi}_4\text{Ti}_3\text{O}_{12}$ as the main crystalline phase in the photocatalytic formulation as well as to the lower recombination rate of the electron-hole pairs as was suggested by the PL results. In fact, the sample with the highest Bi content diminishes the degradation degree to values nearly to the obtained using TiO_2 . In general terms, thin films containing bismuth exhibit a better photocatalytic activity than pure TiO_2 thin film.

Table 3 shows the values of the kinetic constant, k_{app} (min^{-1}), obtained from a fitting of the concentration as a function of the reaction time assuming a pseudo-first order expression using a least square data treatment with an acceptable precision [20]. These values agree with the photocatalytic degradation degree reached for each thin film. Additionally, the mineralization degree was followed by the quantification of the total organic carbon (TOC) through the reaction time. The degradation degrees determined by TOC and UV-Vis measurements are quite similar as it can be seen from Table 4. This indicates that the photodegradation process follows the route of mineralization of the organic dye tested. Further studies with reactive trap molecules indicate that mineralization of MG is mainly through the electron route, specifically by the $\text{O}_2^{\bullet -}$ superoxide radicals.

4. Conclusions

Bi-modified TiO_2 thin films were prepared by the sol-gel and spin coating techniques. In this way, films with Bi contents from 0.5 to 25.4 at. % were obtained. The sol-gel technique induces the Bi incorporation into the TiO_2 lattice with the consequent formation of bismuth titanate, $\text{Bi}_4\text{Ti}_3\text{O}_{12}$, at higher Bi contents. Additionally, the Bi content in the thin

TABLE 3: Kinetic rate constant (k_{app}) for photocatalytic formulations as a function of bismuth content, determined using a least square data treatment [20].

Bismuth content (at. %)	k_{app} (min^{-1})
Uncatalyzed	0.0029 ± 0.00006
0	0.0038 ± 0.00009
0.5	0.0038 ± 0.00009
4.9	0.0048 ± 0.00007
10.4	0.0038 ± 0.00008
21.5	0.0063 ± 0.00009
25.4	0.0036 ± 0.00006

TABLE 4: Mineralization degree through TOC and photodegradation percent of Malachite Green dye through UV-VIS at 180 min of irradiation time, using a solar simulator as irradiation source.

Bismuth content (at. %)	TOC (ppm)	Mineralization degree (TOC)	Degradation degree (UV-Vis)
Reference	9.2	0	0
Uncatalyzed	8.4	9.1	28.1
0	5.9	35.8	34.9
0.5	6.3	31.7	38.5
4.9	5.0	45.2	47.4
10.4	5.7	38.2	38.4
21.5	4.1	55.8	64.6
25.4	5.8	37.5	35.6

films has a strong effect on the band gap energy which decreases from 3.3 eV to values as low as 2.7 eV making these materials potentially photoactive under solar radiation. This is due to the higher wavelength required to generate the electron-hole pairs increasing the absorption spectral window of these materials. However, this lower band gap energy can be responsible for a higher recombination rate of the photogenerated charge carriers. The improved photocatalytic activity leading to the MG degradation under simulated solar light can be attributed to the $\text{Bi}_4\text{Ti}_3\text{O}_{12}$ phase at a bismuth content of 21.5 at. %.

Additional Points

Highlights. The perovskite-type structure of bismuth titanate was obtained. The incorporation of Bi makes photocatalysts active with solar radiation. Bismuth titanate, $\text{Bi}_4\text{Ti}_3\text{O}_{12}$, enhances the photocatalytic activity.

Conflicts of Interest

The authors declare that there is no conflict of interests regarding the publication of this paper.

Acknowledgments

The authors thank CONACYT for the provided equipment through the CB-168827 and CB-240998 project. The authors would like to thank Dr. Uvaldo Hernández Balderas, M. en C. Alejandra Nuñez, Dra. Melina Tapia, M. en C. Lizbeth Triana, and LIA Citlalit Martínez Soto for their technical assistance.

References

- [1] M. Yasmina, K. Mourad, S. H. Mohammed, and C. Khaoula, "Treatment heterogeneous photocatalysis; factors influencing the photocatalytic degradation by TiO_2 ," *Energy Procedia*, vol. 50, pp. 559–566, 2014.
- [2] S. Bagwasi, Y. Niu, M. Nasir, B. Tian, and J. Zhang, "The study of visible light active bismuth modified nitrogen doped titanium dioxide photocatalysts: role of bismuth," *Applied Surface Science*, vol. 264, pp. 139–147, 2013.
- [3] M. Pelaez, N. T. Nolan, S. C. Pillai et al., "A review on the visible light active titanium dioxide photocatalysts for environmental applications," *Applied Catalysis B: Environmental*, vol. 125, pp. 331–349, 2012.
- [4] D. A. Solís-Casados, L. Escobar-Alarcón, L. M. Gómez-Oliván, E. Haro-Poniatowski, and T. Klimova, "Photodegradation of pharmaceutical drugs using Sn-modified TiO_2 powders under visible light irradiation," *Fuel*, vol. 198, pp. 3–10, 2017.
- [5] H. Cheng, B. Huang, J. Lu et al., "Synergistic effect of crystal and electronic structures on the visible-light-driven photocatalytic performances of Bi_2O_3 polymorphs," *Physical Chemistry Chemical Physics*, vol. 12, no. 47, pp. 15468–15475, 2010.
- [6] W. Raza, M. M. Haque, M. Muneer, T. Harada, and M. Matsumara, "Synthesis, characterization and photocatalytic performance of visible light induced bismuth oxide nanoparticle," *Journal of Alloys and Compounds*, vol. 648, pp. 641–650, 2015.
- [7] H. Zhang, M. Lü, S. Liu et al., "Preparation and photocatalytic properties of sillenite $\text{Bi}_{12}\text{TiO}_{20}$ films," *Surface and Coatings Technology*, vol. 202, no. 20, pp. 4930–4934, 2008.
- [8] X. Lin, P. Lv, Q. Guan, H. Li, H. Zhai, and C. Liu, "Bismuth titanate microspheres: directed synthesis and their visible light photocatalytic activity," *Applied Surface Science*, vol. 258, no. 18, pp. 7146–7153, 2012.
- [9] C. Du, D. Li, Q. He et al., "Design and simple synthesis of composite $\text{Bi}_{12}\text{TiO}_{20}/\text{Bi}_4\text{Ti}_3\text{O}_{12}$ with a good photocatalytic quantum efficiency and high production of photo-generated hydroxyl radicals," *Physical Chemistry Chemical Physics*, vol. 18, no. 38, pp. 26530–26538, 2016.
- [10] R. A. Golda, A. Marikani, and D. P. Padiyan, "Mechanical synthesis and characterization of $\text{Bi}_4\text{Ti}_3\text{O}_{12}$ nanopowders," *Ceramics International*, vol. 37, no. 8, pp. 3731–3735, 2011.
- [11] D. A. Solís-Casados, L. Escobar-Alarcón, A. Arrieta-Castañeda, and E. Haro-Poniatowski, "Bismuth–titanium oxide nanopowders prepared by sol–gel method for photocatalytic applications," *Materials Chemistry and Physics*, vol. 172, pp. 11–19, 2016.
- [12] A. Murphy, "Band-gap determination from diffuse reflectance measurements of semiconductor films, and application to photoelectrochemical water-splitting," *Solar Energy Materials and Solar Cells*, vol. 91, no. 14, pp. 1326–1337, 2007.
- [13] R. López and R. Gómez, "Band-gap energy estimation from diffuse reflectance measurements on sol–gel and commercial TiO_2 : a comparative study," *Journal of Sol-Gel Science and Technology*, vol. 61, no. 1, pp. 1–7, 2012.
- [14] E. Haro-Poniatowski, R. Rodríguez-Talavera, H. M. de la Cruz, O. Cano-Corona, and R. Arroyo-Murillo, "Crystallization of nanosized titania particles prepared by the sol-gel process," *Journal of Materials Research*, vol. 9, no. 08, pp. 2102–2108, 1994.
- [15] C. Jovalekic, M. Zdujic, and L. J. Atanasoska, "Surface analysis of bismuth titanate by Auger and X-ray photoelectron spectroscopy," *Journal of Alloys and Compounds*, vol. 469, no. 1–2, pp. 441–444, 2009.
- [16] L. Wang and W. Ma, " $\text{Bi}_4\text{Ti}_3\text{O}_{12}$ synthesized by high temperature solid phase method and its visible catalytic activity," *Procedia Environmental Sciences*, vol. 18, pp. 547–558, 2013.
- [17] Č. Jovalekić, M. Pavlović, P. Osmokrović, and L. J. Atanasoska, "X-ray photoelectron spectroscopy study of $\text{Bi}_4\text{Ti}_3\text{O}_{12}$ ferroelectric ceramics," *Applied Physics Letters*, vol. 72, no. 9, pp. 1051–1053, 1998.
- [18] Z. Hu, H. Gu, Y. Hu, Y. Zou, and D. Zhou, "Microstructural, Raman and XPS properties of single-crystalline $\text{Bi}_{3.15}\text{Nd}_{0.85}\text{Ti}_3\text{O}_{12}$ nanorods," *Materials Chemistry and Physics*, vol. 113, no. 1, pp. 42–45, 2009.
- [19] P. Malathy, K. Vignesh, M. Rajarajan, and A. Suganthi, "Enhanced photocatalytic performance of transition metal doped Bi_2O_3 nanoparticles under visible light irradiation," *Ceramics International*, vol. 40, no. 1, pp. 101–107, 2014.
- [20] G. Lente, *Deterministic Kinetics in Chemistry and Systems Biology*, Springer, London, UK, 2015.

Research Article

Photovoltaic Energy-Assisted Electrocoagulation of a Synthetic Textile Effluent

Thelma Beatriz Pavón-Silva ¹, **Hipólito Romero-Tehuiztil**,² **Gonzálo Munguia del Río**,² and **Jorge Huacuz-Villamar**²

¹Unidad Académica Profesional-Acolman, Universidad Autónoma del Estado de México, Camino de Caleros No. 11, Ejidos de Santa Catarina, Acolman, MEX, Mexico

²Instituto Nacional de Electricidad y Energías Limpias, Av. Reforma 113, Col. Palmira, 62490 Cuernavaca, MOR, Mexico

Correspondence should be addressed to Thelma Beatriz Pavón-Silva; th.pavon@gmail.com

Received 13 July 2017; Revised 9 October 2017; Accepted 7 November 2017; Published 7 March 2018

Academic Editor: Carlos A. Martínez-Huitle

Copyright © 2018 Thelma Beatriz Pavón-Silva et al. This is an open access article distributed under the Creative Commons Attribution License, which permits unrestricted use, distribution, and reproduction in any medium, provided the original work is properly cited.

The feasibility of using photovoltaic modules to power a continuous 14 L electrochemical reactor applied to remove an azo dye with an efficiency of 70% is reported. The photovoltaic modules were directly connected, and the system efficiency was observed properly maintained when currents were applied in the range of 2.5 to 7.9 A. This value depends on solar radiation. Likewise, it was found that the efficiency depends mainly on the current density and the flow rate prevailing in the reactor.

1. Introduction

The problem of industrial wastewater is a topic that deserves special attention, particularly for industries that use dyes and thus generate large volumes of polluted wastewater. Due to their high molecular weights, complex structures, and especially high solubility in water, dyes persist once discharged into a natural environment, for example, textile [1, 2], pharmaceutical [3], cosmetics and food industry [4], and industrial wastewater [5]. Specifically for the textile industry, the chemical structure of these compounds is complex, generally of the type azo [6–8]. This group consists of colored substances with a complex chemical structure (many functional groups) and a high molecular weight. Thus, their removal from industrial effluents is also a subject of major importance from the environmental point of view. The removal of dissolved organic matter by coagulation is widely reported in literature [9], where the primary mechanism consists of two methods [10]. The first is binding the metal species to anionic sites of the organic molecules, thereby neutralizing their charge and resulting in reduced solubility. The second is the absorption of organic substances on amorphous metal hydroxide precipitates.

Chemical coagulation/flocculation is the most widely used technique for textile wastewater treatment; they have some disadvantages, such as needing pH adjustment before and after treatment, producing large amounts of sludge, and adding undesirable inorganic chemicals like aluminum, iron, sulfate, and chloride to the environment [11].

The results for the optimization of the effect of the coagulation–flocculation showed the rate of dye removal increased from 11.25% to 13.20 for the methylene blue and from 27.5% to 29.25 for the indigo carmine when the concentration of coagulant and flocculant were varied from 40 to 120 mg·L^{−1}. These results confirm the poor applicability of this process for the elimination of such dyes. Assadia et al. [12] show that ferric chloride and alum at optimum concentration were capable of removing dye and COD by 79.63% and 84.83% and 53% and 55%, respectively.

The electrocoagulation process is deemed an economical and environmental choice to minimize the drawbacks of conventional wastewater treatment technologies [13]; it provides a number of benefits, such as low cost, compatibility, and safety [14]. In addition, electrocoagulation has been proven to eliminate complex contaminants in wastewater that require a combination of physicochemical and biological

methods [15–17]. Its combination with other processes, like ozonation [18], has also been demonstrated to be highly effective for complex matrix wastewater remediation. The application of electrocoagulation, however, has been restricted at some extent by the cost that implies electrical energy usage. Moreover, climate change motivates research and development of new forms of renewable energy [19, 20] such as photovoltaic (PV) power [8], whose advantages include its free use and abundant availability, is a renewable resource, decentralized, with long life span and low maintenance costs, and does not result in contamination.

In this research, a PV system was evaluated in a pilot electrochemical wastewater reactor using a synthetic wastewater model containing azo dye, in this case remazol yellow dye 3GL (RYD), which is mainly used in textile industry [4, 8, 21]. This was first accomplished with batch tests and then with continuous tests in a pilot reactor, both of which are based on previously reported studies [8].

2. Experimental

The experimental setup is shown in Figure 1 and consists of the following: (1) the sun as a renewable energy source; (2) photovoltaic modules to convert sunlight into electricity; (3) an acrylic cylindrical reactor with a 0.15 m diameter and one meter length (14 L of water was treated); (4) direct connection of the sun to the electrochemical reactor, two aluminum electrodes formed by 39 circular blades (0.12 m diameter) with total surface area of 0.44 m², separated from each other by one centimeter. (5) Registration data and continuous monitoring was performed by a data acquisition system: current, voltage, and solar radiation. (6) The pH, conductivity, and temperature were measured with an electrical conductivity meter.

2.1. Reagents. The working solution was prepared by dissolving remazol yellow dye (RYD) 3GL (DyStar SA™) in potable water and was used as wastewater model containing azo dye (RYD) as pollutant. Table 1 summarizes its characteristics.

The conductivity was set at 366–380 $\mu\text{S}/\text{cm}$, and this in concordance with Can et al. [22], who stated this parameter to be lower than 500 $\mu\text{S}/\text{cm}$. They investigated the conductivity between 250 and 4000 $\mu\text{S}/\text{cm}$ using NaCl as the support electrolyte and noticed that above 500, the remazol red dye removal efficiency decreases. In our case, due to the size of the reactor (14 L pilot reactor), it was decided to work with potable water that already has a conductivity of 302–315 $\mu\text{S}/\text{cm}$, so an electrolyte support was not added. Thus, as reported by Can et al., the decline in the fading efficiency with increasing conductivity can be attributed to a change in ionic strength due to the change in conductivity of the aqueous medium. Ionic strength affects the kinetics and equilibrium of reactions between charged species during electrocoagulation.

2.2. Determination of Remazol Yellow Dye (RYD). RYD concentration was determined by UV-Vis spectrophotometry in a Perkin Elmer Lambda 2 spectrophotometer. The concentration of the molecule was determined by its

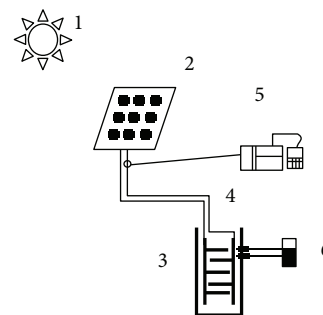


FIGURE 1: Scheme of the experimental system: 1, solar energy; 2, photovoltaic module; 3, electrochemical reactor; 4, direct connection of the power supply; 5, parameter control: current, voltage, and solar radiation; 6, pH, conductivity, and temperature control.

TABLE 1: Characterization of the remazol yellow dye.

Parameter	Valor
Color index	Remazol yellow
Chromophore	Azo
Molar mass ($\text{g}\cdot\text{mol}^{-1}$)	362.27
Percentage of pure dye	68%
pKa	3.77
Water solubility at 293 K ($\text{g}\cdot\text{L}^{-1}$)	80
Acute oral toxicity LD50 ($\text{mg}\cdot\text{kg}^{-1}$)	>2000
pH value (at 10 $\text{g}\cdot\text{L}^{-1}$ water)	6.1
Conductivity ($\text{mS}\cdot\text{cm}^{-1}$)	302–308

absorption at 269.2 nm. The calibration curve was carried out between 0 and 100 $\text{mg}\cdot\text{L}^{-1}$ of RYD obtaining the following model: $A = 0.0301(C) - 0.0003$, where A = absorption and C = concentration of RYD. The determination coefficient was $r^2 = 0.9994$. Color determination was conducted in a Hach DR/3000 spectrophotometer.

2.3. Removal Efficiency of RYD. The removal efficiency of RYD was calculated as

$$E(\%) = \frac{C_1 - C_f}{C_1} * 100, \quad (1)$$

where C_1 is the initial dye concentration and C_f is the final dye concentration, both in $\text{mg}\cdot\text{L}^{-1}$; this expression was also used in case of color determination where C_1 and C_f are color intensities in Pt/Co units [23].

2.4. Chemical Oxygen Demand. Chemical oxygen demand was determined according to standard techniques, APHA/AWWA/WPCE [24].

The removal efficiency or percentage of COD removal (%RE) was then calculated as follows [25, 26]:

$$E(\%) = \frac{\text{COD}_0 - \text{COD}_f}{\text{COD}_0} * 100, \quad (2)$$

where COD_0 is the initial chemical oxygen demand and COD_f is the final chemical oxygen demand, both in $mg \cdot L^{-1}$.

2.5. Sampling. The determination of RYD and the removal efficiency of RYD and COD correspond to the samples taken in the upper part of the reactor and later filtered with Whatman paper number 1. The samples were withdrawn from the reactor every 5 min for analysis.

2.6. Applied Current Intensity. The experimental tests were divided into two stages. First, a series of discontinuous tests with current intensities of 4, 6, 8, and 10 A controlled by a power supply during 60 minutes (system DC power supply, Agilent Technologies N5700 series) were carried out and then with current intensities of 2, 3, 4, and 5. The second phase was carried out in a continuous flow, during approximately 6 hours; the current intensity was applied according to the results obtained in the discontinuous tests.

The objective in this stage was to evaluate the intensity of the current that is variable, depending on the following flow rates: 300, 500, 700, and 1000 $mL \cdot min^{-1}$, in order to check the contact time between the dye and the electrode to evaluate the percentage of removal of RYD through photovoltaic live connection.

The electrodes were treated by rinsing them with a 1 M HCl solution and distilled water at the end of each test.

2.7. Photovoltaic Array. The photovoltaic array consisted of two Siemens Solar photovoltaic (PV) modules Solar 75 Wp, SP-75. The solar module characteristics were verified using the I-V Checker MP140 Portable PV Device Evaluation Instrument, for which the PV module was first determined, and afterwards, with two PV modules connected in parallel [8], the short circuit current increases with the number of modules connected in parallel. The experiments were carried out at the Institute of Electrical Research (latitude 18°52' 40.99" N, longitude 99°13 '6.89" O, inclination 19°, and south oriented).

Table 2 shows the PV module characterization for one and two PV modules connected in parallel. If one solar module is considered, the acquired current is 3.8 A and is sufficient to obtain similar removal results as accomplished by the power source. In the case of a cloudy day where there is low solar radiation, the application of two modules would be required. Parallel-connected solar PV modules would offer a required minimum current intensity in the reaction performance with reasonable efficiency. The calibration of both modules set in parallel array produces a current intensity of 7.9 A.

3. Results and Discussion

3.1. Batch Tests with Artificial Power Source. Table 3 shows that COD removal is time dependent while applying different current intensities. At lower current intensity, the removal efficiency of COD is higher; this variation can be attributed to an interference during COD determination caused by the presence of aluminum ions when applying more current. The electrochemical reaction will produce a higher number

TABLE 2: Characterization of solar PV modules.

Parameter	1 PV module	2 PV module
Solar irradiance (W/m^2)	1007.3	1046.5
Ambient temperature ($^{\circ}C$)	25	25
Cell temperature ($^{\circ}C$)	58.4	57
Short current (A)	4.4	9.0
Open voltage (V)	18.5	18.8
Max power (W)	51.5	107.3
Max power current (A)	3.8	7.9
Max power voltage (V)	13.5	13.6
Fill factor (FF)	0.63	0.63

TABLE 3: Removal efficiency of COD $mg \cdot L^{-1}$ by different current intensities.

Time (min)	Current (A)			
	4.0	6.0	8.0	10.0
15	52.9	48.0	42.2	37.8
30	70.6	48.0	39.0	76.5
45	77.5	41.2	61.8	64.3
60	43.1	40.2	49.0	57.7

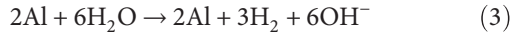
of aluminum ions, and this explains why the removal efficiency decreases during the treatment time.

It is known that the current intensity applied to the system determines the amount of released ions and therefore the amount of the resulting coagulant. Thus, the higher the amount of dissolved Al^{3+} ions in a solution, the greater the rate of $Al(OH)_3$ formation, and consequently a higher COD removal efficiency is expected to be achieved. In addition, the increase of current density promotes the generation of H_2 bubbles and decreases its size, which should lead to a higher removal of pollutants by flotation. However, higher current values may promote a higher turbulence in the system, and consequently, the particles responsible for coagulation do not have enough time to agglomerate themselves and remove the pollutants [27] as stated by Fajardo et al. (2015).

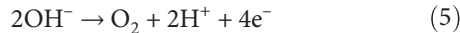
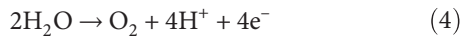
The ions generated in the electrode are $Al(aq)^{3+}$ and OH^- ; the combination of these ions is expected to form various monomeric species such as $Al(OH)^{2+}$, $Al(OH)_2^+$, $Al_2(OH)_2^{4+}$, and $Al(OH)_4^-$ and polymeric species such as $Al_6(OH)_{15}^{3+}$, $Al_7(OH)_{17}^{4+}$, $Al_8(OH)_{20}^{4+}$, $Al_{13}(OH)_{34}^{5+}$, and $Al_{13}(OH)_{37}^{2+}$ [23, 24]. By relating these species with the report about super-faradaic efficiencies [28, 29], they are more significant at low current densities, that is, $1.75 mA \cdot cm^{-2}$. In the case of aluminum, experimental results are significantly over the expected values for a 100%-efficiency process according to Faraday's law, (3). This super-faradaic efficiency is explained in terms of a chemical dissolution process, which corresponds to the oxidation of the aluminum sheets with the simultaneous reduction of water to form hydrogen. It has also been mentioned that the amount of generated aluminum seems to depend on the pH, and this has been explained in terms of chemical

dissolution of the aluminum electrode. In this case, the pH was initially between 5.6 and 6.3. However, it was observed that as current increases, pH rapidly decreases. For example, at $I = 4, 6, 8,$ and 10 A, the pH was 4.8, 2.3, 2.2, and 1, respectively. Gu et al. suggest that (4) and (5) for the oxidation of water will decrease solution pH [30] and this was observed in this work, so, the super-faradaic efficiencies are greater for aluminum than those for iron [29].

The pKa of the remazol yellow dye is 3.77. Therefore, above this pH, the species of ionic form will be found, and its chromophore groups will be negatively charged. When the removal efficiency decreases, it is suggested that the precipitated hydroxide metal may have tended to dissolve in liquid thus adversely affecting the performance of the process. This fact may take place as the medium turns extremely acidic or alkaline as previously reported [31–33]. The cationic metal species are responsible for the destabilization of the particles (charge neutralization), leading to the formation of flocculating particles, which will have the power to sediment contaminants [33]. In situ generation of coagulants has the advantage of reducing the amount of chemical reagents introduced into the system; however, this may lead to a change in pH. In this context, the pH of the batch tests has been reported acidic and in the continuous tests, the pH fluctuated between 7.8 and 8.9, so the predominant reaction will be represented by (3) [29].



According to the diagram of Pourbaix [34], at pH less than 4, Al^{3+} ions are expected, and between 4 and 8, there may be passivation by Al_2O_3 . For this study, however, it is observed that the pH and therefore the predominant reactions depend on the flow regime, that is, in batch tests, an acidic pH is observed and (4) and (5) predominate, and in tests under continuous flow, the pH is between neutral and slightly alkaline, and without considering the effect of passivation, (3) is the predominant one as already mentioned.



Another phenomenon is the production of aluminum, so in Table 3, there is an increase of COD, although the color tends to decrease. As it is known, this production is a function of the applied current. Thus, considering the electrode area (0.44 m^2) and applying Faraday's law (6), the following values of Al^{3+} are calculated, 0.32, 0.48, 0.64, and 0.81 g, for currents of 4, 6, 8, and 10 A, accordingly. It is possible to have an excess of ions and for this reason, the COD value does not fall [5].

$$n = \frac{MIt}{zF}, \quad (6)$$

where n is the metal (g), M molecular mass of electrode, I current intensity, t operating time, z number of electron transferred, and F Faraday's constant (96,500 C/mol).

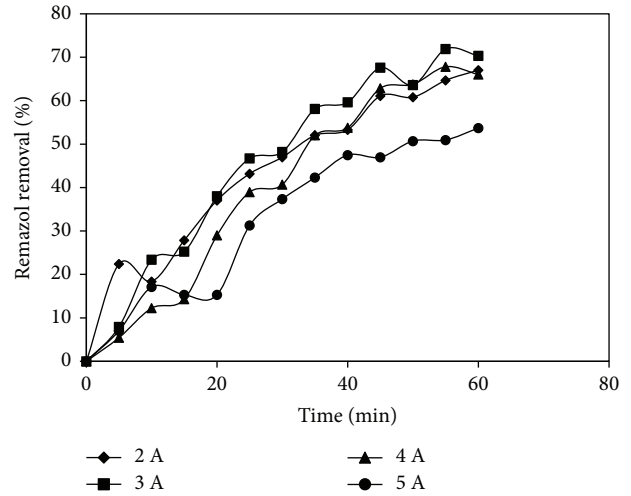


FIGURE 2: Removal of RYD at different current intensities: 2 A, 3 A, 4 A, and 5 A.

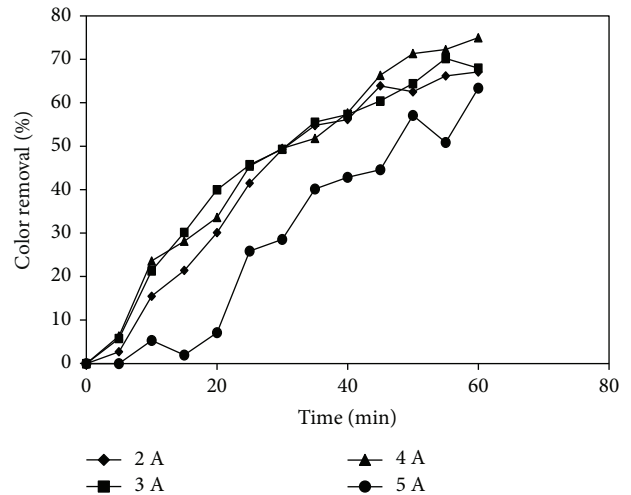


FIGURE 3: Color removal at different current intensities: 2 A, 3 A, 4 A, and 5 A.

In the case of aluminum, experimental results are significantly over the expected values for a 100%-efficiency process according to Faraday's law. This super-faradaic efficiency is explained in terms of a chemical dissolution process, which corresponds to the oxidation of the aluminum sheets with the simultaneous reduction of water to form hydrogen, according to (3) [29].

3.2. Optimization of the Applied Current with the Power Source. According to the results of Table 3, the applied current must be less than 6 A; so for these tests, currents to be evaluated were selected from 2, 3, 4, and 5 A. Figure 2 shows the dye removal percentage at these current intensities where a significant difference does not appear when applying 2, 3, or 4 A, as compared to 5 A ANOVA and Duncan test ($p > 0.5$) [35].

Figure 3 shows the dye color removal percentage at the same currents; these current intensities have the same behavior as in the removal of dye concentration.

In Figures 2 and 3, a similar behavior is observed regarding the elimination of the dye elaborated with the UV-Vis spectrophotometer and the elimination of the color; they have very similar efficiencies. When performing the ANOVA, it is similar to the dye efficiency tests that with a current of 2, 3, and 4 A, there is no significant difference in the results and with respect to 5 A, if there is a significant difference ($p > 0.5$).

3.3. Batch Examinations with PV Modules. Table 1 shows that one PV module is enough to generate a current of 4 A under good solar radiation conditions, and two solar PV modules in parallel array are capable to generate 7.9 A. This means that in cloudy weather conditions, the current generated by two solar PV modules must be in the necessary range to carry out the RYD removal tests. Then, under this assumption, Figure 4 shows the comparison for RYD removal with the power source in 3 A and 4 A and one solar PV module. During this testing period, the solar PV module had an average solar radiation of 747 W/m^2 and a current of 3.1 A, with an average voltage of 2.37 V; the pH dropped slightly from 8 to 6.5 units, while the temperature in the electrocoagulation reactor increased from 18.5 to 20°C . As shown in Figure 4, there are no differences in the RYD results from the power source and solar PV modules. Observing that the removal efficiency is lower for 5 A, it is established that the appropriate conditions for the work of the system with the solar panel will be sufficient if it reaches between 2 and 4 A of current. This will depend on the solar irradiation of the moment; since the solar modules are connected directly, the solar irradiation impacts directly to the electrochemical reactor, generating greater or less quantity of ions to participate in the electrocoagulation. If there is a sunny and cloudless day, adequate solar radiation is guaranteed, which is why 1 or 2 photovoltaic panels are used. This is a complement of Figures 2 and 3 where we observe the similarity in the color and concentration removals of the RYD, and if we contrast this with Figure 4 which is already an experimental process, it is possible to use one or two photovoltaic modules, considering the use of only one module for the conditions treated in these experiments.

3.4. Examination in Continuous Flow Rate. Figure 5 shows how the removal of the dye and color removal (65–70%) are kept constant in the test from 1.5 hours and onwards with a flow rate of $300 \text{ mL}\cdot\text{min}^{-1}$ and the PV current supplied by either one or two PV modules. Contrasting this graph with Figure 6, the radiation in either case, with one and two photovoltaic modules, can be observed. It is worth noting that there is a significant variation with the use of two photovoltaic modules. This can be ascribed to the day being cloudy and although it worked with the two modules reaching currents from 3.08 to 7.93 and 0.78 to 3.92 with one module, a variation is reflected although in an appropriate range for the minimum current needed for the electrochemical process. Thus, the use of two modules allows to attain currents

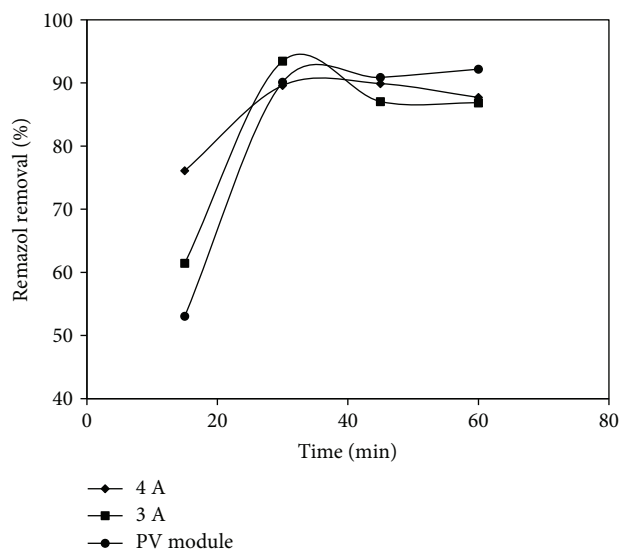


FIGURE 4: Comparison between current intensity controlled with the power source and one module solar: 4 A, 3 A, and PV module.

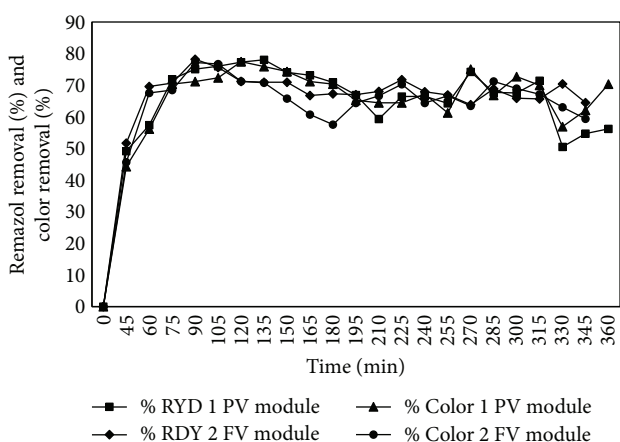


FIGURE 5: Remazol removal and color removal under continuous flow with the application of photovoltaic modules: liquid flow rate: $300 \text{ mL}\cdot\text{min}^{-1}$; initial concentration of RYD: $100 \text{ mg}\cdot\text{L}^{-1}$. % RYD one PV module, % RYD one PV module, color one PV module, and color two PV module.

higher than 3 A at all times. According to Figure 4, this value is sufficient for the process to occur. When only one module is used, the current will depend on the daytime and the variation may be rather rapid. For example, at 9:00 in the morning, a 0.78 A current was obtained, while 50 minutes later, the measured current was already 2 A. This trend usually prevails until 15: h. On the other hand, when two solar modules are used, the minimum attained current is 3.08 A, and between 10:00 and 15:30, the current is always higher than 3 A. Therefore, it can be concluded that two modules will always provide the adequate current regardless of the solar radiation intensity during daytime.

The tests by different flow rates are shown in Figure 7. As it can be observed, the differences of the dye removal efficiencies are not significant for flow rates of 500, 700,

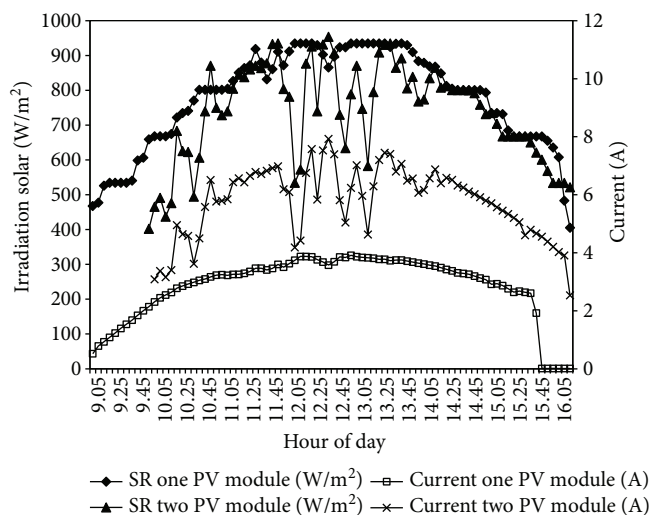


FIGURE 6: Solar irradiation profiles as function of time: SR one PV module, SR two PV module, current one PV module, and current two PV module.

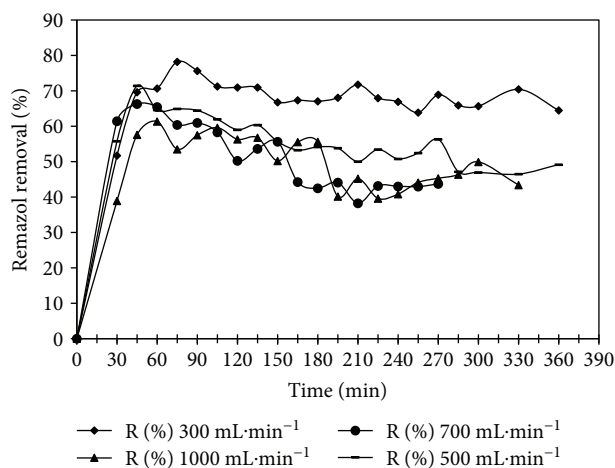


FIGURE 7: Effect of removal percentage rate on RYD initial concentration remazol 100 mg·L⁻¹: % RYD 300 mL·min⁻¹, % RYD 500 mL·min⁻¹, % RYD 700 mL·min⁻¹, and % RYD 1000 mL·min⁻¹.

and 1000 mL·min⁻¹; however, at 300 mL·min⁻¹ flow rate, the difference is around 20% [36, 37]. This effect was expected since lower flow rates also imply higher residence time. It can be concluded that RYD removal efficiency is favored when the retention time, electric current, and flow rate are low [38, 39].

Table 4 shows the average, maximum, and minimum values of solar radiation, current intensity, and voltage for the accomplished tests by different flow rates comparing each one of 300 mL·min⁻¹ with the remaining other. It is possible to observe that the current intensity is lower at 300 and 500 mL·min⁻¹; however, the removal efficiency is better in the low flow rate. This proves that current above 5 A does not increase the removal efficiency.

As shown, there is variation in the current intensity for each test, because it is not possible to compare them,

TABLE 4: Evaluated parameters during different RYD flow rate.

Flow rate (mL·min ⁻¹)	Solar radiation (W/m ²)	Voltage (V)	Current intensity (A)
300	741.4 (437.5–954)	3.9 (1.92–4.9)	5.7 (2.53–7.93)
500	624.4 (461–777)	4.3 (3.9–4.9)	5.5 (3.94–6.97)
700	861.7 (688–957)	6.6 (4.5–7.56)	7.4 (3.52–8.41)
1000	857.4 (602–977)	6.2 (3.34–8.23)	7.4 (3.45–8.45)

Average value (minimum–maximum).

however, since they are connected live; it depends on the solar radiation received on the day of the test; it can only be confirmed that it will be necessary to modify the water flow rate according to the received radiation so that it is proportional to what is reported in the literature as suitable to produce the amount of aluminum to react with the dye; nevertheless, it should not be forgotten that the phenomenon of super-faradaic production of the ion that helps the dye removal is also present. Under continuous flow, there is a synergy during treatment since after 1 hour of treatment, a stationary state is reached and a dye removal efficiency of 70% is attained. Worth noticing is that this value is kept constant until the treatment is complete (Figure 4). It is considered that it is necessary to establish a chain of batteries that are charged with photovoltaic energy to be able to carry out the elimination of pollutants continuously throughout the day, without being contingent to the solar radiation. That is, to store the energy and use it at the moment that it is required.

3.5. Energy Consumption. Figure 8 shows the energy consumption to remove 1 g of RYD by means of direct current and photovoltaic current at a flow rate of 300 mL·min⁻¹. It can be seen that under controlled current supply with a DC power system, the energy consumption to remove RYD was constant and linear, 5.38 Wh·g⁻¹.

For RYD removal by means of PV current, this was dependent on solar radiation, reaching a maximum value of solar radiation around 1:00 p.m. and descended to the lowest value by the sunset.

Valero et al. [39, 40] demonstrated that the use of photovoltaic energy (i) reduces the cost of investment by avoiding the use of batteries, solar inverters, and power supplies and (ii) reduces the cost of maintenance, since there is no waste of batteries to properly dispose.

However, the disadvantage of this process is that in Mexico, it could only be applied from 9:30 am to 4:00 p.m., since it is the time in which there is adequate solar radiation in a sunny day. Sunny days are not constant through the year though. In order to overcome this, the use of hybrid energies combining solar photovoltaic with wind could be considered. This approach, however, should be evaluated taking into account that the increase of air is in the evening, so the working hours of an electrochemical reactor can be increased [41], considering the proposal of [39].

According to Figure 8, energy consumption to remove RYD color was dependent on the generated current by one or two PV modules. However, at the highest energy

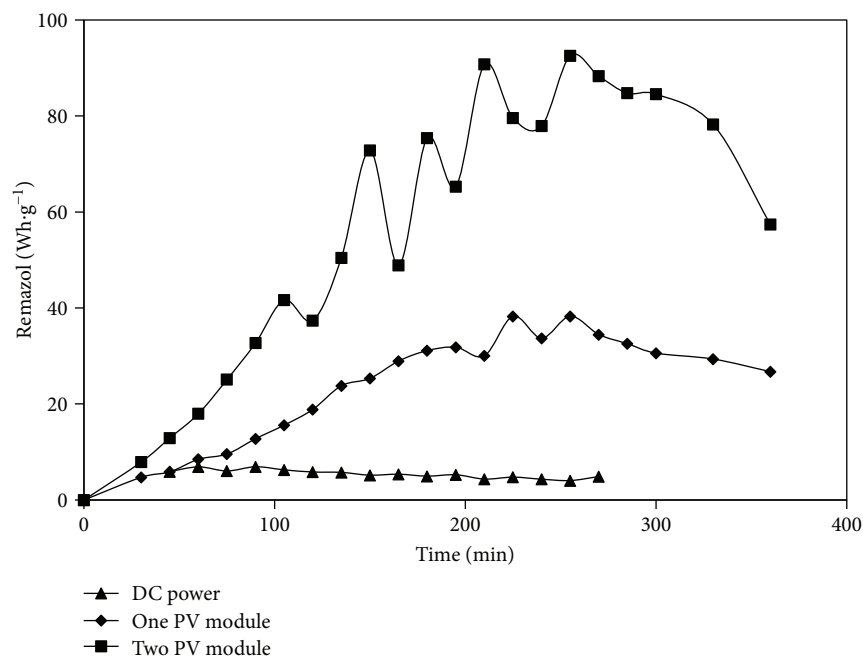


FIGURE 8: Comparison between CD and PV module.

consumption, RYD color removal shows a decay behavior due probably to a passivation phenomenon of the aluminum electrodes (see Section 3.1) and the consequent rising of electrical resistance thus causing the energy consumption increase.

Results reported at industrial scale show a parallel and series arrangement of the photovoltaic modules in order to obtain the electric current for the wastewater pollutant removal. However, the conditions of the photovoltaic arrangement will depend on the climatic conditions [40]. The setup for the pilot reactor of this work was two-module photovoltaic in parallel for a cloudy day and one-module photovoltaic for a sunny day.

Finally, regarding the PV energy costs, it will be possible to get a PV system at a low cost for the wastewater treatment. "Production costs for industry-leading Chinese crystalline-silicon (c-Si) PV module manufacturers – such as Jinko Solar, Renesola, Trina Solar and Yingli Green Energy – will fall from 50 cents per watt in the fourth quarter of 2012 to 36 cents per watt by the end of 2017," according to a new report from GTM Research. The report, *PV Technology and Cost Outlook, 2013-2017* [42], predicts that the majority of these cost declines will derive from technology innovations such as diamond wire sawing for PV wafers, advanced metallization solutions, and increased automation in place of manual labor.

4. Conclusions

It is possible to use the photovoltaic modules to conduct wastewater treatment by electrocoagulation. In this work, the highest attained removal efficiency of RYD and color were 70% for both under continuous flow. The achieved current from one PV module was enough to generate

electrocoagulation and remove RYD and color in a sunny day or two PV modules in parallel on a cloudy day. In order to obtain the electrocoagulation reaction, the current intensity should be between 3 and 4 A. The recommended operation flow rate in the system is $300 \text{ mL} \cdot \text{min}^{-1}$; if the flow rate is increased, the removal efficiency decreases.

It is important to take into account the costs and the innovation in photovoltaics, since its implementation for scaling will depend on these, as well as on being able to install a complete system for storing solar energy and control the power to the system, always looking for the better pollutant removal efficiencies.

Conflicts of Interest

The authors declare that they have no conflicts of interest.

References

- [1] C. Chienhung, N. Ervin, J. Yaju, and H. Chihpin, "Electrochemical decolorization of dye wastewater by surface-activated boron-doped nanocrystalline diamond electrode," *Journal of Environmental Sciences*, vol. 45, pp. 100–107, 2016.
- [2] C. Davide, C. Giacomo, and M. Panizza, "Electrochemical oxidation of a synthetic dye using a BDD anode with a solid polymer electrolyte," *Electrochemistry Communications*, vol. 75, pp. 21–24, 2017.
- [3] J. Rajeev, N. Sharma, and K. Radhapyari, "Electrochemical treatment of pharmaceutical azo dye amaranth from waste water," *Journal of Applied Electrochemistry*, vol. 39, pp. 577–582, 2009.
- [4] V. David, G.-G. Vicente, E. Eduardo, A. Antonio, and M. Vicente, "Electrochemical treatment of wastewater from almond industry using DSA-type anodes: direct connection

- to a PV generator," *Separation and Purification Technology*, vol. 123, pp. 15–22, 2014.
- [5] M. Kobya, E. Gengec, and E. Demirbas, "Operating parameters and costs assessments of a real dyehouse wastewater effluent treated by a continuous electrocoagulation process," *Chemical Engineering and Processing: Process Intensification*, vol. 101, pp. 87–100, 2016.
 - [6] A. Amour, B. Merzouk, L. Jean-Pierre, and F. Lapicque, "Removal of reactive textile dye from aqueous solutions by electrocoagulation in a continuous cell," *Desalination and Water Treatment*, vol. 57, no. 48–49, pp. 22764–22773, 2015.
 - [7] B. K. Korbahti and K. M. Turan, "Evaluation of energy consumption in electrochemical oxidation of Acid Violet 7 textile dye using Pt/Ir electrodes," *Journal of Turkish Chemical Society, Section A: Chemistry*, vol. 3, no. 3, pp. 75–92, 2016.
 - [8] D. Valero, J. M. Ortiz, E. Expósito, V. Montiel, and A. Aldaz, "Electrocoagulation of a synthetic textile effluent powered by photovoltaic energy without batteries: direct connection behaviour," *Solar Energy Materials and Solar Cells*, vol. 92, no. 3, pp. 291–297, 2008.
 - [9] A. Masion, A. Vilg -Ritter, J. Rose et al., "Coagulation-flocculation of natural organic matter with al salts: speciation and structure of the aggregates," *Environmental Science & Technology*, vol. 34, no. 15, pp. 3242–3246, 2000.
 - [10] J. Gregory, "Laminar dispersion and the monitoring of flocculation processes," *Journal of Colloid and Interface Science*, vol. 118, pp. 397–409, 1987.
 - [11] A. Dalvand, E. Gholibegloo, M. R. Ganjali et al., "Comparison of *Moringa stenopetala* seed extract as a clean coagulant with Alum and *Moringa stenopetala*-Alum hybrid coagulant to remove direct dye from textile wastewater," *Environmental Science and Pollution Research*, vol. 23, no. 16, pp. 16396–16405, 2016.
 - [12] A. Assadia, A. Soudavaria, and M. M. Fazlia, "Comparison of electrocoagulation and chemical coagulation processes in removing reactive red 196 from aqueous solution," *Journal of Human Environment and Health Promotion*, vol. 1, no. 3, pp. 172–182, 2016.
 - [13] C. Ricordel, A. Darchen, and D. Hadjiev, "Electrocoagulation-electroflotation as a surface water treatment for industrial uses," *Separation and Purification Technology*, vol. 74, no. 3, pp. 342–347, 2010.
 - [14] A. Othmani, A. Kesraoui, and M. Seffen, "The alternating and direct current effect on the elimination of cationic and anionic dye from aqueous solutions by electrocoagulation and coagulation flocculation," *Euro-Mediterranean Journal for Environmental Integration*, vol. 2, no. 1, 2017.
 - [15] S. L. P rez, M. O. Rodriguez, S. Reyna et al., "Oil refinery wastewater treatment using coupled electrocoagulation and fixed film biological processes," *Physics and Chemistry of the Earth, Parts A/B/C*, vol. 91, pp. 53–60, 2016.
 - [16] H. Ahmad, W. K. Lafi, K. Abushgair, and J. M. Assbeihat, "Comparison of coagulation, electrocoagulation and biological techniques for the municipal wastewater treatment," *International Journal of Applied Engineering Research*, vol. 11, no. 22, pp. 11014–11024, 2016.
 - [17] C. Barrera-D az, G. Roa-Morales, L.  vila-C rdoba, T. Pav n-Silva, and B. Bilyeu, "Electrochemical treatment applied to food-processing industrial wastewater," *Industrial & Engineering Chemistry Research*, vol. 45, no. 1, pp. 34–38, 2006.
 - [18] C. Barrera-D az, L. A. Bernal-Mart nez, R. Natividad, and J. M. Peralta-Hern ndez, "Synergy of electrochemical/O₃ process with aluminum electrodes in industrial wastewater treatment," *Industrial and Engineering Chemistry Research*, vol. 51, no. 27, pp. 9335–9342, 2012.
 - [19] ISES, "Transici n hacia un futuro basado en las fuentes renovables de energ a," *Asociaci n Internacional de Energ a Solar*, 2003, https://mba.americaeconomia.com/sites/mba.americaeconomia.com/files/paper_ises_dieter_holm.pdf.
 - [20] S. M. Lucas, R. Mosteo, M. I. Maldonado, S. Malato, and J. A. Peres, "Solar photochemical treatment of winery wastewater in a CPC reactor," *Journal of Agricultural and Food Chemistry*, vol. 57, no. 23, pp. 11242–11248, 2009.
 - [21] A. M. S. Solano, C. K. Costa, D. Araujo et al., "Decontamination of real textile industrial effluent by strong oxidant species electrogenerated on diamond electrode: viability and disadvantages of this electrochemical technology," *Applied Catalysis B: Environmental*, vol. 130–131, pp. 112–120, 2013.
 - [22] O. T. Can, M. Bayramoglu, and M. Kobya, "Decolorization of reactive dye solutions by electrocoagulation using aluminum electrodes," *Industrial & Engineering Chemistry Research*, vol. 42, no. 14, pp. 3391–3396, 2003.
 - [23] P. K. Holt, *Electrocoagulation: Unravelling and Synthesising the Mechanisms behind a Water Treatment Process*, [Ph.D. thesis], Chemical Engineering, University of Sydney, Australia, 2002.
 - [24] American Public Health Association, American Water Works Association, and Water Environment Federation, *Standard Methods for the Examination of Water and Wastewater*, L. S. Clesceri, A. E. Greenberg and A. D. Eaton, Eds., Washington, DC, USA, 1995, <https://ses.library.usyd.edu.au/handle/2123/624>.
 - [25] P. Aravind, V. Subramanyan, S. Ferro, and R. Gopalakrishnan, "Eco-friendly and facile integrated biological-cum-photo assisted electrooxidation process for degradation of textile wastewater," *Water Research*, vol. 93, pp. 230–241, 2016.
 - [26] T. Harif and A. Adin, "Characteristics of aggregates formed by electroflocculation of a colloidal suspension," *Water Research*, vol. 41, no. 13, pp. 2951–2961, 2007.
 - [27] A. S. Fajardo, R. F. Rodrigues, R. C. Martins, L. M. Castro, and R. M. Quinta-Ferreira, "Phenolic wastewaters treatment by electrocoagulation process using Zn anode," *Chemical Engineering Journal*, vol. 275, pp. 331–341, 2015.
 - [28] P. Ca izares, C. Jim nez, F. Mart nez, C. S ez, and M. A. Rodrigo, "Study of the electrocoagulation process using aluminum and iron electrodes," *Industrial & Engineering Chemistry Research*, vol. 46, no. 19, pp. 6189–6195, 2007.
 - [29] E. Lacasa, P. Ca izares, and M. A. Rodrigo, "Production of coagulant reagents for electro-coagulation processes at low current densities," *Desalination and Water Treatment*, vol. 45, no. 1–3, pp. 256–262, 2012.
 - [30] Z. Gu, Z. Liao, M. Schulz, R. J. Davis, C. J. Baygents, and J. Farrell, "Estimating dosing rates and energy consumption for electrocoagulation using iron and aluminum electrodes," *Industrial & Engineering Chemistry Research*, vol. 48, no. 6, pp. 3112–3117, 2009.
 - [31] H. Inan, A. Dimoglo, H.  im ek, and M. Karpuzcu, "Olive oil mill wastewater treatment by means of electro-coagulation," *Separation and Purification Technology*, vol. 36, no. 1, pp. 23–31, 2004.

- [32] Ü. T. Ün, S. Uğur, A. S. Koparal, and Ü. B. Ögütveren, "Electrocoagulation of olive mill wastewaters," *Separation and Purification Technology*, vol. 52, pp. 136–141, 2006.
- [33] A. S. Fajardo, R. C. Martins, and R. M. Quinta-Ferreira, "Treatment of a synthetic phenolic mixture by electrocoagulation using Al, Cu, Fe, Pb, and Zn as anode materials," *Industrial & Engineering Chemistry Research*, vol. 53, no. 47, pp. 18339–18345, 2014.
- [34] M. Pourbaix, *Atlas of Electrochemical Equilibria in Aqueous Solutions*, Pergamon Press, Oxford, 1st edition, 1966.
- [35] O. Nurgul and S. Y. Adife, "Factorial experimental design for Remazol Yellow dye sorption using apple pulp/apple pulp carbone–titanium dioxide co-sorbent," *Journal of Cleaner Production*, vol. 100, pp. 333–343, 2015.
- [36] M. A. Sandoval, J. L. Nava, O. Coreno, G. Carreno, L. A. Arias, and D. Mendez, "Sulfate ions removal from an aqueous solution modeled on an abandoned mine by electrocoagulation process with recirculation," *International Journal of Electrochemical Science*, vol. 12, pp. 1318–1330, 2017.
- [37] S. Liu, X. Ye, H. Kuang, Y. Chen, and H. Yongyou, "Simultaneous removal of Ni(II) and fluoride from a real flue gas desulfurization wastewater by electrocoagulation using Fe/C/Al electrode," *Journal of Water Reuse and Desalination*, vol. 7, no. 3, pp. 288–297, 2017.
- [38] K. Wang Lawrence, H. Yung-Tse, and K. Shammaz Nazih, Eds., "Advanced physicochemical treatment technologies," in *Handbook of Environmental Engineering*, vol. 5, p. 305, Humana Press, 2007.
- [39] D. Valero, J. M. Ortiz, V. García, E. Expósito, V. Montiel, and A. Aldaz, "Electrocoagulation of wastewater from almond industry," *Chemosphere*, vol. 84, no. 9, pp. 1290–1295, 2011.
- [40] D. Valero, V. García-García, E. Expósito, A. Aldaz, and V. Montiel, "Electrochemical treatment of wastewater from almond industry using DSA-type anodes: direct connection to a PV generator," *Separation and Purification Technology*, vol. 123, pp. 15–22, 2014.
- [41] M. M. Quintero, S. T. Pavón, M. G. Roa, and R. Ruiz Meza, "Remoción de un colorante en medio acuoso utilizando un proceso electroquímico y energía eólica," in *Tercer Congreso Internacional de Ciencias Ambientales. Sustentabilidad y Cambio Climático*, Universidad Autónoma del Estado de México, Toluca, Estado de México, 2016.
- [42] S. Lacey, Ed., *Producing Solar Below 70 Cents a Watt*, 2010, <http://www.renewableenergyworld.com/rea/news/podcast/2010/09/producing-solar-at-70-cents-a-watt>.

Research Article

A Comparative Analysis of 2-(Thiocyanomethylthio)-Benzothiazole Degradation Using Electro-Fenton and Anodic Oxidation on a Boron-Doped Diamond Electrode

Armando Vázquez,¹ Lucía Alvarado,² Isabel Lázaro ¹, Roel Cruz,¹ José Luis Nava,³ and Israel Rodríguez-Torres ¹

¹Instituto de Metalurgia, Facultad de Ingeniería, Universidad Autónoma de San Luis Potosí, Av. Sierra Leona 550, 78210 San Luis Potosí, SLP, Mexico

²Departamento de Ingeniería en Minas, Metalurgia y Geología, Universidad de Guanajuato, Ex. Hacienda de San Matías s/n Fracc. San Javier, 36025 Guanajuato, GTO, Mexico

³Departamento de Ingeniería Geomática e Hidráulica, Universidad de Guanajuato, Av. Juárez 77, 36000 Guanajuato, GTO, Mexico

Correspondence should be addressed to Israel Rodríguez-Torres; learsi@uaslp.mx

Received 18 October 2017; Accepted 3 January 2018; Published 1 March 2018

Academic Editor: Reyna Natividad-Rangel

Copyright © 2018 Armando Vázquez et al. This is an open access article distributed under the Creative Commons Attribution License, which permits unrestricted use, distribution, and reproduction in any medium, provided the original work is properly cited.

2-(Thiocyanomethylthio)-benzothiazole (TCMTB) is used as fungicide in the paper, tannery, paint, and coatings industries, and its study is important as it is considered toxic to aquatic life. In this study, a comparison of direct anodic oxidation (AO) using a boron-doped diamond electrode (BDD) and electro-Fenton (EF) processes for TCMTB degradation in acidic chloride and sulfate media using a FM01-LC reactor was performed. The results of the electrolysis processes studied in the FM01-LC reactor showed a higher degradation of TCMTB with the anodic oxidation process than with the electro-Fenton process, reaching 81% degradation for the former process versus 47% degradation for the latter process. This difference was attributed to the decrease in H_2O_2 during the EF process, due to parallel oxidation of chlorides. The degradation rate and current efficiency increased as a function of volumetric flow rate, indicating that convection promotes anodic oxidation and electro-Fenton processes. The results showed that both AO and EF processes could be useful strategies for TCMTB toxicity reduction in wastewaters.

1. Introduction

The paper industry has been identified as a major source of pollutants to aquatic environments due to the large volume of wastewater generated per ton of paper produced. The effluents generated during the paper production process cause damage to the receiving waters as they contain high levels of total organic carbon (TOC) and exhibit a chemical oxygen demand (COD) above the permissible limits [1]. Studies on the treatments of wastewater from the paper industry have reported a content of at least 300 different compounds, including certain compounds of biocide nature [2], such as 2-(thiocyanomethylthio)-benzothiazole (TCMTB), which is often used as a biocide in the wood [3] and tannery industries [4]. TCMTB is listed as hazardous by the Environmental

Protection Agency of the United States, and it is considered highly toxic to freshwater fish, freshwater invertebrates, estuarine/marine fish, and estuarine/marine invertebrates [5]. Hence, it is important to develop and apply techniques for the degradation of TCMTB.

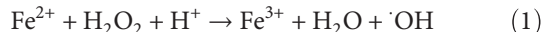
Reemtsma et al. [6] achieved an incomplete TCMTB degradation (75%) in an anaerobic and aerobic wastewater treatment pilot plant, yielding mercaptobenzothiazole (MTB), benzothiazole (BT), and hydroxybenzotriazole (OHBT) as the degradation products, which however are harmful compounds that cause dermatitis [7], cell apoptosis [8], and respiratory tract irritation [9], respectively. De Wever et al. [10, 11] carried out studies to investigate the biodegradation of these compounds and established that MTB is a recalcitrant compound. Recalcitrant compounds or persistent

organic pollutants (POPs) are characterized by a high stability against sunlight irradiation and a high resistance to either microbial attack (biological processes) or temperature.

Advanced oxidation processes (AOPs) are effective methods that have been developed for POP treatment. These methods primarily involve hydrogen peroxide, ozone, UV-near visible light in the presence of TiO_2 , the Fenton reagent, sonolysis, and the sulfate radical-based AOP [12]. Advanced electrooxidation processes (AEOPs) have been proposed as alternative methods for the removal of organics; these processes employ electrochemical cells in which oxidants are produced in situ on the electrode surface [13].

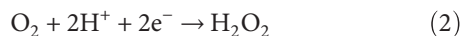
In recent years, the development of AEOPs has significantly increased, particularly oriented to processes of POP degradation. AEOPs are based on the generation of strong oxidizing species, such as the hydroxyl radical ($\cdot\text{OH}$), which can alter the chemical structure of the contaminants [14]. The hydroxyl radical is considered the most important free radical in chemistry due to its strong oxidizing nature ($E^\circ = 2.8 \text{ V}$), which is exceeded only by fluorine ($E^\circ = 3.05 \text{ V}$). The oxidizing power of $\cdot\text{OH}$ destroys most organic pollutants until total mineralization is achieved, that is, conversion to CO_2 , water, and inorganic ions.

In this context, one method of generating the hydroxyl radical is through the Fenton reaction. The Fenton process mechanism is initiated by the formation of the homogeneous hydroxyl radical in accordance with the classical Fenton reaction in acidic medium, as follows [14]:



This technique becomes an attractive choice because only a small catalytic amount of Fe^{2+} is required during the entire process due to the continuous regeneration of the ion from the Fenton-like reaction [15].

Another interesting aspect of $\cdot\text{OH}$ production from H_2O_2 is that it can be generated by electrochemical reduction from O_2 in aqueous solution under acidic conditions, as follows [14, 16]:



Electro-Fenton (EF) technology is based on the continuous electrogeneration of H_2O_2 on a suitable cathode (generally, carbon-based), which is fed with either O_2 or air [14], and the addition of an iron catalyst to produce the oxidant hydroxyl radical at the bulk via the Fenton reaction, according to (1).

Another electrochemical process that could generate $\cdot\text{OH}$ radicals is the anodic oxidation of water [17–19]:



Hydroxyl radical formation is favored on boron-doped diamond (BDD) thin film anodes; this reaction is based on the use of high O_2 overvoltage anodes favoring heterogeneous hydroxyl radical production, $\text{BDD}(\cdot\text{OH})$. It has been reported that organic compounds can be destroyed by anodic oxidation using BDD electrodes, resulting in their complete mineralization [20].

This study compares TCMTB degradation via the electro-Fenton (EF) process and the anodic oxidation process in a filter press reactor FM01-LC. For the EF process, a reticulated vitreous carbon was used as the cathode along with a dimensionally stable anode (DSA) made of Ti with a cover of $\text{IrO}_2/\text{Ta}_2\text{O}_5$; for the AO process, a BDD electrode was used as anode, and a stainless steel electrode was used as cathode.

2. Materials and Methods

2.1. Reagents and Physicochemical Analysis. All of the chemicals used were of analytical grade, and deionized water ($18 \text{ M}\Omega \text{ cm}$) was employed for the preparation of solutions. The organic compound TCMTB was purchased from Insu-mos Agrícolas Company (industrial grade, 30% purity). The pH measurements were obtained using a Thermo Orion pH meter 420A. The H_2O_2 concentration was determined using the $\text{Ti}(\text{SO}_4)_2$ colorimetric method and analyzed by UV-vis spectrophotometry at $\lambda = 410 \text{ nm}$ [21]. The performance of the process was evaluated following TCMTB UV-vis absorbance at $\lambda = 290 \text{ nm}$ [3] in a Shimadzu UV/VIS/NIR spectrophotometer UV-3600 with a scanning stage step of 250 nm . Total organic carbon (TOC) was measured with a Shimadzu total organic carbon analyzer 5000A, and chemical oxygen demand (COD) tests were run according to standard protocols [22].

2.2. Microelectrolysis

2.2.1. Experimental Devices. A three-electrode system was used for voltammetric experiments using a 100 mL Pyrex electrochemical cell. The potential was applied using a Princeton Applied Research potentiostat-galvanostat VersaSTAT, and Versa software was used to record the data. For the AO study, a BDD rotating disc electrode (RDE) with a surface area of 0.03141 cm^2 and a DSA (Ti with a cover of $\text{IrO}_2/\text{Ta}_2\text{O}_5$) with a surface area of 0.096 cm^2 were used as working electrodes. For the cathodic production of hydrogen peroxide, RDE made of vitreous carbon and stainless steel 304 were used, both with a surface area of 0.196 cm^2 . The BDD was cleaned using an anodic polarization treatment (1 M HClO_4) for 30 min at 10 mA cm^{-2} [23].

A graphite rod was used as the counter electrode in both sets of experiments. Potential measurements were obtained versus a saturated mercurous sulfate reference electrode (SSE) with a potential of 0.6415 V . All the potential measurements shown in this study were referred to the standard hydrogen electrode (SHE). To ensure reproducibility, all of the experiments were performed in triplicate.

2.2.2. Voltammetric Studies. To determine the best current density and electrode potential domain to be applied to favor both the electro-Fenton process (cathodic H_2O_2) and the anodic oxidation (anodic $\cdot\text{OH}$), a microelectrolysis study was performed. For this study, two types of solutions were used: (a) a blank solution (0.02 M NaCl and $0.03 \text{ M Na}_2\text{SO}_4$) and (b) a synthetic solution (0.02 M NaCl , $0.03 \text{ M Na}_2\text{SO}_4$, and 0.07 M TCMTB). The concentration of the blank solution was fixed to an ionic strength similar to that registered in wastewater from the paper industry [24]. The TCMTB

concentration was set to achieve a 570 mg L^{-1} TOC (similar to the concentration found in paper industry effluents), which is equivalent for a turbidity of approximately 383 NTU (nephelometric turbidity unit).

Prior to starting the EF experiments, each solution was aerated for 60 min to insure O_2 saturation and acidified with 1 M H_2SO_4 to reach a pH of 3.

A series of anodic and cathodic potential pulses were applied on static electrodes for 30 s from the open-circuit potential (OCP) to positive potentials for the anodic process and to negative potentials for the cathodic process. From the current transients obtained, j -E curves were constructed using current density data sampled at different times for each potential applied.

2.3. Macroelectrolysis

2.3.1. Experimental Devices. Macroelectrolysis experiments were performed in an FM01-LC electrochemical reactor [25, 26]. Figure 1(a) shows an expanded view, including the turbulence promoter type D [27]. The flow distributor thickness was 0.6 cm; a stainless steel plate (64 cm^2 exposed area) and reticulated vitreous carbon (RVC) of $16 \times 4 \text{ cm}$ and 0.4 cm of thickness (10 pores per inch (ppi), porosity of 0.99, and specific surface area of 4.92 cm^{-1}) were used as cathodes, and BDD and DSA plates (64 cm^2) were used as anodes. The volume of electrolyte to fill the reactor was 28.2 cm^3 . A mercury/mercurous sulfate reference electrode $\text{Hg}/\text{Hg}_2\text{SO}_4$ was connected to the electrochemical reactor to measure the electrode potential. More details of the FM01-LC are described in detail in [25].

An undivided mode configuration with a single electrolyte compartment and electrolyte flow circuit for the FM01-LC cell is shown in Figure 1(b). The electrolyte was contained in a 2.5 L acrylic reservoir; a Marathon Electric™ 1/3 HP centrifugal coupled pump 335AD-MD was used, and flow rates were measured by a Cole-Parmer variable area plastic flow meter F44500. The electrolyte flow circuit was constructed using 0.5-inch internal diameter PVC tubing and valves as well as three-way connectors constructed of the same material. The experiments were conducted using a Sorensen high-power DC power supplies. In experiments to evaluate H_2O_2 production, the electrochemical reactor was fitted with a RVC as cathode and a stainless steel electrode as anode. For the EF process, the reactor was equipped with the RVC as cathode and DSA as anode; for the AO method, a stainless steel electrode as cathode and a BDD as anode were used.

2.3.2. Electrochemical Degradation of TCMTB in a FM01-LC Filter Press-Type Electrochemical Cell. All of the experiments in the FM01-LC cell were performed at three different volumetric flows (Q_v): 5.67, 9.46, and 13.24 L min^{-1} . For each experiment, the final TOC values were measured, and the integral current efficiency was calculated using [25]

$$\phi = \frac{4FV[\text{TOC}_{(0)} - \text{TOC}_{(t)}]}{IT}, \quad (4)$$

where F is the Faraday constant with a value of $96,485 \text{ C mol}^{-1}$, V is the solution volume (L), I is the current

applied (A), and t is the time of electrolysis (s), which for these experiments was 180 minutes.

For electro-Fenton experiments, H_2O_2 generation was achieved using RVC as the cathode, DSA as the anode, and a blank solution as the electrolyte applying a constant current density. This value was determined by varying the current density until reaching the electrode potential determined by the microelectrolysis experiments, which was within $-1.15 \leq E \leq -0.95 \text{ V/SHE}$. The RVC cathode was supported on a stainless steel plate (current feeder) using conductive carbon paint glue (SPI supplies™).

Prior to starting the EF experiments, each solution was aerated for 60 min to be saturated with O_2 and acidified with 1 M H_2SO_4 to reach a pH of 3. As an initial step, the concentration of H_2O_2 generated in the blank solution was monitored. For the case of H_2O_2 production in the synthetic solution (in presence of TCMTB), it was not possible to measure its concentration using the colorimetric method because the organic compound caused interference. To determine the current density to be applied to the synthetic solution, the same methodology was used; subsequently, the Fenton reaction was promoted by the addition of 0.5 mM Fe^{2+} , which is a similar concentration to that reported by other studies Peralta et al. [15] and Pérez et al. [28], where it was shown mineralization percentages of around 50%.

For the anodic oxidation tests, a BDD was used as the anode and a stainless steel plate was used as the cathode, applying a constant current density that enabled control of the potential at the anode to obtain $(\text{OH})\text{BDD}$.

3. Results and Discussion

3.1. Microelectrolysis Studies of the Electro-Fenton Process. Typical sampled current density (j -E) curves constructed from current density transients (not shown) are illustrated in Figure 2. The j -E curves were obtained at different constant potential pulses and sampling times from 1 to 30 s, using a vitreous carbon electrode for both the blank solution (continuous lines) and the synthetic solution (semi-continuous and dashed lines).

The curves for the blank solution exhibit three electrochemical processes: Ia electrochemical generation of H_2O_2 from -0.95 to -1.15 V/SHE , (2); IIa electrochemical generation of water from -1.35 to -1.5 V/SHE , (5); and IIIa water reduction below -1.65 V/SHE , (6).



When the organic compound was added (semi-continuous and dashed lines), a new process Ib is observed at potentials from -0.33 to -0.66 V/SHE , which is related to TCMTB but it does not seem to depend on concentration. Then, a similar Ia process is observed at the same potential region observed for the blank solution (-0.95 to -1.15 V); however, TCMTB seems to favor the electrochemical production of H_2O_2 given that the current density is enhanced as the concentration of this organic compound is increased (from 0.035 to 0.07 M). At potentials around -1.36 V/SHE , the

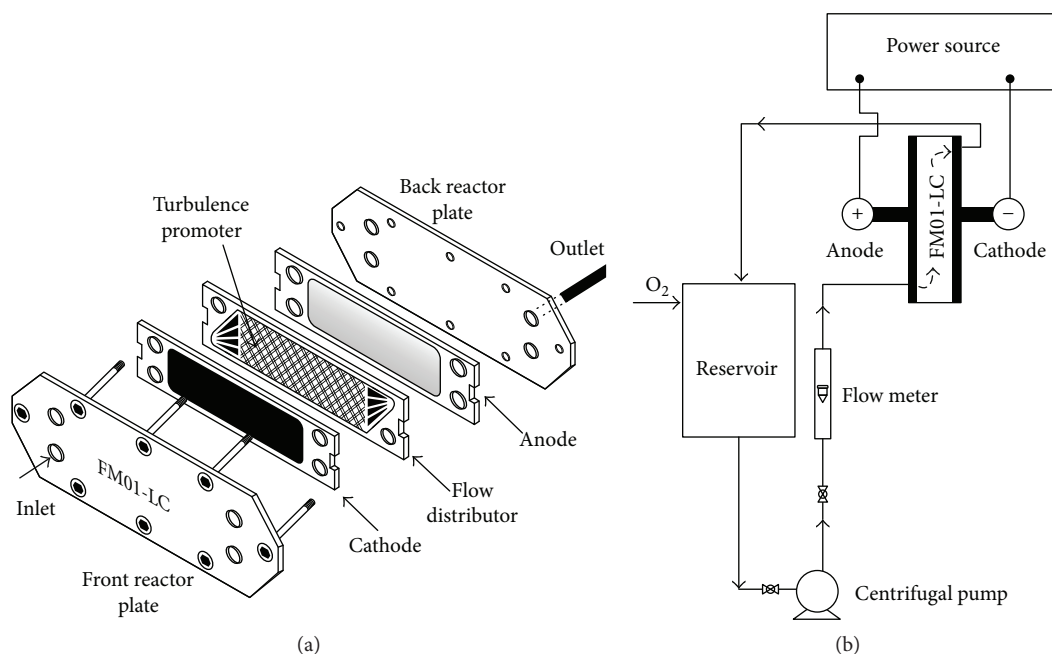


FIGURE 1: (a) Expanded view of the FM01-LC cell in the undivided mode. (b) Electrical and flow circuits for the electrochemical flow experiments.

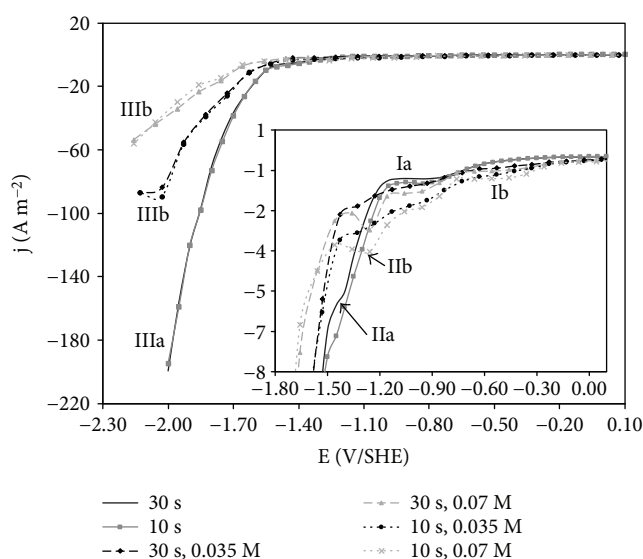


FIGURE 2: Typical j - E curves obtained by sampling current density at different times from current transients obtained at potential pulses between $-2 \text{ V} < E < 0.1 \text{ V}$ using a vitreous carbon RDE in a blank solution (NaCl 0.02 M and Na_2SO_4 0.03 M, pH 3; continuous lines) and in a synthetic solution (0.02 M NaCl and 0.03 M Na_2SO_4 , pH 3, 0.07 M TCMTB—semi-continuous lines; 0.035 M TCMTB—dashed lines). The inset shows an enhanced view. $A_{\text{RDE}} = 0.196 \text{ cm}^2$.

observed peak (IIb) corresponds to a two-electron reduction process by molecule of TCMTB as reported [4].

Likewise, the reduction of water is shifted to more negative potentials (IIIb), as TCMTB concentration is increased. It is observed that for the two types of solutions, with and without TCMTB, the current density for all of the processes

decreases as the sampling time increases, indicating a mass transport limitation. Moreover, in Figure 2, current density plateaus appeared for the process Ia, which decreased relative to the sampling time, indicating that this process (electrochemical production of H_2O_2) is limited by diffusion.

The anodic processes on the DSA electrode in the blank solution and the synthetic solution were evaluated (Figure 3), and the obtained curves showed that in both solutions, the oxidation becomes important at potentials above 1.4 V/SHE. The low currents obtained in the presence of TCMTB, with respect to blank solution, suggest that in addition to the oxidation processes, part of the energy is also being used for the possible oxidation of the compound. Thus, the oxidation process in the synthetic solution might include the oxidation of hydrogen peroxide, chloride to produce active chlorine, TCMTB with anodically electrogenerated species, and the OER (oxygen evolution reaction); therefore, a careful potential control during the process becomes important [29, 30].

3.2. Microelectrolysis Studies of Anodic Oxidation on the BDD Electrode. A voltammetric study of the cathodic reactions on stainless steel shows only the reduction of the medium from -1.5 V/SHE for both solutions (Figure 4). No sign of TCMTB reduction was observed. A comparison of the results obtained for the synthetic solution on vitreous carbon (Figure 2) and on stainless steel (Figure 4) revealed that the reduction of water in the first case occurred at more negative potentials. This result indicates that the use of stainless steel as a cathode for this system could decrease the cell potential.

Figure 5 shows the curves of current density versus anodic potential pulse on the BDD in different solutions: (a) 1 M HClO_4 , (b) blank solution, and (c) synthetic solution. In addition, Figure 5 shows a Tafel plot for the HClO_4 media, revealing that the current density increases as a function of

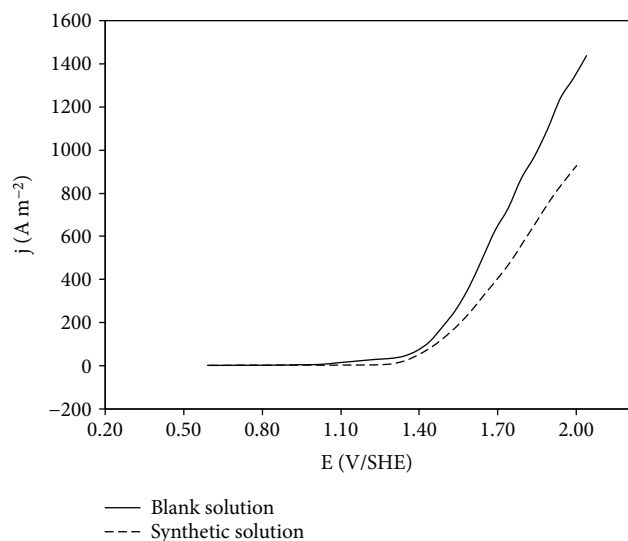


FIGURE 3: Typical j - E curves obtained by sampling current density at different times from typical current transients obtained at potential pulses between $0.5 \text{ V} < E < 2 \text{ V}$ using a DSA electrode in a blank solution (NaCl 0.02 M and Na_2SO_4 0.03 M , pH 3; continuous lines) and in a synthetic solution (0.07 M TCMTB, 0.02 M NaCl and 0.03 M Na_2SO_4 , pH 3; dashed lines). $A_{\text{RDE}} = 0.09621 \text{ cm}^2$.

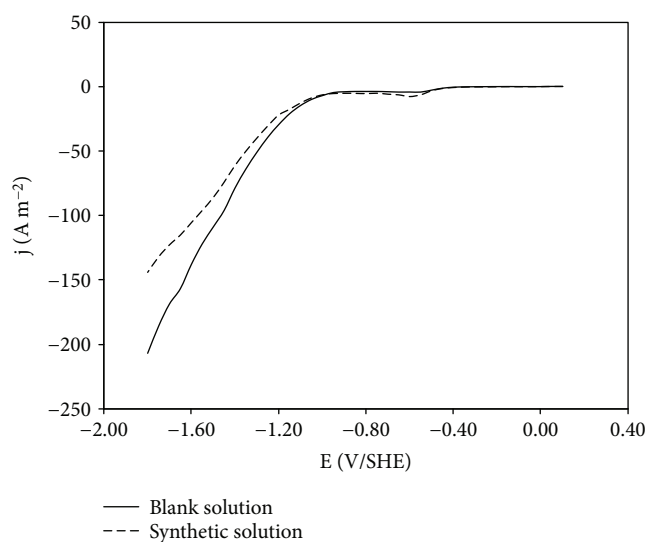


FIGURE 4: Typical j - E curves obtained by sampling current density at different times from typical current transients obtained at potential pulses between $-1.8 \text{ V} < E < 0.1 \text{ V}$ using a stainless steel electrode in a blank solution (NaCl 0.02 M and Na_2SO_4 0.03 M , pH 3; continuous lines) and in a synthetic solution (0.07 M TCMTB, 0.02 M NaCl , and 0.03 M Na_2SO_4 , pH 3; dashed lines). $A_{\text{RDE}} = 0.196 \text{ cm}^2$.

the imposed potential, which shows that detection of the faradaic current began above 2.3 V , which is consistent with the response of the BDD because this type of electrode requires higher overpotentials to oxidize water [25].

The Tafel slope from Figure 5(a) (insert) was evaluated over a potential range of $2.3 \leq E \leq 2.75 \text{ V/SHE}$, and a value of $290 \text{ mV decade}^{-1}$ was observed, which was similar to that reported by Michaud et al. [17], who determined a value of

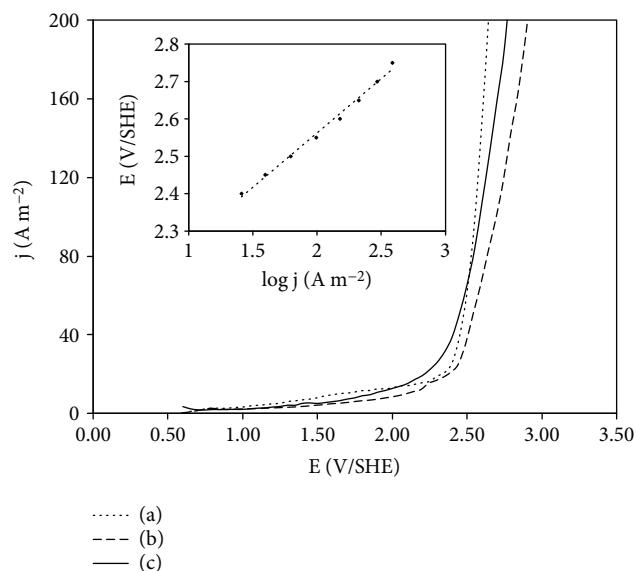
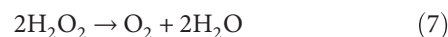


FIGURE 5: Typical j - E curves obtained by sampling current density at different times from typical current transients obtained at potential pulses between $0.6 \text{ V} < E < 3 \text{ V}$ using a BDD RDE for (a) 1 M HClO_4 , (b) 0.02 M NaCl and 0.03 M Na_2SO_4 at pH 3, and (c) 0.07 M TCMTB in 0.02 M NaCl and 0.03 M Na_2SO_4 at pH 3. The inset shows the Tafel plot for j - E curves in (a). $A_{\text{RDE}} = 0.031416 \text{ cm}^2$.

$250 \text{ mV decade}^{-1}$ over a potential range of $2.4 \leq E \leq 2.9 \text{ V/SHE}$ in which the water oxidation was a one-electron process and the hydroxyl radical formation occurred according to (3). An analysis of the Tafel slopes over the potential range of $2.3 \leq E \leq 2.6 \text{ V}$ for the curves in Figures 5(b) and 5(c) (not shown) exhibited similar values in all cases. In addition, a certain amount of TCMTB adsorption on the BDD surface could be present in Figure 5(c), as indicated by the decrease in the current density. However, TCMTB would be oxidized through $(\cdot\text{OH})\text{BDD}$ over the interval of $2.3 \leq E \leq 2.75 \text{ V/SHE}$ in addition to the active chlorine produced on the BDD surface, which will be discussed later.

3.3. Comparison between the Electrochemical Degradation of TCMTB by Electro-Fenton and by Anodic Oxidation on a BDD. A 2.4 mA cm^{-2} cathodic current density was applied to the RVC in the FM01-LC reactor to maintain the electrode potential over the range of $-0.95 \leq E \leq -1.15 \text{ V/SHE}$ and to promote the electrochemical generation of H_2O_2 on the RVC in the blank solution. As it is shown in Figure 6, the H_2O_2 concentration increases linearly with the volumetric flow rate over the first 30 min, and then it decreases for a short time; this behavior is repeated. This result is attributed to the instability of the H_2O_2 molecule, which is accompanied by its exothermic decomposition to oxygen and water, as follows [31]:



At room temperature (ca. 23°C), the rate of decomposition is slow; however, as the temperature increases, the rate of decomposition also increases [32]; in this study, the batch mode employed provoked a temperature solution of 60°C ,

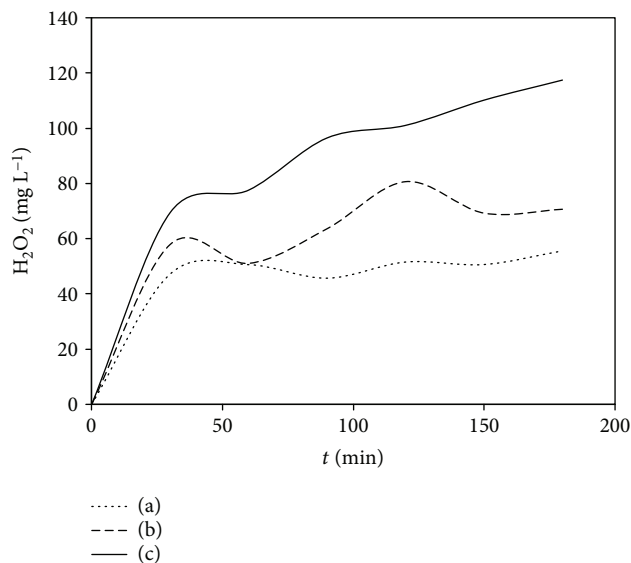
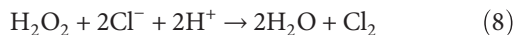


FIGURE 6: Influence of the volumetric flow rate on electrochemical generation of H_2O_2 on the RVC cathode fitted in the FM01-LC reactor. Electrolyte: 0.02 M NaCl and 0.03 M Na_2SO_4 at pH 3. $A_{\text{RVC}} = 125.95 \text{ cm}^2$, $A_{\text{stainless steel}} = 64 \text{ cm}^2$. 2.4 mA cm^{-2} . (a) 5.67 L min^{-1} , (b) 9.46 L min^{-1} , and (c) 13.24 L min^{-1} .

because of fluid recirculation. In addition, hydrogen peroxide could react with the chloride ions in solution [30], resulting in the formation of chlorine gas and water (8), which would explain the 8% decrease in the chloride concentration in all of the experiments using the blank solution.



Similar to other studies [33], the results obtained in this work showed that there is a mass transport limitation during cathodic H_2O_2 production, which decreases its concentration. However, as it has been reported even with the lowest H_2O_2 concentration (45 mg L^{-1} , $Q_v = 5.6 \text{ L min}^{-1}$) achieved, it is possible to get an adequate Fenton reaction performance [31].

The current efficiency obtained for the electrochemical generation of H_2O_2 in RVC is shown in Table 1, demonstrating that the current efficiency increases as the volumetric flow increases. This result is attributed to the decrease in the resistance to mass transfer because the convection process is favored.

For the electro-Fenton studies, a current density of 2.8 mA cm^{-2} was maintained ($-0.65 \leq E \leq -0.8 \text{ V}$) using the synthetic solution (0.07 M TCMTB, 0.03 M Na_2SO_4 , and 0.02 M NaCl at pH 3) and using 0.5 mM Fe^{2+} . The presence of Fe^{2+} allows the generation of the homogeneous $\cdot\text{OH}$ radical. According to Figure 7, TCMTB degradation is possible given that a decrease in absorbance is observed from 2.2 to 1.5 ($\lambda = 290 \text{ nm}$) at $Q_v = 5.67 \text{ L min}^{-1}$ in 180 min.

For the anodic oxidation, the BDD anodic potential was maintained between $2.3 \leq E \leq 2.6 \text{ V}$ (a potential range over which BDD($\cdot\text{OH}$) is generated) by setting the current density to 6.8 mA cm^{-2} . All of the electrolysis experiments were

TABLE 1: Current efficiencies for electrochemical generation of H_2O_2 at different volumetric flows ($j = 2.4 \text{ mA cm}^{-2}$).

$Q_v (\text{L min}^{-1})$	Current efficiency (%)
5.67	24
9.46	32
13.24	51

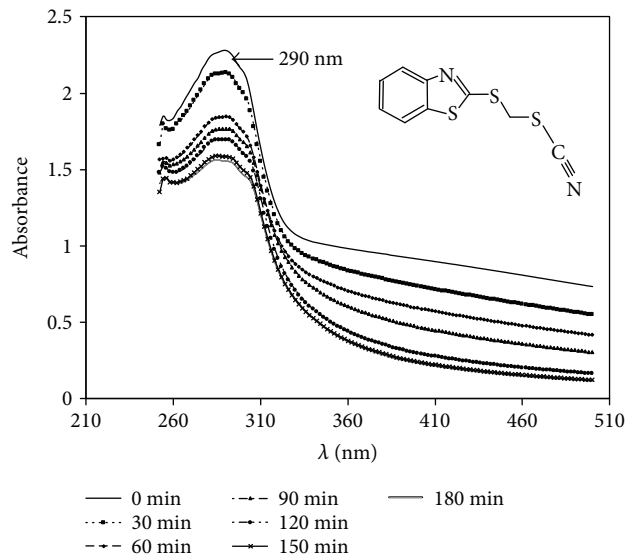


FIGURE 7: Change in the UV-vis spectra of TCMTB as a function of electrolysis time by the electro-Fenton process in the FM01-LC reactor equipped with an RVC cathode and DSA. Electrolyte: 0.02 M NaCl, 0.03 M Na_2SO_4 , and 0.5 mM Fe^{2+} at pH 3. $Q_v = 5.67 \text{ L min}^{-1}$, 2.8 mA cm^{-2} . $A_{\text{RVC}} = 125.95 \text{ cm}^2$, $A_{\text{DSA}} = 64 \text{ cm}^2$.

performed in an undivided FM01-LC reactor, and the electrode potential was controlled over the range in which the desirable electrochemical processes are favored. Figure 8 shows that the turbidity (absorbance) decreases with time in all of the experiments ($\lambda = 290 \text{ nm}$). For the electro-Fenton process, it is observed that by increasing the feed rate, a higher rate of TCMTB degradation is achieved. As previously discussed, an increase in the flow rate increases the H_2O_2 concentration; thus, the amount of $\cdot\text{OH}$ radicals also increases in the bulk solution, favoring the degradation of the TCMTB molecules. A similar phenomenon can be observed in the anodic oxidation process in which an increase in the flow rate also increases the rate of TCMTB degradation. This phenomenon is explained in terms of the effect of increasing the volume flow on the transport of the organic compound from the bulk solution to the electrode surface where radicals are physisorbed BDD($\cdot\text{OH}$). A comparison of the EF and AO processes shows that higher percentages of degradation are achieved by anodic oxidation (81%) because the BDD($\cdot\text{OH}$) radical is constantly produced on the BDD surface. In EF, the production of homogeneous radicals is limited by the amount of H_2O_2 available for the process because H_2O_2 reacts not only with Fe^{2+} but also with chloride ions, in addition to undergoing its natural decomposition.

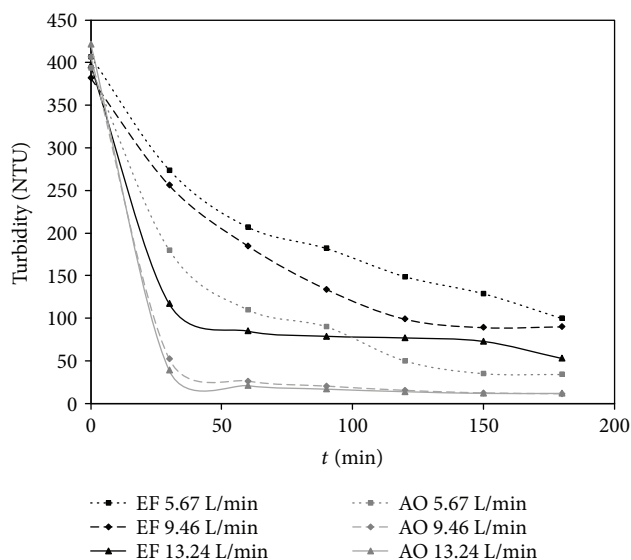
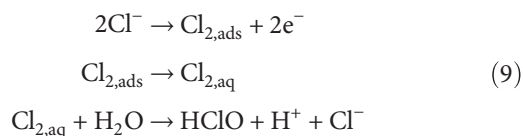


FIGURE 8: Decrease in turbidity as a function of electrolysis time measured at 290 nm during the EF process in the FM01-LC reactor equipped with an RVC cathode and DSA (at 3 mA cm^{-2} , 0.5 mM Fe^{2+}) and the AO process in the FM01-LC reactor equipped with a stainless steel cathode and BDD anode at 6.8 mA cm^{-2} . $A_{\text{RVC}} = 125.95 \text{ cm}^2$, $A_{\text{DSA}} = 64 \text{ cm}^2$, $A_{\text{stainless steel}} = 64 \text{ cm}^2$, and $A_{\text{BDD}} = 64 \text{ cm}^2$. Electrolyte: 0.07 M TCMTB in 0.02 M NaCl and $0.03 \text{ M Na}_2\text{SO}_4$.

Although the absorbance for the turbidity values decreases, the TOC values do not decrease at the same rate (Figure 9), indicating that TCMTB is degraded into simpler organic compounds, as has been reported by several authors [10]. It is important to mention that chromatographic studies might help elucidating the differences between the decrease in absorbance and TOC; however, these studies were beyond the scope of this paper. Based on the results obtained here, it is clear that for the anodic oxidation on BDD using a flow rate of 13.24 L min^{-1} , it was possible to achieve up to 57% TCMTB mineralization during the 180 minutes of electrolysis. This achievement was aided by the constant electrogeneration of BDD(OH) radicals and the favored transport of TCMTB molecules to the electrode interface.

However, chloride ions affect the percentage of mineralization because they react in a complex mechanism to produce adsorbed chlorine (although weakly sorbed at the electrode surface) and dissolved chlorine, which reacts with water and yields hypochlorous acid, as follows [30]:



These reactions could explain why the concentration of chloride ions decreases significantly in the AO experiments, as shown in Table 2. The formed hypochlorous acid could react with hydroxyl radicals to form chlorine dioxide and

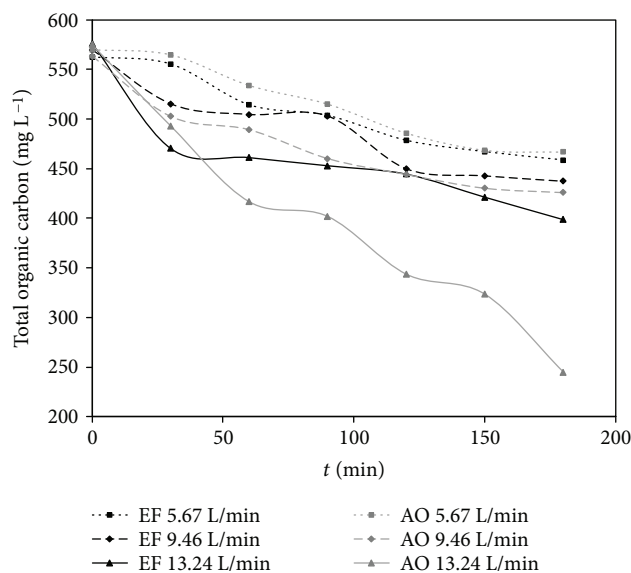
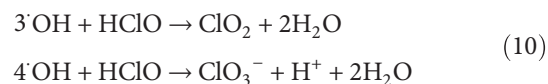


FIGURE 9: Influence of the volumetric flow rate on TOC removal during the EF and AO processes in the FM01-LC reactor. EF: 2.8 mA cm^{-2} , 0.5 mM Fe^{2+} , $A_{\text{DSA}} = 64 \text{ cm}^2$, $A_{\text{RVC}} = 125.95 \text{ cm}^2$. AO: 6.8 mA cm^{-2} , $A_{\text{BDD}} = 64 \text{ cm}^2$, $A_{\text{stainless steel}} = 64 \text{ cm}^2$. Electrolyte: 0.07 M TCMTB in 0.02 M NaCl and $0.03 \text{ M Na}_2\text{SO}_4$.

chlorate [30], thus diminishing the concentration of hydroxyl radicals and preventing higher percentages of mineralization.



According to Polcaro et al. [30], for chloride ion concentrations on the BDD anode surface, similar to those in our study, approximately 40% of the current would be used in the formation of chlorine, possibly causing the low current efficiencies observed, which are similar other reports in the literature [23]. However, the removal of chlorides was higher when the volumetric flow was increased, resulting in a major mass transport in the reactor. Moreover, the percentage of mineralization also increased due to the higher mass transport. For the case of sulfates, the concentration did not change in this study.

Table 2 shows that the current efficiency and the mineralization of TCMTB are favored by the increase of Q_v . This increase of current efficiency due to convection flow agrees well with the results reported by Panizza et al. [34]. In addition, the formation of active chlorine species can also aid the TCMTB degradation. A higher Q_v value particularly favors anodic oxidation; thus, better results are obtained than those with the electro-Fenton process. However, the consumption of energy for AO is twice that of EF.

4. Conclusions

Macroelectrolysis studies showed that anodic oxidation produces better percentages of degradation than the electro-Fenton process. This result was most likely due to the

TABLE 2: Summary of the results obtained during the different experiments.

Experiment	% removal absorbance	% removal TOC	% removal COD	% removal Cl^-	Integral current efficiency, ϕ (%)	Energy consumption (kWh m^{-3})
EF (5.67 L min^{-1})	40	18	42	8	11	0.113
EF (9.46 L min^{-1})	40	23	45	12	13	0.123
EF (13.24 L min^{-1})	47	31	72	12	18	0.116
AO (5.67 L min^{-1})	71	18	32	42	9	0.248
AO (9.46 L min^{-1})	81	24	55	46	12	0.225
AO (13.24 L min^{-1})	81	57	78	52	56	0.225

decreased H_2O_2 concentration caused by different reactions that could occur in the solution in the EF process.

Microelectrolysis studies indicated that the degradation and partial mineralization of TCMTB by anodic oxidation were achieved via hydroxyl radicals formed by the oxidation of water in the BDD electrode under galvanostatic conditions.

Electrolysis in the undivided FM01-LC reactor at different volumetric flows at a current density of 6.8 mA cm^{-2} revealed that the oxidation rate and current efficiency increased as a function of Q_v . This result demonstrates that convection flow favors the influx of TCMTB to the BDD(OH) surface, increasing its degradation.

The electrochemical transformation of TCMTB by the electro-Fenton and anodic oxidation processes could be a useful strategy for toxicity reduction.

Nomenclature

BDD:	Boron-doped diamond
COD:	Chemical oxygen demand (mol L^{-1})
DSA:	Dimensionless stable anode
F :	Faraday constant ($96,485 \text{ C mol}^{-1}$)
I :	Current applied during electrolysis (A)
j :	Current density (A cm^{-2})
Q_v :	Volumetric flow (L min^{-1})
RVC:	Reticulated vitreous carbon
TCMTB:	2-(Thiocyanomethylthio)-benzothiazole
$\text{TOC}_{(0)}$:	Initial total organic carbon (mol L^{-1})
$\text{TOC}_{(t)}$:	Total organic carbon at time t (mol L^{-1})
t :	Time of electrolysis (s)
V :	Solution volume (L)
ϕ :	Current efficiency (%).

Conflicts of Interest

The authors declare that they have no conflicts of interest.

Acknowledgments

The authors are grateful for the SEP-CONACyT grant from the National Council of Science and Technology of Mexico (CONACyT) through the Project no. 240522. Armando Vázquez would like to thank the CONACyT for the doctoral scholarship 217508. The authors also thank the financial support for the publication from SEP-PRODEP. The authors are indebted to Nubia V. Arteaga for laboratory support.

References

- [1] D. Pokhrel and T. Viraraghavan, "Treatment of pulp and paper mill wastewater – a review," *Science of The Total Environment*, vol. 333, no. 1-3, pp. 37–58, 2004.
- [2] A. Latorre, A. Rigol, S. Lacorte, and D. Barceló, "Organic compounds in paper mill wastewaters," in *The Handbook of Environmental Chemistry*, D. Barceló and A. G. Kostianoy, Eds., vol. 2 of Part O, Springer-Verlag, Berlin Heidelberg, 2005.
- [3] K. Tumirah, S. Salamah, A. Rozita, U. Salmiah, and M. A. M. Nasir, "Determination of 2-thiocyanomethylthio benzothiazole (TCMTB) in treated wood and wood preservative using ultraviolet-visible spectrophotometer," *Wood Science and Technology*, vol. 46, no. 6, pp. 1021–1031, 2012.
- [4] E. Meneses, M. Arguelho, and J. Alves, "Electroreduction of the antifouling agent TCMTB and its electroanalytical determination in tannery wastewaters," *Talanta*, vol. 67, no. 4, pp. 682–685, 2005.
- [5] United States Environmental Protection Agency, "Reregistration eligibility decision for 2-(thiocyanomethylthio) benzothiazole (TCMTB), prevention, pesticides and toxic substances (7510P), EPA739-R-05-003," 2006, October 2017, http://www3.epa.gov/pesticides/chem_search/reg_actions/reregistration/red_PC-035603_1-Aug-06.pdf.
- [6] T. Reemtsma, O. Fienh, G. Kalnowski, and M. Jekel, "Microbial transformations and biological effects of fungicide-derived benzothiazoles determined in industrial wastewater," *Environmental Science & Technology*, vol. 29, no. 2, pp. 478–485, 1995.
- [7] A. K. Adams and E. M. Warshaw, "Allergic contact dermatitis from mercapto compounds," *Dermatitis*, vol. 17, no. 2, pp. 56–70, 2006.
- [8] M. Rajabi, "2-(3,5-Dihydroxyphenyl)-6-hydroxybenzothiazole arrests cell growth and cell cycle and induces apoptosis in breast cancer cell lines," *DNA and Cell Biology*, vol. 31, no. 3, pp. 388–391, 2012.
- [9] G. Ginsberg, B. Toal, and T. Kurland, "Benzothiazole toxicity assessment in support of synthetic turf field human health risk assessment," *Journal of Toxicology and Environmental Health, Part A*, vol. 74, no. 17, pp. 1175–1183, 2011.
- [10] H. De Wever and H. Verachtert, "Biodegradation and toxicity of benzothiazoles," *Water Research*, vol. 31, no. 11, pp. 2673–2684, 1997.
- [11] H. De Wever, H. Verachtert, and P. Besse, "Microbial transformations of 2-substituted benzothiazoles," *Applied Microbiology and Biotechnology*, vol. 57, no. 5-6, pp. 620–625, 2001.
- [12] A. Al-Kadasi, A. Idris, K. Saed, and C. T. Guan, "Treatment of textile wastewater by advanced oxidation processes – a review," *Global NEST Journal*, vol. 6, pp. 222–230, 2004.

- October 2015, <http://journal.gnest.org/sites/default/files/Journal%20Papers/Al-kdasi-222-230.pdf>.
- [13] H. Särkkä, A. Bhatnagar, and M. Sillanpää, "Recent developments of electro-oxidation in water treatment – a review," *Journal of Electroanalytical Chemistry*, vol. 754, pp. 46–56, 2015.
- [14] E. Brillas, I. Sirés, and M. Oturan, "Electro-Fenton process and related electrochemical technologies based on Fenton's reaction chemistry," *Chemical Reviews*, vol. 109, no. 12, pp. 6570–6631, 2009.
- [15] J. M. Peralta-Hernández, Y. Meas-Vong, F. J. Rodríguez, T. W. Chapman, M. I. Maldonado, and L. A. Godínez, "In situ electrochemical and photo-electrochemical generation of the Fenton reagent: a potentially important new water treatment technology," *Water Research*, vol. 40, no. 9, pp. 1754–1762, 2006.
- [16] E. L. Gyenge and C. W. Oloman, "Influence of surfactants on the electro-reduction of oxygen to hydrogen peroxide in acid and alkaline electrolytes," *Journal of Applied Electrochemistry*, vol. 31, no. 2, pp. 233–243, 2001.
- [17] P. A. Michaud, M. Panizza, L. Outtara, T. Diaco, G. Foti, and C. H. Comninellis, "Electrochemical oxidation of water on synthetic boron-doped diamond thin film anodes," *Journal of Applied Electrochemistry*, vol. 33, no. 2, pp. 151–154, 2003.
- [18] C. A. Martínez-Huitle and E. Brillas, "Decontamination of wastewaters containing synthetic organic dyes by electrochemical methods: a general review," *Applied Catalysis B: Environmental*, vol. 87, no. 3–4, pp. 105–145, 2009.
- [19] C. Barrera-Díaz, P. Cañizares, F. J. Fernández, R. Natividad, and M. A. Rodrigo, "Electrochemical advanced oxidation processes: an overview of the current applications to actual industrial effluents," *Journal of the Mexican Chemical Society*, vol. 58, pp. 256–275, 2014.
- [20] J. A. Garrido, E. Brillas, P. L. Cabot, F. Centellas, C. Arias, and R. M. Rodríguez, "Mineralization of drugs in aqueous medium by advanced oxidation processes," *Portugaliae Electrochimica Acta*, vol. 25, no. 1, pp. 19–41, 2007.
- [21] G. Eisenberg, "Colorimetric determination of hydrogen peroxide," *Industrial and Engineering Chemistry, Analytical Edition*, vol. 15, no. 5, pp. 327–328, 1943.
- [22] A. D. Eaton, L. S. Clesceri, E. W. Rice, and A. E. Greenberg, *Standard Methods for the Examination of Water and Wastewater*, APHA, AWWA, & WEF, Washington, USA, 21st edition, 2005.
- [23] J. L. Nava, I. Sirés, and E. Brillas, "Electrochemical incineration of indigo. A comparative study between 2D (plate) and 3D (mesh) BDD anodes fitted into a filter-press reactor," *Environmental Science and Pollution Research*, vol. 21, no. 14, pp. 8485–8492, 2014.
- [24] A. Vázquez, J. L. Nava, R. Cruz, I. Lázaro, and I. Rodríguez, "The importance of current distribution and cell hydrodynamic analysis for the design of electrocoagulation reactors," *Journal of Chemical Technology and Biotechnology*, vol. 89, no. 2, pp. 220–229, 2014.
- [25] J. L. Nava, F. Núñez, and I. González, "Electrochemical incineration of p-cresol and o-cresol in the filter-press-type FM01-LC electrochemical cell using BDD electrodes in sulfate media at pH 0," *Electrochimica Acta*, vol. 52, no. 9, pp. 3229–3235, 2007.
- [26] E. Butrón, M. E. Juárez, M. Solis, M. Teutli, I. González, and J. L. Nava, "Electrochemical incineration of indigo textile dye in filter-press-type FM01-LC electrochemical cell using BDD electrodes," *Electrochimica Acta*, vol. 52, no. 24, pp. 6888–6894, 2007.
- [27] M. Griffiths, C. Ponce de León, and F. Walsh, "Mass transport in the rectangular channel of a filter-press electrolyzer (the FM01-LC reactor)," *AIChE Journal*, vol. 51, no. 2, pp. 682–687, 2005.
- [28] T. Pérez, S. García-Segura, A. El-Ghenymy, J. L. Nava, and E. Brillas, "Solar photoelectro-Fenton degradation of the antibiotic metronidazole using a flow plant with a Pt/air-diffusion cell and a CPC photoreactor," *Electrochimica Acta*, vol. 165, pp. 173–181, 2015.
- [29] E. Petrucci, D. Montanaro, and L. Di Palma, "A feasibility study of hydrogen peroxide electrogeneration in seawater for environmental remediation," *Chemical Engineering Transactions*, vol. 28, pp. 91–96, 2012.
- [30] A. M. Polcaro, A. Vacca, M. Mascia, S. Palmas, and J. Rodríguez Ruiz, "Electrochemical treatment of waters with BDD anodes: kinetics of the reactions involving chlorides," *Journal of Applied Electrochemistry*, vol. 39, no. 11, pp. 2083–2092, 2009.
- [31] A. Alvarez-Gallegos and D. Pletcher, "The removal of low level organics via hydrogen peroxide formed in a reticulated vitreous carbon cathode cell, Part 1. The electrosynthesis of hydrogen peroxide in aqueous acidic solutions," *Electrochimica Acta*, vol. 44, no. 5, pp. 853–861, 1998.
- [32] Z. Qiang, J. H. Chang, and C. P. Huang, "Electrochemical generation of hydrogen peroxide from dissolved oxygen in acidic solutions," *Water Research*, vol. 36, no. 1, pp. 85–94, 2002.
- [33] K. Cruz-González, O. Torres-López, A. García-León et al., "Determination of optimum operating parameters for Acid Yellow 36 decolorization by electro-Fenton process using BDD cathode," *Chemical Engineering Journal*, vol. 160, no. 1, pp. 199–206, 2010.
- [34] M. Panizza, M. Delucchi, and G. Cerisola, "Electrochemical degradation of anionic surfactants," *Journal of Applied Electrochemistry*, vol. 35, no. 4, pp. 357–361, 2005.

Research Article

The Effect of Microcrack Length in Silicon Cells on the Potential Induced Degradation Behavior

Xianfang Gou,^{1,2} Xiaoyan Li,¹ Shaoliang Wang,³ Hao Zhuang^{ID},² Xixi Huang,²
and Likai Jiang²

¹Beijing University of Technology, Beijing 100124, China

²CECEP Solar Energy Technology (Zhenjiang) Co., Ltd., Zhenjiang 212132, China

³Beijing Jiaotong University, Beijing 100044, China

Correspondence should be addressed to Hao Zhuang; zhuanghao@cecsec.cn

Received 26 October 2017; Accepted 9 January 2018; Published 18 February 2018

Academic Editor: Reyna Natividad-Rangel

Copyright © 2018 Xianfang Gou et al. This is an open access article distributed under the Creative Commons Attribution License, which permits unrestricted use, distribution, and reproduction in any medium, provided the original work is properly cited.

The presence of microcracks may lead to loss in the module output power and safety hazard of the module. This paper investigated whether the existed microscopic microcracks in cells will facilitate the PID behavior. Cells with different degrees of microcracks were fabricated into small modules to undergo the simulated PID test. The *I*-*V* performance and EL images of the modules were characterized before and after the PID test. The obtained results demonstrate that with the increase in the microcracked area or length, the modules would show a more serious PID behavior. The mechanism of this microcrack length-related degradation under high negative bias was proposed.

1. Introduction

Microcracks refer to the invisible cracks that cannot be easily perceived by the naked eye when a wafer is subjected to mechanical or thermal stress. There are several stages related to the generation of microcracks [1–8]: (i) the cutting process of an ingot or crystal bar due to a local uneven force; (ii) the cell or module fabrication process due to external factors; (iii) improper module installation; and (iv) the power plant operation period due to external factors such as wind or ground subsidence. Since the microcracked silicon wafer is not completely broken apart, microcracks can be detected only through the electroluminescence (EL) test [9]. The presence of microcracks may cause part of the cells to be inactive, leading to the loss in the output power and safety hazard of the module [9].

In a crystalline silicon cell, current is collected from fingers to the busbar and then through the string connector to the output from the junction box. The generated current of a cell is proportional to the cell active area. The inactive area can be judged by whether the current collection from the finger to the busbar is blocked or not. According to the inactive area of the cell, the number of microcracked cells, and the

impact on the output power of modules, microcracks can be divided into three categories: microscopic microcrack, general microcrack, and serious microcrack. Modules with seriously microcracked cells generally need to be replaced in a power station, and those with general microcracks will not affect the power output in the initial stage and will be disposed according to their working condition. Microscopic microcracks generally refer to the microcracks that are single or partial flakes located not at the busbars and basically do not cause failure of the area, and the power degradation of the module with microscopic microcracks should meet the industry standard (i.e., the first-year power degradation less than 2.5%). Therefore, it becomes necessary to develop the means of quantifying the risk of power loss in PV modules with cracked solar cells to ensure their output during the lifetime, and some standards may be discussed and set in the future.

In solar power stations, it is known that modules must be connected in series and parallel to build arrays to meet the load requirements. The connection of single modules in series will produce a high voltage relative to the plane of zero potential (ground). The efficiency of the modules may probably degrade due to this high negative bias under heat and

TABLE 1: Electrical performance of five groups of solar cells before and after the PID test.

Sample	PID test	Voc (V)	Isc (A)	FF (%)	Eta (%)	Rsh (Ω)	Irev2 (A)	Degradation
A	Before	0.64	9.511	73.5	18.38	187.78	0.081	2.61%
	After	0.635	9.425	72.8	17.9	11.03	2.057	
B	Before	0.64	9.575	73.67	18.55	57.83	0.171	32.02%
	After	0.617	8.675	57.37	12.61	0.44	12.277	
C	Before	0.639	9.536	73.58	18.43	57.09	0.4	33.80%
	After	0.576	8.268	62.31	12.2	0.35	12.277	
D	Before	0.639	9.502	73.56	18.36	78.94	0.117	37.53%
	After	0.602	8.505	54.49	11.47	0.33	12.277	
E	Before	0.64	9.449	73.79	18.33	75.15	0.396	49.32%
	After	0.587	8.28	46.52	9.29	0.21	12.28	

humidity, which is known as the potential induced degradation, PID [10, 11]. A number of factors [12–21], such as stacking faults in the silicon wafer, refractive index of the antireflection coating, resistance of the encapsulant material, and design of the power station, have been found and demonstrated to be related with the PID behavior. However, it has never been investigated whether the existed microscopic microcracks in cells will facilitate the PID behavior of modules.

Herein, we fabricated a series of small modules using solar cells with different microcrack lengths. The small modules were then kept in a climate chamber with constant temperature and humidity for the PID simulation test. The I - V curves and EL images of the small modules were measured before and after the PID test. The obtained results demonstrate that with the increase in the microcrack length, the modules would show a more serious PID behavior. Our work reveals the underlying relationship between the microcrack length in cells and PID of modules.

2. Materials and Methods

Conventional cells with different microcrack lengths were selected via EL and divided into 5 groups with 10 cells each group according to the microcrack length: A (0 cm), B (0–0.9 cm), C (1–2 cm), D (4–5 cm), and E (9–10 cm). The length was measured by the maximum length of the cracked area. Then the cells were fabricated into small modules using the normal process and kept in a climate chamber with constant temperature and humidity for the PID simulation test, after which the I - V and EL of the small modules were measured and analyzed.

3. Results and Discussion

The power loss in crystalline silicon-based photovoltaic modules due to microcracks was investigated by Köntges et al. in 2011 [9]. They analyzed the direct impact of microcracks on the module power and the consequences after artificial aging. The approach of artificial aging they adopt was 200 humidity freeze cycles. The main focus of their research is on the degradation of power due to crack propagation after artificial aging.

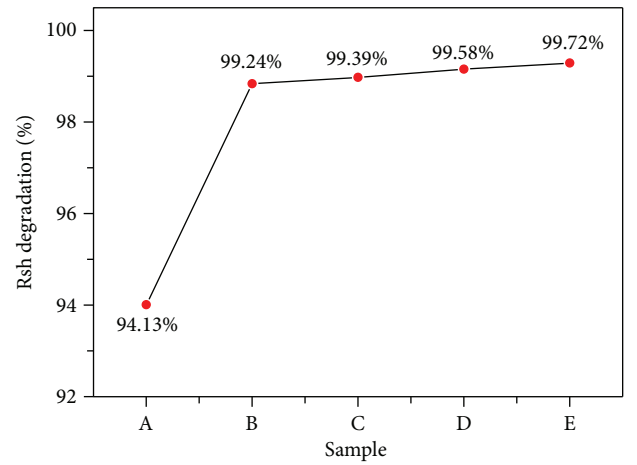


FIGURE 1: Rsh variations of five sample groups with different microcrack lengths after the PID test.

Herein, to investigate the effect of microcrack length in silicon cells on the potential induced degradation behavior, in our work, five groups of cells with different degrees of microcracks were fabricated into small modules. After performing the PID test in an environmental test chamber (85°C, 85% RH), the electrical performance was measured using a Pasan tester. The obtained data are listed in Table 1.

As can be seen from Table 1, after the PID test, degradation was observed for the open-circuit voltage (Voc), short-circuit current (Isc), and fill factor (FF). Figure 1 shows the trend of degradation with microcrack length. It can be clearly noted that with the increase in the microcrack length, a larger degradation would occur. The decrease of the parallel resistance (Rsh) is 94.13%, 99.24%, 99.39%, 99.58%, and 99.72% for groups A to E, respectively. These results demonstrate that the longer the microcrack length, the faster the Rsh degrades after the PID test, which increases the probability of providing the shunt for the current, and the trace current Irev2 is greatly improved after the PID test.

From Table 1, it can be also seen that after the PID test, the module efficiency also exhibits a larger degradation with the increase of the microcrack length. The power degradation of module group A without a microcrack is 2.61% after the test, which meets the <5% standard for IEC 62804. Modules

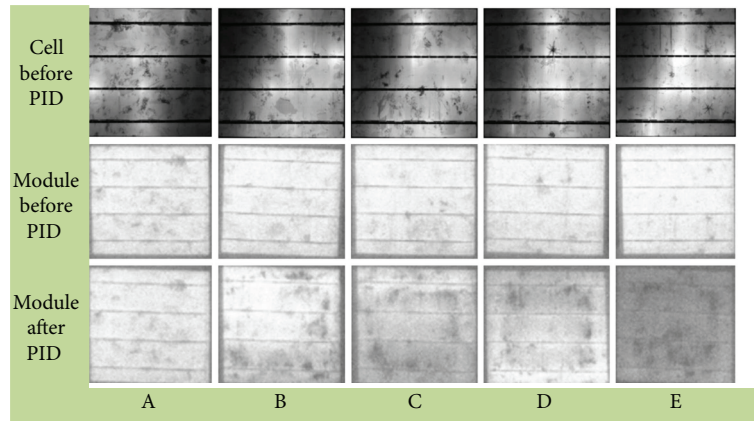
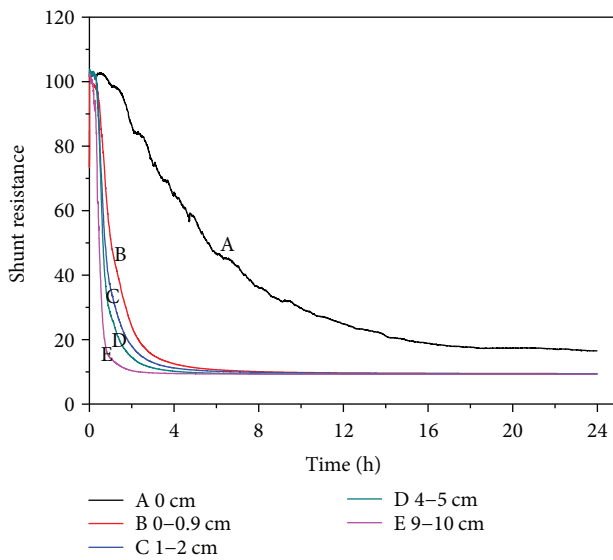


FIGURE 2: EL images of five groups with different microcrack lengths after the PID test.

FIGURE 3: Plot of the R_{sh} versus PID testing time of five groups of solar cells.

of groups B, C, D, and E degraded by 32.02%, 33.80%, 37.53%, and 49.32%, respectively, showing a serious PID phenomenon.

It is shown that with increasing microcrack length, positive charges are easy to gather on the surface of the cell under long-term high bias and high-temperature and humidity conditions. Under the in-built electric field, a large amount of negative charges is attracted to the surface. If a microcrack then exists in the wafer, it can provide a diversion channel for the surface charges, leading to current leakage, which decreases the efficiency of the cell. The larger the microcracked area is, the more leakage occurs, and the greater the efficiency declines.

Figure 2 shows the EL pictures of the cells and small modules before and after the PID test. By comparing these EL pictures, we can find that with the increase in the microcrack length, the EL of the cells after the PID test gradually tarnishes, which is consistent with the degradation trend of modules.

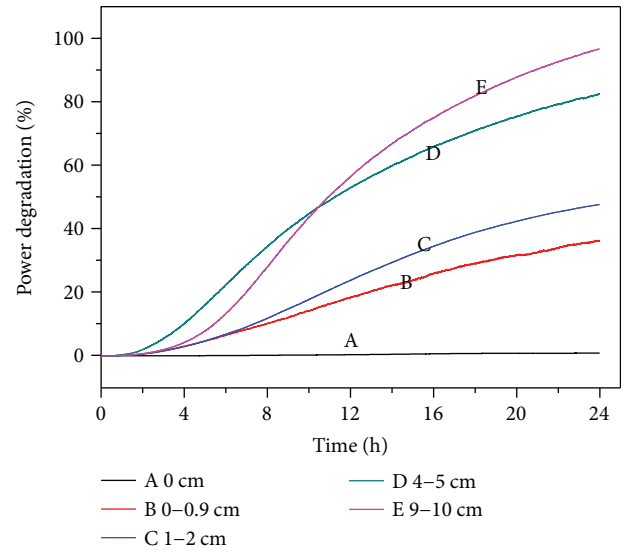
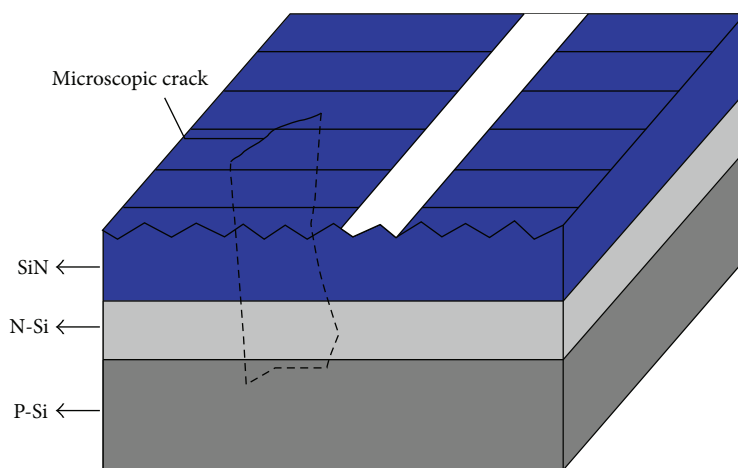


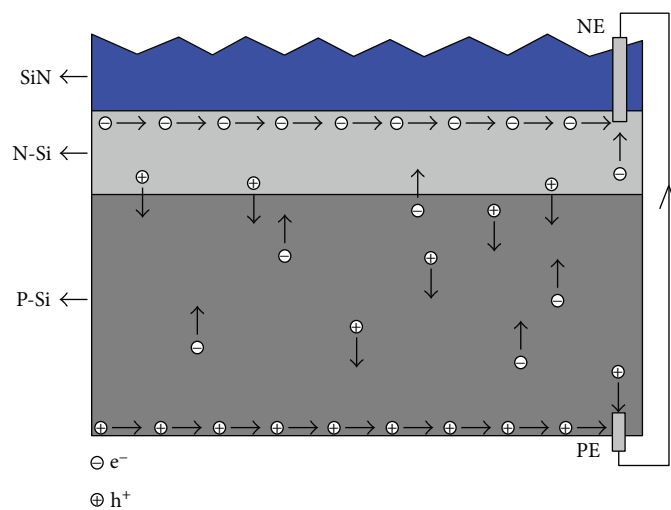
FIGURE 4: Plot of the efficiency degradation versus PID testing time of five groups of solar cells.

To further verify the obtained results, PIDcon equipment was used to simulate the anti-PID performance of the five sample groups. The parallel resistance change of the samples with test time is shown in Figure 3. It can be seen from the figure that the parallel resistance of sample group A (i.e., without microcrack) first decreased quickly in the initial 12 hours and gradually became steady after that. The R_{sh} of the B, C, D, and E sample groups decreased rapidly within the initial two hours of the test, especially for group E. After the initial two-hour rapid decrease, it slowly became stable and constant till the end of this test. These results further demonstrate that the increasing microcrack length generally gives a faster decrease rate of parallel resistance after the PID test, indicating a more serious current leakage. Figure 4 shows the PID degradation of modules with different microcrack lengths, and modules are found to degrade less with decreasing microcrack length.

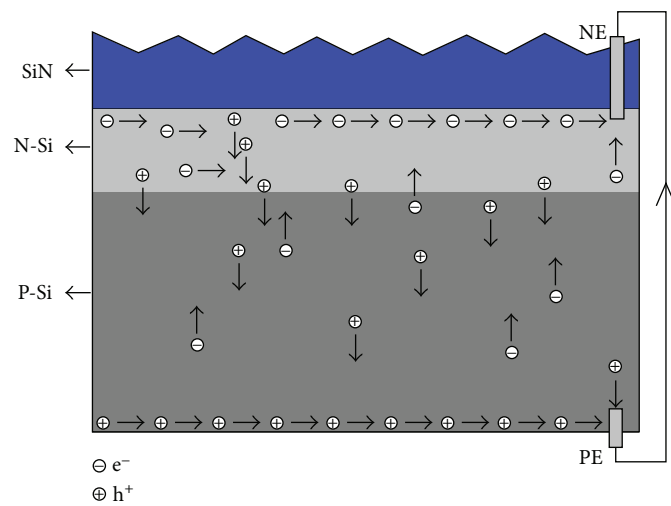
Based on these results, the mechanism of the effect of the wafer microcrack defect on PID is proposed and depicted in



(a)



(b)



(c)

FIGURE 5: Continued.

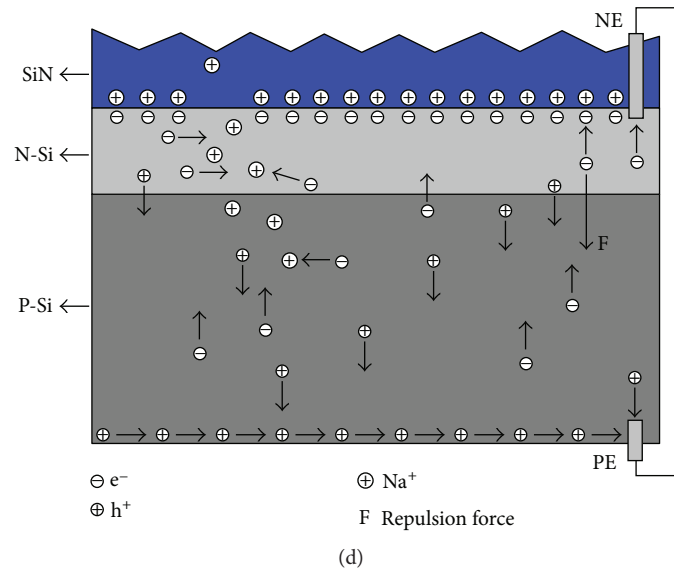


FIGURE 5: Schematic diagrams of the effect of microcracks of silicon wafer on PID: (a) diagram of part of solar cells; (b) conductive diagram of solar cells without microcracks; (c) conductive diagram of solar cells with microcracks; (d) PID conductive diagram of solar cells with microcracks.

Figure 5. The overall crack interface is shown as the dotted area. Figure 5(a) is a scheme of part of the cell, in which the microcrack is located in the cell grid area. The microcrack vertically penetrates through the PN junction. Figure 5(b) is a schematic diagram of the normal crack-free cell. Under light irradiation, photon excites the motion of nonequilibrium carriers in the silicon wafer, and the minorities (i.e., electrons) of the P-type silicon region move to the N-type silicon region. The holes, the minorities of the N-type silicon region, move toward the P-type silicon region and converge through the silver finger to the busbar to generate current. Figure 5(c) is the scheme of charge flow in a microcracked cell. During the lateral or longitudinal movement of electrons and holes, the presence of a microcrack will block the movement of electrons and holes, impeding the transportation of electrons and hence reducing the output current. Due to the limited microcrack area, the degradation in output power is not significant enough to be observed. Figure 5(d) is the scheme of the PID mechanism in a microcracked cell, when the cell is under high temperature/humidity and negative bias; the sodium ions migrate from the glass to the silicon nitride film. Therefore, sodium ions gradually accumulate at the SiN_x/Si interface. In the microcrack-free region, the positive charges of sodium ions will attract a large amount of electrons to the silicon surface, which reduces the convergence of electrons to the silver electrodes.

On the other hand, due to the accumulation of negative charges on the silicon surface, the fixed negative charges repel the electrons moving from the P-type silicon side and simultaneously attract the positive charges, thus reducing the number of electrons and holes. In the microcracked region, while the movement of electrons and holes are hindered, sodium ions are impeded when arriving at the silicon nitride layer and the P- and N-microcracked interface regions. Therefore, the sodium ions are easy to gather at

the edge of the microcracked region to capture the electrons and become the recombination center for the minorities. When more and more sodium ions accumulate in the microcracked region, the collection of current is largely reduced, leading to current leakage.

4. Conclusions

This paper focused on the effect of existing microscopic microcracks in cells on the potential induced degradation behavior. Cells with different degrees of microcrack were fabricated into small modules to undergo a simulated PID test. The I - V performance and EL images of the modules were characterized before and after the PID test. The obtained results indicated that with the increase in the microcrack length, the modules would show a more serious PID behavior. The mechanism of this microcrack length-related degradation under high negative bias was proposed.

Conflicts of Interest

The authors declare that there is no conflict of interests regarding the publication of this paper.

Acknowledgments

This study was financially supported by the research program 13RD1 CECEP (Zhenjiang).

References

- [1] V. A. Popovich, A. Yunus, M. Janssen, I. M. Richardson, and I. J. Bennett, "Effect of silicon solar cell processing parameters and crystallinity on mechanical strength," *Solar Energy Materials & Solar Cells*, vol. 95, no. 1, pp. 97–100, 2011.

- [2] M. Demant, S. Rein, J. Krisch et al., "Detection and analysis of micro-cracks in multicrystalline silicon wafers during solar cell production," in *Proceedings of the 37th IEEE Photovoltaic Specialists Conference*, Seattle, 2011.
- [3] J. I. Mülken, U. A. Yusufoglu, A. Safiei et al., "Impact of micro-cracks on the degradation of solar cell performance based on two-diode model parameters," *Energy Procedia*, vol. 27, pp. 167–172, 2012.
- [4] H. Kim, P. Sungeun, B. Kang et al., "Effect of texturing process involving saw-damage etching on crystalline silicon solar cells," *Applied Surface Science*, vol. 284, pp. 133–137, 2013.
- [5] I. Berardone, M. Corrado, and M. Paggi, "A generalized electric model for mono and polycrystalline silicon in the presence of cracks and random defects," *Energy Procedia*, vol. 55, pp. 22–29, 2014.
- [6] S. S. Ko, C. S. Liu, and Y. C. Lin, "Optical inspection system with tunable exposure unit for micro-crack detection in solar wafers," *Optik- International Journal for Light and Electron Optics*, vol. 124, no. 19, pp. 4030–4035, 2013.
- [7] V. T. Dragišić, "Silicon solar wafers: quality control and improving the mechanical properties," *Procedia Engineering*, vol. 117, pp. 459–464, 2015.
- [8] K. O. Davis, M. P. Rodgers, G. Scardera et al., "Manufacturing metrology for c-Si module reliability and durability part II: cell manufacturing," *Renewable and Sustainable Energy Reviews*, vol. 59, pp. 225–252, 2016.
- [9] M. Köntges, I. Kunze, S. K. Schröder, X. Breitenmoser, and B. Bjørneklett, "The risk of power loss in crystalline silicon based photovoltaic modules due to micro-cracks," *Solar Energy Materials & Solar Cells*, vol. 95, no. 4, pp. 1131–1137, 2011.
- [10] S. Pingel, O. Frank, M. Winkler et al., "Potential induced degradation of solar cells and panels," in *Proceedings of the 35th IEEE Photovoltaic Specialists Conference (PVSC)*, Honolulu, Hawaii, USA, 2010.
- [11] V. Fjallstrom, S. PMP, A. Hultqvist et al., "Potential-induced degradation of thin film solar cells," *IEEE Journal of Photovoltaics*, vol. 3, no. 3, pp. 1090–1094, 2013.
- [12] H. Nagel, A. Metz, and K. Wangemann, "Crystalline Si solar cells and modules featuring excellent stability against potential-induced degradation," in *Proceedings of the Eu-Pvsec*, Hamburg, Germany, 2011.
- [13] W. Herrmann, M. Schweiger, and G. Mathiak, "Potential-induced degradation – comparison of different test methods and low irradiance performance measurements," in *Proceedings of the 27th European Photovoltaic Solar Energy Conference and Exhibition*, Frankfurt, Germany, 2012.
- [14] V. Naumann, D. Lausch, and C. Hagendorf, "Sodium decoration of PID-s crystal defects after corona induced degradation of bare silicon solar cells," *Energy Procedia*, vol. 77, pp. 397–401, 2015.
- [15] A. Raykov, H. Hahn, K.-H. Stegemann et al., "Towards a root cause model for the potential-induced degradation in crystalline silicon photovoltaic cells and modules," in *Proceedings of the European Photovoltaic Solar Energy Conference and Exhibition*, Paris, France, 2013.
- [16] S. Koch, D. Nieschalk, J. Berghold, S. Wendlandt, S. Krauter, and P. Grunow, "Potential induced degradation effects on crystalline silicon cells with various antireflective coatings," in *Proceedings of the European Photovoltaic Solar Energy Conference and Exhibition*, Frankfurt, Germany, 2012.
- [17] K. Mishina, A. Ogishi, K. Ueno et al., "Investigation on anti-reflection coating for high resistance to potential induced degradation," *Japanese Journal of Applied Physics*, vol. 53, no. 3S1, article 03CE01, 2014.
- [18] S. Koch, C. Seidel, P. Grunow, S. Krauter, and M. Schoppa, "Polarization effects and tests for crystalline silicon cells," in *Proceedings of the 26th European Photovoltaic Solar Energy Conference and Exhibition*, Hamburg, Germany, 2011.
- [19] V. Naumann, D. LAUSCH, A. Hähnel et al., "Explanation of potential-induced degradation of the shunting type by Na decoration of stacking faults in Si solar cells," *Solar Energy Materials & Solar Cells*, vol. 120, pp. 383–389, 2014.
- [20] S. Jonai, K. Hara, Y. Tsutsui, H. Nakahama, and A. Masuda, "Relationship between cross-linking conditions of ethylene vinyl acetate and potential induced degradation for crystalline silicon photovoltaic modules," *Japanese Journal of Applied Physics*, vol. 54, no. 8S1, article 08KG1, 2015.
- [21] S. Koch, J. Berghold, O. Okoroafor, S. Krauter, and P. Grunow, "Encapsulation influence on the potential induced degradation of crystalline silicon cells with selective emitter structures," in *Proceedings of the European Photovoltaic Solar Energy Conference and Exhibition*, Frankfurt, Germany, 2012.

Research Article

Modelling and Simulation of the Radiant Field in an Annular Heterogeneous Photoreactor Using a Four-Flux Model

O. Alvarado-Rolon,¹ R. Natividad ,² R. Romero ,² L. Hurtado ,²
and A. Ramírez-Serrano ¹

¹Facultad de Química, Universidad Autónoma del Estado de México, Paseo Colon esq. Paseo Toluca s/n, 50120 Toluca, MEX, Mexico

²Facultad de Química, Centro Conjunto de Investigación en Química Sustentable UAEM-UNAM, Universidad Autónoma del Estado de México, Carretera Toluca-Atlacomulco, Km 14.5, Unidad San Cayetano, 50200 Toluca, MEX, Mexico

Correspondence should be addressed to R. Natividad; reynanr@gmail.com and A. Ramírez-Serrano; aramirezs@uaemex.mx

Received 7 May 2017; Revised 22 July 2017; Accepted 26 July 2017; Published 28 January 2018

Academic Editor: Detlef W. Bahnemann

Copyright © 2018 O. Alvarado-Rolon et al. This is an open access article distributed under the Creative Commons Attribution License, which permits unrestricted use, distribution, and reproduction in any medium, provided the original work is properly cited.

This work focuses on modeling and simulating the absorption and scattering of radiation in a photocatalytic annular reactor. To achieve so, a model based on four fluxes (FFM) of radiation in cylindrical coordinates to describe the radiant field is assessed. This model allows calculating the local volumetric rate energy absorption (LVREA) profiles when the reaction space of the reactors is not a thin film. The obtained results were compared to radiation experimental data from other authors and with the results obtained by discrete ordinate method (DOM) carried out with the Heat Transfer Module of Comsol Multiphysics® 4.4. The FFM showed a good agreement with the results of Monte Carlo method (MC) and the six-flux model (SFM). Through this model, the LVREA is obtained, which is an important parameter to establish the reaction rate equation. In this study, the photocatalytic oxidation of benzyl alcohol to benzaldehyde was carried out, and the kinetic equation for this process was obtained. To perform the simulation, the commercial software COMSOL Multiphysics v. 4.4 was employed.

1. Introduction

In the last decades, photocatalytic processes have been the subject of different studies such as wastewater treatment [1–6], air purification in polluted environments with volatile organic compounds [7–9], and synthesis of fine organic compounds such as benzaldehyde [10, 11]. According to literature [1, 3–6, 11–16], the following different variables are crucial in a photocatalytic process efficiency: (a) catalyst type and concentration, (b) reagent type and concentration, (c) geometry and type of reactor, and (d) characteristics of the radiation inside the photoreactor. Because of the number of variables and the interaction among them, the modeling of this type of processes is expected to be rather useful not only for reactor design but also to achieve a better insight and understanding of the process.

The mathematical modeling and simulation of a photocatalytic reactor imply a great challenge due to the numerous

involved variables; however, the computational analysis of these variables aids to accomplish such a task. Furthermore, the computational analysis allows evaluating hydrodynamic effects and kinetics without employing physical prototypes. The full modeling of photocatalytic reactors requires to include several submodels to simulate the physical phenomena occurring inside the reactor. Some of these necessary submodels are (a) radiation emission and incidence, (b) radiation absorption and scattering, (c) photoconversion kinetics, and (d) hydrodynamics [5, 13–15, 17, 18]. These are the result of mass, energy, and momentum balances, as well as radiation distribution and optical characterization of reaction space [6, 16, 19, 20]. These submodels are strongly interlinked. For example, the kinetics is a function of radiation absorption, which is in turn a function of catalyst characteristics and hydrodynamics. The conversion and performance of a photocatalytic reaction are a function of the local volumetric rate energy absorption (LVREA), which is

defined as the energy due to photons absorbed per time and volume inside the photoreactor [21]. To evaluate the LVREA is necessary to solve the radiation transfer equation (RTE) [22–25].

$$\frac{dI_\lambda(x, \Omega)}{dx} = -\beta_\lambda I_\lambda(x, \Omega) + \frac{\sigma_\lambda}{2} \int_{4\pi} I_\lambda(x, \Omega') p(\Omega \rightarrow \Omega') d\Omega, \quad (1)$$

where $I_\lambda(x, \Omega)$ is the spectral radiation intensity, λ represents the wavelength, β_λ is the extinction coefficient, which is the sum of the absorption coefficient, κ_λ , and σ_λ is the scattering coefficient. The ratio $\omega = \sigma_\lambda/\beta_\lambda$ is the scattering albedo coefficient which is inherent to each photocatalyst since it represents its photon absorption capacity. Ω is the solid angle, and $p(\Omega \rightarrow \Omega')$ is the phase function representing the redistribution of radiation after the scattering event. According to the first term in the right side of (1), the intensity is diminished by the effect of mainly two phenomena, scattering and absorption. This decrease is characterized by the extinction coefficient. There is also an increase in the intensity due to the scattering from other directions, and it is represented by the second term in the right-hand side of (1) [24, 26, 27].

The analytical solution of the RTE is a rather complex task, unless it is limited to simple reactor geometries with specific assumptions. Even when using specialized software, the radiation field simulation is a task that requires a high computational effort. Comsol Multiphysics v. 4.4 contains the physics of radiation in participating media (rpm), in the Heat Transfer Module, which is designed to solve 3D radiation transfer problems, taking into account the phenomena of emission, dispersion, and absorption of radiation. The Comsol Multiphysics v. 4.4 Heat Transfer Module employs the discrete ordinate method (DOM). This method consists the transformation of the integral-differential RTE into a system of algebraic equations to describe the transport of photons in such way that can be solved following the direction of propagation, starting from the values provided by the boundary conditions. However, RTE is solved by discretizing the solid angle at every discrete position in the 3D domain, which is computationally very demanding and may result in unrealistic results when the discretization of the solid angle is not refined enough.

A viable alternative is to employ numerical computational methods as the statistical method Monte Carlo (MC), which is known as highly accurate but requires a great computational effort [21, 28, 29]. Also, it is possible to employ analytical simplified methods like the two-flux model (TFM) and the six-flux model (SFM). These models consist of several algebraic equations developed for flat slab geometries [15–17, 30], which were obtained by solving a system of differential equations with specific boundary conditions, for example, the outer wall of the reactor is opaque. SFM is very accurate for cylindrical geometries [14] in which the space where the reaction occurs, δ , is much smaller than the radius of the reactor, R_R .

$$\delta \ll R_R, \quad \frac{R_R}{R_R + \delta} \sim 1. \quad (2)$$

However, in this investigation, a reactor in which the lamp is immersed in the reaction medium was used, so (2) is not satisfied. The geometry used in this work is shown in Figure 1. This paper aims to evaluate the effectiveness of a modified model based on four flux of radiation (FFM), whose equations are based on a cylindrical geometry, to mathematically represent the radiation field in a stirred annular photoreactor. This model is coupled to a reaction rate model representing the benzyl alcohol oxidation. The FFM evaluates the incident radiation in each point of the reaction space. This model considers that the incident radiation is the sum of radiation fluxes traveling from the light source towards this point and the fluxes due from both axial and radial scattering. As this model is developed from cylindrical geometries, its solution is expected to better represent the radiant field inside an annular photocatalytic reactor than the models developed from slab plane geometries where the reaction space is only a thin film.

The main objective of this work was to validate the proposed four-flux model, which is specifically designed for annular photocatalytic reactors with a relationship, that is, the reactor is not thin-walled. FFM is tested against the results with experimental data of the photocatalytic and selective oxidation of benzyl alcohol towards benzaldehyde. Moreover, the radiation profiles were compared to those calculated by MC, DOM, and SFM. The FFM and DOM were carried out with commercial software Comsol Multiphysics 4.4, which is a powerful differential equation solver.

2. Methodology

The main objective of this work was to test a proposed FFM to efficiently represent the radiant field inside an annular reactor when the reaction space is not a thin film. In order to validate the proposed model, the profiles obtained with FFM were compared to those previously reported in the literature. Also, the FFM was applied to describe the radiant field in a batch annular photoreactor employed to experimentally obtain benzyl alcohol oxidation data. Then, the kinetics of this reaction was established as function of LVREA.

2.1. Source Data

2.1.1. System 1. The profiles obtained in a thin-film slurry reactor of inner wall (TFSIW) reported by Li Puma et al. [5, 14, 17] and obtained by the six flow model were replicated for comparison purposes. In this case, the relation $R_R/(R_R + \delta) = 0.76$. The characteristics of the system are summarized in Table 1.

2.1.2. System 2. This photoreactor was previously reported [28, 29] and was named Photo-CREC Water II and employs TiO_2 (anatase) as a catalyst. In such a reaction system, the lamp is annulus centered. The relationship

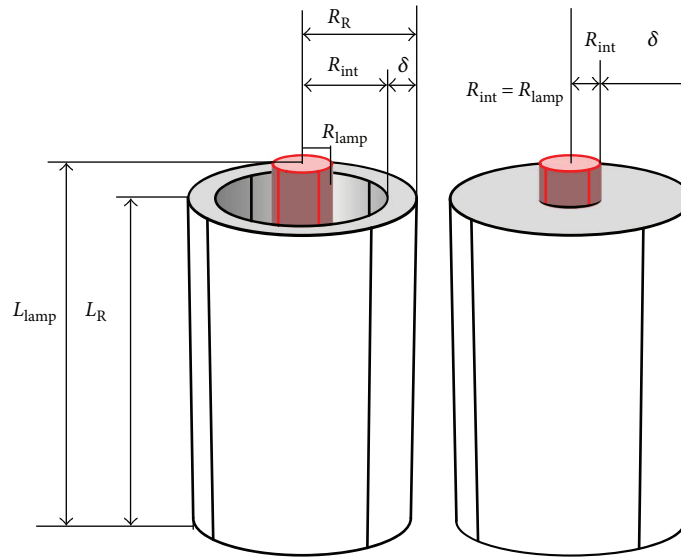


FIGURE 1: Schematic representation of the geometry of the assessed annular photocatalytic reactor.

TABLE 1: Characteristics of systems.

	Catalyst	Lamp characteristics	Reactor characteristics
System 1 Li Puma [14]	TiO ₂ DP 25	Power: 4 W	Length: 0.225 m
	(i) $\sigma_\lambda = 1.02 C_{\text{cat}}$ (1/m) (ii) $\kappa_\lambda = 0.338 C_{\text{cat}}$ (1/m)	Wavelength: 300 nm Radius: 0.00775 m Length: 0.213 m	Ext. radius: 0.019 m Int. radius: 0.013 m $R_R/(R_R + \delta) = 0.76$
System 2 Moreira et al. [28, 29]	TiO ₂ anatase	Power: 8 W	Length: 0.445 m
	(i) $\sigma_\lambda = 3.1149 C_{\text{cat}}$ (1/m) (ii) $\kappa_\lambda = 0.3957 C_{\text{cat}}$ (1/m)	Wavelength: 250 nm Radius: 0.0133 m Length: 0.413 m	Ext. radius: 0.0444 m Int. radius: 0.01755 m $R_R/(R_R + \delta) = 0.62315$
System 3	LiVMoO ₆	Power: 8 W	Length: 0.25 m
	(i) $\sigma_\lambda = 0.24128 C_{\text{cat}}$ (1/m) (ii) $\kappa_\lambda = 0.03092 C_{\text{cat}}$ (1/m)	Wavelength: 254 nm Radius: 0.005 m Length: 0.23 m	Ext. radius: 0.025 m Int. radius: none $R_R/(R_R + \delta) = 0.5555$

$R_R/(R_R + \delta) = 0.62315$. The characteristics of the system are also summarized in Table 1.

2.1.3. System 3. Once the radiation model was validated with data reported in systems 1 and 2, this model was applied to simulate the radiation field in system 3 during benzyl alcohol selective oxidation towards benzaldehyde. Experimental data of benzyl alcohol oxidation were obtained in an annular cylindrical photocatalytic reactor. It is worth pointing out that in this reaction system, the lamp was placed at the center of the reactor without any additional physical protection (e.g., quartz sleeve). For this reason, the relationship $R_R/(R_R + \delta) = 0.5555$.

The employed catalyst was LiVMoO₆, and a detailed characterization has been previously reported [31]. The characteristics of the system are shown in Table 1. The FFM was used to describe the radiant field in this reactor and to obtain the kinetics of benzyl alcohol oxidation as a function of LVREA.

2.2. Mathematical Modeling of Radiation Emission. The emission of radiation from the cylindrical lamp is modeled using the linear source spherical emission (LSSE). This model considers that the lamp is a linear source, and each point on the line emits radiation isotropically and in every direction. It is assumed that the radiation emitted by each point of the lamp is constant along the axial length of the lamp [5]. According to the literature, the intensity of the incident radiation entering the inner wall of the annulus can be calculated as

$$I_{R_{\text{int}},Z} = \frac{S_1}{4\pi R_{\text{int}}} \left[a \tan\left(\frac{2z - L_R + L_{\text{lamp}}}{2R_{\text{int}}}\right) - a \tan\left(\frac{2z - L_R - L_{\text{lamp}}}{2R_{\text{int}}}\right) \right], \quad (3)$$

where

$$S_1 = 2\pi R_{\text{lamp}} I_w. \quad (4)$$

The experimental emitted radiation was measured by a UVX radiometer equipped with a sensor of 254 nm placed at the lamp wall and 0.01 m from the lamp.

2.3. Mathematical Modeling of Absorption and Scattering Radiation. To establish the mathematical FFM, the following assumptions were made: (a) reactor with slurry catalyst, (b) heterogeneous model, (c) isothermal process, (d) perfect mixing and therefore the catalyst concentration is homogeneous at all reaction space, (e) photons are absorbed only by catalyst particles, (f) the flux of photons occurs only in four directions, two radial, and two axial directions, (g) the emission of photons by the lamp is isocratic, (h) oxygen bubbles do not affect the radiation fluxes, and (i) the scattering of photons by the catalyst is isotropic.

FFM was employed to evaluate the incident radiation on a given point inside the reaction space. In this model, the total radiation flux is taken as the sum of the flux of photons traveling from the light source towards that point and flux of photons from scattering in both two axial directions and two both radial directions. In concordance, a photon balance was performed in a differential volume element shell shaped in cylindrical coordinates (Figure 2).

The flux of incident radiation (g_f), the flux entering the differential element due to backscattering (g_b), and the fluxes entering from bottom and upper walls (g_a and g_c) are the four fluxes that this model accounts for. The parameters p_b , p_a , and p_c represent the probabilities of occurring backscattering in the corresponding directions. These parameters were calculated by MC method employing an isotropic phase function, and their values are $p_f = 0.405$, $p_b = 0.303$, $p_a = 0.146$, and $p_c = 0.146$ for LiVMoO_6 and $p_f = 0.357$, $p_b = 0.351$, $p_a = 0.146$, and $p_c = 0.146$ for TiO_2 . The number and external area of the catalytic particles are n_p and a_p , respectively, so in order to establish that the FFM is necessary to perform a balance of incident radiation (g_f), in the four considered directions. For example, the following radiation balance in the radial direction can be written as

$$\{\text{Input photons}\} - \{\text{output photons}\} = \{\text{absorbed photons}\}. \quad (5)$$

So the balance is

$$\begin{aligned} & g_f(2\pi r \Delta z)|_r - g_f(2\pi r \Delta z)|_{r+\Delta r} + g_b \omega(2\pi r \Delta r \Delta z)(n_p a_p p_b) \\ & + g_a \omega(2\pi r \Delta r \Delta z)(n_p a_p p_a) + g_c \omega(2\pi r \Delta r \Delta z) \\ & \cdot (n_p a_p p_c) - g_f(n_p a_p (\omega p_a + \omega p_b + \omega p_c)) \\ & \cdot (2\pi r \Delta r \Delta z) \\ & = g_f(1 - \omega)(n_p a_p)(2\pi r \Delta r \Delta z). \end{aligned} \quad (6)$$

By reordering and applying $\lim_{\Delta r \rightarrow 0}$,

$$\frac{d(r g_f)}{dr} = \left(\frac{r}{\beta \cdot C_{\text{cat}}} \right) (\omega(g_b p_b + g_a p_a + g_c p_c) - g_f(1 - \omega p_f)), \quad (7)$$

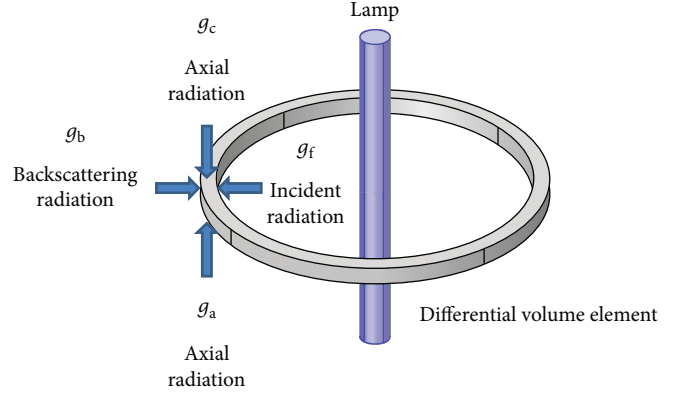


FIGURE 2: Directions of the fluxes of photons in the four-flux model.

where

$$\omega p_b + \omega p_a + \omega p_c + \omega p_f + (1 - \omega) = 1, \quad (8)$$

$$\left(\frac{1}{(1/n_p a_p)} \right) = \left(\frac{1}{\beta C_{\text{cat}}} \right). \quad (9)$$

The term $(1/(1/n_p a_p))$ is the extinction characteristic length. It has been suggested [5] that the extinction characteristic length can be replaced by the inverse of the extinction volumetric coefficient $(1/\beta C_{\text{cat}})$. Physically, this represents the mean free path of the photons in the slurry. Doing a similar balance in the backscattering directions, the following equations are obtained:

$$\frac{d(r g_b)}{dr} = \left(\frac{r}{\beta \cdot C_{\text{cat}}} \right) (\omega(g_f p_b + g_a p_c = g_c p_a) - g_b(1 - \omega p_f)), \quad (10)$$

$$\frac{d(r g_a)}{dz} = \left(\frac{r}{\beta C_{\text{cat}}} \right) (\omega(g_f p_c + g_b p_a + g_c p_b) - g_a(1 - \omega p_f)), \quad (11)$$

$$\frac{d(r g_c)}{dz} = \left(\frac{r}{\beta \cdot C_{\text{cat}}} \right) (\omega(g_f p_a + g_a p_b + g_b p_c) - g_c(1 - \omega p_f)). \quad (12)$$

Equations (7), (10), (11), and (12) are simultaneously solved by applying the following boundary conditions.

(1) BC 1: at wall lamp or inner wall:

$$\begin{aligned} g_f(r = R_{\text{lamp}}) &= I_{r,z} A_{\text{lamp}} p_f \\ g_b(r = R_{\text{lamp}}) &= (g_f + g_a + g_c) p_b \\ g_a(r = R_{\text{lamp}}) &= (g_f + g_b + g_c) p_a \\ g_c(r = R_{\text{lamp}}) &= (g_f + g_a + g_b) p_c. \end{aligned} \quad (13a)$$

(2) BC 2: at external reactor wall (opaque wall):

$$\begin{aligned}
g_f(r=R_R) &= (I_{r,z} p_f) \exp(-\beta \delta) \\
g_b(r=R_R) &= 0 \\
g_a(r=R_R) &= (g_f + g_b + g_c) p_a \\
g_c(r=R_{\text{lamp}}) &= (g_f + g_a + g_b) p_c.
\end{aligned} \tag{13b}$$

(3) BC 3: at upper and bottom wall:

$$g_a(z=L_R) = g_c(z=0) = 0. \tag{13c}$$

These boundary conditions are shown in Figure 3. Furthermore, considering an infinitely long reactor, the following condition can be established, along the axial axis:

$$\frac{\partial g_a}{\partial z} = \frac{\partial g_c}{\partial z} = 0. \tag{14}$$

The LVREA using the four-flux model can be calculated by the following expression:

$$\text{LVREA} = \frac{g_{\text{total}} \kappa_\lambda}{V} \left(\frac{R_{\text{lamp}} \delta}{4r^2} \right). \tag{15}$$

2.4. Simulation of Radiant Field. The software COMSOL Multiphysics version 4.4 and subroutines performed in Matlab® were employed to solve the FFM and kinetic models, respectively. To carry out the simulation, the geometric domain of both, reaction space and lamp, was established. The model is two-dimensional and symmetric with respect to the axial axis. A nonuniform mesh was used, with a size of element calibrated to plasma, giving major emphasis on the inner wall of the annulus, using a fine mesh at this boundary and coarser in the outer wall of the reactor to accurately assess each border (Figure 4(a)). As a result, color maps are obtained, which represent the distribution of LVREA within the photocatalytic reactor. The red zone represents the highest values, and the colors are decreasing towards blue which represents low values of LVREA. The modeling instructions for FFM can be found in the complementary content (Appendix A).

The results obtained by FFM were compared with the following.

- (A) Discrete ordinate method (DOM) carried out with the physics of radiation in participating media of the Heat Transfer Module of Comsol Multiphysics 4.4. To do so, the geometric domain of reaction space was established as 3D model. Several preliminary simulations were run using this method. In these trials, the mesh in all domains was refined incrementally until the physical ram limit of the workstation (8 Gb) was reached. Geometry and mesh employed are shown in Figure 4(b). The modeling instructions for DOM can be found in the complementary content (Appendix B).
- (B) Six-flux model (SFM) was implemented in programming language Matlab according to the methodology reported by Li Puma [14, 17].
- (C) Monte Carlo Method (MC) was also implemented in programming language Matlab based on Moreira

et al. [28, 29]. In this case, the number of used photons was 1×10^7 . In addition, subroutines were programmed to generate random numbers.

The codes to solve the applied models, SFM and MC, are rather lengthy. However, they can be provided upon request.

2.5. Kinetic Model. To determine the radiation effect on reaction rate, a kinetic expression as function of LVREA can be obtained.

$$\frac{dC_{AB}}{dt} = k_r f(C_{AB}) g(\text{LVREA}), \tag{16}$$

where $f(C_{AB})$ is a function of reagent concentration (benzyl alcohol) and the dependence of reaction rate with LVREA is given by $g(\text{LVREA})$. To describe $f(C_{AB})$ is possible to employ a power law model. This is accepted when the reagent absorption on the catalytic surface is negligible and therefore the LHHW model becomes a pseudo first-order equation. Although this kind of equation does not include the effect of reactive intermediaries, it still provides reasonable results [6, 11]. Several authors have studied the kinetics of photocatalytic oxidation of aromatic alcohols to corresponding aldehydes, and they claim a first-order kinetics regarding alcohol concentration [10, 11].

$$-\frac{dC_{AB}}{dt} = K_{Ap} C_{AB}, \tag{17}$$

where K_{Ap} is the apparent kinetic coefficient that includes the effect of catalyst concentration, temperature, oxidant concentration, and so forth. Furthermore, since there is reaction due to photolysis only (without catalyst), this can be considered within the reaction rate expression.

$$\left(\frac{-dC_{AB}}{dt} \right)_{\text{Total}} = \left(\frac{-dC_{AB}}{dt} \right)_{\text{Without catalyst}} + \left(\frac{-dC_{AB}}{dt} \right)_{\text{With catalyst}}, \tag{18}$$

$$\left(\frac{-dC_{AB}}{dt} \right)_{\text{Total}} = k_{r1} C_{AB} + k_{r2} C_{AB} = (k_{r1} + k_{r2}) C_{AB} = K_{Ap} C_{AB}, \tag{19}$$

where k_{r1} is the intrinsic constant of reaction rate without catalyst and k_{r2} is the reaction rate constant with catalyst, which is a function of LVREA. Therefore, K_{Ap} can be expressed as

$$K_{Ap} = k_{r1} + k_{r2} = k_{r3} (\text{LVREA})^m, \tag{20}$$

by linear regression, both the order of LVREA and k_{r3} were calculated. Employing the FFM method, the values of averaged LVREA corresponding to each catalyst concentration were calculated. The contribution due to photolysis is negligible; for this reason, the LVREA due to the reactive species was not added in the photolysis term. It is worth noticing that in other cases, when the reactant molecule has a strong absorption of photons, this contribution must also be taken into account. This also applies for intermediaries. In the present case, however, the reaction kinetics was established with

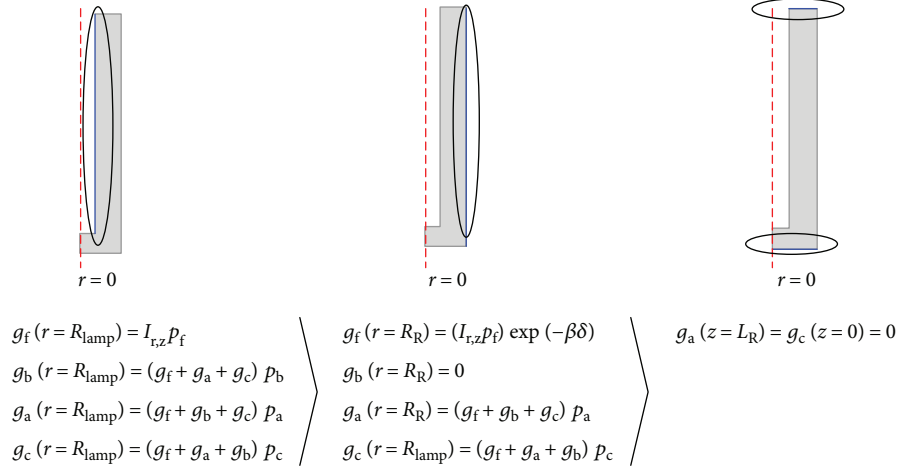


FIGURE 3: Boundary conditions used in the four-flux model.

very low conversion data and therefore the presence of intermediaries was considered rather low as to contribute to LVREA.

3. Results

3.1. Emission Model. Figure 5 shows the emitted radiation profiles calculated by both, MC and LSSE methods. In addition, the radiation values experimentally measured by a UVx radiometer equipped with a detector 254 nm were plotted. Figure 5(a) shows the values of the emitted radiation, $I_{(R_{\text{lamp}},z)}$ on the wall of the lamp, and Figure 5(b) shows the values of $I_{(R_{\text{lamp}}+0.01m,z)}$ at 0.01 m from the wall of the lamp. It can be seen that both methods are in good agreement with experimentally obtained data, which justifies the use of both Monte Carlo method and LSSE model in this research.

3.2. Absorption of Radiation Model. The results of the proposed model ((7), (8), (9), (10), (11), (12), (13a), (13b), (13c), (14), and (15)) were compared with those obtained by MC, SFM, and DOM. It was assumed that MC is the method that best represents the radiant field in the photocatalytic reactor. Even though the DOM is robust, it requires a very refined mesh to give congruent results.

3.2.1. System 1: TFSIW. The first analyzed photocatalytic reactor was a TFSIW reported by Li Puma et al. [5, 14, 17]. This reactor has a radius ratio $R_R/(R_R + \delta) = 0.76$. Figure 6 shows the radial profiles of LVREA at $z = L_R/2$ for this system, calculated by the four methods and parity diagram. It can be seen that SFM and DOM represent LVREA profiles better than the FFM with regard MC, especially when the catalyst concentration is low. However, FFM results can be considered to be adequate also if a rapid estimation of LVREA is required. Both the FFM and the SFM have small deviations in the inner wall when the catalyst loading is large. With the mesh used for the DOM, the computing time was approximately 40 minutes. Using a finer mesh could increase the computing time by several hours. The solving time for

FFM was about 2 minutes regardless the elements number in the mesh.

3.2.2. System 2 (Photo-CREC II). The results obtained by FFM method are in agreement with the data previously reported by Moreira et al., which were obtained from MC for Photo-CREC water II [28, 29]. Figure 7 shows the radial profiles for the LVREA at different photocatalyst concentrations for TiO_2 anatase and parity diagram obtained by SFM, DOM, and FFM versus MC. In this case, it is observed that the results obtained by FFM and DOM are quite congruent although they tend to deviate slightly from those obtained by MC. This reactor has a ratio of radius $R_R/(R_R + \delta) = 0.6231$. The mesh used in DOM for this relationship can be considered as semicoarse and give good results in about 1 hour of computing time.

3.2.3. System 3. This system was theoretically and experimentally studied. Figure 8 shows the comparison of the LVREA profiles obtained from the three methods for the catalyst LiVMoO_6 . It is worth noticing that the catalyst with the highest extinction coefficient values ($\beta = \sigma + \kappa$) (TiO_2 DP 25) produces higher values of LVREA at the same catalyst concentration. The values of LVREA obtained by LiV-MoO_6 catalyst are smaller than the values obtained by TiO_2 catalyst; however, the special interest on LiVMoO_6 catalyst resides on that it presents catalytic activity even in the visible spectrum [31].

In Figure 8, it can be observed that near the lamp wall (dimensionless radius = 0.4), LVREA is maximum and rapidly decreases as dimensionless radius increases. This effect is considered by both, MC and FFM; however, the SFM does not account for it. This can be attributed to SFM being explicitly developed for thin-walled annular reactors and presents significant deviations when $R_R/(R_R + \delta) \ll 1$. Also, DOM presents a great deviation with respect to MC. This is because the meshing is not fine enough. However, using a more refined mesh causes the available RAM to be exceeded.

Table 2 shows a comparison of correlation coefficients for SFM, FFM, and DOM considering that MC is the most

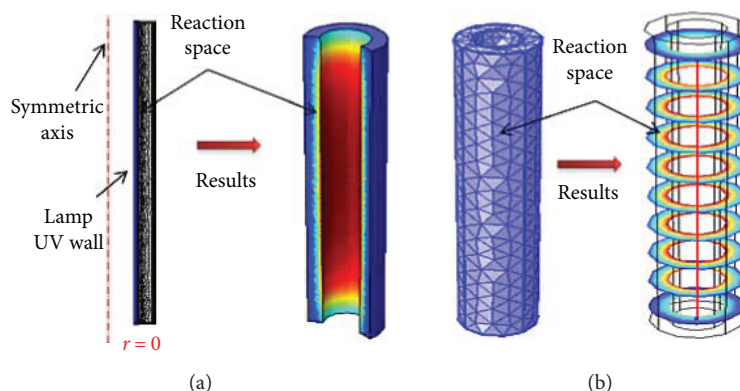


FIGURE 4: Graphical representation of photocatalytic reactor and geometry employed to solve (a) four-flux model and (b) discrete ordinate method, in COMSOL Multiphysics.

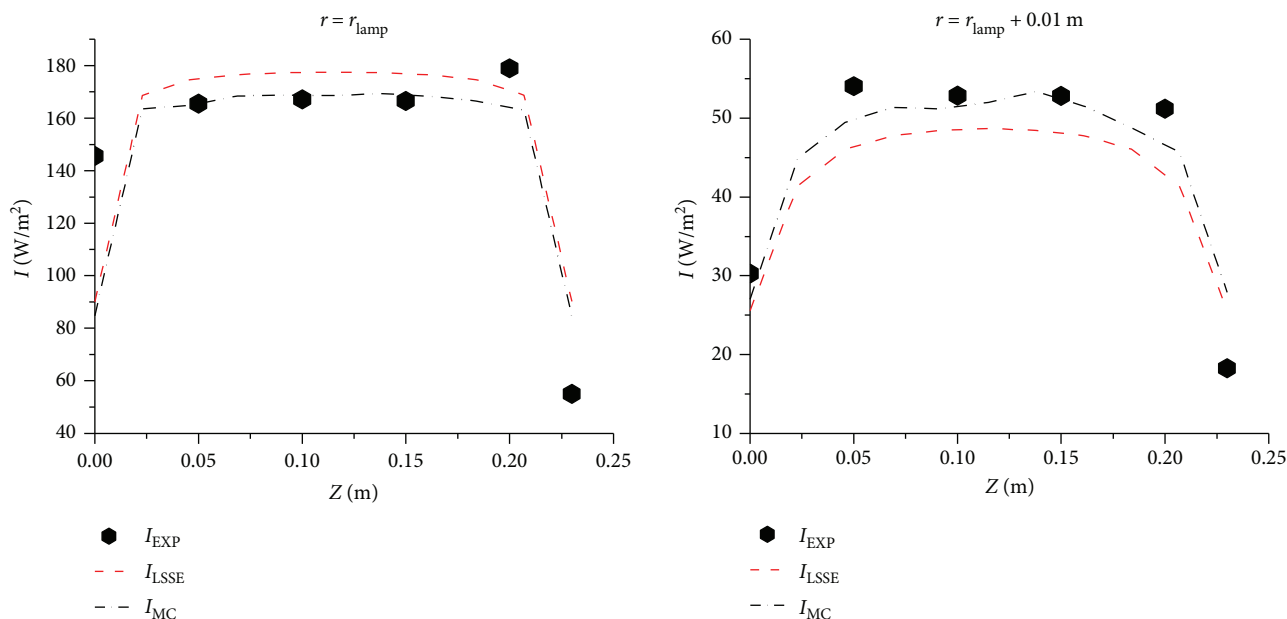


FIGURE 5: Emission model results. Calculated and experimental incident radiation profiles.

accurate one. The percentage of the area under the curve of the radiation profiles obtained by the different methods in relation to the area under the Monte Carlo method curve is also shown. It can be seen that the FFM better predicts the profiles of LVREA when $R_R/(R_R + \delta) \ll 1$ and the catalyst loading is relatively low, for example in system 3.

Through Figures 6, 7, and 8, it can be seen that near the inner wall of the reaction space, LVREA is maximum and rapidly decreases as dimensionless radius increases. This can be ascribed to an obstruction effect produced by catalyst particles. One can also notice that in cases where the photocatalyst concentration is relatively high, the particles closer to the inner radius absorb most of the radiation entering the reactor. According to the results, it may be seen that low values of LVREA are obtained at low catalyst concentrations; however, the effectively irradiated zone is greater. At high catalyst concentrations, high values of LVREA are

achieved near the wall of the lamp; however, the effectively irradiated zone is drastically diminished in the radial direction. It is important to note this effect since it is desirable to obtain high values of LVREA, but at the same time maximize the irradiated zone. In dark zones, absorption of photons does not occur, which provokes the effective volume of the reaction being smaller, that is, the reactor volume is being subutilized. This effect is shown in Figure 9. A sufficiently high photocatalyst concentration produces zones with dark areas towards the external radius. Therefore, there is an optimal catalyst concentration that provides an optimal irradiated reactor space. Photocatalyst concentrations above this maximum show an essentially negligible effect on LVREA. This optimal concentration can be seen in Figure 10, and it is in agreement with those reported [28, 29] for TiO_2 catalyst (system 1 and system 2). For system 3, the optimal concentration is achieved at 1 kg/m^3 .

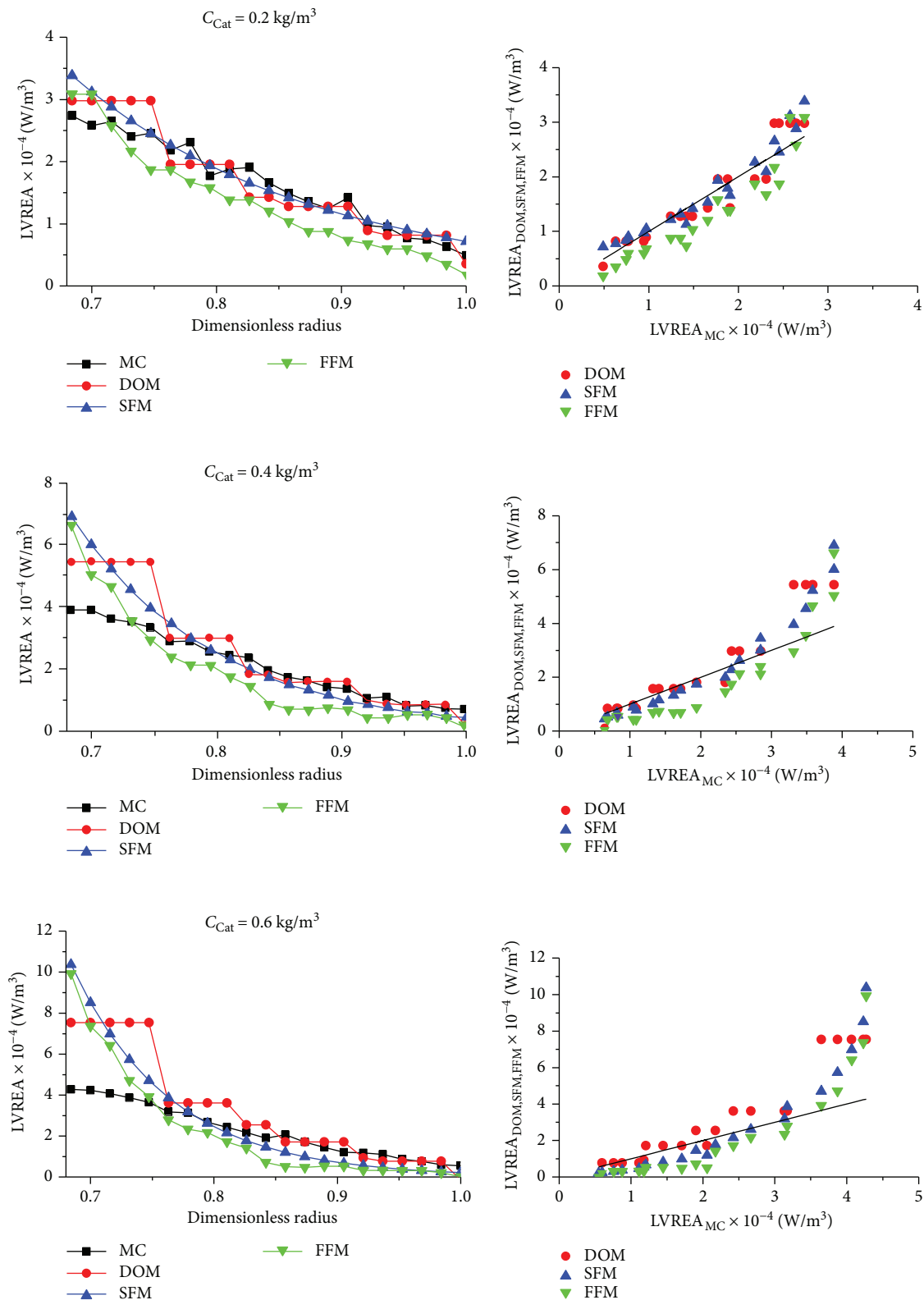


FIGURE 6: Radial profiles of local volumetric rate energy absorption (LVREA) obtained with four-flux model at different concentrations of catalyst for system 1 and its comparison with the other models.

3.3. Kinetic Model. To obtain a kinetic expression for photocatalytic oxidation of benzyl alcohol, the integral method was employed. An adjust by least squares was performed

for different models, including the LHHW model, and it was found that the better adjustment is at pseudo first order in respect of concentration of benzyl alcohol. This

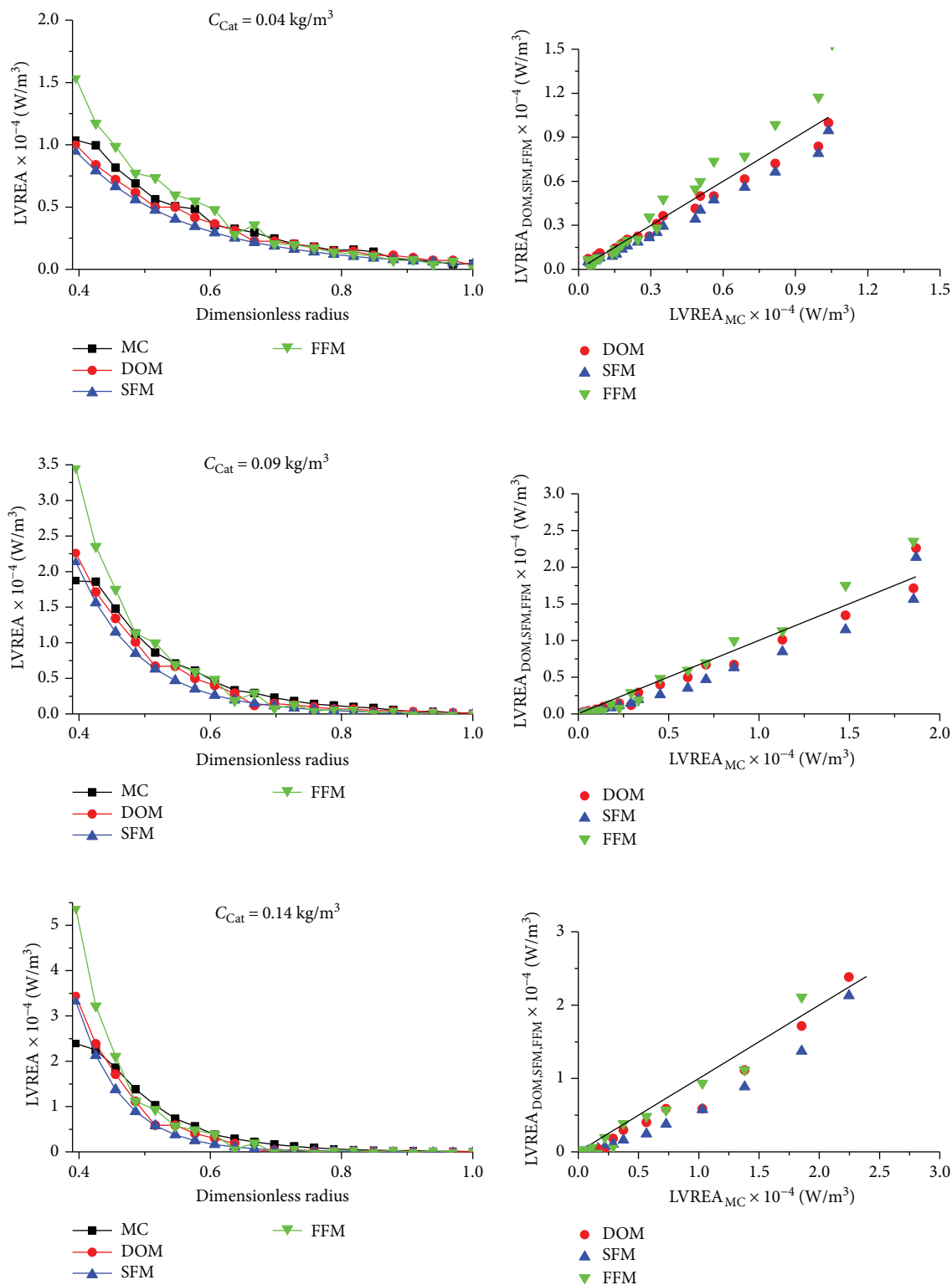


FIGURE 7: Radial profiles of local volumetric rate energy absorption (LVREA) obtained with four-flux model at different catalyst concentration for system 2 and its comparison with the other models.

result is in agreement with the results reported by [10, 11], albeit with other catalysts. Figure 11 shows the comparison of the results for the adjustment by least squares according to experimental data of benzyl alcohol oxidation, at

different catalyst loading, employing a pseudo first-order power model.

Taking into account the data of concentration—time obtained at each catalyst loading, an adjustment by least

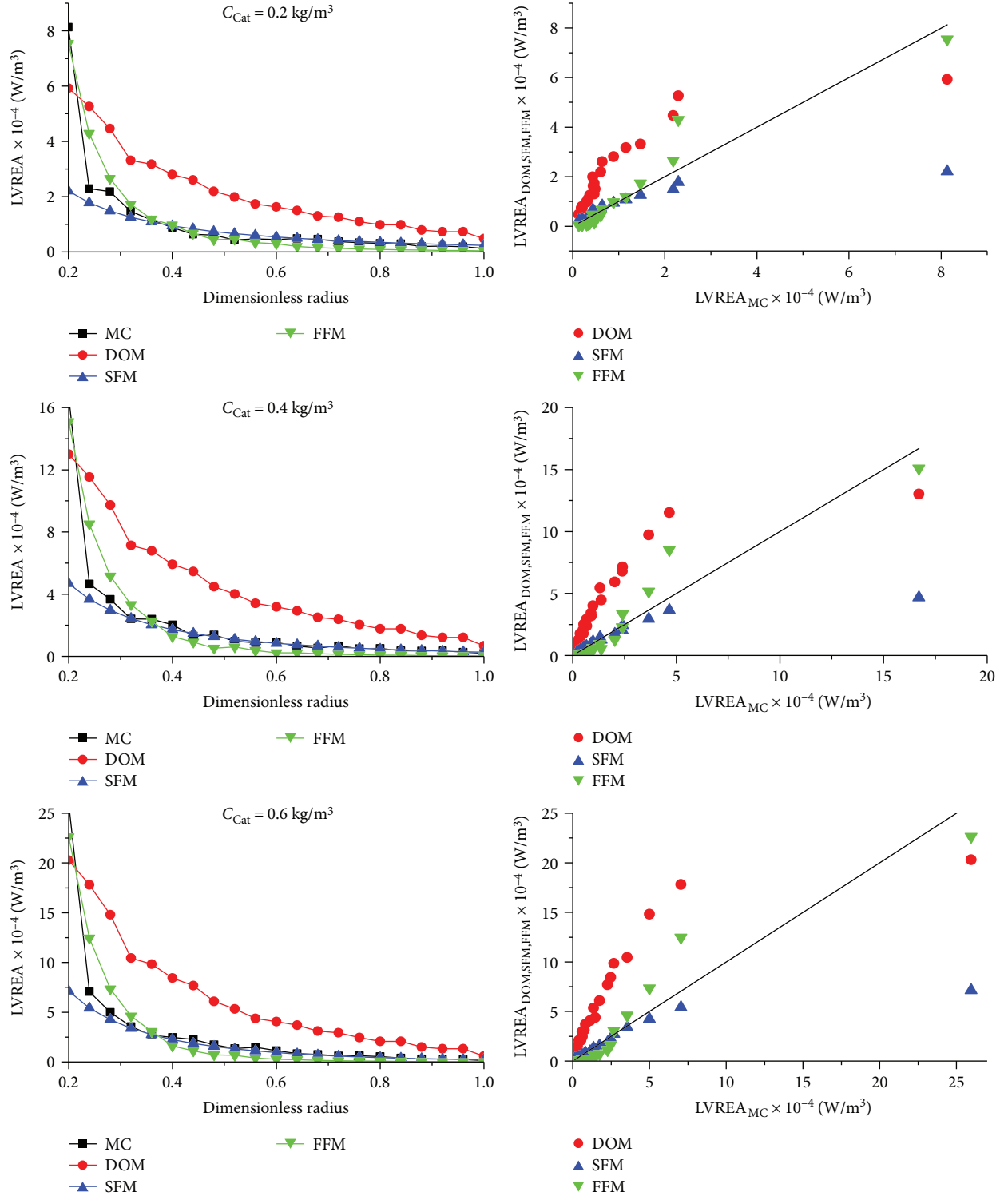


FIGURE 8: Radial profiles of local volumetric rate energy absorption (LVREA) obtained by four-flux model at different concentration of catalyst (LiVMoO_6) for system 2 and its comparison with the other models.

squares was performed to obtain the dependence of rate constants with the LVREA (Table 3).

Figure 12 shows the plot of $\ln(K_{Ap} - k_{r1})$ as a function of $\ln(\text{LVREA})$. The slope of the line represents the order of the reaction with respect to the LVREA, and the intercept provides

the $\ln(k_{r3})$. Hence $k_{r1} = 0.0101 \text{ h}^{-1}$, intrinsic reaction constant without catalyst; $k_{r3} = 0.01887 \text{ h}^{-1} (\text{W/m}^3)^{-0.1464}$; and $m = 0.1467$ is the power of LVREA. This fractional exponent of LVREA was expected. It has even been reported that the exponent is equal to 0.5 in the presence of TiO_2 for system 1 [18]. It

TABLE 2: Comparison of correlation coefficients of different radiation absorption models for studied systems.

System	Catalyst	C_{CAT} (mg/L)	DOM		SFM		FFM	
			R^2	$\%A_{MC}$	R^2	$\%A_{MC}$	R^2	$\%A_{MC}$
1 $R_R/(R_R + \delta) = 0.76$	TiO_2	0.20	0.9530	101.69	0.9611	103.21	0.9458	80.78
		0.40	0.9602	120.54	0.9583	110.80	0.9167	84.22
		0.60	0.9595	143.91	0.9242	116.33	0.8906	94.20
2 $R_R/(R_R + \delta) = 0.62315$	TiO_2 anatase	0.04	0.9943	91.83	0.9945	80.09	0.9868	114.16
		0.09	0.9833	88.33	0.9744	73.70	0.9642	110.29
		0.14	0.9629	87.47	0.9421	73.52	0.9285	113.02
3 $R_R/(R_R + \delta) = 0.5555$	$LiVMoO_6$	0.20	0.8089	237.11	0.8468	81.79	0.9605	100.88
		0.40	0.8004	257.06	0.8518	76.16	0.9553	95.18
		0.60	0.7984	258.14	0.8571	70.79	0.9564	95.73

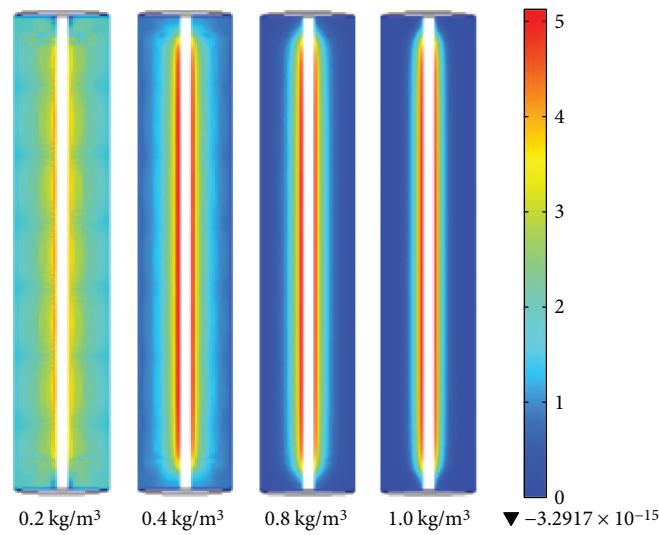


FIGURE 9: Effect of catalyst concentration on the reactor radial section where photon absorption occurs (LVREA map) in system 3.

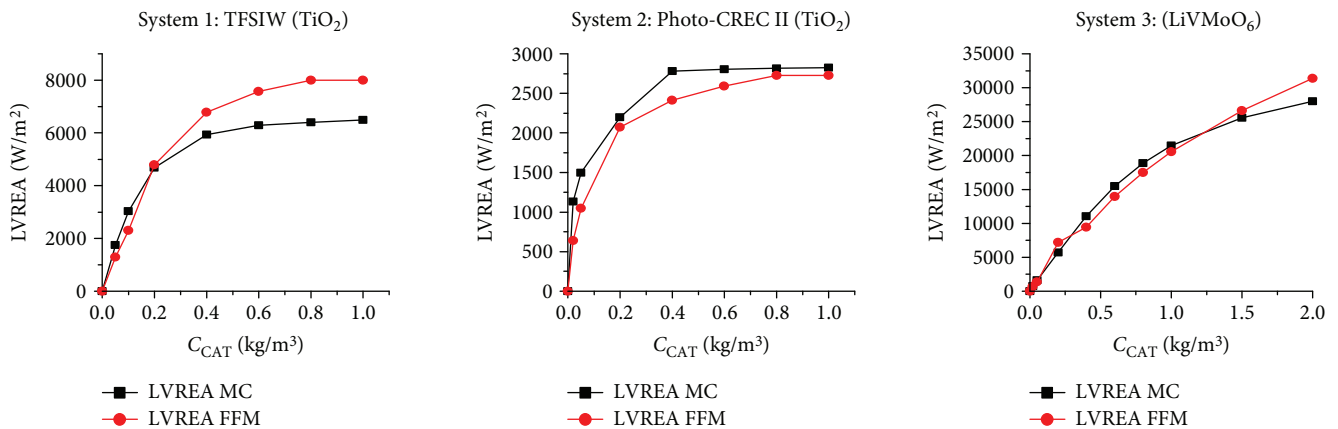


FIGURE 10: Simulated results of incident radiation as function catalyst loading.

should be noted that the value of m is relatively independent on the type of substrate. Instead, it should be dependent on the radiation intensity level over the catalyst. A fractional order

dependence of photocatalytic reaction rate from the LVRPA is obtained when the rate of electron-hole recombination in the catalyst particles becomes predominant [18].

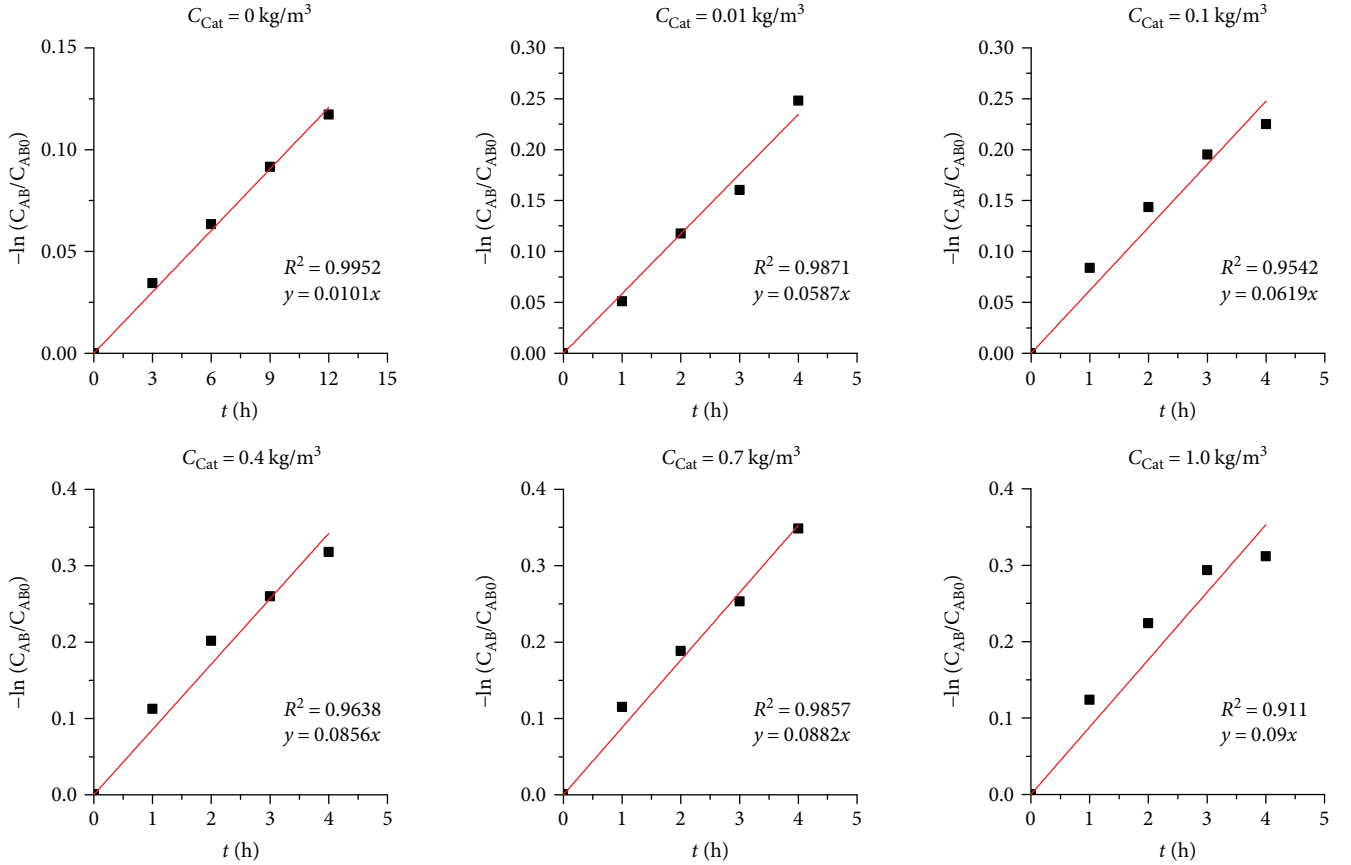


FIGURE 11: Test for a pseudo first-order kinetics as a function of concentration.

TABLE 3: First-order kinetic constants and values of LVREA at different catalyst loadings.

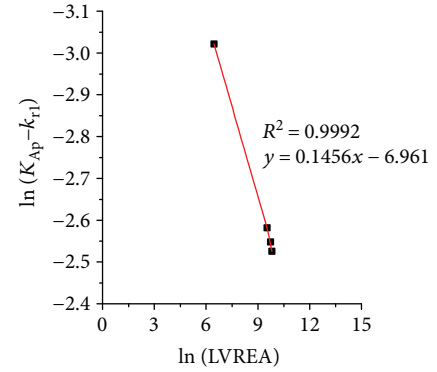
$C_{cat} \text{ (kg/m}^3\text{)}$	$K_{Ap} \text{ (h}^{-1}\text{)}$	LVREA $\text{(W/m}^3\text{)}$
0.00	0.0101	0.00
0.01	0.0587	630.00
0.10	0.0750	5300.00
0.40	0.0856	13600.00
0.70	0.0882	16700.00
1.00	0.0900	18000.00

Therefore, the kinetic equation that describes the photocatalytic oxidation of benzyl alcohol to benzaldehyde is

$$-\frac{dC_{AB}}{dt} = \left(0.0101 \text{ h}^{-1} + 0.01887 \text{ h}^{-1} \left(\frac{\text{W}}{\text{m}^3} \right)^{-0.1464} (\text{LVREA})^{0.1464} \right) C_{AB}. \quad (21)$$

Equation (20) shows that the reaction rate depends on the LVREA values and the amount of irradiated catalyst. Figure 13 shows the concordance of the proposed mathematical model with experimental data of benzyl alcohol oxidation at different catalyst loadings.

In Figure 13, a linear decrease of benzyl alcohol concentration is observed. This is in agreement with that previously

FIGURE 12: Adjustment for dependence of K_{Ap} with the LVREA.

reported [10, 11]. On the other hand, the conversion increases with the catalyst loading up to a point where a further increase on catalyst loading does not produce a significant improvement on conversion, due to LVREA reaches a maximum at this point, establishing that the optimal catalyst loading is 1.0 kg/m^3 for LiVMoO_6 .

4. Conclusions

The proposed mathematical model (FFM) describes the radiant field in a photocatalytic annular reactor. Its

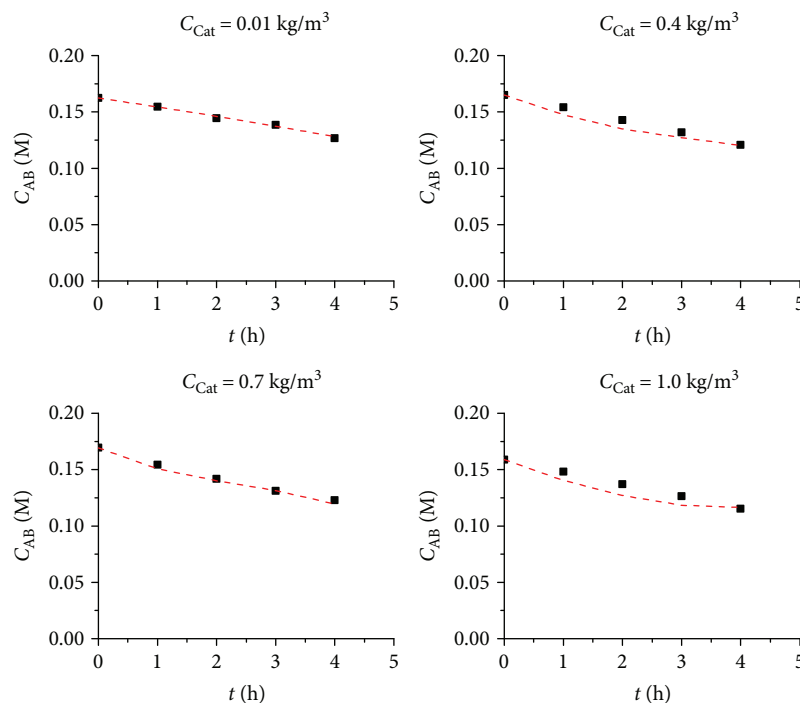


FIGURE 13: Comparison of experimental concentration profiles (dots) with those obtained by the proposed model.

numerical solution corresponds appropriately with experimental and numerical data, and it requires a minor computational effort than the other models, such as DOM, which is very robust and accurate but requires a high RAM capacity. The FFM was specifically designed for cylindrical geometries with the lamp located at the axial axis of the reactor submerged in reaction medium. The FFM predicts the LVREA profiles better than the other models when $R_R/(R_R + \delta) \ll 1$, and the catalyst loading is low.

The obtained kinetic equation describes the reaction rate in the photocatalytic reactor for selective oxidation of benzyl alcohol as function of the LVREA. The FFM allows the evaluation of LVREA at different catalyst loadings, power lamp, or reactor dimensions. Therefore, it allows the calculation of reaction rates at different experimental setups.

Within the range of studied variables, the reaction rate of the selective oxidation of benzyl alcohol adequately fits a first-order kinetics, where the kinetic coefficient is a function of LVREA, and this depends on catalyst loading, power lamp, and annulus width.

Appendix

A. Simulation of Radiant Field Employing the Four-Flux Model (FFM) in Comsol Multiphysics v. 4.4

- (1) Model 2D: from the File menu, choose New. In the New window, click Model Wizard and select a 2D axisymmetric model.
- (2) Interface for ordinary differential equations, ODE: in the Select Physics tree, select Mathematics > ODEs

Interface > ODEs in general form (g). Click Add. The Study is Stationary.

- (3) Parameters: go to Global definitions section and insert Parameters. In the Settings window for Parameters, locate the Parameters section and add the necessary parameters, such as reactor dimensions (reactor length, internal radius, and external radius), dispersion probabilities (p_p , p_b , p_a , and p_c), characteristics of the lamp (power, dimensions, and wavelength), catalyst charge, and optical properties of catalyst (absorption, κ_s ; dispersion, σ_s ; and extinction coefficients, β_s), from Table 1.
- (4) Global variable: go to Global definitions section and insert Variables. In the Settings windows for Variable, write the expression for radiation intensity (I_{rz}), according to (3) and (4).
- (5) Geometry: set reactor geometry as rectangular section that represents the 2D axial section of the reactor. It can be drawn as a simple rectangle.
- (6) Model definitions: in model definitions, insert section for variables. In the Settings windows for Variable, insert the LVREA expression. It can be introduced with (15).
- (7) Set of differential equations: in the ODE interfaces, select all domains. Go to the ODE general form window settings and introduce the differential equations system defined for (7), (10), (11), and (12).

- (8) Incident intensity boundary: in ODE interfaces, insert a Dirichlet boundary condition. In this setting section, select the internal boundary (inner radius of reaction section). Locate boundary condition field and introduce (13a).
- (9) External wall boundary condition: in ODE interfaces, insert a Dirichlet boundary condition. In this setting section, select the external boundary (external radius of reaction section). Locate boundary condition field and introduce (13b).
- (10) Upper and bottom wall boundary condition: in ODE interfaces, insert a Dirichlet boundary condition. In this setting section, select the upper and bottom boundary. Locate boundary condition field and introduce (13c).
- (11) Weak form of ODE: in ODE interfaces, insert a Weak Form for ODE condition. In this setting section, select all domains. In Weak expression field, introduce the following expressions:

WEAK = 0; 0; $-\text{test}(\text{gaz}) * \text{gaz} + \text{test}(\text{ga}); -\text{test}(\text{gcz}) * \text{gcz} + \text{test}(\text{gc}).$

- (12) Mesh: in the mesh section, introduce a mesh using the option of free quadratic mesh. You can try different mesh sizes. In free quadratic mesh, add distribution, select inner wall and locate the input section, and introduce 500 in number of elements.
- (13) Go to the study section and Run model.

B. Simulation of Radiant Field Employing the Discrete Ordinate Method (DOM) in Comsol Multiphysics v. 4.4

- (1) Model 3D: from the File menu, choose New. In the New window, click Model Wizard and select a 3D model.
- (2) Radiation in participating media: in the Select Physics tree, select Heat Transfer > Radiation > Radiation in Participating Media (rpm). Click Add. The Study is Stationary.
- (3) Parameters: go to Global definitions section and insert Parameters. In the Settings window for Parameters, locate the Parameters section and add the necessary parameters, such as reactor dimensions (reactor length, internal radius, and external radius), characteristics of the lamp (power, dimensions, and wavelength), catalyst charge, and optical properties of catalyst (absorption, κ_s ; dispersion, σ_s ; and extinction coefficients, β_s)
- (4) Global variable: go to Global definitions section and insert variables. In the Settings windows for Variable, write the expression for radiation intensity (Irz), according to (3) and (4).

- (5) Geometry: set reactor geometry as annular section. It can be drawn as a Boolean difference from two cylinders.
- (6) Model definitions: in model definitions, insert section for variables. In the Setting windows for Variable, insert the LVREA expression. It can be introduced as $\text{LVREA} = \text{rpm} \cdot G \cdot \kappa_a$.
- (7) Radiation in participating media (rpm): in the physics for radiation in participating media go to Radiation with participating media window settings and introduce dispersion and absorption coefficients in the model input sections.
- (8) In radiation in participating media, insert Incident intensity section. In this setting section, select the internal boundaries. Locate the incident intensity field and introduce Irz variable.
- (9) Opaque surface: in radiation in participating media, insert opaque surface. In the setting section, select external boundaries of contours of the domain. In wall adjust, select Black Wall.
- (10) Mesh: in the mesh section, introduce a mesh using the option of free tetrahedral mesh. You can try different mesh sizes. A too fine mesh can cause the available RAM to be exceeded.
- (11) Go to the study section and Run model.

Nomenclature

a_{lamp} :	Area of lamp (m^2)
a_p :	Catalytic particle area (m^2)
C_{AB} :	Benzyllic acid concentration ($\text{mol} \cdot \text{dm}^{-3}$)
C_{cat} :	Catalyst concentration ($\text{kg} \cdot \text{m}^{-3}$)
g_f :	Flux incident radiation ($\text{Watts} \cdot \text{m}^{-2}$)
g_a :	Upwards flux scattering radiation ($\text{Watts} \cdot \text{m}^{-2}$)
g_b :	Flux backscattering radiation ($\text{Watts} \cdot \text{m}^{-2}$)
g_c :	Downwards flux scattering radiation ($\text{Watts} \cdot \text{m}^{-2}$)
I_λ :	Spectral radiation intensity ($\text{Watts} \cdot \text{m}^{-2} \cdot \text{sr}^{-1}$)
K_{Ap} :	Apparent reaction constant (s^{-1})
k_{r1} :	Intrinsic reaction constant without catalyst (s^{-1})
k_{r2} :	Reaction constant with catalyst (s^{-1})
k_{r3} :	Intrinsic reaction constant with catalyst ($\text{Watts}^{(-m)} \cdot \text{m}^{(3m)}$)
L :	Length (m)
L_{lamp} :	Length of lamp (m)
L_{Reac} :	Length of the reactor (m)
LVREA:	Local volumetric rate of absorption of energy ($\text{Watts} \cdot \text{m}^{-3}$)
m :	Reaction order with respect to LVREA
n_p :	Number of catalyst particles (m^{-3})
p_a :	Probabilities of scattering toward up
p_b :	Probabilities of backscattering
p_f :	Probabilities of forward scattering
$p(\Omega \rightarrow \Omega')$:	Phase function

r :	Radial coordinate (m)
R_{int} :	Inner radius of the annulus (m)
R_{lamp} :	Radius of lamp (m)
R_R :	Radius of reactor (m)
t :	Time (h)
V :	Volume (m^3)
X :	Conversion
z :	Coordinate axial (m).

Greek Letters

β_λ :	Extinction coefficient (m^{-1})
Δ :	Thickness of the annulus (m)
κ_λ :	Absorption coefficient (m^{-1})
λ :	Wavelength
σ_λ :	Scattering coefficient (m^{-1})
ω :	Albedo coefficient
Ω :	Solid angle (sr).

Acronyms

DOM:	Discrete ordinate method
FFM:	Four-flux model
LVREA:	Local volumetric rate of energy absorption
LHHW:	Langmuir-Hinshelwood-Hougen-Watson kinetic model
MC:	Monte Carlo model
RTE:	Radiation transfer equation
SFM:	Six-flux model
TFM:	Two-flux model
TFSIW:	Thin-film slurry reactor of inner wall.

Conflicts of Interest

The authors declare that they have no conflicts of interest.

Acknowledgments

The authors are grateful to PRODEP for the financial support through Project 103.5/13/5257 and CONACYT through Project 269093. Mr. O. Alvarado-Rolon is grateful to CONACYT for the financial support (Scholarship 401273) to conduct postgraduate studies. Citlalit Martínez Soto is acknowledged for the technical support.

References

- [1] H. I. De Lasa, B. Serrano, and M. Salaices, *Photocatalytic Reaction Engineering*, Springer, 2005, April 2016 <http://link.springer.com/content/pdf/10.1007/0-387-27591-6.pdf>.
- [2] L. F. Garcés Giraldo, E. A. Mejía Franco, and J. J. Santamaría Arango, "La fotocatálisis como alternativa para el tratamiento de aguas residuales," *Revista Lasallista de investigación*, vol. 1, pp. 83–92, 2004.
- [3] G. Li Puma and P. L. Yue, "A novel fountain photocatalytic reactor for water treatment and purification: modeling and design," *Industrial and Engineering Chemistry Research*, vol. 40, no. 23, pp. 5162–5169, 2001.
- [4] L. Zhang, W. Anderson, and Z. Zhang, "Development and modeling of a rotating disc photocatalytic reactor for wastewater treatment," *Chemical Engineering Journal*, vol. 121, no. 2-3, pp. 125–134, 2006.
- [5] G. Li Puma, J. N. Khor, and A. Brucato, "Modeling of an annular photocatalytic reactor for water purification: oxidation of pesticides," *Environmental Science & Technology*, vol. 38, no. 13, pp. 3737–3745, 2004.
- [6] G. Li Puma and P. L. Yue, "Modelling and design of thin-film slurry photocatalytic reactors for water purification," *Chemical Engineering Science*, vol. 58, no. 11, pp. 2269–2281, 2003.
- [7] G. E. Imoberdorf, A. E. Cassano, H. A. Irazoqui, and O. M. Alfano, "Simulation of a multi-annular photocatalytic reactor for degradation of perchloroethylene in air: parametric analysis of radiative energy efficiencies," *Chemical Engineering Science*, vol. 62, no. 4, pp. 1138–1154, 2007.
- [8] F. Shiraiishi, T. Nomura, S. Yamaguchi, and Y. Ohbuchi, "Rapid removal of trace HCHO from indoor air by an air purifier consisting of a continuous concentrator and photocatalytic reactor and its computer simulation," *Chemical Engineering Journal*, vol. 127, no. 1–3, pp. 157–165, 2007.
- [9] S. Romero-Vargas Castrillón and H. I. de Lasa, "Performance evaluation of photocatalytic reactors for air purification using computational fluid dynamics (CFD)," *Industrial and Engineering Chemistry Research*, vol. 46, no. 18, pp. 5867–5880, 2007.
- [10] V. Augugliaro, H. Kisch, V. Loddo et al., "Photocatalytic oxidation of aromatic alcohols to aldehydes in aqueous suspension of home prepared titanium dioxide," *Applied Catalysis A: General*, vol. 349, no. 1-2, pp. 189–197, 2008.
- [11] S. Higashimoto, N. Kitao, N. Yoshida et al., "Selective photocatalytic oxidation of benzyl alcohol and its derivatives into corresponding aldehydes by molecular oxygen on titanium dioxide under visible light irradiation," *Journal of Catalysis*, vol. 266, no. 2, pp. 279–285, 2009.
- [12] N. Qi, H. Zhang, B. Jin, and K. Zhang, "CFD modelling of hydrodynamics and degradation kinetics in an annular slurry photocatalytic reactor for wastewater treatment," *Chemical Engineering Journal*, vol. 172, no. 1, pp. 84–95, 2011.
- [13] A. Gora, B. Toepfer, V. Puddu, and G. Li Puma, "Photocatalytic oxidation of herbicides in single-component and multi-component systems: reaction kinetics analysis," *Applied Catalysis B: Environmental*, vol. 65, no. 1-2, pp. 1–10, 2006.
- [14] G. Li Puma, "Modeling of thin-film slurry photocatalytic reactors affected by radiation scattering," *Environmental Science & Technology*, vol. 37, no. 24, pp. 5783–5791, 2003.
- [15] G. Li puma, "Dimensionless analysis of photocatalytic reactors using suspended solid photocatalysts," *Chemical Engineering Research and Design*, vol. 83, no. 7, pp. 820–826, 2005.
- [16] A. Brucato, A. E. Cassano, F. Grisafi, G. Montante, L. Rizzuti, and G. Vella, "Estimating radiant fields in flat heterogeneous photoreactors by the six-flux model," *AIChE Journal*, vol. 52, no. 11, pp. 3882–3890, 2006.
- [17] G. Li Puma and A. Brucato, "Dimensionless analysis of slurry photocatalytic reactors using two-flux and six-flux radiation absorption-scattering models," *Catalysis Today*, vol. 122, no. 1-2, pp. 78–90, 2007.
- [18] G. Li Puma, V. Puddu, H. K. Tsang, A. Gora, and B. Toepfer, "Photocatalytic oxidation of multicomponent mixtures of estrogens (estrone (E1), 17 β -estradiol (E2), 17 α -ethynylestradiol (EE2) and estriol (E3)) under UVA and UVC

- radiation: photon absorption, quantum yields and rate constants independent of photon absorption," *Applied Catalysis B: Environmental*, vol. 99, no. 3-4, pp. 388-397, 2010.
- [19] G. E. Imoberdorf, A. E. Cassano, H. A. Irazoqui, and O. M. Alfano, "Optimal design and modeling of annular photocatalytic wall reactors," *Catalysis Today*, vol. 129, no. 1-2, pp. 118-126, 2007.
 - [20] V. K. Pareek and A. A. Adesina, "Light intensity distribution in a photocatalytic reactor using finite volume," *AIChE Journal*, vol. 50, no. 6, pp. 1273-1288, 2004.
 - [21] M. e. M. Zekri and C. Colbeau-Justin, "A mathematical model to describe the photocatalytic reality: what is the probability that a photon does its job?," *Chemical Engineering Journal*, vol. 225, pp. 547-557, 2013.
 - [22] M. L. Satuf, R. J. Brandi, A. E. Cassano, and O. M. Alfano, "Scaling-up of slurry reactors for the photocatalytic degradation of 4-chlorophenol," *Catalysis Today*, vol. 129, no. 1-2, pp. 110-117, 2007.
 - [23] M. L. Satuf, R. J. Brandi, A. E. Cassano, and O. M. Alfano, "Modeling of a flat plate, slurry reactor for the photocatalytic degradation of 4-chlorophenol," *International Journal of Chemical Reactor Engineering*, vol. 5, no. 1, 2007.
 - [24] S. L. Orozco, C. A. Arancibia-Bulnes, and R. Suárez-Parra, "Radiation absorption and degradation of an azo dye in a hybrid photocatalytic reactor," *Chemical Engineering Science*, vol. 64, no. 9, pp. 2173-2185, 2009.
 - [25] Y. Boyjoo, M. Ang, and V. Pareek, "Light intensity distribution in multi-lamp photocatalytic reactors," *Chemical Engineering Science*, vol. 93, pp. 11-21, 2013.
 - [26] M. L. Satuf, R. J. Brandi, A. E. Cassano, and O. M. Alfano, "Experimental method to evaluate the optical properties of aqueous titanium dioxide suspensions," *Industrial and Engineering Chemistry Research*, vol. 44, no. 17, pp. 6643-6649, 2005.
 - [27] G. Sagawe, M. L. Satuf, R. J. Brandi et al., "Analysis of photocatalytic reactors employing the photonic efficiency and the removal efficiency parameters: degradation of radiation absorbing and nonabsorbing pollutants," *Industrial and Engineering Chemistry Research*, vol. 49, no. 15, pp. 6898-6908, 2010.
 - [28] J. Moreira, B. Serrano, A. Ortiz, and H. de Lasa, "Evaluation of photon absorption in an aqueous TiO₂ slurry reactor using Monte Carlo simulations and macroscopic balance," *Industrial and Engineering Chemistry Research*, vol. 49, no. 21, pp. 10524-10534, 2010.
 - [29] J. Moreira, B. Serrano, A. Ortiz, and H. de Lasa, "TiO₂ absorption and scattering coefficients using Monte Carlo method and macroscopic balances in a photo-CREC unit," *Chemical Engineering Science*, vol. 66, no. 23, pp. 5813-5821, 2011.
 - [30] G. L. Puma and P. L. Yue, "A laminar falling film slurry photocatalytic reactor. Part I—model development," *Chemical Engineering Science*, vol. 53, no. 16, pp. 2993-3006, 1998.
 - [31] L. Hurtado, R. Natividad, E. Torres-García, J. Farias, and G. Li Puma, "Correlating the photocatalytic activity and the optical properties of LiVMoO₆ photocatalyst under the UV and the visible region of the solar radiation spectrum," *Chemical Engineering Journal*, vol. 262, pp. 1284-1291, 2015.

Research Article

Determination of Ketorolac in the Effluent from a Hospital Treating Plant and Kinetics Study of Its Photolytic Degradation

Hector Hugo Ortega Soto, Jorge Javier Ramírez García, Paula Gamboa Suárez, and Angie Michelle Dávila Estrada

Laboratorio de Análisis Instrumental, Facultad de Química, Universidad Autónoma del Estado de México, Paseo Colón Esq. Paseo Toluca, 50120 Toluca, MEX, Mexico

Correspondence should be addressed to Jorge Javier Ramírez García; jjramirezg@uaemex.mx

Received 8 June 2017; Revised 20 November 2017; Accepted 23 November 2017; Published 31 December 2017

Academic Editor: Juan M. R. Rodriguez

Copyright © 2017 Hector Hugo Ortega Soto et al. This is an open access article distributed under the Creative Commons Attribution License, which permits unrestricted use, distribution, and reproduction in any medium, provided the original work is properly cited.

In this work, two specific, sensitive, and rapid analytical methods were developed. One of them was for the determination of ketorolac in a hospital wastewater treatment plant where there is no interference with other organic substances; the other one was for the determination of the degradation kinetics in aqueous medium. Ketorolac was extracted from wastewater samples through solid-phase extraction (SPE) cartridges, then it was identified and quantified by high-performance liquid chromatography (HPLC). Ketorolac was detected in concentrations between 0.1376 and 0.2667 $\mu\text{g/L}$. Photolytic degradation was performed on aqueous solutions of ketorolac tromethamine reference substance, at a concentration of 50 $\mu\text{g/mL}$. Samples were in direct contact with ultraviolet light in a dark chamber, equipped with two mercury lamps (254 nm) at a radiation source of 15 W. The results of the photolytic degradation were adjusted to a first-order model, obtaining a half-life of 4.8 hrs.

1. Introduction

Ketorolac is a drug that has analgesic, anti-inflammatory, and antipyretic properties and is indicated in the short-term treatment of mild to moderate pain postoperatively and in musculoskeletal trauma, in addition to pain caused by nephritic colic. This drug is contraindicated when the patient has active gastroduodenal ulcer, gastrointestinal bleeding, in patients with moderate or severe renal impairment [1].

The analgesic activity of ketorolac is due to the elimination of formation of prostaglandins, through the inhibition of the enzyme prostaglandin system [1]. The chemical structure of ketorolac is shown in Figure 1.

Ketorolac is metabolized by hydroxylation and conjugation with glucuronic acid. The renal route is the primary route of excretion of both the drug and its metabolites, which is approximately 92% of the dose, about 40% as metabolites

and 60% as ketorolac. Approximately 6% of the dose is excreted in feces [2].

Data obtained in a study to determine the toxic effects of ketorolac on *Cyprinus carpio*, Galar-Martínez and collaborators in 2014, concluded that ketorolac in a concentration range of 1 to 60 mg/L caused oxidative stress and cytotoxicity, specifically in the liver, brain, and blood.

Different authors indicate that the wastewater treatment plants do not remove the drugs in their entirety, because they do not have unitary operations that devote their process to the removal or elimination of drugs, since they depend on the physicochemical properties of each substance for which, in some cases, a decrease in the quantity of drugs after treatment barely persists [3–5].

Several studies have determined the presence of ketorolac in different matrices. For example, Gómez et al. in 2006 determined that the amount of ketorolac in the effluent of a hospital treatment plant ranged between 0.2 $\mu\text{g/L}$ and

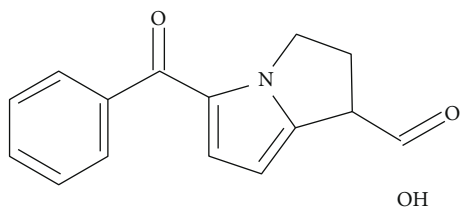


FIGURE 1: Chemical structure of ketorolac.

59.5 $\mu\text{g/L}$. Oliveira et al. in 2015 determined ketorolac in influent and effluent from wastewater treatment plants of different hospitals, finding it in concentration ranges from 0.03 $\mu\text{g/L}$ to 1.15 $\mu\text{g/L}$ [5, 6].

Because drug concentrations in wastewater are in the order of $\mu\text{g/L}$ and in some cases ng/L , the use of high-performance liquid chromatography coupled to a mass spectrometry detector is very common, which is significantly more sensitive than spectrophotometry detectors, but has the disadvantage that it is more expensive. However, the methodology presented in this research uses UV spectrophotometry detection, and a suitable sensitivity has been demonstrated by validation that can allow the quantification of ketorolac in wastewater in a less expensive way and can be replicated in other laboratories that do not have a mass spectrometry detector.

The objective of this work is to develop and validate analytical methodologies by high-resolution liquid chromatography for the quantification of ketorolac in wastewater of a hospital treatment plant and a second methodology that is capable of separating and quantifying ketorolac in solution and that can be used for the determination of the kinetics of photolytic degradation, and thus determine the persistence of ketorolac in the effluent of a hospital treatment plant.

2. Methodology

2.1. Materials and Instruments. Sigma-Aldrich® ketorolac tromethamine reference substance was used, formic acid of the brand Fermont® 88% analytical reagent grade. The Fermont brand chromatographic grade methanol and the water used were HPLC grade from the Millipore® Milli-Q brand purification equipment, and the cartridges used for solid-phase extraction (SPE) were Sep-Pak®, vac 6 cc (1 g) C18, corresponding to the Waters® brand.

The high-performance liquid chromatography equipment used for the development and validation of analytical methods was Waters brand and consisted of a model 1525 pump, a model 717 automatic injector system, and a model 2487 dual wave spectrophotometric detector. The software controller of the chromatographic system was Waters Breeze®.

2.2. Analytical Methodology

2.2.1. Quantification of Ketorolac in Wastewater. The reference solutions and samples used are of a concentration of 10 $\mu\text{g/mL}$ of ketorolac, using ketorolac tromethamine

reference substance, which is dissolved in chromatographic grade methanol.

The mobile phase is a mixture of methanol with acidified water in a ratio of 60%:40% v/v . The acidified water is prepared by the dilution of 5.6 mL of 88% formic acid brought to 1000 mL capacity with Milli-Q water.

Validation of the methodology and analysis of the samples were carried out under the following chromatographic conditions: the column used is an Agilent® Zorbax SB C8 brand of 250 \times 4.6 mm with a particle size of 5 μm , flow velocity of 1.0 mL/min, and injection volume of 20 μL at a wavelength for detection of 318 nm.

The samples from the hospital treatment plant were extracted by SPE; the cartridges were previously conditioned with 5 mL of methanol chromatographic grade and later with 5 mL of Milli-Q water. The extraction was carried out to 250 mL of residual water, at the end, washing was performed with 10 mL of Milli-Q water. The elution of the sample was performed with 5 mL of methanol chromatographic grade. This solution was injected into the liquid chromatograph under the above-described conditions and quantified by comparing the external standard of 10 $\mu\text{g/mL}$ of ketorolac.

2.2.2. Ketorolac Determination in Aqueous Solution. The reference solutions and samples used are of a concentration of 50 $\mu\text{g/mL}$ of ketorolac, using ketorolac tromethamine reference substance, which is dissolved in Milli-Q water.

The mobile phase is a mixture of methanol with acidified water in a 50%:50% v/v ratio. The acidified water is prepared by the dilution of 5.6 mL of 88% formic acid and brought to 1000 mL capacity with Milli-Q water.

Validation of the methodology and analysis of the samples were carried out under the following chromatographic conditions: the column used is an Agilent Zorbax SB C8 brand of 250 \times 4.6 mm with a particle size of 5 μm ; flow rate of 1.5 mL/min; the injection volume of 20 μL at a wavelength for detection of 323 nm.

2.2.3. Validation of the Analytical Method. The analytical methodologies were validated based on the guide for the validation of analytical methods of the International Conference on Harmonization (ICH) determining the parameters of specificity, suitability, system accuracy, system linearity, method linearity, repeatability, detection, and quantification limits [7].

The evaluation of the specificity was carried out by means of the injection, under the previously described conditions, from different samples that could interfere with the ketorolac analytical signal. These injected samples belong to a target, reference solution, and forced degradations by stress conditions of the reference solutions (acid, basic, and photolytic degradation).

A sixfold injection of a ketorolac reference solution determined the suitability of the system. The calculation of the chromatographic parameters was performed using the Breeze liquid chromatograph software.

The determination of linearity of the system was performed by analyzing 8 levels of ketorolac reference concentration (by triplicate), corresponding to 10% to 400%

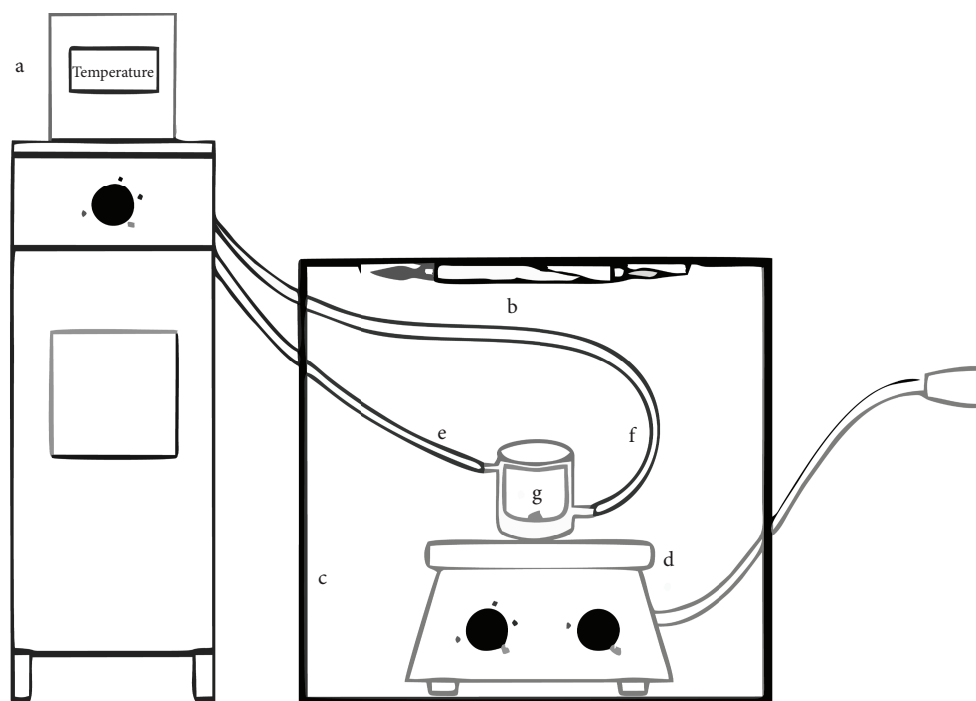


FIGURE 2: Photolytic degradation: (a) water, (b) radiation source, (c) container, (d) agitation plate, (e) and (f) in and off recirculation water, and (g) reaction cell.

of the working concentration ($10 \mu\text{g/mL}$ for the residual water quantification and $50 \mu\text{g/mL}$ for determination of photolytic degradation). The slope, ordered to the origin, and coefficient of determination by linear regression were calculated, in addition to the calculation of confidence interval for the slope ($IC_{\beta 1}$).

The precision parameter was performed at three levels: system, repeatability, and intermediate accuracy. The evaluation of the precision of the system was carried out by the injection of 6 reference solutions of ketorolac at work concentration, coming from the same stock, calculating the average, standard deviation, and coefficient of variation.

The determination of the repeatability was performed by independently preparing a sixfold solution of ketorolac at the working concentration, for its subsequent quantification with the comparison with an external standard, determining the percentage of recovery, the average recovery rate of the six solutions, the standard deviation, and the coefficient of variation.

Intermediate precision was evaluated by quantifying 3 samples containing the working concentration; the analysis was carried out by 2 analysts on two different days ($n = 12$). The average of recovery, standard deviation, and coefficient of variation was obtained.

Accuracy was determined by calculating the recovery of three levels of ketorolac in triplicate ($n = 9$), quantification using an external standard, and obtaining the recovery of each of the samples, the mean recovery, the standard deviation, coefficient of variation, and confidence interval for the mean (IC_{μ}).

The limits of detection and quantification were determined by performing a calibration curve at three levels of

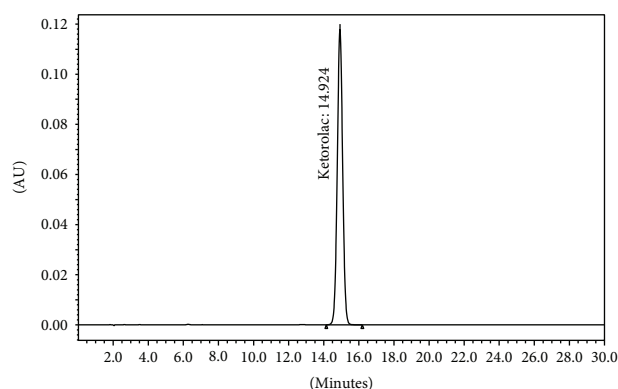


FIGURE 3: Chromatogram for the reference solution of ketorolac.

concentration. Subsequently, the slope, ordered to the origin, standard deviation of the regression, and coefficient of determination were calculated, all by linear regression.

2.2.4. Quantification of Wastewater Samples from the Treatment Plant. The samples were taken in a timely manner from a wastewater treatment plant of a hospital located in the city of Toluca, in the state of Mexico, Mexico. The samples were refrigerated immediately after being taken for further processing by SPE using the methodology indicated above.

2.3. Photolytic Degradation Kinetics. The system for the determination of degradation kinetics consists mainly of the following components: a quartz cell placed on a stirring grid that contains the sample and allows the flow

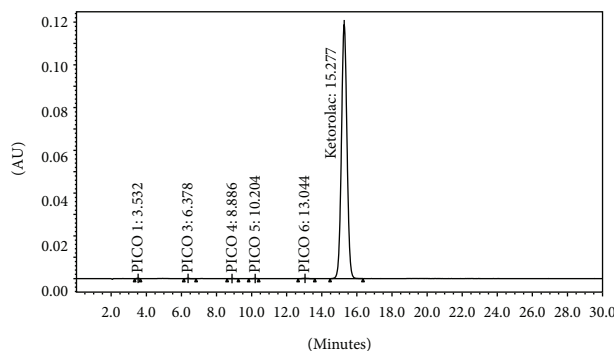


FIGURE 4: Chromatogram for the photolytic degradation of ketorolac and its degradation products.

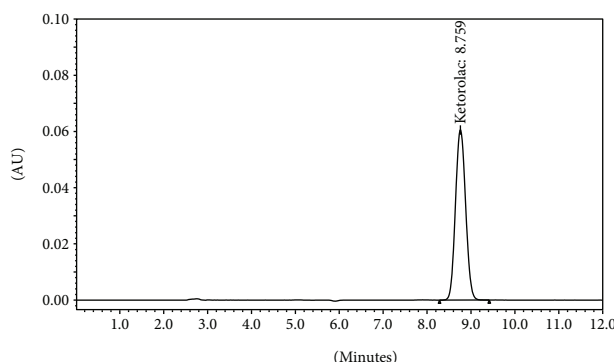


FIGURE 5: Chromatogram for the reference solution of ketorolac in wastewater determination.

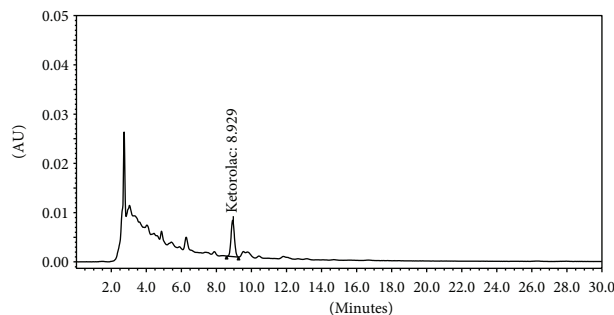


FIGURE 6: Chromatogram for the sample wastewater hospital treatment plant.

of radiation, a recirculating water bath keeping the cell at a constant temperature, and a source of UV radiation from a mercury lamp at 254 nm. These components were inside a glass tank lined with black polyethylene that prevents reflection of the radiation. Figure 2 shows the scheme for the photolytic degradation.

For the experimentation, 100 mL of a solution of ketorolac in water with a concentration of 50 $\mu\text{g/mL}$ (2.0×10^{-4} mol/L approx.) was placed inside the reaction cell and initiated the radiation, keeping the temperature of the cell at 18°C. Samples of 2 mL of the ketorolac solution were taken at different times. Subsequently, each sample was placed inside vials for analysis

TABLE 1: Suitability results for the system.

Parameter	Ketorolac in wastewater	Ketorolac and degradation products
Retention time (Rt)	8.7 min	14.1 min
Peak area	973919.0	2888463.2
Theoretical plates (N)	6830.1	11096.6
Capacity factor (K')	3.9	6.8
Tailing (T)	1.1	1.0

TABLE 2: Precision results for ketorolac in wastewater.

	Precision of the system ($n = 6$)	Precision Repeatability ($n = 6$)	Interday precision ($n = 12$)
Average	956364.8	99.8	99.8
Standard deviation	7733.2	0.7	1.8
RSD (%)	0.8	0.7	1.8
Statistic $T_{0.95}$	—	2.571	—
$IC_{(\mu)}$	—	100.6	—
	—	99.1	—

TABLE 3: Precision results for ketorolac and its degradation products.

	Precision of the system ($n = 6$)	Precision Repeatability ($n = 6$)	Interday precision ($n = 12$)
Average	2911596.8	101.1	100.1
Standard deviation	41727.1	1.0	0.9
RSD (%)	1.4	1.0	0.9
Statistic $T_{0.95}$	—	2.571	—
$IC_{(\mu)}$	—	102.17	—
	—	100.01	—

TABLE 4: Linearity results for the system.

Parameter	Ketorolac in wastewater	Ketorolac and degradation products
Slope	96078.6	61337.7
Origin	-21767.2	-29360.2
Range	2.07–41.5	5.05–107.8
R^2	0.9970	0.9986
$IC_{(\beta_0)}$	93773.5–98383.7	60356.8–62318.6

by HPLC under the conditions described above. This methodology was carried out in triplicate for each of the radiations.

3. Results and Discussion

3.1. Analytical Method Validation for the Quantification of Ketorolac and Its Degradation Products. The specificity of the analytical methodologies was demonstrated by the chromatograms obtained from the individual injection of

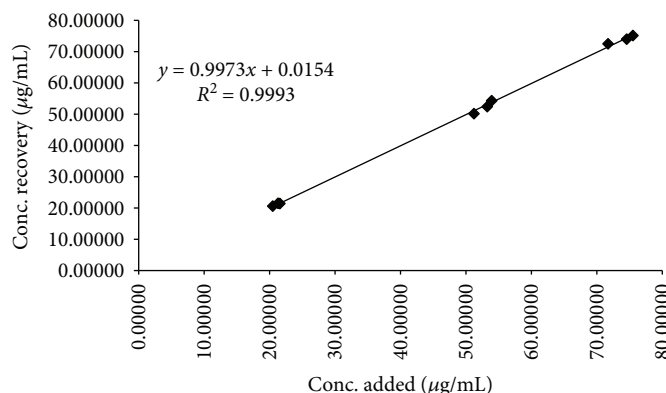


FIGURE 10: Accuracy for ketorolac in the degradation products.

factor. Table 1 shows the results obtained in the test for the two methodologies.

The results obtained in the precision parameter for quantification of ketorolac in residual water are shown in Table 2.

The results obtained in the precision parameter for quantification of ketorolac and degradation products are shown in Table 3.

The linearity was evaluated at 8 levels of concentration and in the two methodologies with a coefficient of determination > 0.98 . Table 4 shows the results obtained for the linearity of the system.

Figures 7 and 8 show graphs with concentration versus area under the curve for the linearity of the system.

The accuracy of the method was determined by quantifying added water with an exact amount of ketorolac at three concentration levels, by triplicate each.

In the case of the determination of ketorolac in residual water, the levels of 40%, 100%, and 400% were evaluated. The results are shown in Table 5, and in all samples analyzed, a recovery between 98.0% and 102.5% is obtained, obtaining a global average ($n=9$) of 100.0%, with a coefficient of variation of 1.8%.

Graphing the data added quantity versus quantity recovered gives a coefficient of determination of 0.999 and slope of 0.9931, and the ordinate to the origin passes through zero (Figure 9).

The accuracy results obtained for ketorolac and degradation products are shown in Table 6; all recovery results are between 98.0% and 101.2%, with a global mean ($n=9$) of 99.8% and a coefficient of variation of 1.1%. By plotting the added concentration versus concentration recovered (Figure 10), a coefficient of determination (R^2) of 0.9993 was obtained as well as a slope of 0.9973, and an ordinate to the origin is near zero.

The limit of detection and quantification for both methodologies was determined by analyzing a standard curve at low concentration levels.

For the quantification of ketorolac in residual water, the limit of detection and quantification were 0.00934 µg/mL and 0.02832 µg/mL, respectively, and R^2 was 0.998. The calibration curve obtained during the determination is shown in Figure 11.

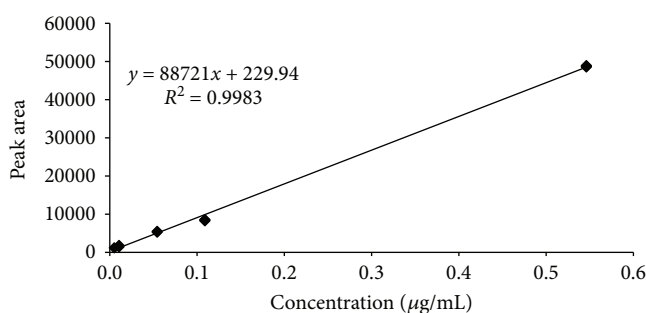


FIGURE 11: LOD and LOQ for ketorolac in wastewater.

Figure 12 shows the curve obtained for the limit of detection and quantification in the methodology for the determination of ketorolac in the presence of its degradation products, which obtained a coefficient of determination of 0.99998. The calculated limit of detection was 0.00283 µg/mL, while the quantification limit was 0.00859 µg/mL.

3.2. Quantification of Ketorolac in Wastewater from a Hospital Treatment Plant. The results obtained by high-resolution liquid chromatography on samples obtained from the effluent from a hospital wastewater treatment plant located in the city of Toluca, State of Mexico, Mexico, are shown in Table 7; each sample was analyzed by triplicate.

3.3. Photolytic Degradation Kinetics. The results obtained by the high-resolution liquid chromatography analysis on the samples generated in photolytic degradation with UV radiation are shown in Table 8.

These results, concentration (mol/L) with respect to time (h), can be observed in Figure 13.

With the data obtained in Table 8, calculations were made for the determination of the order of reaction according to the equations indicated by Fogler. Slope, ordered to the origin, and coefficient of determination (R^2) were determined in each of the reaction orders. The results are shown in Table 9.

As seen in Table 9, the order of reaction 1 or first order has the highest determination coefficient with respect to the others; doing a study of residuals, it is observed that there is no marked tendency.

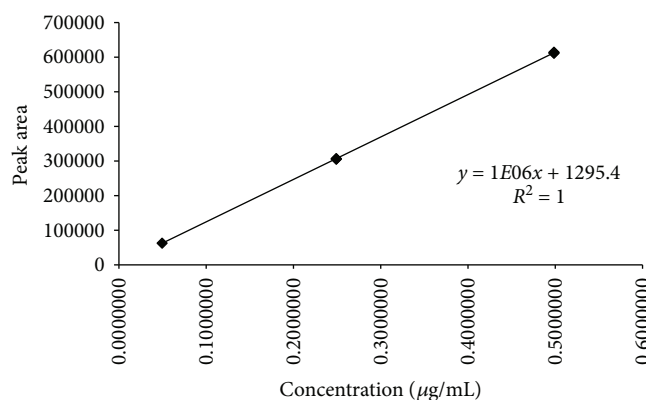


FIGURE 12: LOD and LOQ for ketorolac the degradation products.

TABLE 7: Quantification results for ketorolac samples in wastewater.

Sample	Conc. (µg/L)	Average	SD	RSD (%)	Global average (n = 9)	Global RSD
M1_1	0.2109					
M1_2	0.2424	0.2258	0.016	7.0		
M1_3	0.2242					
M2_1	0.2590					
M2_2	0.2667	0.2559	0.013	5.0	0.2117	22.3
M2_3	0.2419					
M3_1	0.1658					
M3_2	0.1376	0.1534	0.014	9.4		
M3_3	0.1568					

Figure 14 shows the first-order kinetics, as mentioned above. This is the model that best fits the data obtained by both coefficient of determination and study of residuals. The plot of residuals for the first-order kinetics for UV photolytic degradation of ketorolac is shown in Figure 15.

The results obtained during the validation process show that there are two methodologies, one for the quantification of ketorolac in residual water and another for the quantification of ketorolac and the presence of its photolytic degradation products, which are accurate and precise, with a limit of detection and quantification low enough to be able to identify and quantify the samples from hospital wastewater that was analyzed.

As observed in the chromatograms obtained in the specificity tests, there is no interference by the matrix or degradation products in the quantification of ketorolac; this can be due to two causes: the first is that there is a good separation between the ketorolac peak and the other components of the sample due to a good selection of the chromatographic conditions and the second is the working wavelength in the detector, since while most organic compounds have their maximum absorption in the region of the spectrum of 200 nm to about 260 nm, the ketorolac under these working conditions had its maximum at 323 nm and 318 nm, respectively.

TABLE 8: Degradation results for ketorolac with ultraviolet radiation.

Time (h)	Sample 1 Ketorolac (mol/L)	Sample 2 Ketorolac (mol/L)	Sample 3 Ketorolac (mol/L)
0	0.0001997875	0.0001997875	0.0001932206
0.5	0.0002023158	0.0002009421	0.0001949987
1	0.0002029341	0.0002005465	0.0001943721
3	0.0002083404	0.0001981625	0.0001913357
4	0.0002037832	0.0001924920	0.0001882330
5	0.0002009338	0.0001825738	0.0001775599
6	0.0002066012	0.0001646013	0.0001573098
7	0.0001835656	0.0001230821	0.0001170299
8	0.0001611106	0.0001001495	0.0000955237
9	0.0001383091	0.0000897662	0.0000864861
22	0.0000135506	0.0000051354	0.0000045894
25	0.0000097583	0.0000024875	0.0000023666
47	0.0000007281	0.0000004353	0.0000004399

The quantification of samples obtained from the effluent from the wastewater treatment plant from a hospital, after being treated by SPE, is as follows: an average concentration of 0.2117 µg/L was obtained, with a CV of 22.3%, which can be considered high and may be due to the type of point sampling and the treatment that was performed, which causes a wide variation.

The results of quantification of ketorolac in wastewater shows that it can be used for this purpose; it is true that liquid chromatography coupled to mass spectrometry detector systems are the most used for this type of application because of their greater sensitivity and more specialized handling; nevertheless, it represents higher costs. That is why, the methodology proposed in this research uses a spectrophotometry detector which is cheaper and widely used; with the results obtained, the samples can be considered as an option in the quantification of traces of ketorolac in residual water.

When the data were obtained during photolytic degradation with UV radiation, it was determined that this kinetics is of the first order, so that the data conform to 1 [8], since the

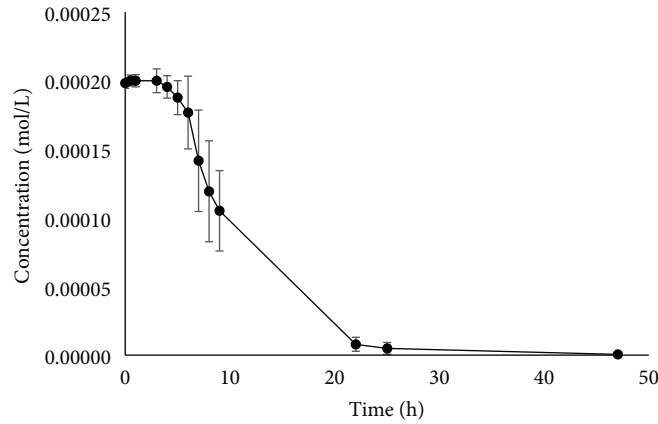


FIGURE 13: Kinetics degradation of ketorolac with ultraviolet radiation.

TABLE 9: Determination of the degradation reaction order of ketorolac with ultraviolet radiation.

	Order zero	First order	Second order	Third order
R^2	0.79859	0.96387	0.79912	0.69190
Slope	$-5.3194E-06$	0.145164843	36424.29224	70745005450
Origin	0.00018896	-0.41326464	-191771.8568	$-4.20727E+11$

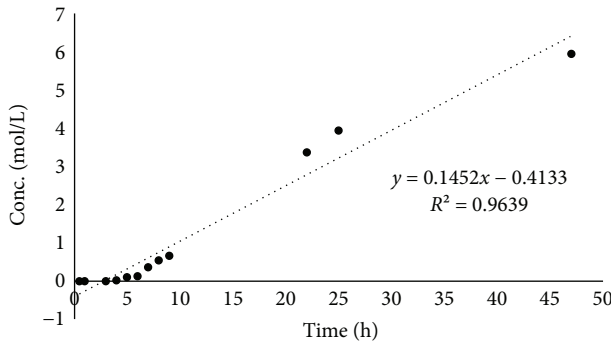


FIGURE 14: First-order kinetics degradation of ketorolac using UV radiation.

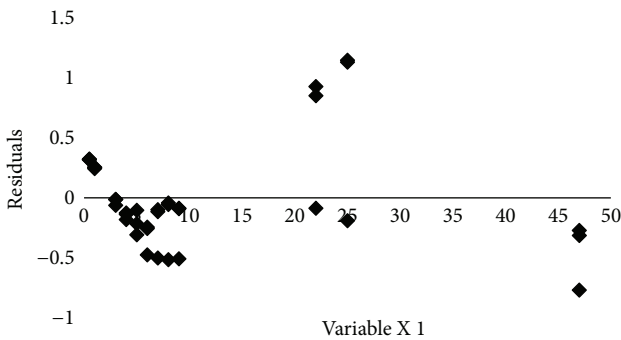


FIGURE 15: First-order residuals analysis.

correlation coefficient was greater than 0.98, in addition to the fact that the study of residuals does not indicate that there is a trend in error:

$$\ln \frac{C_0}{C_A} = k t. \quad (1)$$

By deducing from the above equation, we can obtain the average half-life for UV radiation which is 4.8 hours.

$$t_{1/2} = \frac{\ln(C_0/C_{1/2})}{k}. \quad (2)$$

4. Conclusions

Two analytical methodologies were obtained for the quantification of ketorolac, the first for its quantification in residual water and the second for the determination of its photolytic degradation products. In both cases, it is guaranteed that the results obtained by these methodologies are reliable because they comply completely with the validation parameters studied.

The quantification of ketorolac in residual water of a wastewater treatment plant of a hospital located in the city of Toluca, Mexico, was carried out, resulting in an average concentration of $0.2117 \mu\text{g/L}$.

Photolytic degradation kinetics studies for ketorolac show that it is of the first order with a half-life of 4.8 hours for degradation with UV radiation.

Conflicts of Interest

The authors declare that they have no conflicts of interest.

Acknowledgments

The authors are grateful to the National Council of Science and Technology (CONACYT) for financing through “Scientific Development Projects to Solve National Problems” with Key 215997. Thanks are also due to CONACYT for the scholarship 501830.

References

- [1] A. L. Olives, V. González-Ruiz, and M. A. Martín, “Insolation and quantitative methods for analysis of non-steroidal anti-inflammatory drugs,” *Anti-Inflammatory & Anti-Allergy Agents in Medicinal Chemistry*, vol. 11, no. 1, pp. 65–95, 2012.
- [2] “U.S. Food And Drug Administration,” July 2015 http://www.accessdata.fda.gov/drugsatfda_docs/nda/2010/022382Orig1s000Approv.pdf.
- [3] R. Amdany, L. Chimuka, and E. Cukrowska, “Determination of naproxen, ibuprofen and triclosan in wastewater using the polar organic chemical integrative sampler (POCIS): a laboratory calibration and field application,” *Water SA*, vol. 40, no. 3, pp. 407–414, 2014.
- [4] M. J. Martínez Bueno, S. Herrera, D. Munaron et al., “POCIS passive samplers as a monitoring tool for pharmaceutical residues and their transformation products in marine environment,” *Environmental Science and Pollution Research*, vol. 23, no. 6, pp. 5019–5029, 2016.
- [5] T. S. Oliveira, M. Murphy, N. Mendola, V. Wong, D. Carlson, and L. Waring, “Characterization of pharmaceuticals and personal care products in hospital effluent and waste water influent/effluent by direct-injection LC-MS-MS,” *Science of the Total Environment*, vol. 518-519, pp. 459–478, 2015.
- [6] M. J. Gómez, M. Petrovic, A. R. Fernández-Alba, and D. Barceló, “Determination of pharmaceuticals of various therapeutic classes by solid-phase extraction and liquid chromatography-tandem mass spectrometry analysis in hospital effluent wastewaters,” *Journal of Chromatography A*, vol. 1114, no. 2, pp. 224–233, 2006.
- [7] International Conference on Harmonisation, *ICH Harmonised Tripartite Guideline. Validation of Analytical Procedures: Text and Methodology Q2(R1)*, 2005.
- [8] S. Fogler, *Elements of Chemical Reaction Engineering*, New Delhi, Prentice-Hall of India Private Limited, 3th edition, 2004.